



ATLAS Note

GROUP-2017-XX



23rd April 2021

Draft version 0.1

1

2 **A Deep Learning Approach to Differential**
3 **Measurements of Higgs - Top Interactions in**
4 **Multilepton Final States**

5

The ATLAS Collaboration

6 Several theories Beyond the Standard Model modify the momentum spectrum of the Higgs
7 Boson, without significantly altering the overall rate of Higgs produced from top quark pairs.
8 A differential measurement of the Higgs transverse momentum provides a way to search for
9 these effects at the LHC. Because of the challenges inherent to reconstructing the Higgs in
10 multilepton final states, a deep learning approach is used to predict the momentum spectrum
11 of the Higgs for events where the Higgs Boson is produced from top quark pairs and decays
12 to final states that include multiple leptons. The regressed Higgs p_T is fit to data for events
13 with two or three leptons in the final state, and estimates of the sensitivity to variations in the
14 Higgs p_T spectrum are given.

© 2021 CERN for the benefit of the ATLAS Collaboration.

15 Reproduction of this article or parts of it is allowed as specified in the CC-BY-4.0 license.

16 **Contents**

| | | |
|----|--|----|
| 17 | I Introduction | 7 |
| 18 | 1 Introduction | 7 |
| 19 | II Theoretical Motivation | 10 |
| 20 | 2 The Standard Model and the Higgs Boson | 10 |
| 21 | 2.1 The Forces and Particles of the Standard Model | 10 |
| 22 | 2.2 The Higgs Mechanism | 13 |
| 23 | 2.2.1 The Higgs Field | 13 |
| 24 | 2.2.2 Electroweak Symmetry Breaking | 15 |
| 25 | 2.3 $t\bar{t}H$ Production | 18 |
| 26 | 2.4 WZ + Heavy Flavor Production | 20 |
| 27 | 2.5 Extensions to the Standard Model | 21 |
| 28 | III The LHC and the ATLAS Detector | 24 |
| 29 | 3 The LHC | 24 |
| 30 | 4 The ATLAS Detector | 27 |
| 31 | 4.1 Inner Detector | 28 |
| 32 | 4.2 Calorimeters | 30 |
| 33 | 4.3 Muon Spectrometer | 31 |
| 34 | 4.4 Trigger System | 32 |
| 35 | IV Measurement of WZ + Heavy Flavor | 33 |
| 36 | 5 Introduction | 33 |
| 37 | 6 Data and Monte Carlo Samples | 35 |
| 38 | 6.1 Data Samples | 35 |
| 39 | 6.2 Monte Carlo Samples | 35 |
| 40 | 7 Object Reconstruction | 36 |
| 41 | 7.1 Trigger | 37 |
| 42 | 7.2 Light leptons | 37 |
| 43 | 7.3 Jets | 38 |
| 44 | 7.4 B-tagged Jets | 39 |
| 45 | 7.5 Missing transverse energy | 41 |

| | | |
|----|--|------------|
| 46 | 7.6 Overlap removal | 41 |
| 47 | 8 Event Selection and Signal Region Definitions | 42 |
| 48 | 8.1 Event Preselection | 42 |
| 49 | 8.2 Fit Regions | 47 |
| 50 | 8.3 Non-Prompt Lepton Estimation | 64 |
| 51 | 8.3.1 $t\bar{t}$ Validation | 64 |
| 52 | 8.3.2 Z+jets Validation | 70 |
| 53 | 9 tZ Interference Studies and Separation Multivariate Analysis | 75 |
| 54 | 9.1 Top Mass Reconstruction | 75 |
| 55 | 9.2 tZ BDT | 77 |
| 56 | 10 Data and Monte Carlo Samples | 82 |
| 57 | 10.1 Data Samples | 82 |
| 58 | 10.2 Monte Carlo Samples | 82 |
| 59 | 11 Object Reconstruction | 83 |
| 60 | 11.1 Trigger | 84 |
| 61 | 11.2 Light leptons | 84 |
| 62 | 11.3 Jets | 85 |
| 63 | 11.4 B-tagged Jets | 86 |
| 64 | 11.5 Missing transverse energy | 88 |
| 65 | 11.6 Overlap removal | 88 |
| 66 | 12 Event Selection and Signal Region Definitions | 89 |
| 67 | 12.1 Event Preselection | 89 |
| 68 | 12.2 Fit Regions | 94 |
| 69 | 12.3 Non-Prompt Lepton Estimation | 111 |
| 70 | 12.3.1 $t\bar{t}$ Validation | 111 |
| 71 | 12.3.2 Z+jets Validation | 117 |
| 72 | 13 tZ Interference Studies and Separation Multivariate Analysis | 122 |
| 73 | 13.1 Top Mass Reconstruction | 122 |
| 74 | 13.2 tZ BDT | 124 |
| 75 | 14 Systematic Uncertainties | 128 |
| 76 | 15 Results | 137 |
| 77 | 15.1 1-jet Fit Results | 138 |
| 78 | 15.2 2-jet Fit Results | 147 |

| | | |
|------------|---|------------|
| 79 | V Differential Studies of $t\bar{t}H$ Multilepton | 156 |
| 80 | 16 Data and Monte Carlo Samples | 156 |
| 81 | 16.1 Data Samples | 157 |
| 82 | 16.2 Monte Carlo Samples | 157 |
| 83 | 17 Object Reconstruction | 159 |
| 84 | 17.1 Trigger Requirements | 160 |
| 85 | 17.2 Light Leptons | 160 |
| 86 | 17.3 Jets | 161 |
| 87 | 17.4 Missing Transverse Energy | 162 |
| 88 | 17.5 Overlap removal | 162 |
| 89 | 18 Higgs Momentum Reconstruction | 163 |
| 90 | 18.1 Decay Candidate Reconstruction | 164 |
| 91 | 18.2 b-jet Identification | 165 |
| 92 | 18.2.1 2lSS Channel | 166 |
| 93 | 18.2.2 3l Channel | 171 |
| 94 | 18.3 Higgs Reconstruction | 174 |
| 95 | 18.3.1 2lSS Channel | 175 |
| 96 | 18.3.2 3l Semi-leptonic Channel | 179 |
| 97 | 18.3.3 3l Fully-leptonic Channel | 183 |
| 98 | 18.4 p_T Prediction | 187 |
| 99 | 18.4.1 2lSS Channel | 188 |
| 100 | 18.4.2 3l Semi-leptonic Channel | 191 |
| 101 | 18.4.3 3l Fully-leptonic Channel | 195 |
| 102 | 18.5 3l Decay Mode | 198 |
| 103 | 19 Signal Region Definitions | 200 |
| 104 | 19.1 Pre-MVA Event Selection | 201 |
| 105 | 19.2 Event MVA | 206 |
| 106 | 19.3 Signal Region Definitions | 214 |
| 107 | 20 Background Rejection MVA | 217 |
| 108 | 20.1 Pre-MVA Event Selection | 218 |
| 109 | 20.2 Event MVA | 220 |
| 110 | 20.3 Signal Region Definitions | 229 |
| 111 | 20.3.1 2lSS | 230 |
| 112 | 20.3.2 3l – Semi – leptonic | 230 |
| 113 | 20.3.3 3l – Fully – leptonic | 230 |
| 114 | 21 Systematic Uncertainties | 230 |
| 115 | 22 Results | 235 |
| 116 | 22.1 Results - 80 fb^{-1} | 236 |

| | | |
|-----|---|-----|
| 117 | 22.2 Projected Results - 140 fb ⁻¹ | 240 |
|-----|---|-----|

| | | |
|-----|----------------------|------------|
| 118 | VI Conclusion | 244 |
|-----|----------------------|------------|

| | | |
|-----|---|------------|
| 119 | Appendices | 251 |
| 120 | .1 Non-prompt lepton MVA | 251 |
| 121 | .2 Non-prompt CR Modelling | 256 |
| 122 | .3 tZ Interference Studies | 261 |
| 123 | .4 Alternate tZ Inclusive Fit | 265 |
| 124 | .4.1 tZ Inclusive Fit | 266 |
| 125 | .4.2 Floating tZ | 267 |
| 126 | .5 DSID list | 268 |
| 127 | A Machine Learning Models | 291 |
| 128 | A.1 Higgs Reconstruction Models | 291 |
| 129 | A.1.1 b-jet Identification Features - 2lSS | 291 |
| 130 | A.1.2 b-jet Identification Features - 3l | 295 |
| 131 | A.1.3 Higgs Reconstruction Features - 2lSS | 300 |
| 132 | A.1.4 Higgs Reconstruction Features - 3lS | 305 |
| 133 | A.1.5 Higgs Reconstruction Features - 3lF | 310 |
| 134 | A.2 Background Rejection MVAs | 314 |
| 135 | A.2.1 Background Rejection MVA Features - 2lSS | 314 |
| 136 | A.2.2 Background Rejection MVA Features - 3l | 318 |
| 137 | A.3 Alternate b-jet Identification Algorithm | 323 |
| 138 | A.4 Binary Classification of the Higgs p _T | 324 |
| 139 | A.5 Impact of Alternative Jet Selection | 325 |

140 Part I

141 Introduction

142 1 Introduction

143 Particle physics is an attempt to describe the fundamental building blocks of the universe and
144 their interactions. The Standard Model (SM) - our best current theory of fundamental particle
145 physics - does a remarkable job of that. All known fundamental particles and (almost) all of the
146 forces underlying their interactions can be explained by the SM, and the predictions from this
147 theory agree with experiment to an incredibly precise degree. This is especially true since the
148 Higgs Boson, the last piece of the SM predicted decades before, was finally discovered at the
149 Large Hadron Collider (LHC) in 2012.

150 Despite the success of the SM, there remains significant work to be done. For one, the
151 SM is incomplete: it fails to provide a description of gravity, to give an explanation for the
152 observation of Dark Matter, or to provide a mechanism for neutrinos to gain mass. Further, a
153 Higgs Boson with a mass of around 125 GeV, as observed at the LHC, gives rise to what is
154 known a hierarchy problem - such a low mass Higgs requires a seemingly unnatural level of “fine
155 tuning” that is unexplained by the SM.

156 A promising avenue for addressing these problems is to study the properties of the Higgs
157 Boson and the way it interacts with other particles, in part simply because these interactions

158 have not been measured before. Its interactions with the Top Quark are a particularly promising
159 place to look. Because the Higgs Field is responsible for allowing particle to acquire mass, the
160 strength of a particle's interaction with the Higgs Boson is proportional to its mass. As the most
161 massive of the fundamental particles, the Top Quark has the strongest coupling to the Higgs
162 Boson, meaning any new physics in the Higgs sector is likely to present itself most prominently
163 in its interaction with the Top Quark.

164 These interactions can be measured by directly by studying the production of a Higgs
165 Boson in association with a pair of Top Quarks ($t\bar{t}H$). While studies have been done measuring
166 the overall rate of $t\bar{t}H$ production, there are several theories of physics Beyond the Standard
167 Model (BSM) that would affect the kinematics of $t\bar{t}H$ production without altering its overall
168 rate. This dissertation attempts to make a differential measurement of the kinematics of the
169 Higgs Boson in $t\bar{t}H$ events in order to search for these BSM effects.

170 The proton-proton collision data collected by the ATLAS detector at the LHC from 2015-
171 2018 provides the opportunity to make this measurement for the first time. The unprecedented
172 energy achieved by the LHC during this period greatly increase the rate at which $t\bar{t}H$ events are
173 produced, and the large amount of data collected provides the necessary statistics for a differential
174 measurement to be performed.

175 A study of $t\bar{t}H$ events with multiple leptons in the final state is performed, using 139 fb^{-1}
176 of data from proton-proton collisions at an energy $\sqrt{s} = 13 \text{ TeV}$ collected by the ATLAS detector
177 from 2015-2018. Events are separated into channels based on the number of light leptons in the

178 final state - either two same-sign leptons, or three leptons. A deep neural network is used to
179 reconstruct the momentum of the Higgs Boson in each event. This momentum spectrum is fit to
180 data for each analysis channel in order to search for evidence of these BSM effects.

181 An additional study of WZ produced in association with a heavy flavor jet (including both
182 b-jets and charm jets) is also included. This process mimics the final state of $t\bar{t}H$ multilpjet
183 events, making it an irreducible background for that analysis. However, this process is poorly
184 understood, and difficult to simulate accurately, introducing large systematic uncertainties for
185 analyses that include it as a background. A measurement of WZ + heavy flavor in the fully
186 leptonic decay mode is performed in an attempt to reduce this uncertainty.

187 This dissertation begins with a brief explanation of the SM, its limitations, and the theor-
188 etical motivation behind this work in Part II. This is followed by a description of the LHC and
189 the ATLAS detector in Part III. Part IV details a measurement of WZ + heavy flavor. Studies
190 of differential measurements of $t\bar{t}H$ are then described in Part V, and preliminary results are
191 presented. Finally, the results of these studies are summarized in the conclusion, Part VI.

192 Part II**193 Theoretical Motivation****194 2 The Standard Model and the Higgs Boson**

195 The Standard Model of particle physics (SM) is a Quantum Field Theory (QFT) describing the
196 known fundamental particles and their interactions. It accounts for three of the four known
197 fundamental force - electromagnetism, the weak nuclear force, and the strong nuclear force, but
198 not gravity. Further, the SM describes a mechanism for combining the weak and electromagnetic
199 forces into a singular interaction, known as the electroweak force. It is a non-Abelian gauge
200 theory, invariant under the Lie Group $SU(3)_C \otimes SU(2)_L \otimes U(1)_Y$, where C refers to color
201 charge, L, the helicity of the particle, and Y, the hypercharge.

202 2.1 The Forces and Particles of the Standard Model

203 The SM particles, summarized in Figure 2.1, can be classified into two general categories based
204 on their spin: fermions, and bosons.

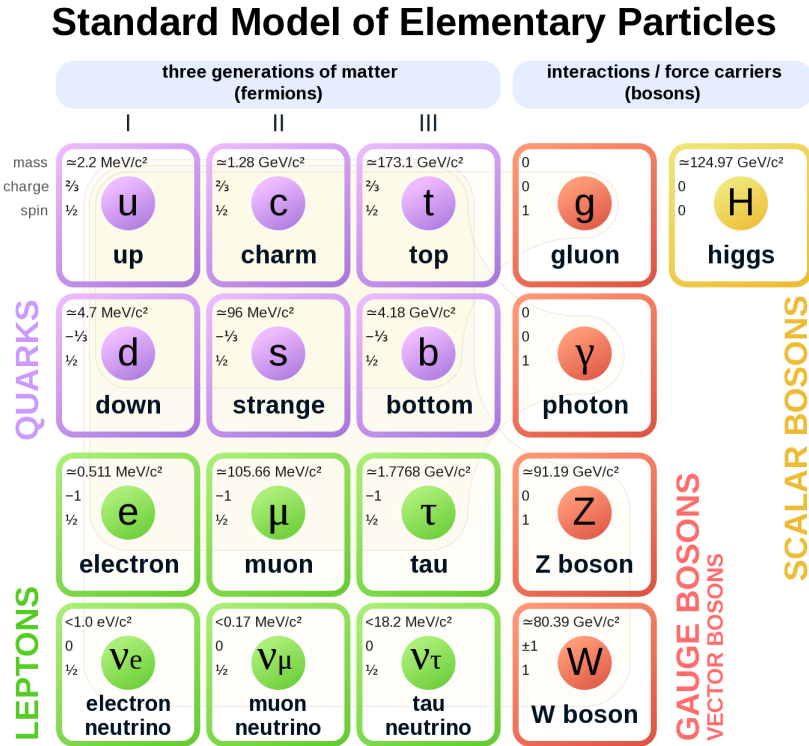


Figure 2.1: A summary of the particles of the Standard Model, including their mass, charge and spin, with the fermions listed on the left, and the bosons on the right. [1]

205 Fermions are particles with $\frac{1}{2}$ -integer spin, which according to the spin-statistics theorem,
 206 causes them to comply with the Pauli-exclusion principle. They can be separated into two groups,
 207 leptons and quarks, each of which consist of three generations of particles with increasing mass.

208 Leptons are fermions which interact via the electroweak force, but not the strong force.
 209 The three generation of leptons consist of the electron and electron neutrino, the muon and muon
 210 neutrino, the tau and tau neutrino. The quarks, by contrast, do interact via the strong force - which
 211 is to say they have color charge - in addition to the electroweak force. The three generations
 212 include the up and down quarks, the strange and charm quarks, and the top and bottom quarks.

213 Each of these generations form left-handed doublets invariant under SU(2) transfor-

214 mations. For the leptons these doublets are:

$$\begin{pmatrix} e^- \\ \nu_e \end{pmatrix}_L, \begin{pmatrix} \mu^- \\ \nu_\mu \end{pmatrix}_L, \begin{pmatrix} \tau^- \\ \nu_\tau \end{pmatrix}_L \quad (2.1)$$

215 And for the quarks:

$$\begin{pmatrix} u \\ d \end{pmatrix}_L, \begin{pmatrix} s \\ c \end{pmatrix}_L, \begin{pmatrix} t \\ b \end{pmatrix}_L \quad (2.2)$$

216 For both leptons and quarks, the heavier generations can decay into the lighter generation

217 of particles, while the first generation does not decay. Hence, ordinary matter generally consists

218 of this first generation of fermions - electrons, up quarks, and down quarks. Each of these

219 fermions has a corresponding anti-particle, which has an equal mass as its partner but opposite

220 charge. The fermions acquire their mass via the Higgs Mechanism, except for the neutrinos,

221 whose mass has been experimentally confirmed but is not accounted for in the SM.

222 Bosons, by contrast, have integer spin, and are therefore unconstrained by the Pauli-

223 exclusion principle. The SM includes two kinds of bosons: Gauge bosons, which are spin-1

224 particles that mediate the interactions between the fermions, and a single scalar, i.e. spin-0,

225 particle - the Higgs Boson. Of the gauge bosons, the W^+ , W^- and Z bosons - which are the

²²⁶ mass eigenstates of the electroweak bosons - mediate the weak interaction, while the photon
²²⁷ mediates the electric force, and the gluon mediates the strong force.

²²⁸ **2.2 The Higgs Mechanism**

²²⁹ A key feature of the SM is the gauge invariance of its Lagrangian. However, any terms added to
²³⁰ the Lagrangian giving mass to the the gauge bosons would violate this underlying symmetry of
²³¹ the theory. This presents a clear problem with the theory: The experimental observation that the
²³² W and Z bosons have mass seems to contradict the basic structure of the SM.

²³³ Rather than abandoning gauge invariance, an alternative way for particles to acquire mass
²³⁴ beyond adding a simple mass term to the Lagrangian was theorized by Higgs, Englert and Brout
²³⁵ in 1964 [2]. This procedure for introducing masses for the gauge bosons while preserving local
²³⁶ gauge invariance, known as the Higgs mechanism, was incorporated into the electroweak theory
²³⁷ by Weinberg in 1967 [3].

²³⁸ **2.2.1 The Higgs Field**

²³⁹ The Higgs mechanism introduces a complex scalar SU(2) doublet, Φ , with the form:

$$\Phi = \begin{pmatrix} \phi^+ \\ \phi^0 \end{pmatrix}_L \quad (2.3)$$

240 This field introduces a scalar potential to the Lagrangian of the form:

$$V(\Phi) = \mu^2 |\Phi^\dagger \Phi| + \lambda (|\Phi^\dagger \Phi|)^2 \quad (2.4)$$

241 Where μ and λ are free parameters of the new field. This represents the most general
 242 potential allowed while preserving $SU(2)_L$ invariance and renormalizability. In the case that
 243 $\mu^2 < 0$, this potential takes the form shown in Figure 2.2.

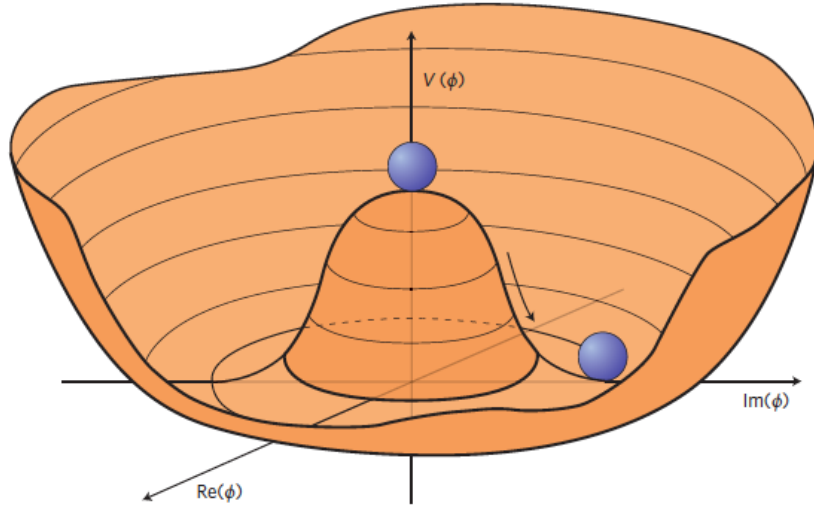


Figure 2.2: The value of the Higgs potential, $V(\Phi)$ as a function of Φ , for the case that $\mu^2 < 0$ [4].

244 The significant feature of this potential is that its minimum does not occur for a value of
 245 $\Phi = 0$. Instead, it is minimized when $|\Phi^\dagger \Phi| = -\mu^2/\lambda$. This means that in its ground state, the
 246 Higgs field takes on a non-zero value - referred to as a vacuum expectation value (VEV). So while
 247 the Higgs potential is globally symmetric, about the minimum this symmetry is broken. Since

²⁴⁸ the minimum is determined only by $\Phi^\dagger \Phi$, there is some ambiguity in the particular definition of

²⁴⁹ the VEV, but it is generally represented as

$$\langle \Phi \rangle = \frac{1}{\sqrt{2}} \begin{pmatrix} 0 \\ v \end{pmatrix} \quad (2.5)$$

²⁵⁰ The full value of Φ can be written as

$$\langle \Phi \rangle = \frac{1}{\sqrt{2}} \begin{pmatrix} 0 \\ v + H/\sqrt{2} \end{pmatrix} \quad (2.6)$$

²⁵¹ with v being the value of the VEV, and H being the real value of the scalar field.

²⁵² 2.2.2 Electroweak Symmetry Breaking

²⁵³ The Electroweak (EWK) interaction is described in the SM by a $SU(2)_L \otimes U(1)_Y$ gauge theory.

²⁵⁴ This theory predicts three $SU(2)_L$ gauge boson, $W_\mu^1, W_\mu^2, W_\mu^3$, and a single $U(1)_Y$ gauge boson,

²⁵⁵ B_μ . The couplings of these bosons to the Higgs field show up in the kinetic terms of the scalar

²⁵⁶ field Φ in the Lagrangian:

$$(D_\mu \Phi)^\dagger (D^\mu \Phi) = |(\partial_\mu - \frac{i g}{2} W_\mu^a \sigma^a - \frac{i g'}{2} B_\mu Y) \phi|^2 \quad (2.7)$$

257 Here D_μ represents the covariant derivative required to preserve gauge invariance, g and
 258 g' represent coupling constant of the gauge bosons, σ^a denotes the Pauli matrices of $SU(2)$,
 259 and Y represents the hypercharge of $U(1)$. The terms in this interaction which contribute to the
 260 masses of the gauge bosons can be written as:

$$\frac{1}{2}(0, v) \left(\frac{g}{2} W_\mu^a \sigma^a - \frac{g'}{2} B_\mu \right)^2 \begin{pmatrix} 0 \\ v \end{pmatrix} \quad (2.8)$$

261 Expanding these terms into the mass eigenstates of the electroweak interaction yields four
 262 physical gauge bosons, two charged and two neutral, which are linear combinations of the fields
 263 W_μ^1 , W_μ^2 , W_μ^3 , and B_μ :

$$\begin{aligned} W_\mu^\pm &= \frac{1}{\sqrt{2}} (W_\mu^1 \pm i W_\mu^2) \\ Z^\mu &= \frac{1}{\sqrt{(g^2 + g'^2)}} (-g' B_\mu + g W_\mu^3) \\ A^\mu &= \frac{1}{\sqrt{(g^2 + g'^2)}} (g B_\mu + g' W_\mu^3) \end{aligned} \quad (2.9)$$

264 And the masses of these fields are given by:

$$\begin{aligned} M_W^2 &= \frac{1}{4} g^2 v^2 \\ M_Z^2 &= \frac{1}{4} (g^2 + g'^2) v^2 \\ M_A^2 &= 0 \end{aligned} \quad (2.10)$$

265 This produces exactly the particles we observe - three massive gauge bosons and a single
 266 massless photon. The massless photon represents the portion of the gauge symmetry, a single
 267 $U(1)$ of the electromagnetic force, that remains unbroken by the VEV.

268 Interactions with the Higgs field also lead to the generation of the fermion masses, which
 269 in the Lagrangian take the form:

$$-\lambda_\psi(\bar{\psi}_L \phi \psi_R + \bar{\psi}_R \phi^\dagger \psi_L) \quad (2.11)$$

270 After symmetry breaking has occurred and ϕ has taken on the value of the VEV as written
 271 in equation 2.5, the mass terms of the fermions become $\lambda_\psi v$. Written this way, the fermion
 272 masses are proportional to their Yukawa coupling to the VEV, λ_ψ .

273 Based on the equation 2.6, an additional mass term, $\mu^2 H^2$ arises from the potential $V(\Phi)$.
 274 This term can be understood as an excitation of the Higgs field, a scalar boson with mass $M_H = \mu$.
 275 This is the Higgs boson, which comes about as a natural prediction of electroweak symmetry
 276 breaking.

277 The fermions' Yukawa couplings to the VEV take the same form as the fermions' coupling
 278 to the Higgs boson - λ_ψ . Therefore, the strength of a fermion's interaction with the Higgs is
 279 directly proportional to its mass. We now have a model that predicts a Higgs boson with mass
 280 $M_H = \mu$, which interacts with the fermions with coupling strength λ_ψ . Because μ and λ_ψ are

²⁸¹ free parameters of the theory, the mass of the Higgs boson and its interactions with the fermions

²⁸² must be measured experimentally.

²⁸³ **2.3 $t\bar{t}H$ Production**

²⁸⁴ The strength of a particles interaction with the Higgs, given by its Yukawa coupling, is propor-
²⁸⁵ tionate to its mass. The top quark - as the heaviest known particle - has the strongest interaction,
²⁸⁶ making this interaction particularly interesting to study. While several processes involve interac-
²⁸⁷ tions between the Higgs and the top, some Higgs production modes include the top interaction
²⁸⁸ only as a part of a loop diagram, such as the gluon-gluon fusion diagram shown in Figure 2.3.

²⁸⁹ This process therefore only allows for an indirect probe of the Higgs-top Yukawa coupling, as
²⁹⁰ the flavor of the quark in this diagram is not unique.

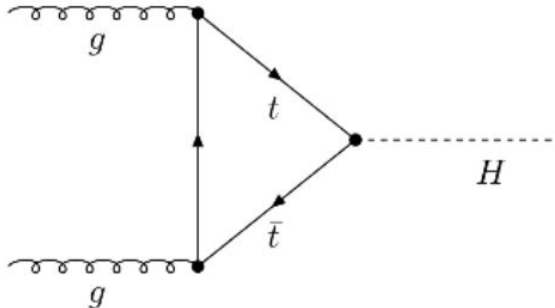


Figure 2.3: Diagram of a Higgs boson produced via gluon-gluon fusion.

²⁹¹ Studying the Higgs produced in association with top quark pairs, $t\bar{t}H$, allows this interac-
²⁹² tion to be measured directly. This process, as shown in Figure 2.4, involves a unique coupling
²⁹³ between the Higgs and the top, which can be identified by the top quark pair in the final state.

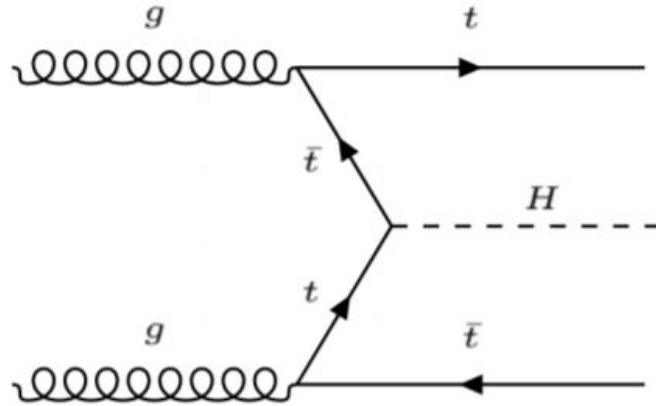


Figure 2.4: Diagram of a Higgs boson produced in association with a pair of top quarks.

294 The Higgs boson, as well as the top quarks, have very short lifetimes - on the order of
 295 10^{-22} s and 10^{-25} s respectively - meaning they can only be observed via their decay products.
 296 Measuring this process is therefore a matter of identifying events with final states consistent
 297 with $t\bar{t}H$ production. This thesis focuses on $t\bar{t}H$ events with multiple leptons in the final state,
 298 $t\bar{t}H - ML$. This includes $H \rightarrow W^+W^-$ events, where at least one of the W bosons decays
 299 leptonically.

300 While the branching ratio of $H \rightarrow W^+W^-$ is smaller than $H \rightarrow b\bar{b}$, it produces a clearer
 301 signal. On the other hand, $H \rightarrow \gamma\gamma$ produces the most easily identifiable signal, but has a much
 302 smaller branching ratio than $H \rightarrow W^+W^-$. Therefore, compared with other final states of $t\bar{t}H$,
 303 the $t\bar{t}H - ML$ channel is an attractive candidate for study, as it involves a good balance between
 304 statistical power and identifiability.

305 2.4 WZ + Heavy Flavor Production

306 Part IV is dedicated to a measurement of WZ produced in association with a heavy flavor jet
 307 - namely, a charm or b-jet - in the fully leptonic channel. In the instance that both the W
 308 and Z bosons decay leptonically, this process produces a final state similar to $t\bar{t}H$, making it
 309 an irreducible background for $t\bar{t}H$ – ML specifically, and any analysis that includes multiple
 310 leptons and b-tagged jets in the final state more broadly.

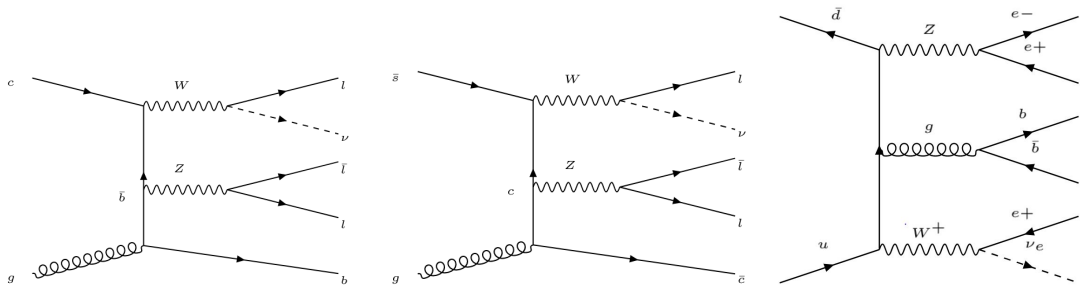


Figure 2.5: Example Feynman diagrams of WZ + heavy flavor production

311 The b-jets produced in this process can be thought of in two different ways: either as
 312 originating from the quark “sea” of the initial state hadrons, or as the result of a gluon from
 313 one the colliding protons splitting into $b\bar{b}$ pairs. However, the heavy flavor contribution to the
 314 parton distribution function (PDF) of the proton is uncertain, and simulations of this process
 315 disagree depending on which of these two approaches one considers. This makes WZ + heavy
 316 flavor difficult to accurately simulate, and introduces a large uncertainty for any analysis which
 317 includes it as a background, motivating a measurement of this process.

318 2.5 Extensions to the Standard Model

319 While the SM has been tested to great precision, particularly at the LHC, it is generally accepted
320 that it is only valid up to a certain energy scale. It is assumed that above a certain energy, at the
321 scale where something like a Grand Unified Theory (GUT) or quantum gravity become relevant,
322 the SM will not be applicable. Further, there are several experimental observations that the SM
323 fails to explain. For example, the SM predicts neutrinos to be massless, despite experimental
324 observation to the contrary, and fails to explain the observation of dark matter and dark energy.

325 Another example, relevant to the Higgs sector, is known as the hierarchy problem: large
326 quantum corrections to the Higgs mass from loop diagrams, such as those shown in Figure 2.6,
327 are many orders of magnitude larger than the Higgs mass itself. The observed value of the Higgs
328 mass therefore requires extremely precise cancellation between these corrections and the bare
329 mass of the Higgs, a cancellation which seems unnatural and suggests something missing in our
330 theoretical picture.

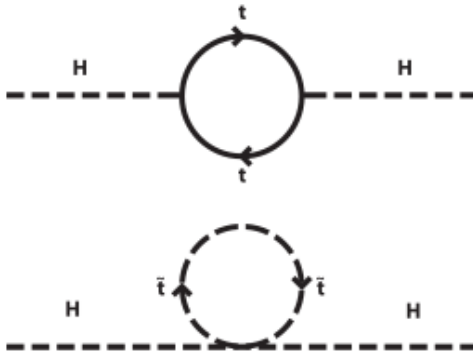


Figure 2.6: Above diagram is the leading order correction to the Higgs mass via a top quark loop, and below is the stop squark loop, coming from a supersymmetric extension of the SM, that provides a potential cancellation of the top diagram.

Because so many of the properties of the Higgs boson have not yet been studied, its interactions are a promising place to search for new physics that could resolve some of the limitations of the SM. As explained above, the interactions of the Higgs with the top quark, as in $t\bar{t}H$ production, are particularly interesting: As the most massive particle in the Standard Model, the top quark is the most strongly interacting with the Higgs. Therefore, any new physics effects are likely to be seen most prominently in this interaction.

These interactions can be measured directly by studying the production of a Higgs Boson in association with a pair of Top Quarks ($t\bar{t}H$). While this process has been observed by both the ATLAS [5] and CMS [6] collaborations, these analyses have focused on measuring the overall rate of $t\bar{t}H$ production. There are several theories of physics Beyond the Standard Model (BSM), however, that would affect the kinematics of $t\bar{t}H$ production without altering its overall rate [7].

343 An Effective Field Theory approach can be used to model the low energy effects of new,
 344 high energy physics, by parameterizing BSM effects as higher dimensional operators. These
 345 additional operators can then be added to the SM Lagrangian to write an effective Lagrangian
 346 that accounts for the effects of these higher energy physics. The lowest order of these that could
 347 contribute to Higgs-top couplings are dimension-six, as represented in Equation 2.12.

$$\mathcal{L}_{\text{eff}} = \mathcal{L}_{\text{SM}} + \frac{f}{\Lambda} O^6 \quad (2.12)$$

348 Here Λ represents the energy scale of the new physics, and f is a Wilson coefficient which
 349 represents the strength of the effective coupling. An experimental observation of any non-zero
 350 value of f would be a sign of BSM physics.

351 The addition of these operators can be shown to modify the transverse momentum (p_T)
 352 spectrum of the Higgs Boson in Higg-top interactions, without effecting the overall rate of $t\bar{t}H$
 353 production [8]. The possible impact of these higher order effects on the Higgs p_T spectrum are
 354 shown in Figure 2.7.

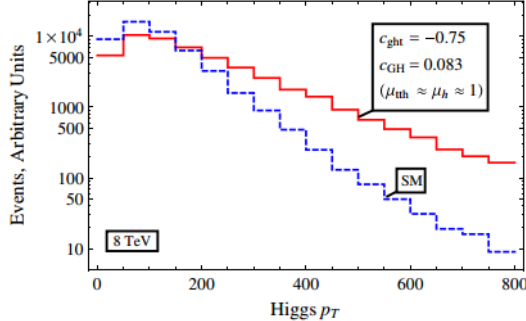


Figure 2.7: The momentum spectrum of the Higgs boson produced via top-quarks with (red) and without (blue) the presence of dimension-six operators.

355 This provides a clear, physics observable that could be used to search for evidence of
 356 BSM physics. The energy and luminosity produced by the LHC now make such a measurement
 357 possible. Reconstructing the momentum spectrum of the Higgs in $t\bar{t}H$ events therefore provides
 358 a means to search for new physics in the Higgs sector.

359 Part III

360 The LHC and the ATLAS Detector

361 3 The LHC

362 The Large Hadron Collider (LHC) is a particle accelerator consisting of a 27 km ring, designed
 363 to collide protons at high energy. Located outside of Geneva, Switzerland and buried about 100
 364 m underground, it consists of a ring of superconducting magnets which are used to accelerate

365 opposing beams of protons - or lead ions - which collide at the center of one of the various
366 detectors located around the LHC ring which record the result of these collisions. These
367 detectors include two general purpose detectors, ATLAS and CMS, which are designed to make
368 precision measurements of a broad range of physics phenomenon, and two more specialized
369 experiments, LHCb and ALICE, which are optimized to study b-quarks and heavy-ion physics,
370 respectively.

371 The LHC first began running in 2009 at a proton-proton center of mass energy of $\sqrt{s} = 8$
372 TeV. It operated at this energy from 2009 to 2012, known as Run 1, and data collected during
373 this period was used in discovering the Higgs Boson. The LHC began running again in 2015,
374 and collected data at an increased energy of $\sqrt{s} = 13$ TeV until 2018, a period referred to as Run
375 2.

376 The LHC consists of a chain of accelerators, which accelerate the protons to higher and
377 higher energies until they are injected into the main ring. This process is summarized in figure
378 3.1. Protons extracted from a tank of ionized hydrogen are fed into a linear accelerator, LINAC2,
379 where they reach an energy of 50 MeV. From there, they enter a series of three separate circular
380 accelerators, before being injected into the main accelerator ring at an energy of 450 GeV. Within
381 the main ring protons are separated into two separate beams moving in opposite directions,
382 and their energy is increased to their full collision energy. Radiofrequency cavities are used to
383 accelerate these particles and sort them into bunches. From 2015-2018, these bunches consisted
384 of around 100 billion protons each with an energy of 6.5 TeV per proton, which collided at a rate
385 of 40 MHz, or every 25 ns.

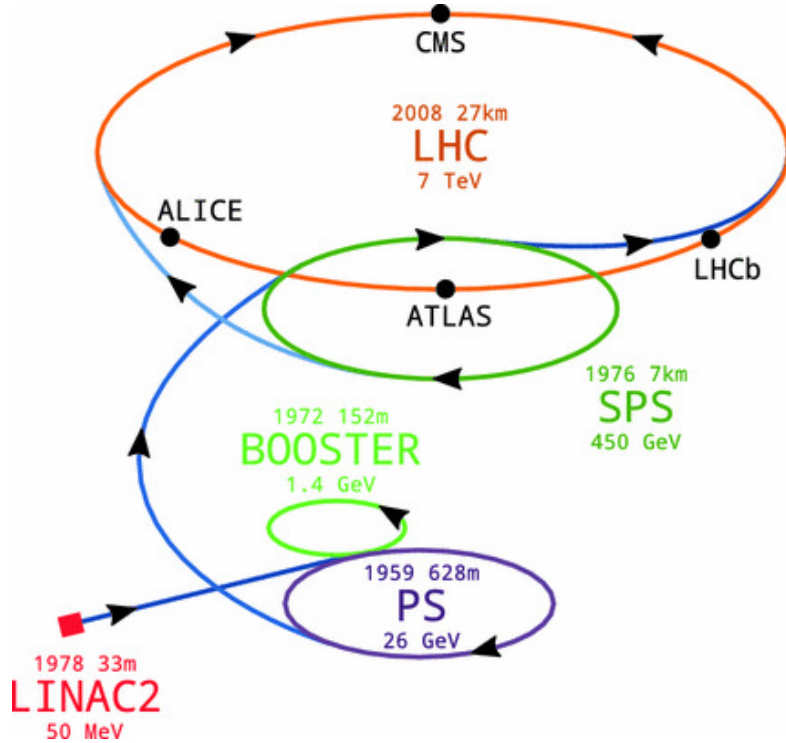


Figure 3.1: A summary of the accelerator chain used to feed protons into the LHC [9].

Because these proton bunches consist of a large number of particles, each bunch crossing consists of not just one, but several direct proton-proton collisions. The number of interactions that occur per bunch crossing, μ , is known as pileup. During Run 2, the average pileup for bunch crossings was around $\langle \mu \rangle = 35$, with values typically ranging between 10 and 70.

The amount of data collected by the LHC is measured in terms of luminosity, which is the ratio of the number of events detected per unit time, $\frac{dN}{dt}$, and the interaction cross-section, σ .

$$\mathcal{L} = \frac{1}{\sigma} \frac{dN}{dt} \quad (3.1)$$

392 The design luminosity of the LHC is $10^{34} \text{ cm}^{-2}\text{s}^{-1}$, however the LHC has achieved a
 393 luminosity of over $2 \times 10^{34} \text{ cm}^{-2}\text{s}^{-1}$. The total luminosity is then this instantaneous luminosity
 394 integrated over time.

$$\mathcal{L}_{\text{int}} = \int \mathcal{L} dt \quad (3.2)$$

395 The integrated luminosity collected by the ATLAS detector as of the end of 2018 is around
 396 140 fb^{-1} , exceeding the expected integrated luminosity of 100 fb^{-1} .

397 4 The ATLAS Detector

398 ATLAS (a not terribly natural acronym for “A Toroidal LHC Apparatus”) is a general purpose
 399 detector designed to maximize the detection efficiency of all physics objects, including leptons,
 400 jets, and photons. This means it is capable of measuring all SM particles, with the exception of
 401 neutrinos, the presence of which can be inferred based on missing transverse momentum. The
 402 detector measures 44 m long, and 25 m tall.

403 The ATLAS detector consists of multiple concentric layers, each of which serves a different
 404 purpose in reconstructing collisions. At the very center of the detector is the interaction point
 405 where the proton beams of the LHC collide.

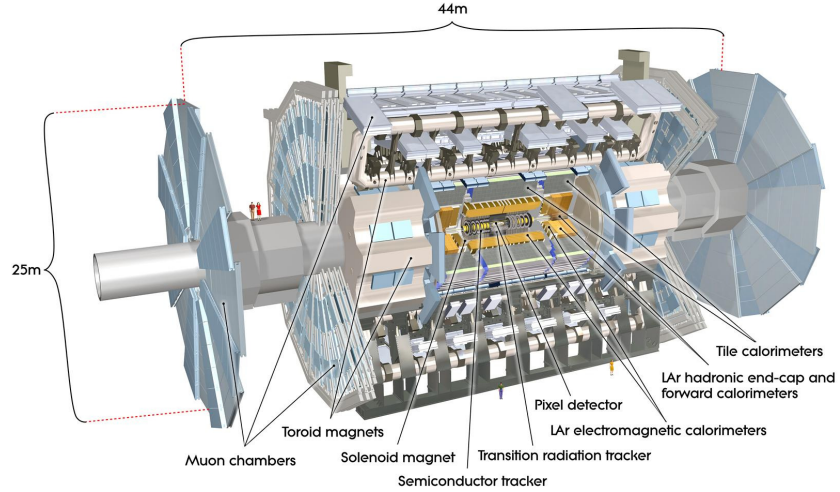


Figure 4.1: Cutaway view of the ATLAS detector, with labels of its major components [10].

406 4.1 Inner Detector

407 Just surrounding the interaction point is the Inner Detector, designed to track the path of charged
 408 particles moving through the detector. An inner solenoid surrounding the Innder Detector is
 409 used to produces a magnetic field of 2 T. This large magnetic field causes the path of charged
 410 particles moving through the Inner Detector to bend. Because this magnetic field is uniform and
 411 well known, it can be used in conjunction with the curvature of a particles path to measure its
 412 charge and momentum.

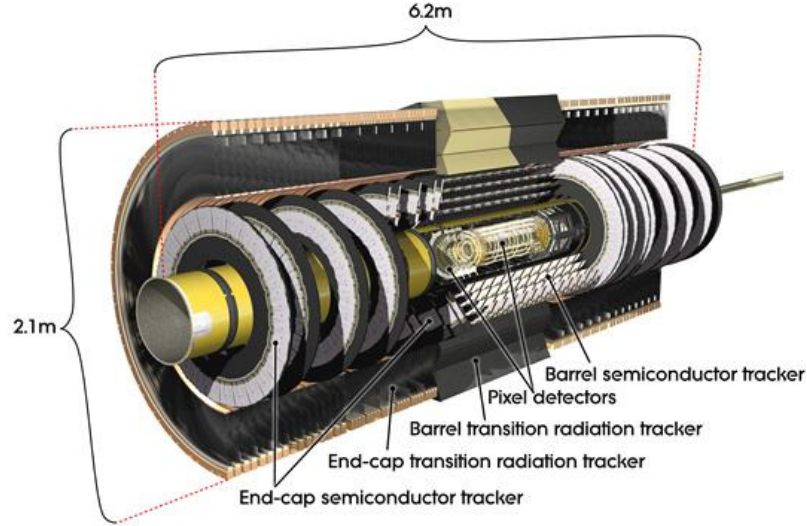


Figure 4.2: Cutaway view of the Inner Detector [11].

413 The Inner Detector consists of three components - the Pixel Detector, the Semi-Conductor
 414 Tracker (SCT), and the Transition Radiation Tracker (TRT). The Pixel Detector is the innermost
 415 of these, beginning just 33.25 mm away from the beam line. It consists of three silicon layers
 416 along the barrel, as well as three endcap layers, covering a range of $|\eta| < 2.5$.

417 The Semiconductor Tracker (SCT) is similar to the Pixel detector, but uses long strips of
 418 silicon rather than small pixels to cover a larger spatial area. It includes over 6 million readout
 419 strips, allowing the position of charged particles to be measured to an accuracy of $17 \mu\text{m}$.

420 The outermost component of the inner detector, the TRT consists of around 300,000 straw
 421 tubes filled with ionizable gas, which produces current through a wire in the center of each tube
 422 when a charged particle passes through. Between these staws are layers of material designed
 423 to produce transition radiation from ultrarelativistic particles as they pass through each material

424 boundary, amplifying the signal. The position uncertainty in the TRT is higher than the other
 425 two, on the order of 200 μm , but covering a much larger area.

426 **4.2 Calorimeters**

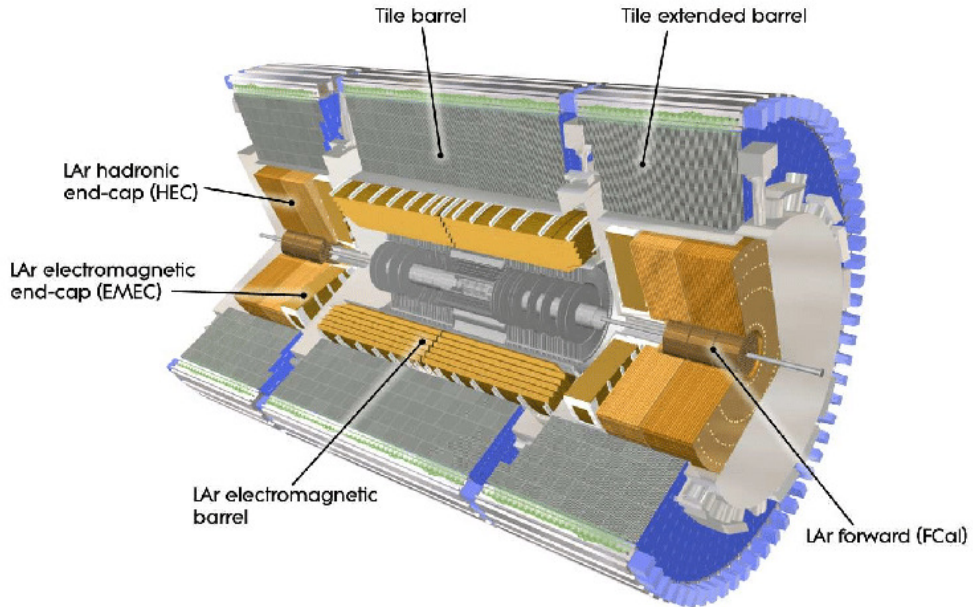


Figure 4.3: Cutaway view of the calorimeter system of the ATLAS detector [11].

427 Situated outside the Inner Detector are two concentric calorimeters. The inner calorimeter
 428 uses liquid argon (LAr) to measure the energy of particles that interact electromagnetically,
 429 which includes photons and any charged particle. The LAr calorimeter is made of heavy metals,
 430 primarily lead and copper, which causes electromagnetically interacting particles to shower,
 431 depositing their energy in the detector. The showering of the high energy particles that pass

432 through the calorimeter cause the liquid argon to ionize, and the ionized electrons are detected
433 by electronic readouts. The LAr calorimeter consists of around 180,000 readout channels.

434 The outer calorimeter measures the energy from particles that pass through the EM
435 calorimeter, and measures the energy of particles that interact via the strong force. This is
436 primarily hadrons. It is composed of steel plates designed to cause hadronic showering and
437 around 500,000 scintillating tiles as the active material. The signals from the hadronic calorimeter
438 are read out by photomultiplier tubes (PMTs).

439 **4.3 Muon Spectrometer**

440 Because muons are heavier than electrons and photons, and do not interact via the strong force,
441 they generally pass through the detector without being stopped by the calorimeters. The outermost
442 components of the detector are designed specifically to measure the energy and momentum of
443 muons produced in the LHC. The muon spectrometer consists of tracking and triggering systems.
444 The largest of the subdetectors, it extends from the outside of the calorimeter system, about a
445 4.25 m radius from the beam line, to a radius of 11 m. This large detector system is necessary
446 to accurately measure the momentum of muons, which is essential not only for measurements
447 involving the muons themselves, but also to accurately estimate the missing energy in each
448 event.

449 Two large toroidal magnets within the muon system generate a large magnetic field which
450 covers an area 26 m long with a radius of 10 m. Because the area covered by this magnet system

451 is so large, a uniform magnetic field like the one produced in the Inner Detector is impractical.
452 Instead, the magnetic field that exists in the muon spectrometer ranges between 2 T and 8 T, and
453 is much less uniform. The path of the muons passing through the spectrometer is bent by this
454 field, allowing their charge to be determined.

455 1200 tracking chambers are placed in the muon system in order to precisely measure the
456 tracks of muons with high spatial resolution. The path of the muons are tracked by Monitored
457 Drift Tubes, which are drift chambers formed by aluminum tubes and filled with ionizing gas.
458 These tubes produce a multi-layer spatial resolution on the order of 50 μm .

459 **4.4 Trigger System**

460 Because of the high collision rate and large amount of data collected by the various subdetectors,
461 ATLAS produces far more data than can actually be stored. Each event produces around 25 Mb
462 of raw data, which multiplied by the bunch crossing rate of 40 MHz, comes out to around a
463 petabyte of data every second. The information from every event cannot practically be stored,
464 therefore a sophisticated trigger system is employed in real time to determine whether events are
465 sufficiently interesting to be worth storing.

466 The trigger system in ATLAS involves multiple levels, each of which select out which
467 events move on to the next level of scrutiny. The level-1 trigger uses hardware information from
468 the calorimeters and muon spectrometer to select events that contain candidates for particles

⁴⁶⁹ commonly used in analysis, such as energetic leptons and jets. The level-1 trigger reduces the
⁴⁷⁰ rate of events from 40 MHz to around 100 kHz.

⁴⁷¹ Events that pass the level-1 trigger move to the High-Level Trigger (HLT). The HLT takes
⁴⁷² place outside of the detector in software, and looks for properties such as a large amount of
⁴⁷³ missing transverse energy, well defined leptons, and multiple high energy jets. Events that pass
⁴⁷⁴ the HLT are stored and used for analysis. Because the specifics of the HLT are determined by
⁴⁷⁵ software rather than hardware, the thresholds can be changed throughout the run of the detector
⁴⁷⁶ in response to run conditions such as changes to pileup and luminosity. After the HLT is applied,
⁴⁷⁷ the event rate is reduced to around 1000 per second, which are recorded for analysis.

⁴⁷⁸ **Part IV**

⁴⁷⁹ **Measurement of WZ + Heavy Flavor**

⁴⁸⁰ **5 Introduction**

⁴⁸¹ The production of WZ in association with a heavy flavor jet represents an important background
⁴⁸² for many major analyses. This includes any process with leptons and b-jets in the final state,
⁴⁸³ such as $t\bar{t}H$, $t\bar{t}W$, and $t\bar{t}Z$. While precise measurements have been made of WZ production
⁴⁸⁴ [12], WZ + heavy flavor remains poorly understood. This is largely because the QCD processes

485 involved in the production of the b-jet make it difficult to simulate accurately. This introduces a
486 large uncertainty for analyses that include this process as a background.

487 Motivated by its relevance to the $t\bar{t}H$ multilepton analysis, we perform a study of the fully
488 leptonic decay mode of this channel; that is, events where both the W and Z decay leptonically.
489 Because WZ has no associated jets at leading order, while the major backgrounds for this channel
490 tend to have high jet multiplicity, events with more than two jets are rejected. This gives a final
491 state signature of three leptons and one or two jets.

492 Events that meet this selection criteria are sorted into pseudo-continuous b-tagging regions
493 based on the DL1r b-tag score of their associated jets. This is done to separate WZ + b-jet events
494 from WZ + charm and WZ + light jets. These regions are fit to data in order to make a more
495 accurate estimate of the contribution of WZ + heavy-flavor, where heavy-flavor jets include
496 b-jets and charm jets. The full Run-2 dataset collected by the ATLAS detector, representing 139
497 fb^{-1} of data from pp collisions at $\sqrt{s} = 13 \text{ TeV}$, is used for this study.

498 Section 10 details the data and Monte Carlo (MC) samples used in the analysis. The
499 reconstruction of various physics objects is described in Section 11. Section 12 describes the
500 event selection applied to these samples, along the definitions of the various regions used in
501 the fit. The multivariate analysis techniques used to separate the tZ background from WZ +
502 heavy flavor are described in Section 13. Section 21 describes the various sources of systematic
503 uncertainties considered in the fit. Finally, the results of the analysis are summarized in Section
504 22, followed by a brief conclusion in Section ??.

505 **The current state of the analysis shows blinded results for the full 2018 dataset.**
506 **Regions containing >5% WZ+b events are blinded, and results are from Asimov, MC only**
507 **fits.**

508 **6 Data and Monte Carlo Samples**

509 **6.1 Data Samples**

510 The study uses a sample of proton-proton collision data collected by the ATLAS detector from
511 2015 through 2018 at an energy of $\sqrt{s} = 13$ TeV, which represents an integrated luminosity of
512 139 fb^{-1} . This data set was collected with a bunch crossing rate of 25 ns. All data used in this
513 analysis was verified by data quality checks.

514 **6.2 Monte Carlo Samples**

515 Several different generators were used to produce Monte Carlo simulations of the signal and
516 background processes. For all samples, the response of the ATLAS detector is simulated using
517 Geant4. The WZ signal samples are simulated using Sherpa 2.2.2 [13]. Specific information
518 about the Monte Carlo samples being used can be found in Table 26.

Table 1: The configurations used for event generation of signal and background processes, including the event generator, matrix element (ME) order, parton shower algorithm, and parton distribution function (PDF).

| Process | Event generator | ME order | Parton Shower | PDF |
|---------------------------------|---------------------------|----------------------|------------------------|-----------------------------------|
| WZ, VV | SHERPA 2.2.2 | MEPS NLO | SHERPA | CT10 |
| tZ | MG5_AMC | NLO | PYTHIA 8 | CTEQ6L1 |
| t̄tW | MG5_AMC (SHERPA 2.1.1) | NLO (LO multileg) | PYTHIA 8 (SHERPA) | NNPDF 3.0 NLO (NNPDF 3.0 NLO) |
| t̄t(Z/γ* → ll) | MG5_AMC | NLO | PYTHIA 8 | NNPDF 3.0 NLO |
| t̄tH | MG5_AMC (MG5_AMC) | NLO (NLO) | PYTHIA 8 (HERWIG++) | NNPDF 3.0 NLO [14] (CT10 [15]) |
| tHqb | MG5_AMC | LO | PYTHIA 8 | CT10 |
| tHW | MG5_AMC (SHERPA 2.1.1) | NLO (LO multileg) | HERWIG++ (SHERPA) | CT10 (NNPDF 3.0 NLO) |
| tWZ | MG5_AMC | NLO | PYTHIA 8 | NNPDF 2.3 LO |
| t̄t̄t, t̄t̄t̄t | MG5_AMC | LO | PYTHIA 8 | NNPDF 2.3 LO |
| t̄tW+W- | MG5_AMC | LO | PYTHIA 8 | NNPDF 2.3 LO |
| t̄t | POWHEG-BOX v2 [16] | NLO | PYTHIA 8 | NNPDF 3.0 NLO |
| t̄tγ | MG5_AMC | LO | PYTHIA 8 | NNPDF 2.3 LO |
| s-, t-channel, Wt single top | POWHEG-BOX v1 [17] | NLO | PYTHIA 6 | CT10 |
| qqVV, VVV | | | | |
| Z → l+l- | SHERPA 2.2.1 | MEPS NLO | SHERPA | NNPDF 3.0 NLO |

7 Object Reconstruction

- 520 All regions defined in this analysis share a common lepton, jet, and overall event preselection.
521 The selection applied to each physics object is detailed here; the event preselection, and the
522 selection used to define the various fit regions, is described in Section 12.

523 **7.1 Trigger**

524 Events are required to be selected by dilepton triggers, as summarized in Table 28.

| Dilepton triggers (2015) | |
|-------------------------------|----------------------------|
| $\mu\mu$ (asymm.) | HLT_mu18_mu8noL1 |
| ee (symm.) | HLT_2e12_lhloose_L12EM10VH |
| $e\mu, \mu e$ (\sim symm.) | HLT_e17_lhloose_mu14 |
| Dilepton triggers (2016) | |
| $\mu\mu$ (asymm.) | HLT_mu22_mu8noL1 |
| ee (symm.) | HLT_2e17_lhvloose_nod0 |
| $e\mu, \mu e$ (\sim symm.) | HLT_e17_lhloose_nod0_mu14 |
| Dilepton triggers (2017) | |
| $\mu\mu$ (asymm.) | HLT_mu22_mu8noL1 |
| ee (symm.) | HLT_2e24_lhvloose_nod0 |
| $e\mu, \mu e$ (\sim symm.) | HLT_e17_lhloose_nod0_mu14 |
| Dilepton triggers (2018) | |
| $\mu\mu$ (asymm.) | HLT_mu22_mu8noL1 |
| ee (symm.) | HLT_2e24_lhvloose_nod0 |
| $e\mu, \mu e$ (\sim symm.) | HLT_e17_lhloose_nod0_mu14 |

Table 2: List of lowest p_T -threshold, un-prescaled dilepton triggers used for 2015-2018 data taking.

525 **7.2 Light leptons**

526 Electron candidates are reconstructed from energy clusters in the electromagnetic calorimeter
 527 that are associated with charged particle tracks reconstructed in the inner detector [18]. Electron
 528 candidates are required to have $p_T > 10$ GeV and $|\eta_{\text{cluster}}| < 2.47$. Muon candidates are
 529 reconstructed by combining inner detector tracks with track segments or full tracks in the muon
 530 spectrometer [19]. Muon candidates are required to have $p_T > 10$ GeV and $|\eta| < 2.5$. Candidates

531 in the transition region between different electromagnetic calorimeter components, $1.37 < | $\eta_{\text{cluster}}| < 1.52$$, are rejected. A multivariate likelihood discriminant combining shower shape
 532 and track information is used to distinguish real electrons from hadronic showers (fake electrons).
 533 To further reduce the non-prompt electron contribution, the track is required to be consistent
 534 with originating from the primary vertex; requirements are imposed on the transverse impact
 535 parameter significance ($|d_0|/\sigma_{d_0} < 5$) and the longitudinal impact parameter ($|\Delta z_0 \sin \theta_\ell| < 0.5$
 536 mm). Electron candidates are required to pass TightLH identification.
 537

538 Muon candidates are reconstructed by combining inner detector tracks with track segments
 539 or full tracks in the muon spectrometer [19]. Muon candidates are required to have $p_T > 10$ GeV
 540 and $|\eta| < 2.5$. The longitudinal impact parameter is the same for both electrons and muons, while
 541 muons are required to pass a slightly tighter transverse impact parameter, $|d_0|/\sigma_{d_0} < 3$. Muons
 542 are also required to pass Medium ID requirements.

543 Leptons are additionally required to pass a non-prompt BDT selection developed by the
 544 $t\bar{t}H$ multilepton/ $t\bar{t}W$ analysis group. This BDT and the WPs used are summarized in Appendix
 545 .1, and described in detail in [20]. Optimized working points and scale factors for this BDT are
 546 taken from that analysis.

547 7.3 Jets

548 Jets are reconstructed from calibrated topological clusters built from energy deposits in the
 549 calorimeters [21], using the anti- k_t algorithm with a radius parameter $R = 0.4$. Particle Flow, or

550 PFlow, jets are used in the analysis, which are hadronic objects reconstructed using information
551 from both the tracker and the calorimeter. Jets with energy contributions likely arising from noise
552 or detector effects are removed from consideration [22], and only jets satisfying $p_T > 25$ GeV
553 and $|\eta| < 2.5$ are used in this analysis. For jets with $p_T < 60$ GeV and $|\eta| < 2.4$, a jet-track
554 association algorithm is used to confirm that the jet originates from the selected primary vertex,
555 in order to reject jets arising from pileup collisions [23].

556 **7.4 B-tagged Jets**

557 In order to make a measurement of $WZ +$ heavy flavor it is necessary to distinguish these events
558 from $WZ +$ light jets. For this purpose, the DL1r b-tagging algorithm is used to distinguish
559 heavy flavor jets from lighter ones. The DL1r algorithm uses jet kinematics, particularly jet
560 vertex information, as input for a neural network which assigns each jet a score designed to
561 reflect how likely that jet is to have originated from a b-quark.

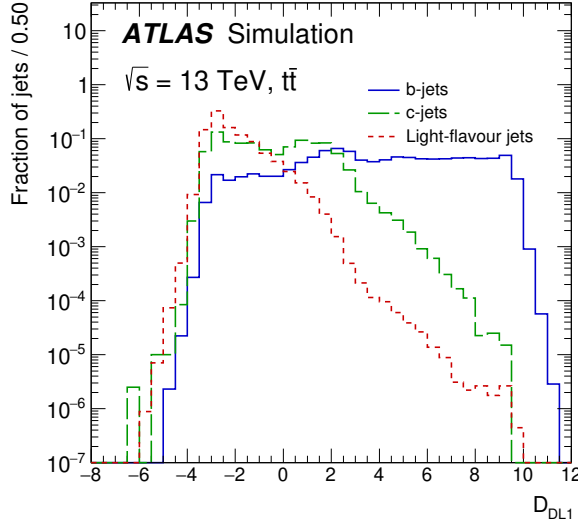


Figure 7.1: Output distribution of the DL1r algorithm for b-jets, charm jets, and light jets

562 From the output of the BDT, calibrated working points (WPs) are developed based on the
 563 efficiency of truth b-jets at particular values of the DL1r algorithm. The working points used in
 564 this analysis are summarized in Table 10.

| WP | none | loose | medium | tight | tightest |
|--------|------|-------|--------|-------|----------|
| b eff. | - | 85% | 77% | 70% | 60% |

Table 3: B-tagging Working Points by tightness and b-jet efficiency

565 A tighter WP will accept fewer b-jets, but reject a higher fraction of charm and light jets.
 566 Generally, analyses that include b-jets will use a fixed working point, for example, requiring that
 567 a jet pass the 70% threshold. By instead treating these working point as bins, e.g. events with
 568 jets that fall between the 85% and 77% WPs fall into one bin, while events with jets passing the
 569 60% WP fall into another, and looking at the full psuedo-continuous DL1r spectrum of the jets,

⁵⁷⁰ additional information can be gained. The psuedo-continuous b-tag spectrum is used in this case
⁵⁷¹ to separate out WZ + b, WZ + charm, and WZ + light.

⁵⁷² **7.5 Missing transverse energy**

⁵⁷³ Missing transverse momentum (E_T^{miss}) is used as part of the event selection. The missing
⁵⁷⁴ transverse momentum vector is defined as the inverse of the sum of the transverse momenta of
⁵⁷⁵ all reconstructed physics objects as well as remaining unclustered energy, the latter of which is
⁵⁷⁶ estimated from low- p_T tracks associated with the primary vertex but not assigned to a hard object,
⁵⁷⁷ with object definitions taken from [24]. Light leptons considered in the E_T^{miss} reconstruction are
⁵⁷⁸ required to have $p_T > 10 \text{ GeV}$, while jets are required to have $p_T > 20 \text{ GeV}$.

⁵⁷⁹ **7.6 Overlap removal**

⁵⁸⁰ To avoid double counting objects and remove leptons originating from decays of hadrons, overlap
⁵⁸¹ removal is performed in the following order: any electron candidate within $\Delta R = 0.1$ of another
⁵⁸² electron candidate with higher p_T is removed; any electron candidate within $\Delta R = 0.1$ of a muon
⁵⁸³ candidate is removed; any jet within $\Delta R = 0.3$ of an electron candidate is removed; if a muon
⁵⁸⁴ candidate and a jet lie within $\Delta R = \min(0.4, 0.04 + 10[\text{GeV}] / p_T(\text{muon}))$ of each other, the jet
⁵⁸⁵ is kept and the muon is removed.

⁵⁸⁶ This algorithm is applied to the preselected objects. The overlap removal procedure is
⁵⁸⁷ summarized in Table 29.

| Keep | Remove | Cone size (ΔR) |
|-------------|-----------------------|---|
| electron | electron (low p_T) | 0.1 |
| muon | electron | 0.1 |
| electron | jet | 0.3 |
| jet | muon | $\min(0.4, 0.04 + 10[\text{GeV}]/p_T(\text{muon}))$ |
| electron | tau | 0.2 |

Table 4: Summary of the overlap removal procedure between electrons, muons, and jets.

588 8 Event Selection and Signal Region Definitions

589 Event are required to pass a preselection described in Section 12.1 and summarized in Table 12.
 590 Those that pass this preselection are divided into various fit regions described in Section 12.2,
 591 based on the number of jets in the event, and the b-tag score of those jets.

592 8.1 Event Preselection

593 Events are required to include exactly three reconstructed light leptons passing the requirement
 594 described in 11.2, which have a total charge of ± 1 .

595 The leptons are ordered in the analysis code as 0, 1, and 2. Lepton 0 is the lepton whose
 596 charge is opposite the other two. Lepton 1 is the lepton closest to the opposite charge lepton, i.e.
 597 the smallest ΔR , leaving lepton 2 as the lepton further from the opposite charge lepton. Lepton
 598 0 is required to have $p_T > 10 \text{ GeV}$, while the same sign leptons, 1 and 2, are required to have
 599 $p_T > 20 \text{ GeV}$ to reduce the contribution of non-prompt leptons.

600 The invariant mass of at least one pair of opposite sign, same flavor leptons is required
 601 to fall within 10 GeV of the mass of the Z boson, 91.2 GeV. Events where one of the opposite
 602 sign pairs have an invariant mass less than 12 GeV are rejected in order to suppress low mass
 603 resonances.

604 An additional requirement is placed on the missing transverse energy, $E_T^{\text{miss}} > 20 \text{ GeV}$,
 605 and the transverse mass of the W candidate, $m(E_T^{\text{miss}} + l_{\text{other}}) > 30 \text{ GeV}$, where E_T^{miss} is the
 606 missing transverse energy, and l_{other} is the lepton not included in the Z-candidate.

607 Events are required to have one or two reconstructed jets passing the selection described
 608 in Section 11.3. Events with more than two jets are rejected in order to reduce the contribution
 609 of backgrounds such as $t\bar{t}Z$ and $t\bar{t}W$, which tend to have higher jet multiplicity.

Event Selection

Exactly three leptons with charge ± 1
 Two same-charge leptons with $p_T > 20 \text{ GeV}$
 One opposite charge lepton with $p_T > 10 \text{ GeV}$
 $m(l^+l^-)$ within 10 GeV of 91.2 GeV
 Transverse mass of W-candidate, $m_T(E_T^{\text{miss}} + l_{\text{ep other}}) > 30 \text{ GeV}$
 Missing transverse energy, $E_T^{\text{miss}} > 20 \text{ GeV}$
 One or two jets with $p_T > 25 \text{ GeV}$

Table 5: Summary of the selection applied to events for inclusion in the fit

610 The event yields in the preselection region for both data and Monte Carlo are summarized
 611 in Table 12.1, which shows good agreement between data and Monte Carlo, and demonstrates
 612 that this region consists primarily of WZ events. The WZ events are split into WZ + b, WZ
 613 + c, and WZ + 1 based on the truth flavor of the associated jet in the event. Specifically, this

614 determination is made based on the HadronConeExclTruthLabelID of the jet, as recommended
 615 by the b-tagging working group [25]. In this ordering b-jet supersedes charm, which supersedes
 616 light. That is, WZ + l events contain no charm and no b jets at truth level, WZ + c contain at
 617 least one truth charm and no b-jets, and WZ + b contains at least one truth b-jet.

| Process | Events |
|------------|-----------------|
| WZ + b | 167.6 ± 6.5 |
| WZ + c | 1080 ± 40 |
| WZ + l | 7220 ± 310 |
| Other VV | 850 ± 140 |
| t̄tW | 16.8 ± 2.3 |
| t̄tZ | 115 ± 17 |
| rare Top | 2.2 ± 0.1 |
| Single top | 0.10 ± 0.45 |
| Three top | 0.01 ± 0.01 |
| Four top | 0.02 ± 0.01 |
| t̄tWW | 0.23 ± 0.05 |
| Z + jets | 600 ± 260 |
| V + γ | 37 ± 54 |
| tZ | 190 ± 70 |
| tW | 5.5 ± 1.2 |
| WtZ | 25.8 ± 1.1 |
| VVV | 26.2 ± 0.9 |
| VH | 94 ± 7 |
| t̄t | 108.68 ± 8 |
| t̄tH | 4.3 ± 0.5 |
| Total | 10600 ± 530 |
| Data | 10574 |

Table 6: Event yields in the preselection region at 139.0 fb^{-1}

618 Here Other VV represents diboson processes other than WZ, and consists predominantly
 619 of ZZ → ll̄ll events where one of the leptons is not reconstructed.

620 Simulations are further validated by comparing the kinematic distributions of the Monte

621 Carlo with data, which are shown in Figure 12.1. Here, bins with 5% or more WZ+b are
622 blinded.

WZ Fit Region - Inclusive

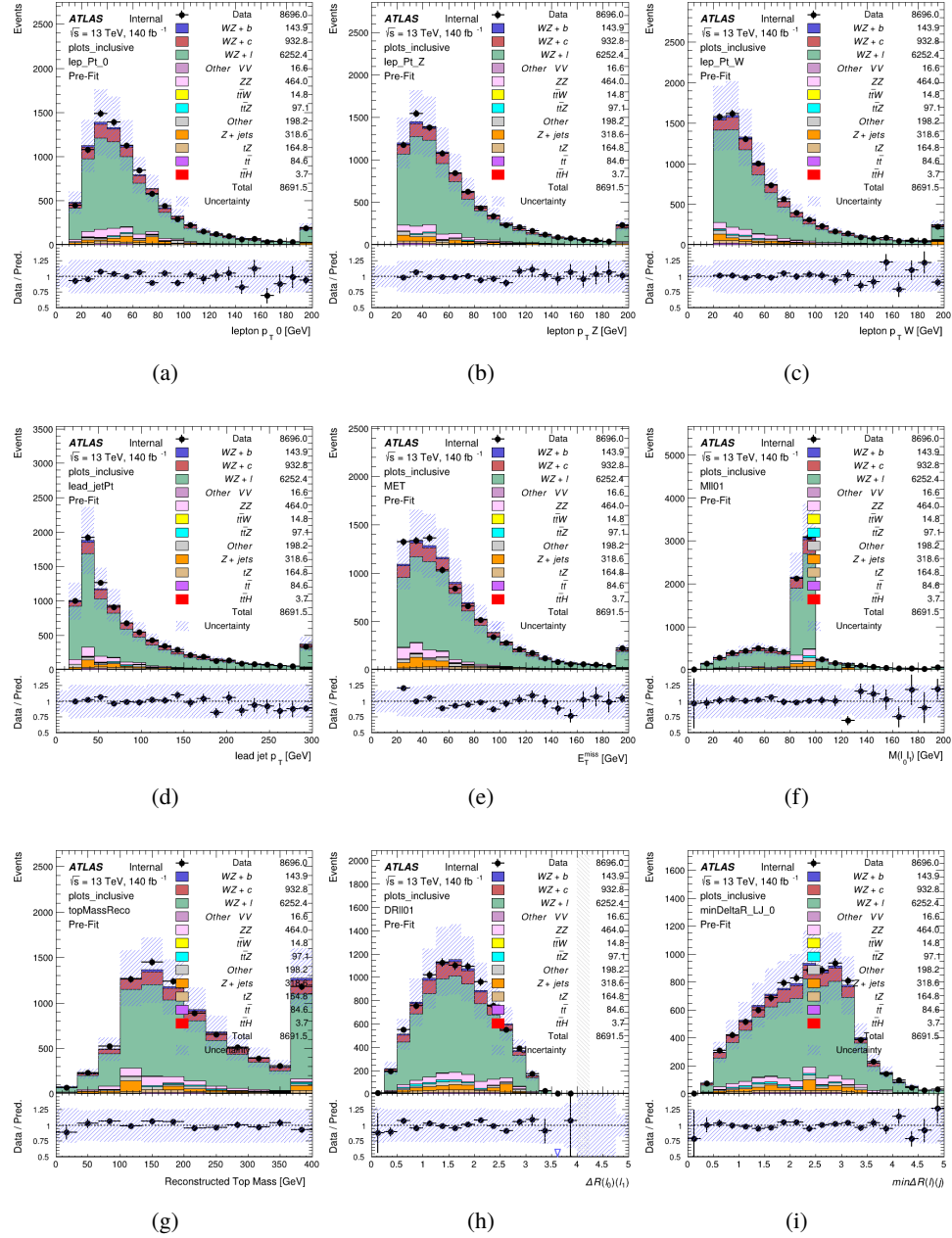


Figure 8.1: Comparisons between the data and MC distributions in the preselection region for (a) the p_T of the opposite sign lepton, (b) the p_T of the other lepton from the Z candidate, (c) the p_T of the lepton from the W candidate, (d) the leading jet p_T , (e) the E_T^{miss} , and (f) the invariant mass of leptons 0 and 1, (g) the reconstructed top mass, (h) $\Delta(R)$ between lepton 0 and 1, (i) the $\Delta(R)$ between the closest lepton and jet.

623 **8.2 Fit Regions**

624 Once preselection has been applied, the remaining events are categorized into one of twelve
 625 orthogonal regions. The regions used in the fit are summarized in Table 14.

Table 7: A list of the regions used in the fit and the selection used for each.

| Region | Selection |
|-------------|--|
| 1j, <85% | $N_{\text{jets}} = 1, n\text{Jets_DL1r_85} = 0$ |
| 1j, 85%-77% | $N_{\text{jets}} = 1, n\text{Jets_DL1r_85} = 1, n\text{Jets_DL1r_77} = 0$ |
| 1j, 77%-70% | $N_{\text{jets}} = 1, n\text{Jets_DL1r_77} = 1, n\text{Jets_DL1r_70} = 0$ |
| 1j, 70%-60% | $N_{\text{jets}} = 1, n\text{Jets_DL1r_70} = 1, n\text{Jets_DL1r_60} = 0$ |
| 1j, >60% | $N_{\text{jets}} = 1, n\text{Jets_DL1r_60} = 1, tZ \text{ BDT} > 0.725$ |
| 1j tZ CR | $N_{\text{jets}} = 1, n\text{Jets_DL1r_60} = 1, tZ \text{ BDT} < 0.725$ |
| 2j, <85% | $N_{\text{jets}} = 2, n\text{Jets_DL1r_85} = 0$ |
| 2j, 85%-77% | $N_{\text{jets}} = 2, n\text{Jets_DL1r_85} \geq 1, n\text{Jets_DL1r_77} = 0$ |
| 2j, 77%-70% | $N_{\text{jets}} = 2, n\text{Jets_DL1r_77} \geq 1, n\text{Jets_DL1r_70} = 0$ |
| 2j, 70%-60% | $N_{\text{jets}} = 2, n\text{Jets_DL1r_70} \geq 1, n\text{Jets_DL1r_60} = 0$ |
| 2j, >60% | $N_{\text{jets}} = 2, n\text{Jets_DL1r_60} \geq 1, tZ \text{ BDT} > 0.725$ |
| 2j tZ CR | $N_{\text{jets}} = 2, n\text{Jets_DL1r_60} \geq 1, tZ \text{ BDT} < 0.725$ |

626 The working points discussed in Section 11.4 are used to separate events into fit regions
 627 based on the highest working point reached by a jet in each event. Because the background
 628 composition differs significantly based on the number of b-jets, events are further subdivided
 629 into 1-jet and 2-jet regions in order to minimize the impact of background uncertainties.

630 An unfolding procedure is performed to account for differences in the number of recon-
 631 structed jets compared to the number of truth jets in each event. The `AntiKt4TruthDressedWZJets`
 632 truth jet collection is used to make this determination. In order to account for migration of WZ+1-
 633 jet and WZ+2-jet events between the 1-jet and 2-jet bins at reco level, the signal samples are
 634 separated based on the number of truth jets. Events with 0 jets or more than 3 jets at truth level,

yet fall within one of the categories listed in Table 14, are categorized as WZ + other, and treated as a background. The migration matrix in the number of jets at truth level versus reco level is shown in Figure 12.2. The composition of the number of truth jets in each reco jet bin is taken from MC, with uncertainties in these estimates described in detail in Section 21.

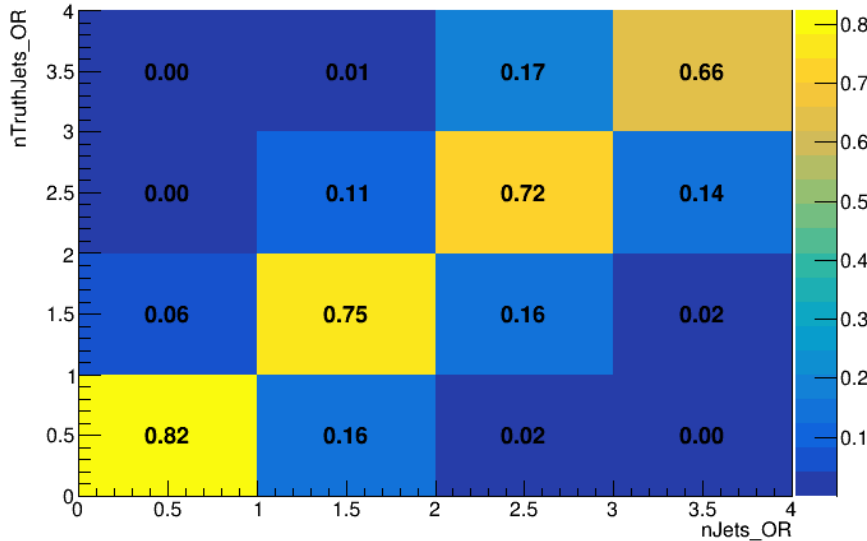


Figure 8.2: Number of truth jets compared to the number of reconstructed jets in each WZ event falling in the preselection region. Each row is normalized to unity.

An additional tZ control region is created based on the BDT described in Section 13. The region with 1-jet passing the 60% working point is split in two - a signal enriched region of events with a BDT score greater than 0.03, and a tZ control region including events with less than 0.03. This cutoff is arrived at by performing an Asimov fit with a variety of cutoffs, and selecting the value that produces the highest significance for the measurement of WZ + b.

The modeling in each region is validated by comparing data and MC predictions for

645 various kinematic distributions. These plot are shown in Figures [12.3-12.16](#).

WZ Fit Region - 1j Inclusive

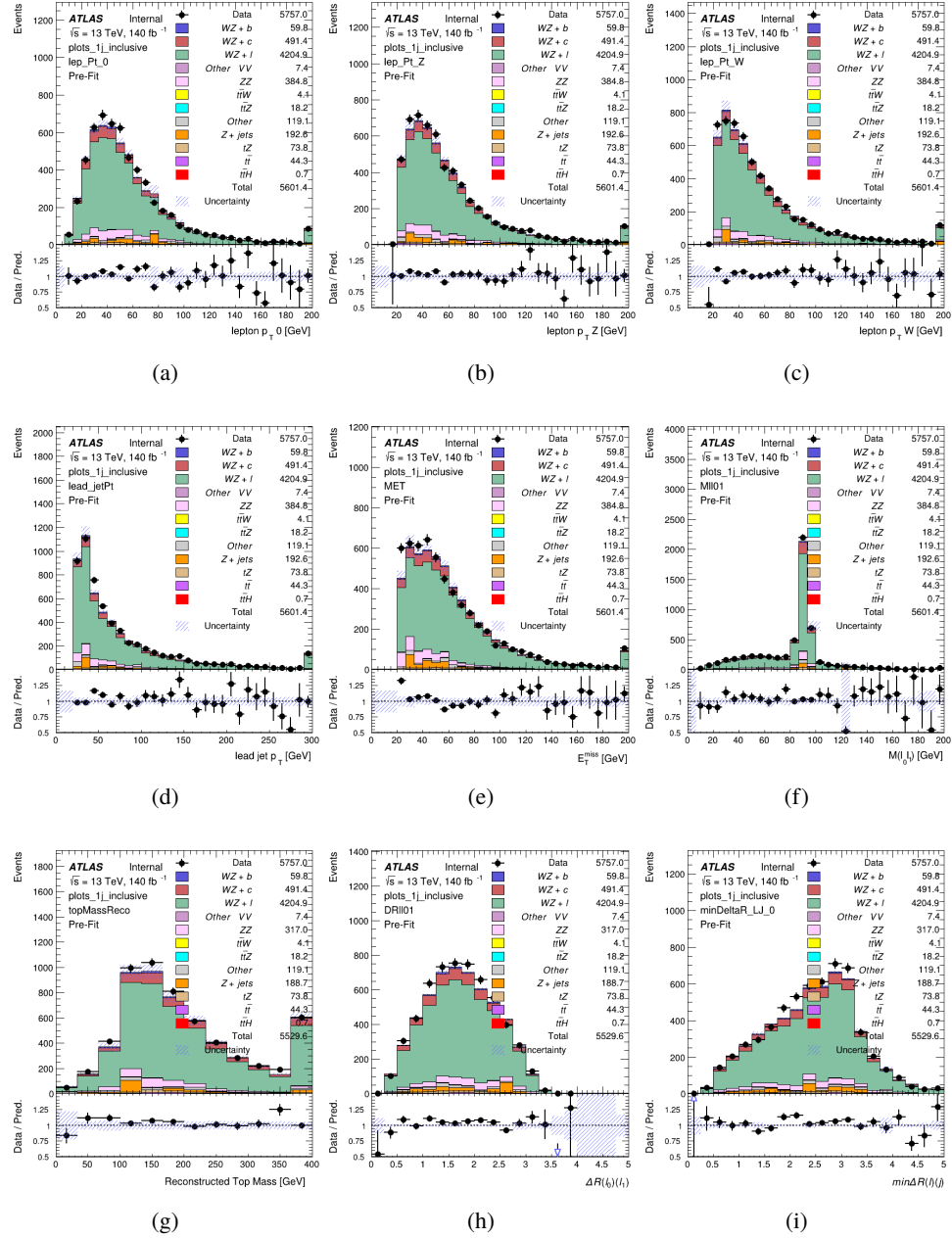


Figure 8.3: Comparisons between the data and MC distributions in the preselection region for (a) the p_T of the opposite sign lepton, (b) the p_T of the other lepton from the Z candidate, (c) the p_T of the lepton from the W candidate, (d) the leading jet p_T , (e) the E_T^{miss} , and (f) the invariant mass of leptons 0 and 1, (g) the reconstructed top mass, (h) $\Delta(R)$ between lepton 0 and 1, (i) the $\Delta(R)$ between the closest lepton and jet.

WZ Fit Region - 1j < 85% WP

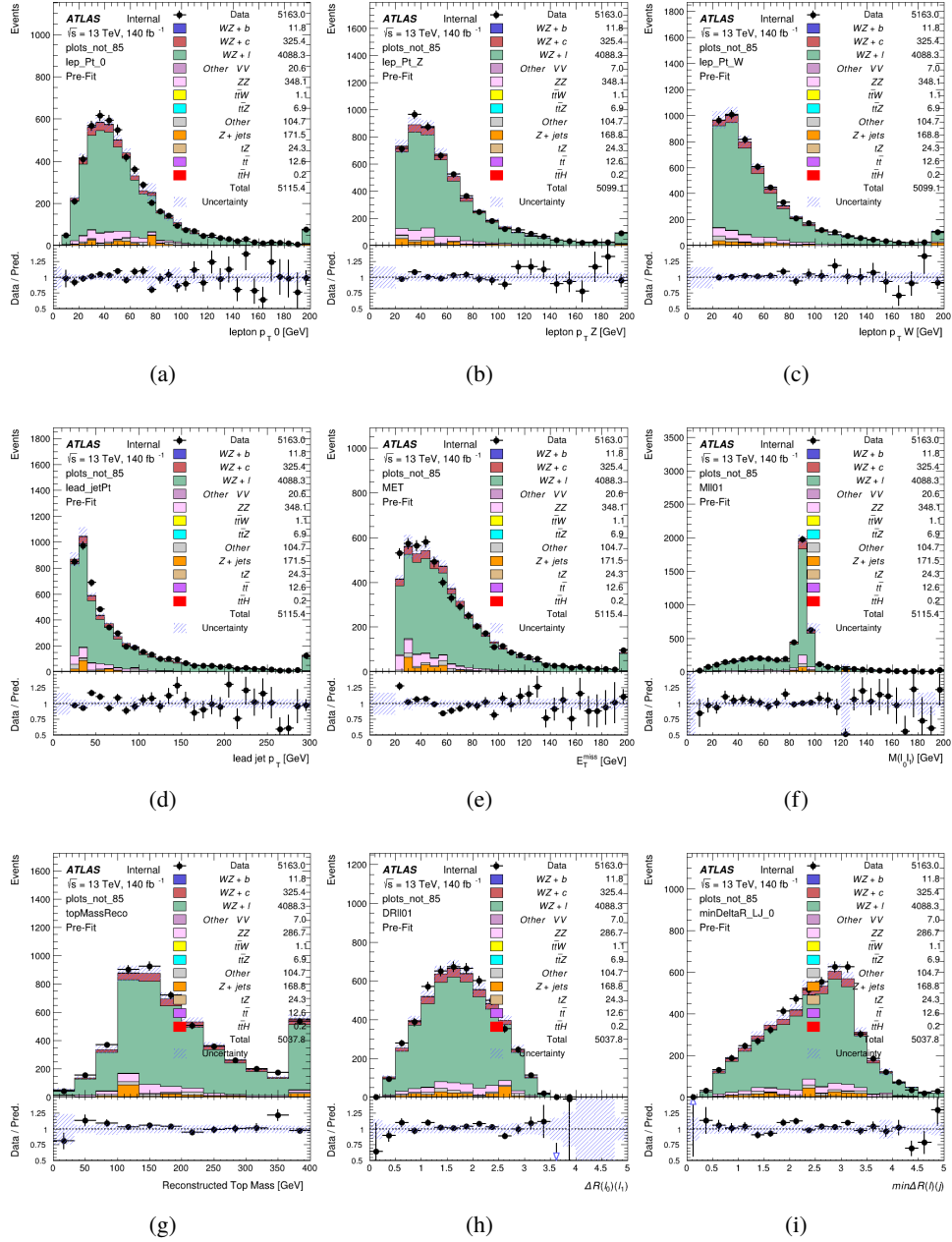


Figure 8.4: Comparisons between the data and MC distributions in the preselection region for (a) the p_T of the opposite sign lepton, (b) the p_T of the other lepton from the Z candidate, (c) the p_T of the lepton from the W candidate, (d) the leading jet p_T , (e) the E_T^{miss} , and (f) the invariant mass of leptons 0 and 1, (g) the reconstructed top mass, (h) $\Delta(R)$ between lepton 0 and 1, (i) the $\Delta(R)$ between the closest lepton and jet.

WZ Fit Region - 1j 77-85% WP

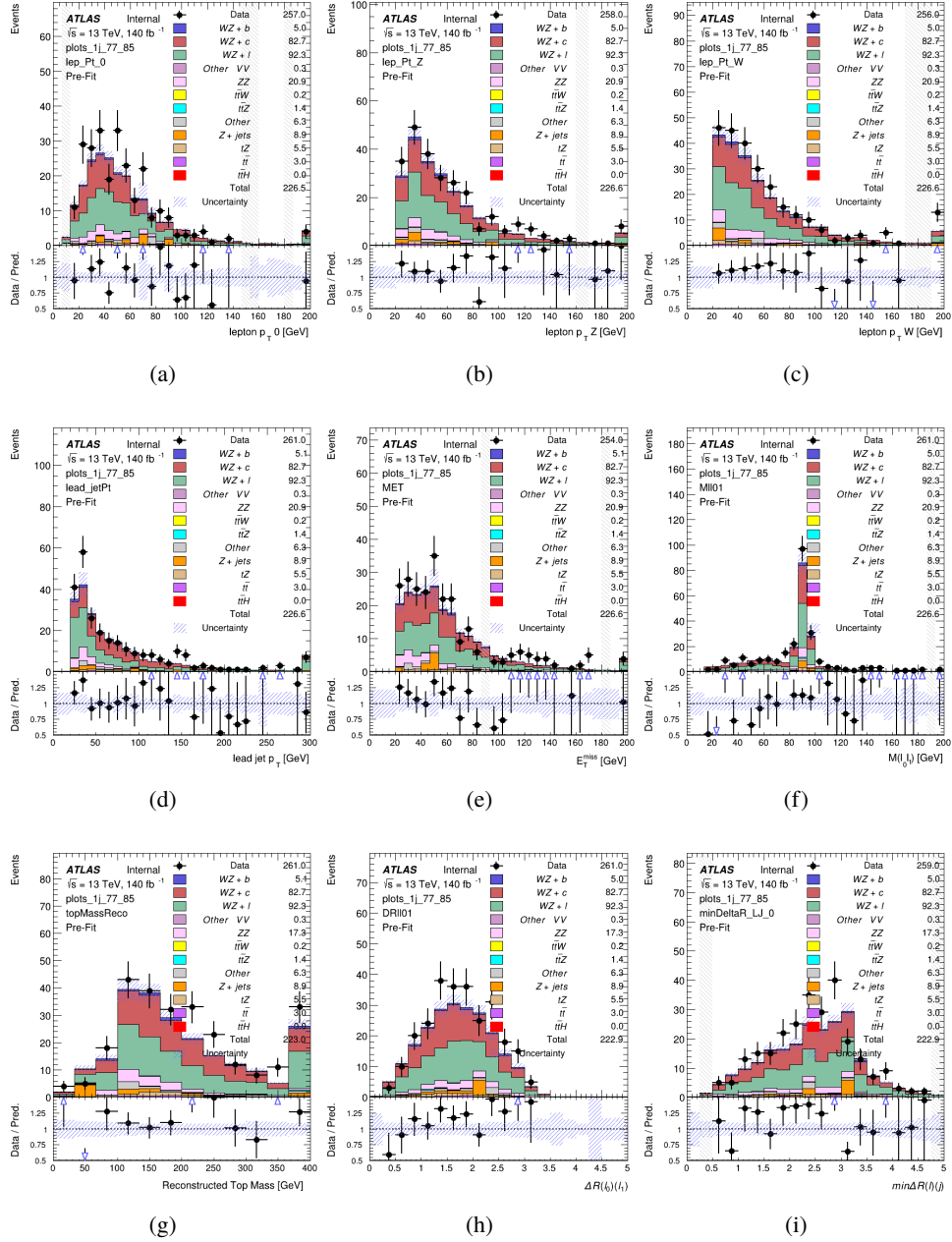


Figure 8.5: Comparisons between the data and MC distributions in the preselection region for (a) the p_T of the opposite sign lepton, (b) the p_T of the other lepton from the Z candidate, (c) the p_T of the lepton from the W candidate, (d) the leading jet p_T , (e) the E_T^{miss} , and (f) the invariant mass of leptons 0 and 1, (g) the reconstructed top mass, (h) $\Delta(R)$ between lepton 0 and 1, (i) the $\Delta(R)$ between the closest lepton and jet.

WZ Fit Region - 1j 70-77% WP

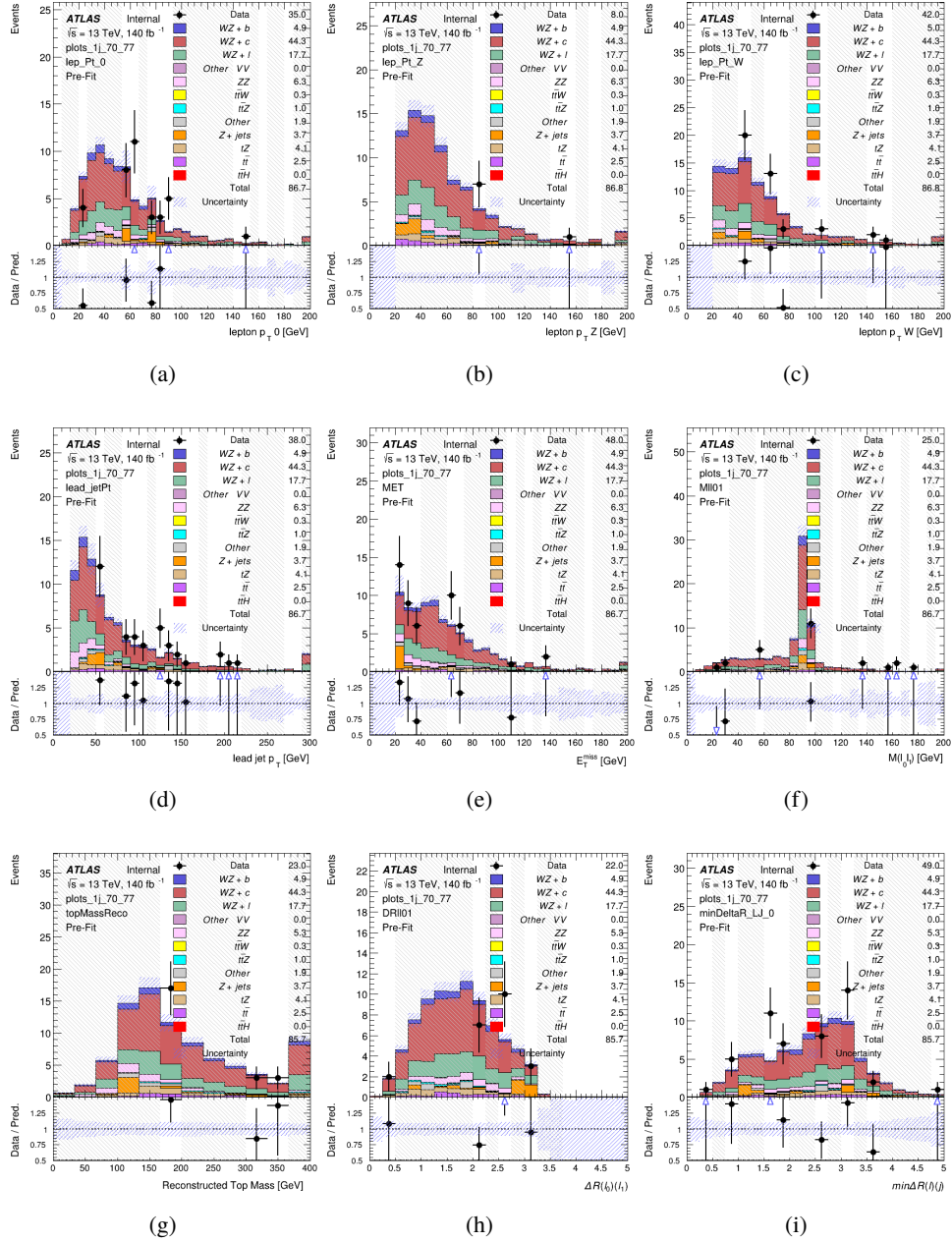


Figure 8.6: Comparisons between the data and MC distributions in the preselection region for (a) the p_T of the opposite sign lepton, (b) the p_T of the other lepton from the Z candidate, (c) the p_T of the lepton from the W candidate, (d) the leading jet p_T , (e) the E_T^{miss} , and (f) the invariant mass of leptons 0 and 1, (g) the reconstructed top mass, (h) $\Delta(R)$ between lepton 0 and 1, (i) the $\Delta(R)$ between the closest lepton and jet.

WZ Fit Region - 1j 60-70% WP

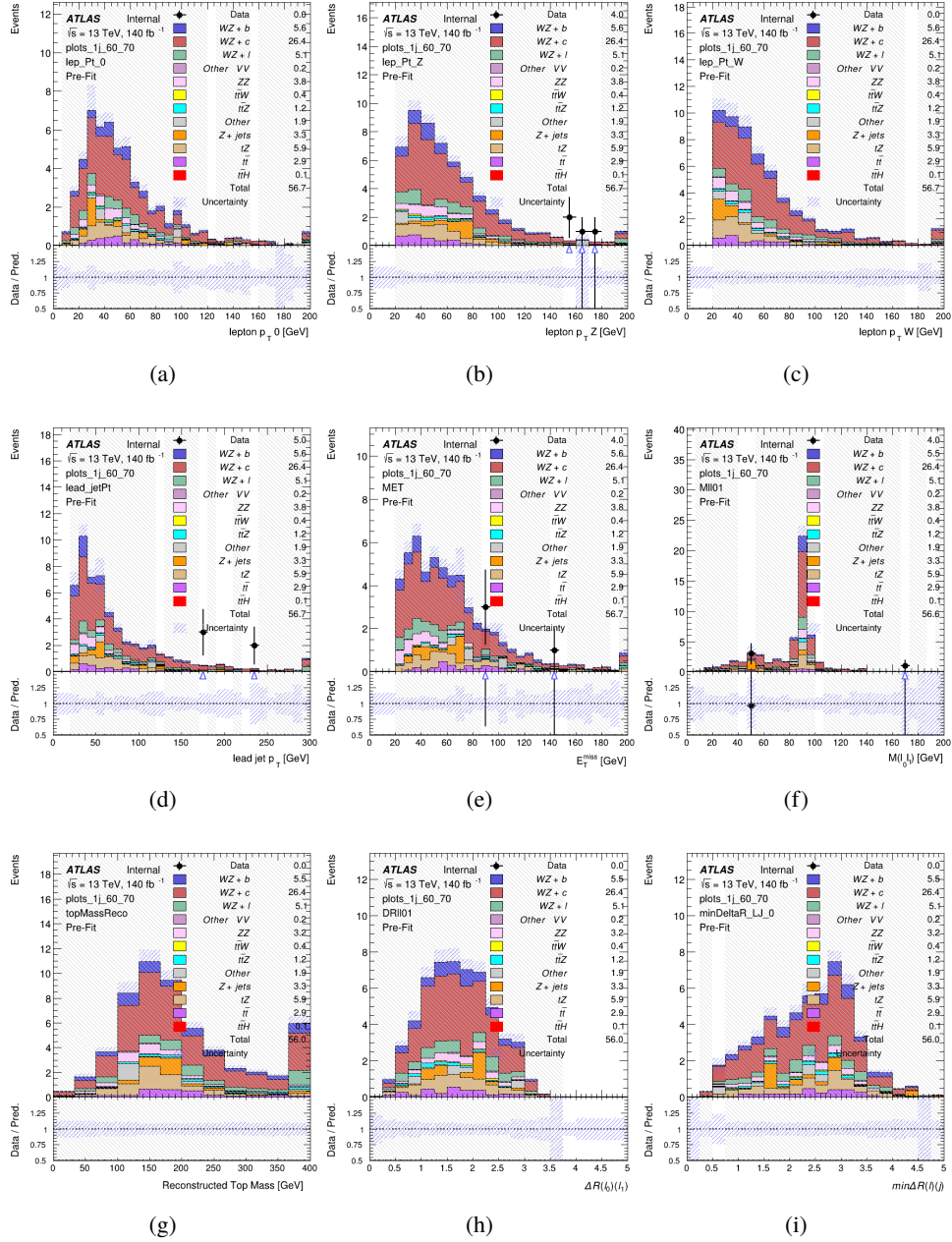


Figure 8.7: Comparisons between the data and MC distributions in the preselection region for (a) the p_T of the opposite sign lepton, (b) the p_T of the other lepton from the Z candidate, (c) the p_T of the lepton from the W candidate, (d) the leading jet p_T , (e) the E_T^{miss} , and (f) the invariant mass of leptons 0 and 1, (g) the reconstructed top mass, (h) $\Delta(R)$ between lepton 0 and 1, (i) the $\Delta(R)$ between the closest lepton and jet.

WZ Fit Region - 1j 60% WP

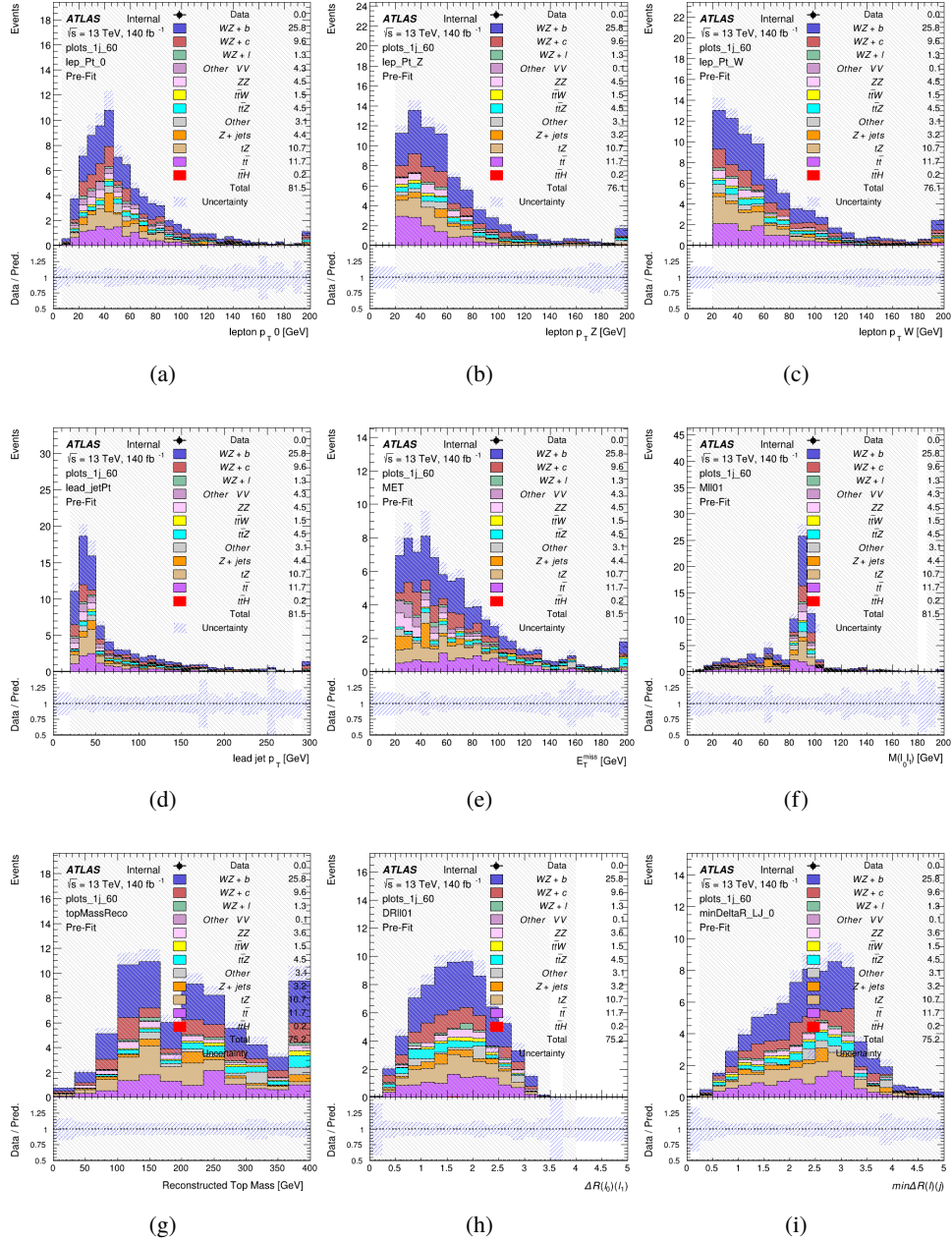


Figure 8.8: Comparisons between the data and MC distributions in the preselection region for (a) the p_T of the opposite sign lepton, (b) the p_T of the other lepton from the Z candidate, (c) the p_T of the lepton from the W candidate, (d) the leading jet p_T , (e) the E_T^{miss} , and (f) the invariant mass of leptons 0 and 1, (g) the reconstructed top mass, (h) $\Delta(R)$ between lepton 0 and 1, (i) the $\Delta(R)$ between the closest lepton and jet.

WZ Fit Region - tZ-CR

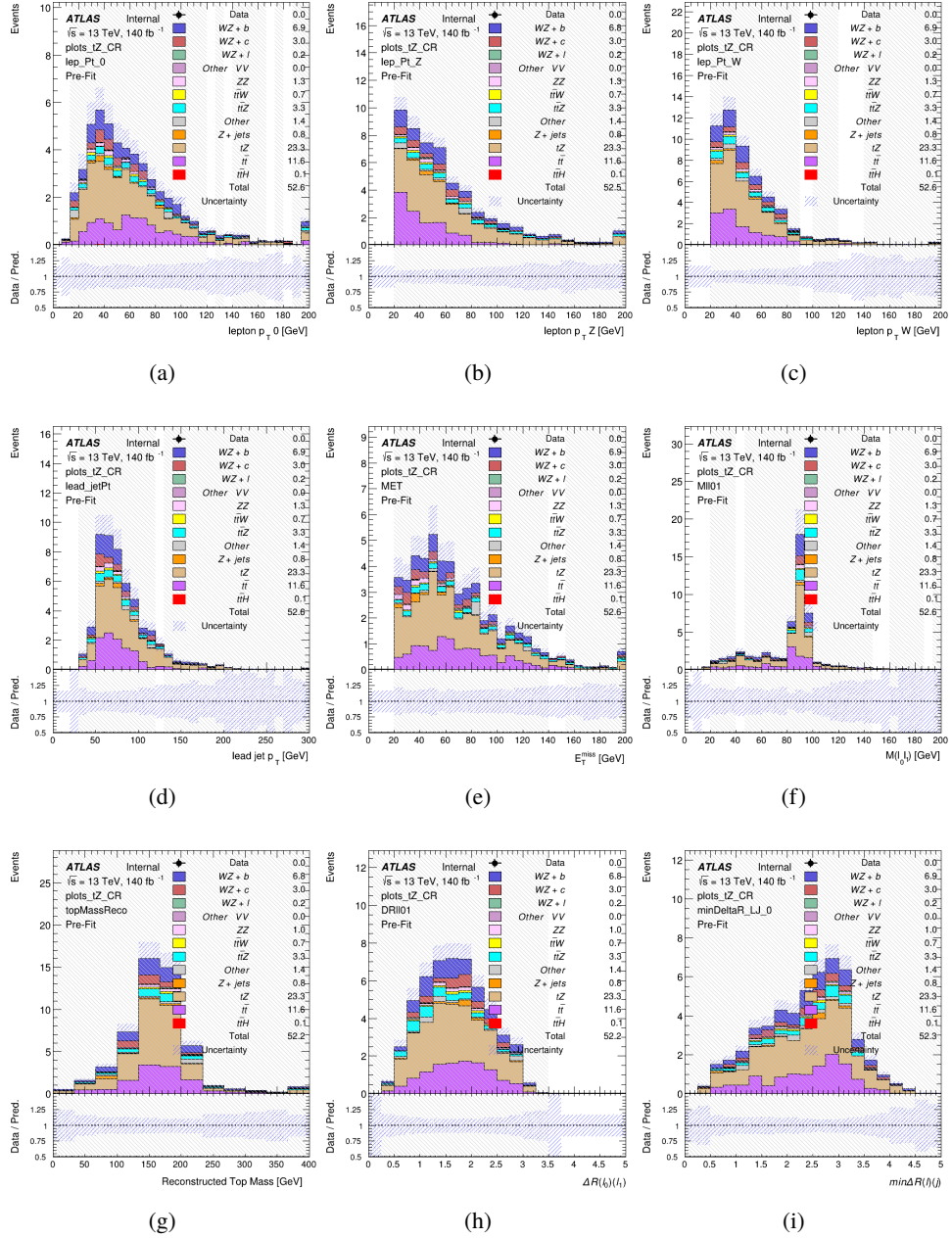


Figure 8.9: Comparisons between the data and MC distributions in the preselection region for (a) the p_T of the opposite sign lepton, (b) the p_T of the other lepton from the Z candidate, (c) the p_T of the lepton from the W candidate, (d) the leading jet p_T , (e) the E_T^{miss} , and (f) the invariant mass of leptons 0 and 1, (g) the reconstructed top mass, (h) $\Delta(R)$ between lepton 0 and 1, (i) the $\Delta(R)$ between the closest lepton and jet.

WZ Fit Region - 2j Inclusive

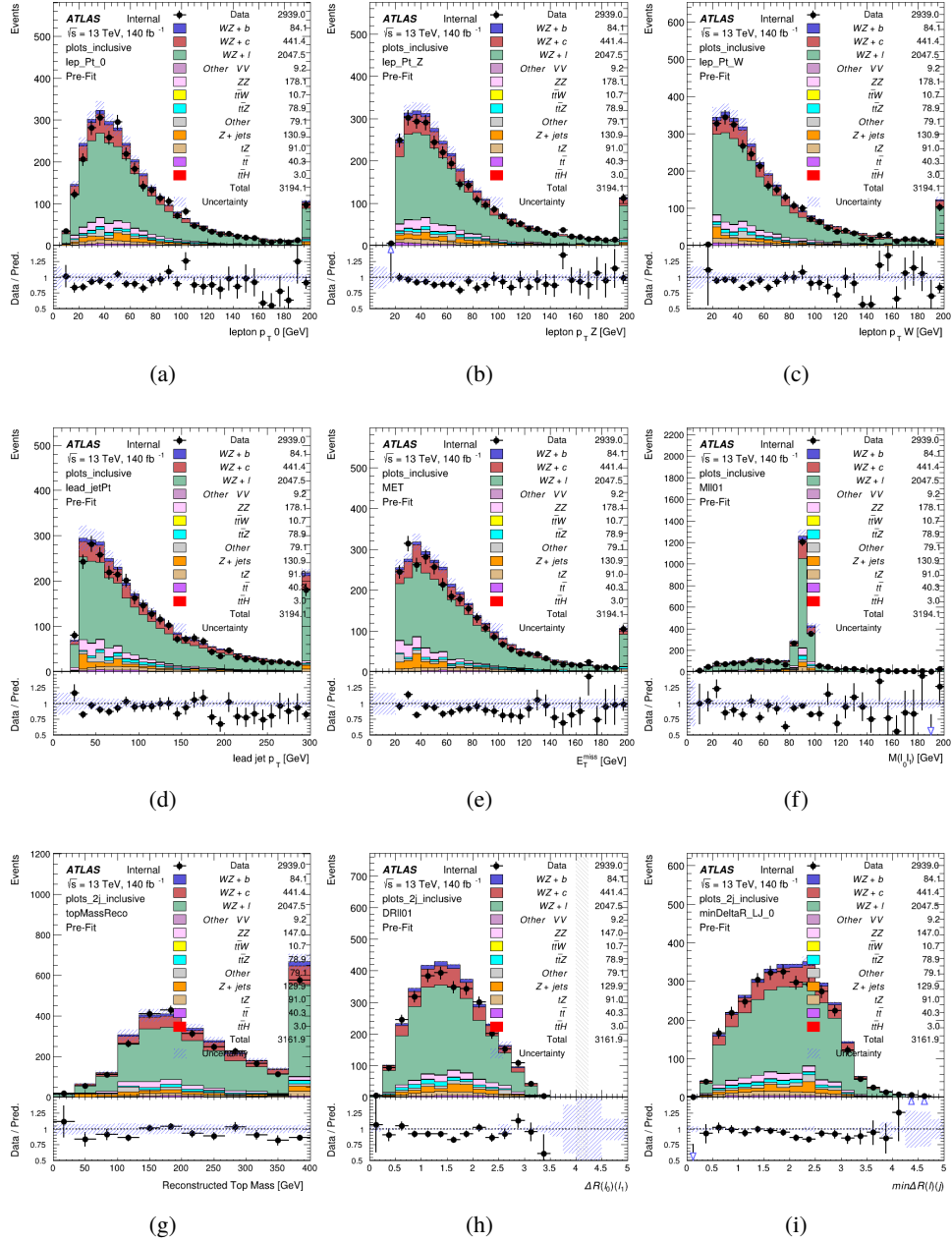


Figure 8.10: Comparisons between the data and MC distributions in the preselection region for (a) the p_T of the opposite sign lepton, (b) the p_T of the other lepton from the Z candidate, (c) the p_T of the lepton from the W candidate, (d) the leading jet p_T , (e) the E_T^{miss} , and (f) the invariant mass of leptons 0 and 1, (g) the reconstructed top mass, (h) $\Delta(R)$ between lepton 0 and 1, (i) the $\Delta(R)$ between the closest lepton and jet.

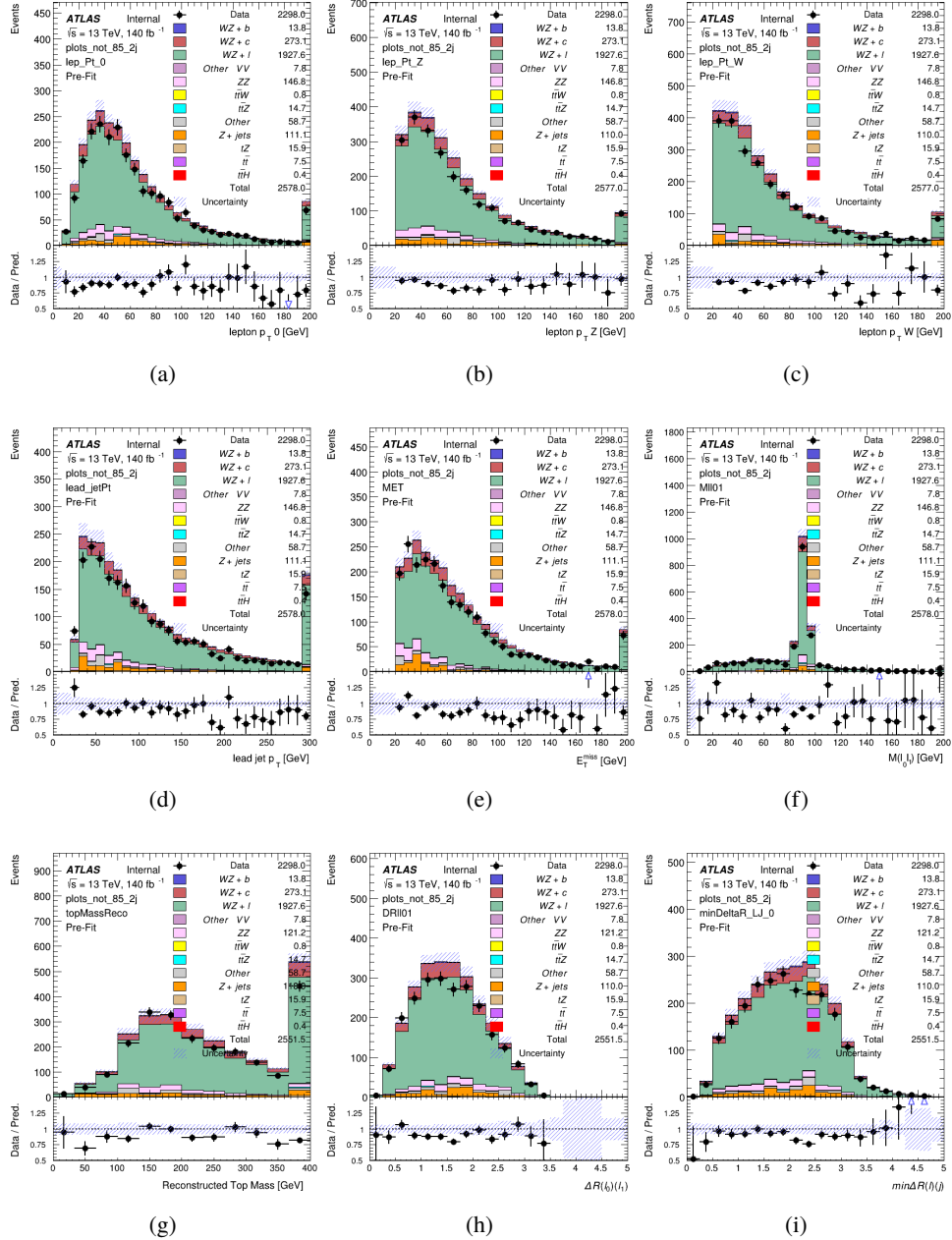
WZ Fit Region - $2j < 85\%$ WP

Figure 8.11: Comparisons between the data and MC distributions in the preselection region for (a) the p_T of the opposite sign lepton, (b) the p_T of the other lepton from the Z candidate, (c) the p_T of the lepton from the W candidate, (d) the leading jet p_T , (e) the E_T^{miss} , and (f) the invariant mass of leptons 0 and 1, (g) the reconstructed top mass, (h) $\Delta(R)$ between lepton 0 and 1, (i) the $\Delta(R)$ between the closest lepton and jet.

WZ Fit Region - 2j 77-85% WP

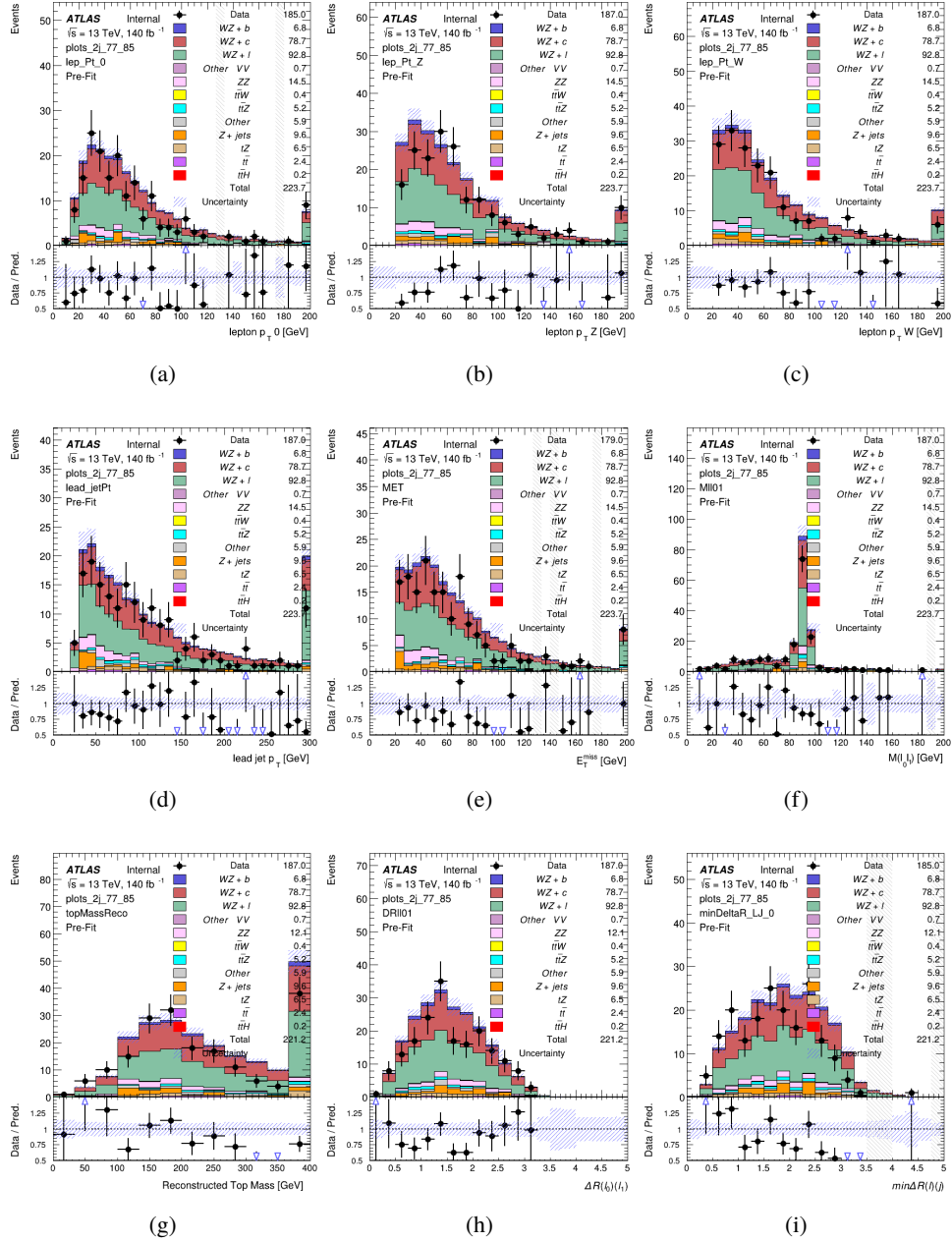


Figure 8.12: Comparisons between the data and MC distributions in the preselection region for (a) the p_T of the opposite sign lepton, (b) the p_T of the other lepton from the Z candidate, (c) the p_T of the lepton from the W candidate, (d) the leading jet p_T , (e) the E_T^{miss} , and (f) the invariant mass of leptons 0 and 1, (g) the reconstructed top mass, (h) $\Delta(R)$ between lepton 0 and 1, (i) the $\Delta(R)$ between the closest lepton and jet.

WZ Fit Region - 2j 70-77% WP

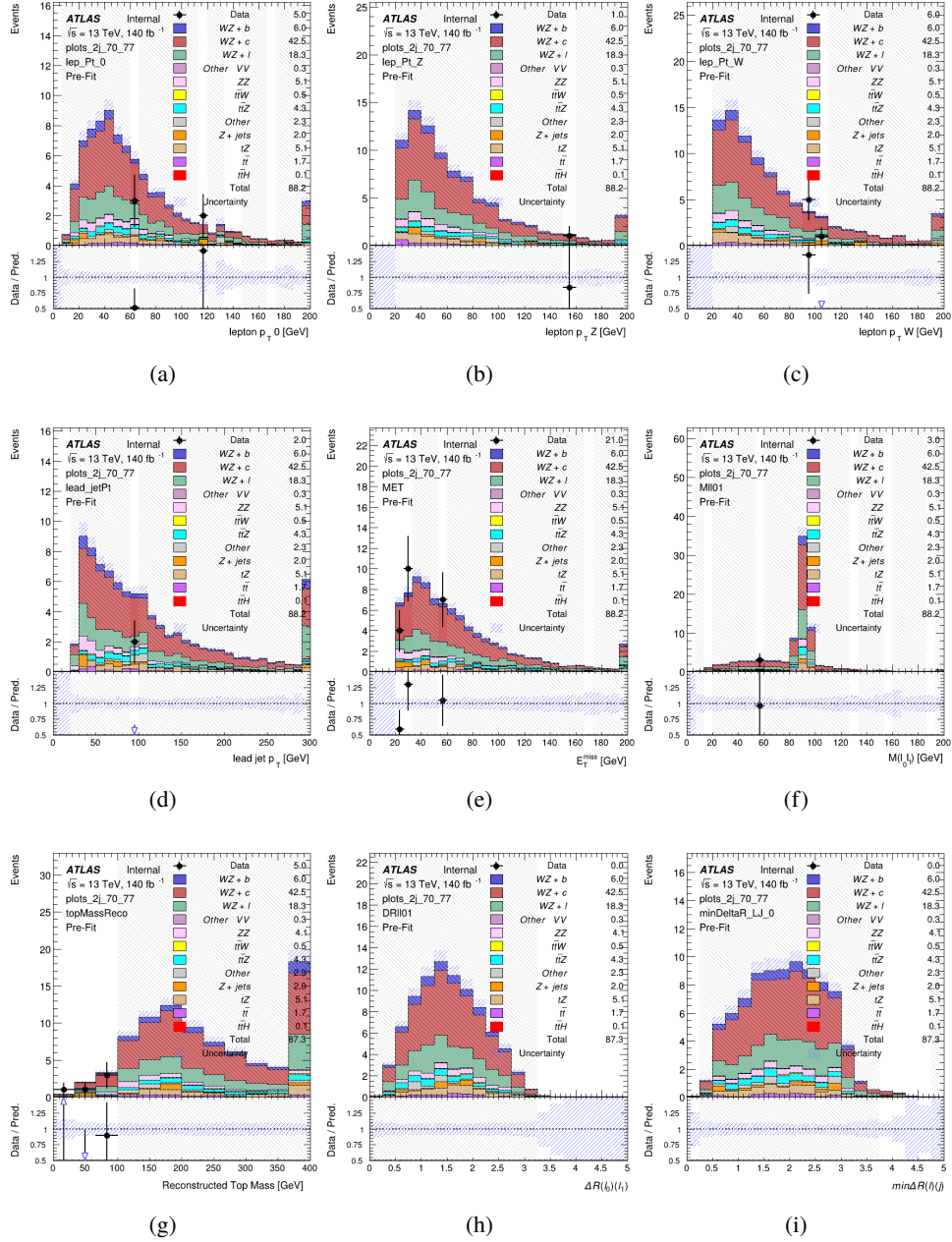


Figure 8.13: Comparisons between the data and MC distributions in the preselection region for (a) the p_T of the opposite sign lepton, (b) the p_T of the other lepton from the Z candidate, (c) the p_T of the lepton from the W candidate, (d) the leading jet p_T , (e) the E_T^{miss} , and (f) the invariant mass of leptons 0 and 1, (g) the reconstructed top mass, (h) $\Delta(R)$ between lepton 0 and 1, (i) the $\Delta(R)$ between the closest lepton and jet.

WZ Fit Region - 2j 60-70% WP

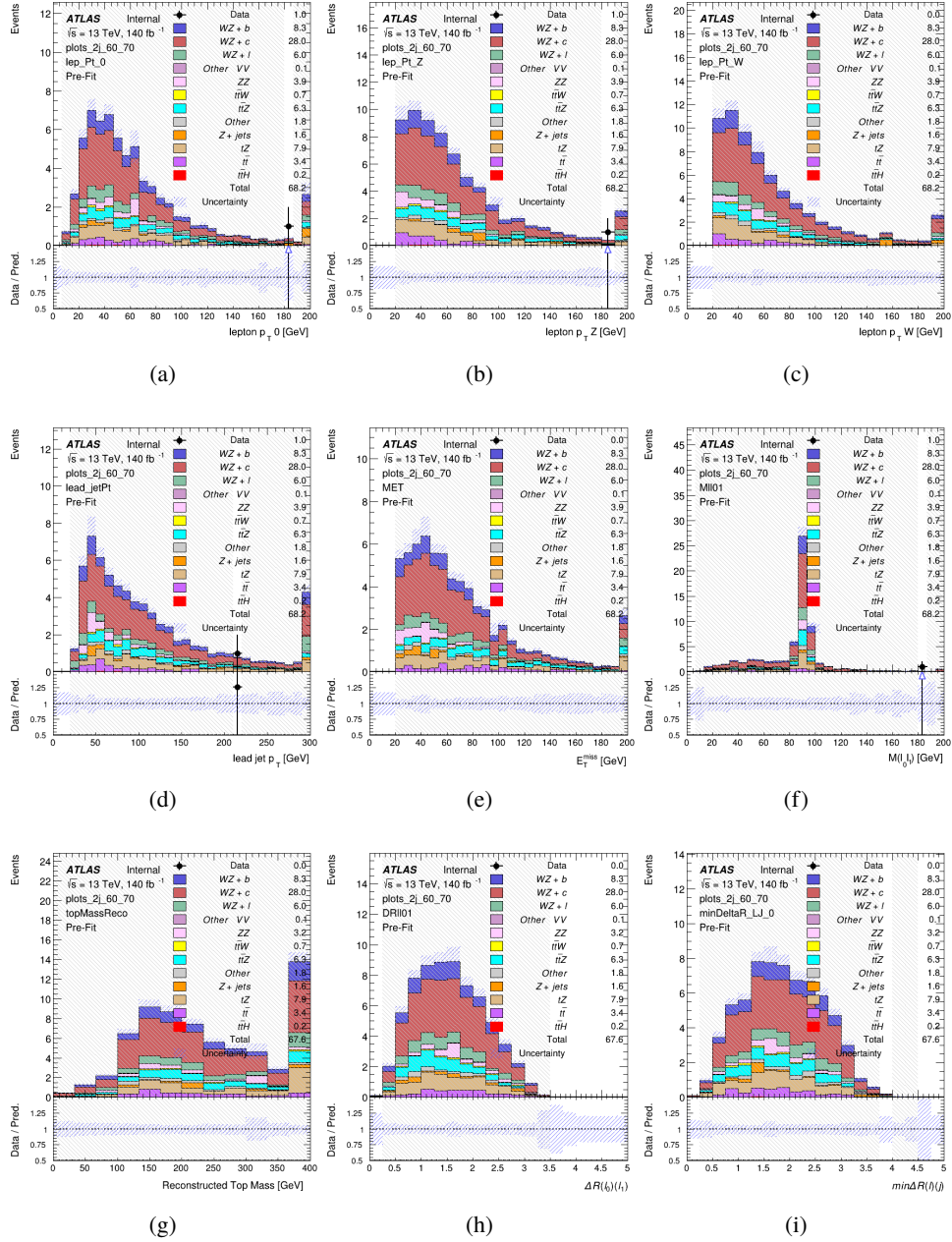


Figure 8.14: Comparisons between the data and MC distributions in the preselection region for (a) the p_T of the opposite sign lepton, (b) the p_T of the other lepton from the Z candidate, (c) the p_T of the lepton from the W candidate, (d) the leading jet p_T , (e) the E_T^{miss} , and (f) the invariant mass of leptons 0 and 1, (g) the reconstructed top mass, (h) $\Delta(R)$ between lepton 0 and 1, (i) the $\Delta(R)$ between the closest lepton and jet.

WZ Fit Region - 2j 60% WP

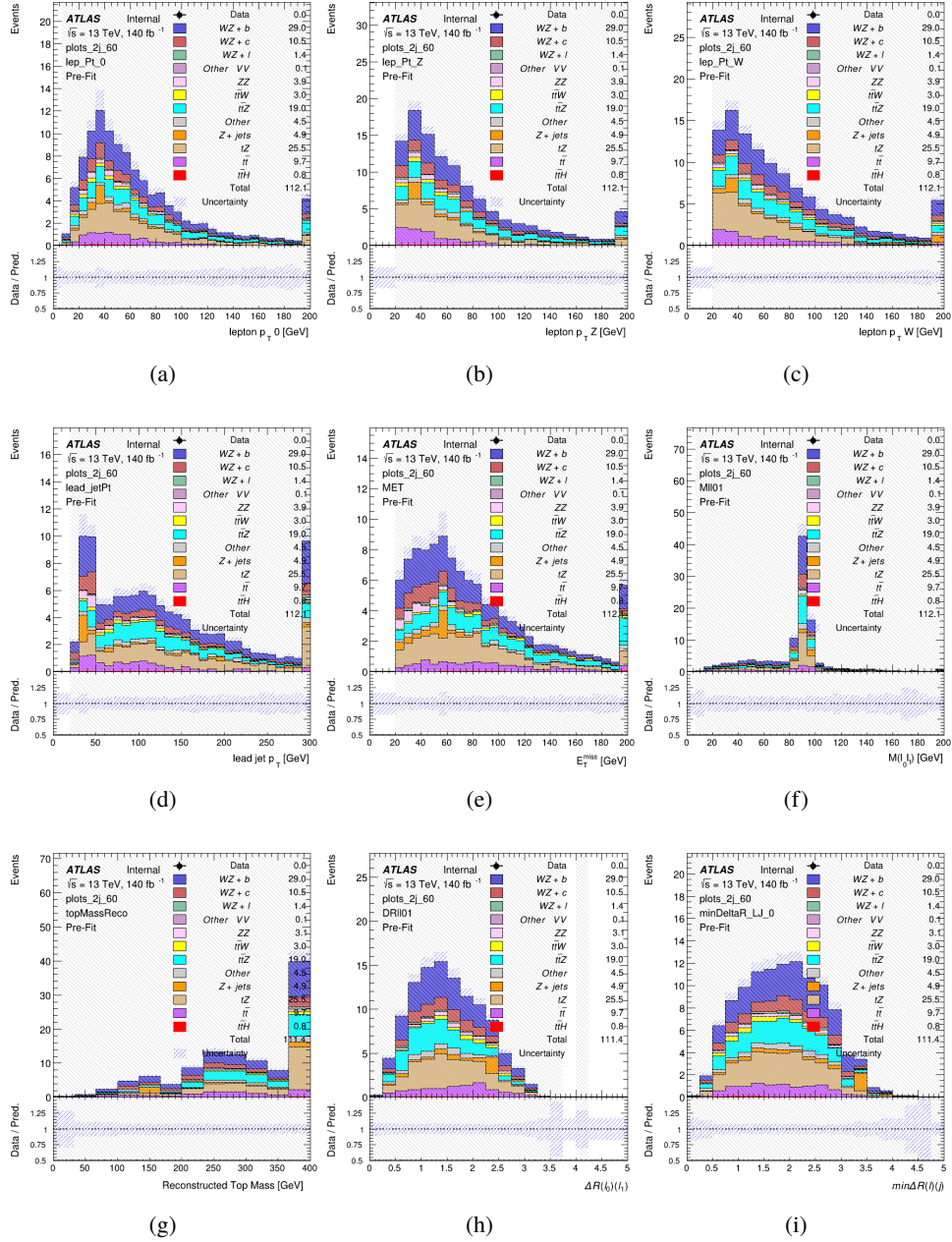


Figure 8.15: Comparisons between the data and MC distributions in the preselection region for (a) the p_T of the opposite sign lepton, (b) the p_T of the other lepton from the Z candidate, (c) the p_T of the lepton from the W candidate, (d) the leading jet p_T , (e) the E_T^{miss} , and (f) the invariant mass of leptons 0 and 1, (g) the reconstructed top mass, (h) $\Delta(R)$ between lepton 0 and 1, (i) the $\Delta(R)$ between the closest lepton and jet.

WZ Fit Region - tZ-CR-2j

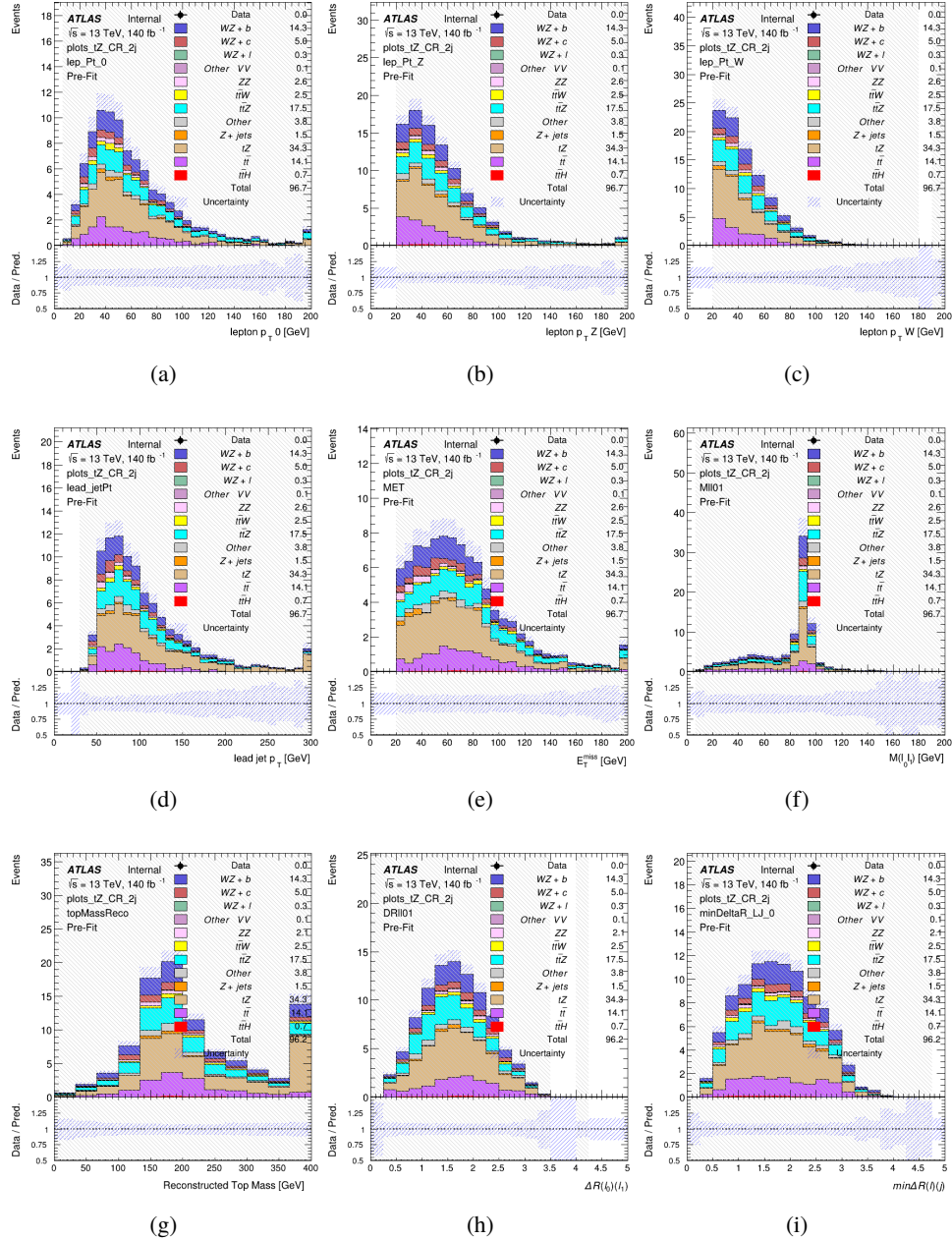


Figure 8.16: Comparisons between the data and MC distributions in the preselection region for (a) the p_T of the opposite sign lepton, (b) the p_T of the other lepton from the Z candidate, (c) the p_T of the lepton from the W candidate, (d) the leading jet p_T , (e) the E_T^{miss} , and (f) the invariant mass of leptons 0 and 1, (g) the reconstructed top mass, (h) $\Delta(R)$ between lepton 0 and 1, (i) the $\Delta(R)$ between the closest lepton and jet.

646 **8.3 Non-Prompt Lepton Estimation**

647 Two processes act as sources of non-prompt leptons appear in the analysis: $t\bar{t}$ and $Z+jet$
 648 production both produce two prompt leptons, and each contribute to the 3l region when an
 649 additional non-prompt lepton appears in the event. The contribution of these processes is
 650 estimated with Monte Carlo simulations, which are validated using enriched control regions.

651 The modelling in the $Z+jets$ and $t\bar{t}$ CRs is further validated for each of the pseudo-
 652 continuous b-tag regions used in the analysis. The relevant lepton p_T spectrum in each b-tag
 653 region is shown in Appendix .2 for these CRs after the correction factors derived below have
 654 been applied.

655 **8.3.1 $t\bar{t}$ Validation**

656 $t\bar{t}$ events can produce two prompt leptons from the decay of each of the tops. These top decays
 657 produce two b-quarks, the decay of which can produce additional non-prompt leptons, which
 658 occasionally pass the event preselection. In order to validate that the Monte Carlo accurately
 659 simulates this process accurately, the MC prediction in a non-prompt $t\bar{t}$ enriched control region
 660 is compared to data.

661 The $t\bar{t}$ control region is similar to the preselection region - three leptons meeting the
 662 criteria described in Section 12 are required, and the requirements on E_T^{miss} remain the same.
 663 However, the selection requiring a lepton pair form a Z-candidate are reversed. Events where the

664 invariant mass of any two opposite sign, same flavor leptons falls within 10 GeV of 91.2 GeV are

665 rejected. This ensures the $t\bar{t}$ control region is orthogonal to the preselection region.

666 Further, because the jet multiplicity of $t\bar{t}$ events tends to be higher than WZ, the number

667 of jets in each event is required to be greater than 1. As b-jets are almost invariably produced

668 from top decays, at least one b-tagged jet passing the 70% DL1r WP in each event is required.

669 Various kinematic plots of this region are shown in Figure 12.17.

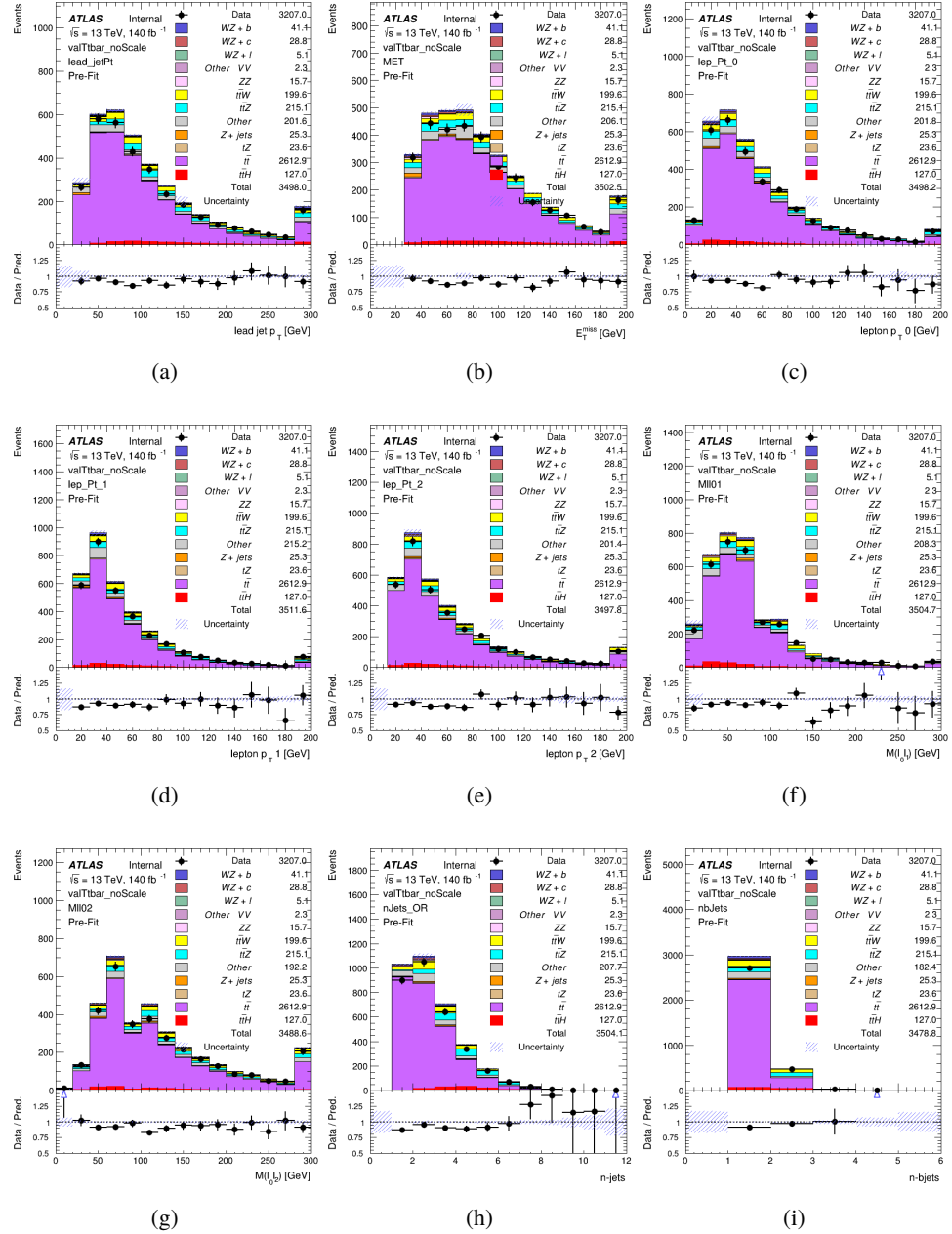


Figure 8.17: Comparisons between the data and MC distributions in the $t\bar{t}$ control region for (a) the p_T of the leading jet, (b) the missing transverse energy, (c) the p_T of lepton 0, (d) p_T of lepton 1, (e) p_T of lepton 2, (f) the invariant mass of leptons 0 and 1, (g) the invariant mass of leptons 0 and 2, (h) the number of jets, (i) the number of b-tagged jets.

670 The shape of each distribution agrees quite well between data and MC, with a constant
671 offset between the two. This is accounted for by applying a constant correction factor of 0.883
672 to the $t\bar{t}$ MC prediction. Plots showing the kinematics of the $t\bar{t}$ VR after this correction factor
673 has been applied are shown in Figure 12.18.

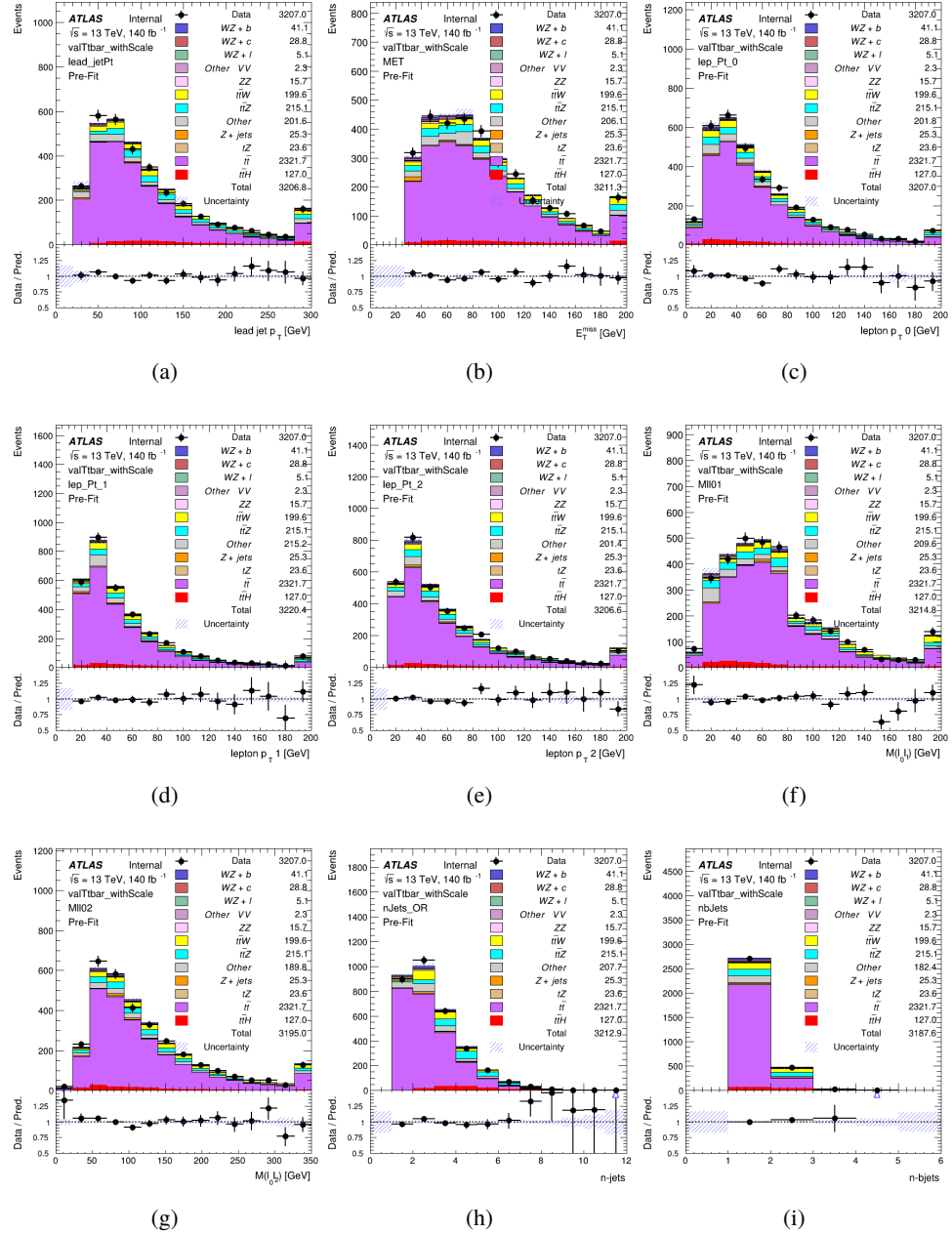


Figure 8.18: Comparisons between the data and MC distributions in the $t\bar{t}$ control region after the correction factor has been applied for (a) the p_T of the leading jet, (b) the missing transverse energy, (c) the p_T of lepton 0, (d) p_T of lepton 1, (e) p_T of lepton 2, (f) the invariant mass of leptons 0 and 1, (g) the invariant mass of leptons 0 and 2, (h) the number of jets, (i) the number of b-tagged jets.

674 The modeling is further validated by looking at the yield in the $t\bar{t}$ VR for each DL1r WP,
 675 giving a clearer correspondence to the signal regions used in the fit. Each region shown in Figure
 676 12.19 requires one or more jets pass the listed WP, with no jets passing the next highest WP.

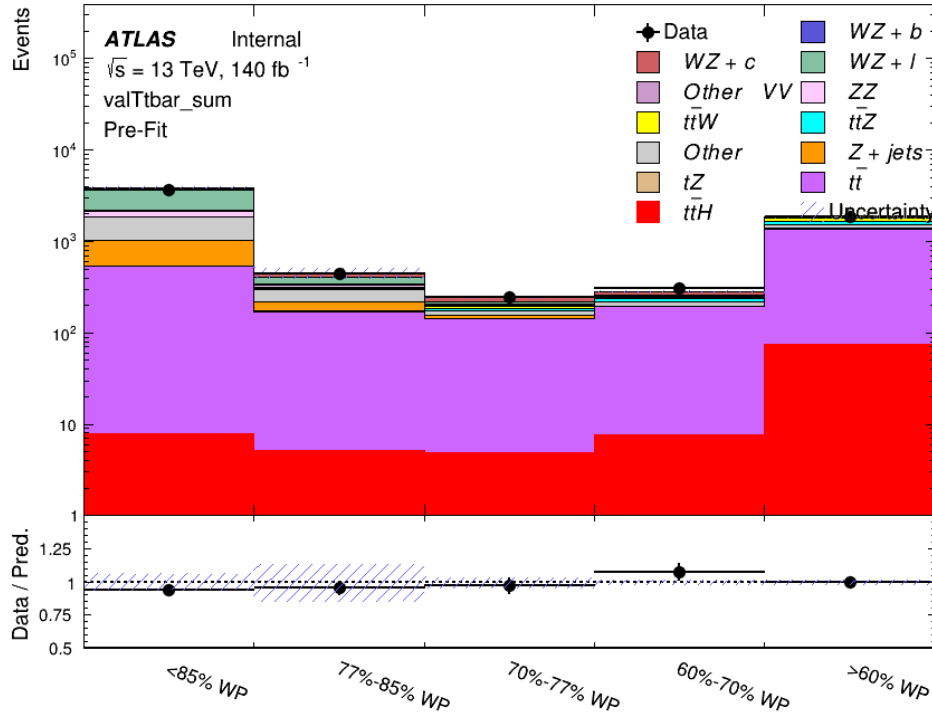


Figure 8.19: Data and MC comparisons for each DL1r WP for both 1-jet and 2-jet regions, after the $t\bar{t}$ VR selection and correction factor have been applied

677 As data and MC are found to agree within 20% for each of these working points, a 20%
 678 systematic uncertainty on the $t\bar{t}$ prediction is included for the analysis.

679 8.3.2 Z+jets Validation

680 Similar to $t\bar{t}$, a non-prompt Z +jets control region is produced in order to validate the MC
681 predictions. The lepton requirements remain the same as the preselection region. Because no
682 neutrinos are present for this process, the E_T^{miss} cut is reversed, requiring $E_T^{\text{miss}} < 30 \text{ GeV}$. This
683 also ensures this control region is orthogonal to the preselection region. Further, the number of
684 jets in each event is required to be greater than or equal to one. Various kinematic plots of this
685 region are shown below. The general agreement between data and MC in each of these suggests
686 that the non-prompt contribution of Z +jets is well modeled by Monte Carlo.

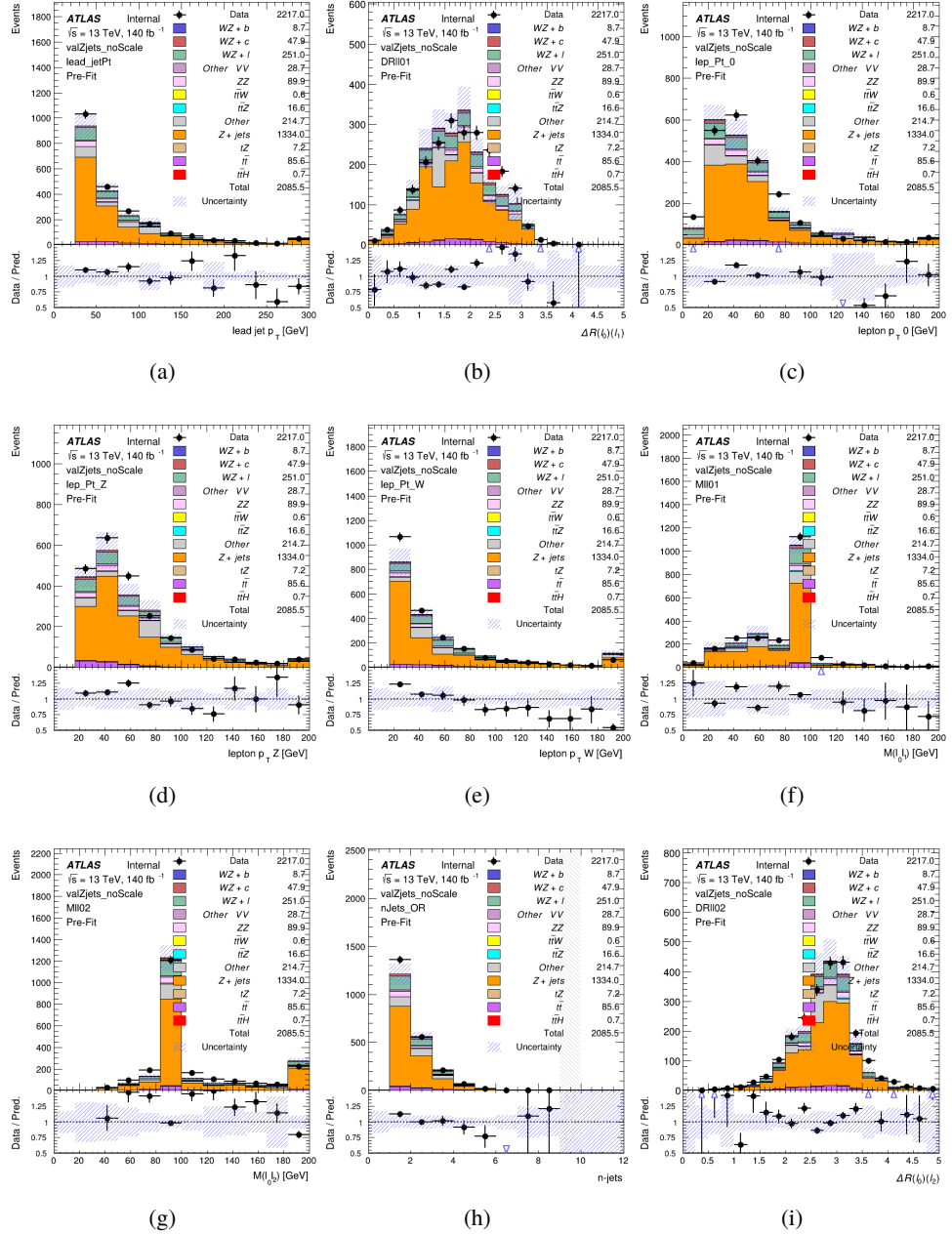


Figure 8.20: Comparisons between the data and MC distributions in the Z+jets control region for (a) the p_T of the leading jet, (b) ΔR between leptons 0 and 1, (c) the p_T of lepton 0, (d) p_T of SS lepton from the Z candidate, (e) p_T of the SS lepton from the W candidate, (f) the invariant mass of leptons 0 and 1, (g) the invariant mass of leptons 0 and 2, (h) the number of jets, (i) ΔR between leptons 0 and 2. Includes only statistical uncertainties

687 While there is general agreement between data and MC within statistical uncertainty, the
688 shape of the p_T spectrum of the lepton from the W is found to differ. To account for this
689 discrepancy, a variable correction factor is applied to Z+jets. χ^2 minimization of the lepton 2 p_T
690 spectrum is performed to derive a correction factor of $1.53 - 6.6 * 10^{-6}(lep_Pt_W)$. Kinematic
691 plots of the Z + jets control region after this correction factor has been aplied are shown in Figure
692 [12.21](#).

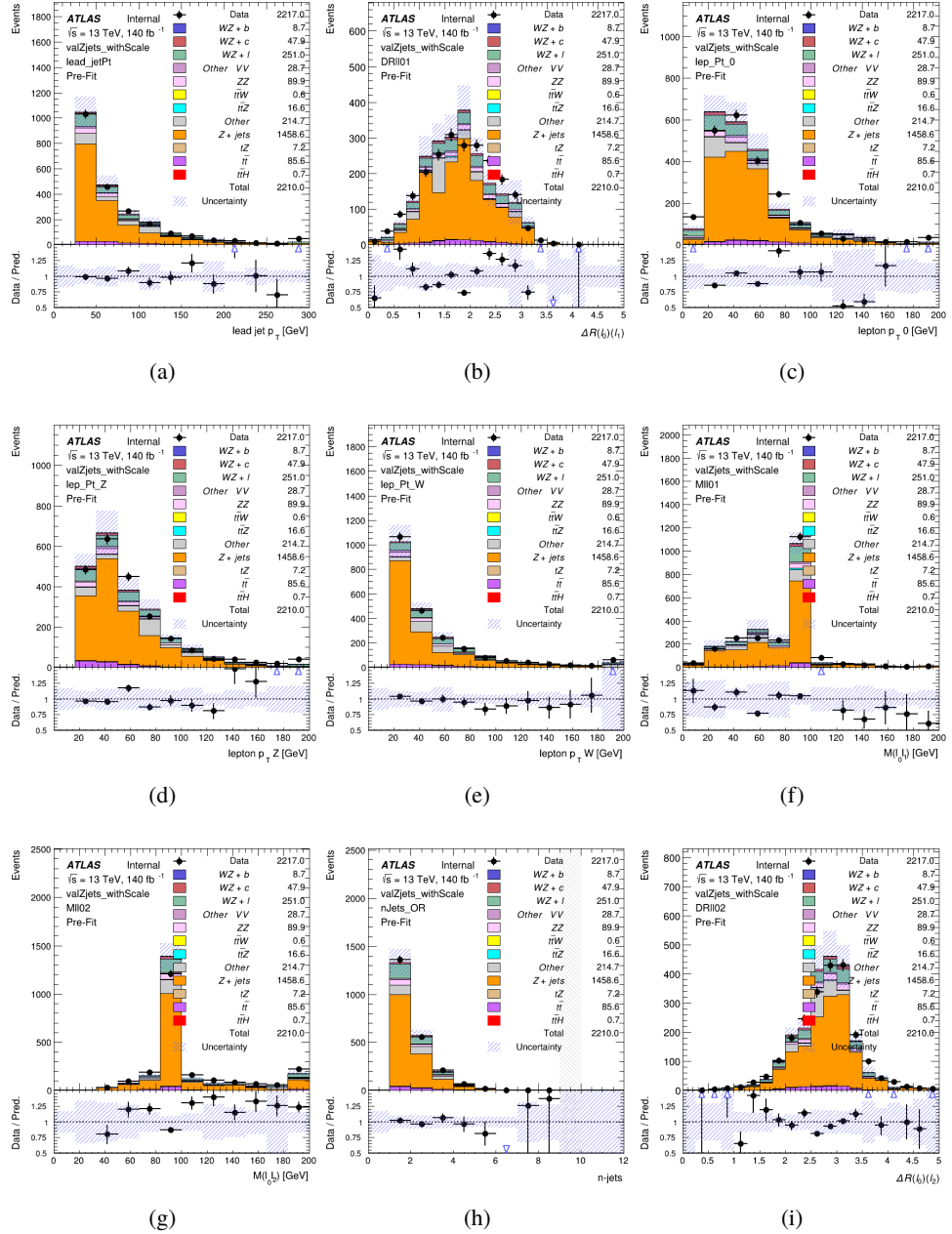


Figure 8.21: Comparisons between the data and MC distributions in the $Z + \text{jets}$ control region after the correction factor has been applied for (a) the p_T of the leading jet, (b) ΔR between leptons 0 and 1, (c) the p_T of lepton 0, (d) p_T of SS lepton from the Z candidate, (e) p_T of the SS lepton from the W candidate, (f) the invariant mass of leptons 0 and 1, (g) the invariant mass of leptons 0 and 2, (h) the number of jets, (i) ΔR between leptons 0 and 2

693 The modeling is further validated by looking at the yield in the Z+jets VR for each DL1r
 694 WP, giving a clearer correspondence to the signal regions used in the fit. Each region shown in
 695 Figure 12.22 requires one or more jets pass the listed WP, with no jets passing the next highest
 696 WP.

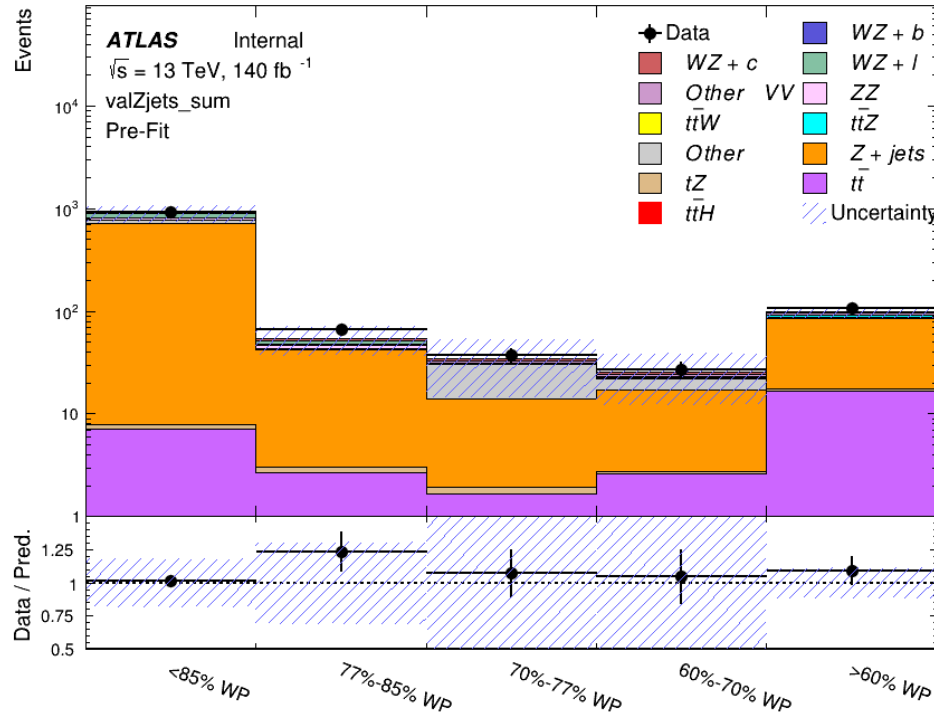


Figure 8.22: Data and MC comparisons for each DL1r WP for both 1-jet and 2-jet regions, after the Z+jets VR selection and correction factor have been applied

697 For each of the b-tagging working points considered, the data falls within 25% of the MC
 698 prediction once this correction factor has been applied. Therefore, a 25% systematic uncertainty
 699 is applied to Z + jets in the analysis.

700 **9 tZ Interference Studies and Separation Multivariate Analysis**

701 Because tZ produces a final state identical to signal, it represents a predominant background in
702 the most signal enriched regions. That is, the region with one jet passing the 60% DL1r WP.
703 Therefore, a boosted decision tree (BDT) algorithm is trained using TMVA [26] to separate WZ
704 + heavy flavor from tZ.

705 Separation between tZ and WZ + heavy flavor is achieved in part by reconstructing the
706 invariant mass of the top candidate, which clusters more closely to the top mass for tZ than WZ
707 + heavy flavor.

708 The result of this BDT is used to create a tZ enriched region in the fit, reducing its impact
709 on the measurement of WZ + heavy flavor.

710 **9.1 Top Mass Reconstruction**

711 The reconstruction of the top mass follows the procedure described in detail in section 6.1 of
712 [27]. The mass of the top quark candidate is reconstructed from the jet, the lepton not included
713 in the Z-candidate, and a reconstructed neutrino. In the case that there is one jet in the event,
714 there is only possible b-jet candidate. For events with two jets, the jet with the highest DL1r
715 score is used.

716 The neutrino from the W decay is expected to be the only source of E_T^{miss} . Therefore, the
 717 E_T and ϕ of the neutrino are taken from the E_T^{miss} measurement. This leaves the z-component
 718 of the neutrino momentum, $p_{\nu z}$ as the only unknown.

719 This unknown is solved for by taking the combined invariant mass of the lepton and
 720 neutrino to give the invariant mass of the W boson:

$$721 \quad (p_l + p_\nu)^2 = m_W^2$$

722 Expanding this out into components, this equation gives:

$$723 \quad \sqrt{p_{T\nu}^2 + p_{z\nu}^2} E_l = \frac{m_W^2 - m_l^2}{2} + p_{T\nu}(p_{lx}\cos\phi_\nu + p_{ly}\sin\phi_\nu) + p_{lz}p_{\nu z}$$

724 This equation gives two solutions for $p_{\nu z}$. For cases where only one of these solutions is
 725 real, that is taken as the value of $p_{\nu z}$. For instances with two real solutions, the one which is
 726 shown to be correct in the largest fraction of simulations is taken. For cases when no real solution
 727 is found, often because of detector effects, the value of E_T^{miss} is varied in decreasing increments
 728 of 100 MeV until a real solution is found.

729 The reconstructed top mass distribution for tZ and WZ + b can be seen in figure 13.1.

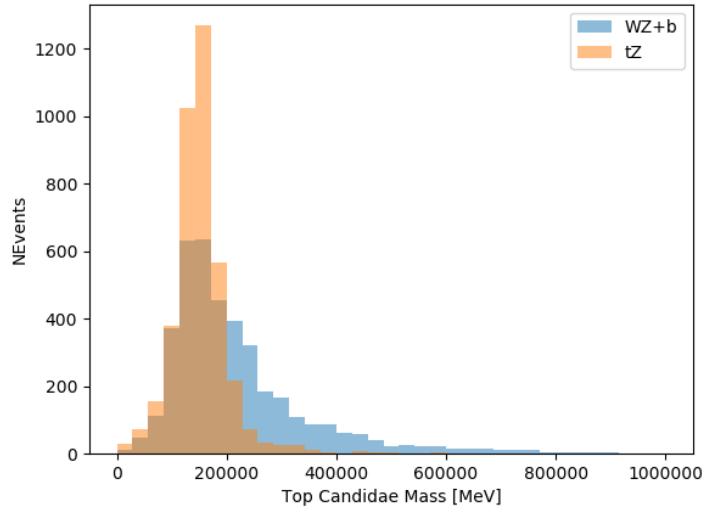


Figure 9.1: Reconstructed top mass distributions for tZ and WZ + b, measured in MeV.

730 9.2 tZ BDT

731 A Boosted Decision Tree (BDT), specifically XGBoost [28], is used to provide separation between
 732 tZ and WZ+b. The following kinematic variables are used as inputs:

733 • The invariant mass of the reconstructed top candidate

734 • p_T of each of the leptons, jet

735 • The invariant mass of each combination of lepton pairs, $M(l\bar{l})$

736 • E_T^{miss}

737 • Distance between each combination of leptons, $\Delta R(l\bar{l})$

- 738 • Distance between each lepton and the jet, $\Delta R(lj)$

739 The training samples included only events meeting the requirements of the 1-jet, >60%
740 region, i.e. passing all the selection described in section 12 and having exactly one jet which
741 passes the tightest (60%) DL1r working point.

742 The distributions of a few of these features for both signal and background is shown in
743 figure 13.2.

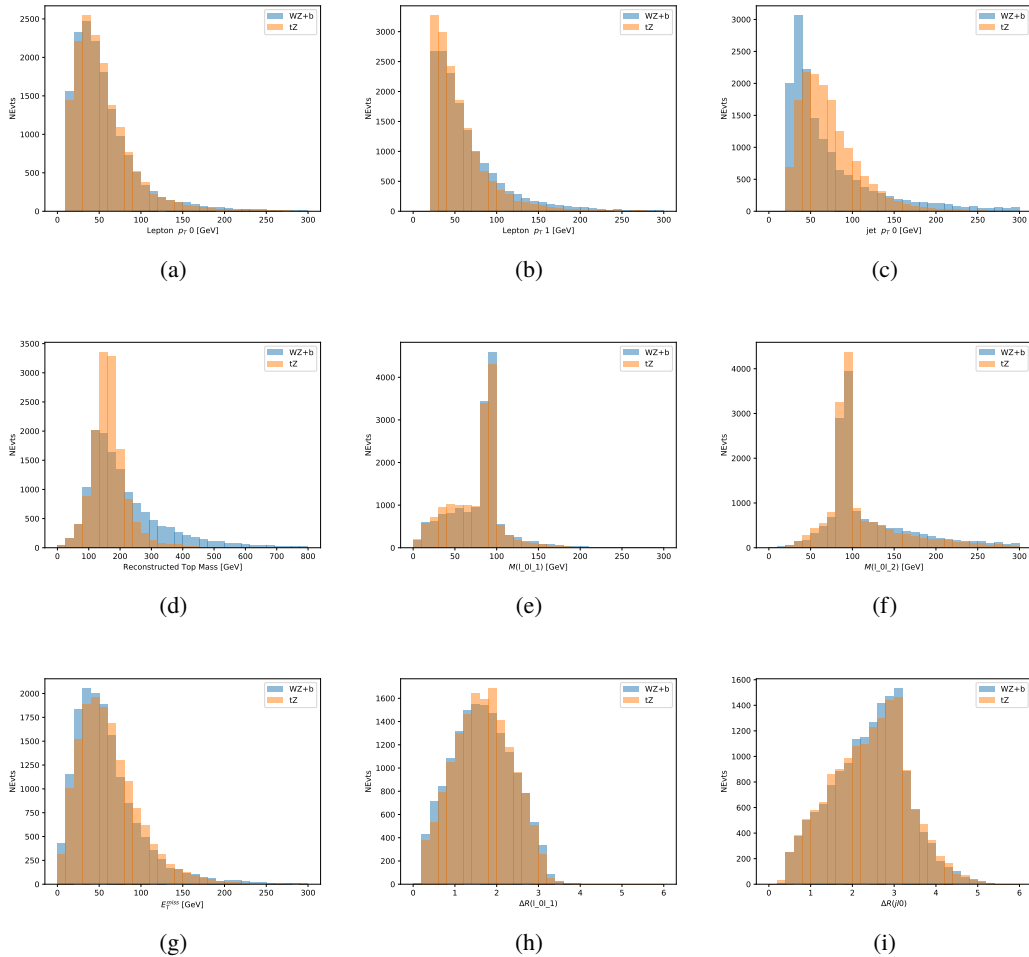


Figure 9.2: Distribution of input features of the BDT for signal (WZ) and background (tZ). Both are scaled to an equal number of events. (a), (b) and (c) show the p_T of lepton 0, lepton 1, and the jet, (d) show the reconstructed top mass, (e) and (f) show the invariant mass of leptons 0 and 1, leptons 0 and 2. (g) shows the E_T^{miss} of each event. (h) and (i) show the ΔR between lepton 0 and lepton 1, and the jet.

744 A sample of 20,000 background (tZ) and signal (WZ+b) Monte Carlo events are used to
 745 train the BDT. And additional 5,000 events are reserved for testing the model, in order to prevent
 746 over-fitting. A total of 750 decision trees with a maximum depth of 6 branches are used to build
 747 the model. These parameters are chosen empirically, by training several models with different

748 parameters and selecting the one that gave the best separation for the test sample.

749 The results of the BDT training are shown in figure 13.3. The output scores for both signal
 750 and background events is shown on the left. The right shows the receiving operating characteristic
 751 (ROC) curve that results from the MVA. The ROC curve represents the background rejection
 752 as a function of signal efficiency, where each point on the curve represents a different response
 753 score. The ROC curve of the BDT is compared to the performance of using an optimal set of flat
 754 selections on the same set of input variables.

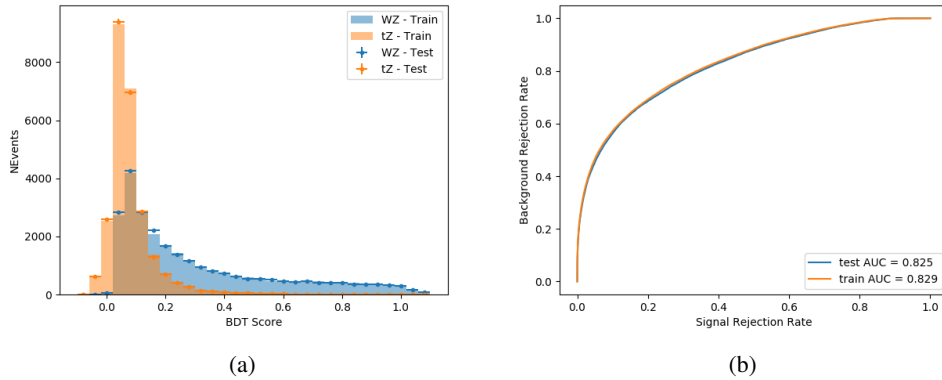


Figure 9.3: Distribution of the BDT response for signal and background events on the left, the ROC curve for the BDT on the right.

755 The relative important of each input feature in the model, measured by how often they
 756 appeared in the decision trees, is shown in figure 13.4.

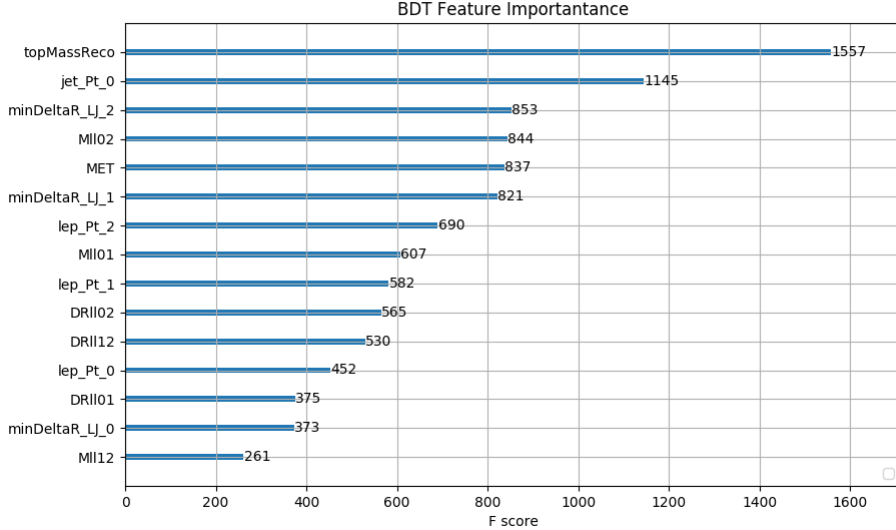


Figure 9.4: Relative importance of each input feature in the model.

757 These results suggest that some amount of separation can be achieved between these two
 758 processes, with a high BDT score selecting a set of events that is pure in $WZ + b$. A BDT score
 759 of 0.725 is selected as a cutoff, where events with scores higher than this form a signal enriched
 760 region, and events with scores lower than this form a $t\bar{Z}$ control region. This cutoff is selected by
 761 varying the value of this cutoff in stat-only Asimov fits, and selecting the value that minimizes
 762 the statistical uncertainty on $WZ + b$.

763 10 Data and Monte Carlo Samples**764 10.1 Data Samples**

765 The study uses a sample of proton-proton collision data collected by the ATLAS detector from
766 2015 through 2018 at an energy of $\sqrt{s} = 13$ TeV, which represents an integrated luminosity of
767 139 fb^{-1} . This data set was collected with a bunch crossing rate of 25 ns. All data used in this
768 analysis was verified by data quality checks.

769 10.2 Monte Carlo Samples

770 Several different generators were used to produce Monte Carlo simulations of the signal and
771 background processes. For all samples, the response of the ATLAS detector is simulated using
772 Geant4. The WZ signal samples are simulated using Sherpa 2.2.2 [13]. Specific information
773 about the Monte Carlo samples being used can be found in Table 26.

Table 8: The configurations used for event generation of signal and background processes, including the event generator, matrix element (ME) order, parton shower algorithm, and parton distribution function (PDF).

| Process | Event generator | ME order | Parton Shower | PDF |
|---------------------------------|---------------------------|----------------------|------------------------|-----------------------------------|
| WZ, VV | SHERPA 2.2.2 | MEPS NLO | SHERPA | CT10 |
| tZ | MG5_AMC | NLO | PYTHIA 8 | CTEQ6L1 |
| t̄tW | MG5_AMC (SHERPA 2.1.1) | NLO (LO multileg) | PYTHIA 8 (SHERPA) | NNPDF 3.0 NLO (NNPDF 3.0 NLO) |
| t̄t(Z/γ* → ll) | MG5_AMC | NLO | PYTHIA 8 | NNPDF 3.0 NLO |
| t̄tH | MG5_AMC (MG5_AMC) | NLO (NLO) | PYTHIA 8 (HERWIG++) | NNPDF 3.0 NLO [14] (CT10 [15]) |
| tHqb | MG5_AMC | LO | PYTHIA 8 | CT10 |
| tHW | MG5_AMC (SHERPA 2.1.1) | NLO (LO multileg) | HERWIG++ (SHERPA) | CT10 (NNPDF 3.0 NLO) |
| tWZ | MG5_AMC | NLO | PYTHIA 8 | NNPDF 2.3 LO |
| t̄t̄t, t̄t̄t̄t | MG5_AMC | LO | PYTHIA 8 | NNPDF 2.3 LO |
| t̄tW+W- | MG5_AMC | LO | PYTHIA 8 | NNPDF 2.3 LO |
| t̄t | POWHEG-BOX v2 [16] | NLO | PYTHIA 8 | NNPDF 3.0 NLO |
| t̄tγ | MG5_AMC | LO | PYTHIA 8 | NNPDF 2.3 LO |
| s-, t-channel, Wt single top | POWHEG-BOX v1 [17] | NLO | PYTHIA 6 | CT10 |
| qqVV, VVV | | | | |
| Z → l+l- | SHERPA 2.2.1 | MEPS NLO | SHERPA | NNPDF 3.0 NLO |

11 Object Reconstruction

All regions defined in this analysis share a common lepton, jet, and overall event preselection.

776 The selection applied to each physics object is detailed here; the event preselection, and the

selection used to define the various fit regions, is described in Section 12.

778 **11.1 Trigger**

779 Events are required to be selected by dilepton triggers, as summarized in Table 28.

| Dilepton triggers (2015) | |
|-------------------------------|----------------------------|
| $\mu\mu$ (asymm.) | HLT_mu18_mu8noL1 |
| ee (symm.) | HLT_2e12_lhloose_L12EM10VH |
| $e\mu, \mu e$ (\sim symm.) | HLT_e17_lhloose_mu14 |
| Dilepton triggers (2016) | |
| $\mu\mu$ (asymm.) | HLT_mu22_mu8noL1 |
| ee (symm.) | HLT_2e17_lhvloose_nod0 |
| $e\mu, \mu e$ (\sim symm.) | HLT_e17_lhloose_nod0_mu14 |
| Dilepton triggers (2017) | |
| $\mu\mu$ (asymm.) | HLT_mu22_mu8noL1 |
| ee (symm.) | HLT_2e24_lhvloose_nod0 |
| $e\mu, \mu e$ (\sim symm.) | HLT_e17_lhloose_nod0_mu14 |
| Dilepton triggers (2018) | |
| $\mu\mu$ (asymm.) | HLT_mu22_mu8noL1 |
| ee (symm.) | HLT_2e24_lhvloose_nod0 |
| $e\mu, \mu e$ (\sim symm.) | HLT_e17_lhloose_nod0_mu14 |

Table 9: List of lowest p_T -threshold, un-prescaled dilepton triggers used for 2015-2018 data taking.

780 **11.2 Light leptons**

781 Electron candidates are reconstructed from energy clusters in the electromagnetic calorimeter
 782 that are associated with charged particle tracks reconstructed in the inner detector [18]. Electron
 783 candidates are required to have $p_T > 10$ GeV and $|\eta_{\text{cluster}}| < 2.47$. Muon candidates are
 784 reconstructed by combining inner detector tracks with track segments or full tracks in the muon
 785 spectrometer [19]. Muon candidates are required to have $p_T > 10$ GeV and $|\eta| < 2.5$. Candidates

786 in the transition region between different electromagnetic calorimeter components, $1.37 <$
 787 $|\eta_{\text{cluster}}| < 1.52$, are rejected. A multivariate likelihood discriminant combining shower shape
 788 and track information is used to distinguish real electrons from hadronic showers (fake electrons).
 789 To further reduce the non-prompt electron contribution, the track is required to be consistent
 790 with originating from the primary vertex; requirements are imposed on the transverse impact
 791 parameter significance ($|d_0|/\sigma_{d_0} < 5$) and the longitudinal impact parameter ($|\Delta z_0 \sin \theta_\ell| < 0.5$
 792 mm). Electron candidates are required to pass TightLH identification.

793 Muon candidates are reconstructed by combining inner detector tracks with track segments
 794 or full tracks in the muon spectrometer [19]. Muon candidates are required to have $p_T > 10$ GeV
 795 and $|\eta| < 2.5$. The longitudinal impact parameter is the same for both electrons and muons, while
 796 muons are required to pass a slightly tighter transverse impact parameter, $|d_0|/\sigma_{d_0} < 3$. Muons
 797 are also required to pass Medium ID requirements.

798 Leptons are additionally required to pass a non-prompt BDT selection developed by the
 799 $t\bar{t}H$ multilepton/ $t\bar{t}W$ analysis group. This BDT and the WPs used are summarized in Appendix
 800 .1, and described in detail in [20]. Optimized working points and scale factors for this BDT are
 801 taken from that analysis.

802 **11.3 Jets**

803 Jets are reconstructed from calibrated topological clusters built from energy deposits in the
 804 calorimeters [21], using the anti- k_t algorithm with a radius parameter $R = 0.4$. Particle Flow, or

805 PFlow, jets are used in the analysis, which are hadronic objects reconstructed using information
806 from both the tracker and the calorimeter. Jets with energy contributions likely arising from noise
807 or detector effects are removed from consideration [22], and only jets satisfying $p_T > 25$ GeV
808 and $|\eta| < 2.5$ are used in this analysis. For jets with $p_T < 60$ GeV and $|\eta| < 2.4$, a jet-track
809 association algorithm is used to confirm that the jet originates from the selected primary vertex,
810 in order to reject jets arising from pileup collisions [23].

811 **11.4 B-tagged Jets**

812 In order to make a measurement of $WZ +$ heavy flavor it is necessary to distinguish these events
813 from $WZ +$ light jets. For this purpose, the DL1r b-tagging algorithm is used to distinguish
814 heavy flavor jets from lighter ones. The DL1r algorithm uses jet kinematics, particularly jet
815 vertex information, as input for a neural network which assigns each jet a score designed to
816 reflect how likely that jet is to have originated from a b-quark.

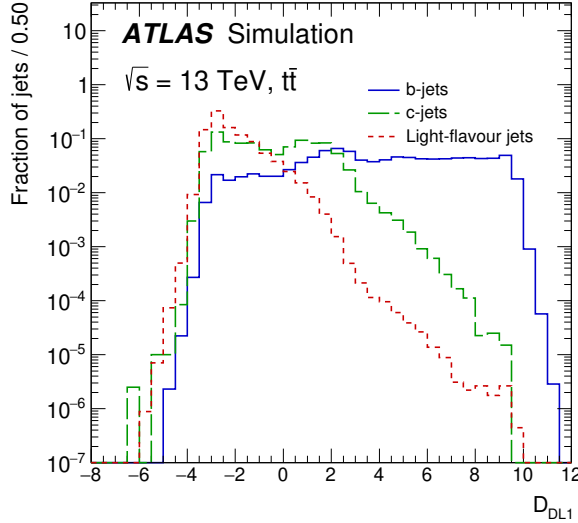


Figure 11.1: Output distribution of the DL1r algorithm for b-jets, charm jets, and light jets

817 From the output of the BDT, calibrated working points (WPs) are developed based on the
 818 efficiency of truth b-jets at particular values of the DL1r algorithm. The working points used in
 819 this analysis are summarized in Table 10.

| WP | none | loose | medium | tight | tightest |
|--------|------|-------|--------|-------|----------|
| b eff. | - | 85% | 77% | 70% | 60% |

Table 10: B-tagging Working Points by tightness and b-jet efficiency

820 A tighter WP will accept fewer b-jets, but reject a higher fraction of charm and light jets.
 821 Generally, analyses that include b-jets will use a fixed working point, for example, requiring that
 822 a jet pass the 70% threshold. By instead treating these working point as bins, e.g. events with
 823 jets that fall between the 85% and 77% WPs fall into one bin, while events with jets passing the
 824 60% WP fall into another, and looking at the full psuedo-continuous DL1r spectrum of the jets,

825 additional information can be gained. The psuedo-continuous b-tag spectrum is used in this case
826 to separate out WZ + b, WZ + charm, and WZ + light.

827 **11.5 Missing transverse energy**

828 Missing transverse momentum (E_T^{miss}) is used as part of the event selection. The missing
829 transverse momentum vector is defined as the inverse of the sum of the transverse momenta of
830 all reconstructed physics objects as well as remaining unclustered energy, the latter of which is
831 estimated from low- p_T tracks associated with the primary vertex but not assigned to a hard object,
832 with object definitions taken from [24]. Light leptons considered in the E_T^{miss} reconstruction are
833 required to have $p_T > 10 \text{ GeV}$, while jets are required to have $p_T > 20 \text{ GeV}$.

834 **11.6 Overlap removal**

835 To avoid double counting objects and remove leptons originating from decays of hadrons, overlap
836 removal is performed in the following order: any electron candidate within $\Delta R = 0.1$ of another
837 electron candidate with higher p_T is removed; any electron candidate within $\Delta R = 0.1$ of a muon
838 candidate is removed; any jet within $\Delta R = 0.3$ of an electron candidate is removed; if a muon
839 candidate and a jet lie within $\Delta R = \min(0.4, 0.04 + 10[\text{GeV}] / p_T(\text{muon}))$ of each other, the jet
840 is kept and the muon is removed.

841 This algorithm is applied to the preselected objects. The overlap removal procedure is
842 summarized in Table 29.

| Keep | Remove | Cone size (ΔR) |
|-------------|-----------------------|---|
| electron | electron (low p_T) | 0.1 |
| muon | electron | 0.1 |
| electron | jet | 0.3 |
| jet | muon | $\min(0.4, 0.04 + 10[\text{GeV}]/p_T(\text{muon}))$ |
| electron | tau | 0.2 |

Table 11: Summary of the overlap removal procedure between electrons, muons, and jets.

843 12 Event Selection and Signal Region Definitions

844 Event are required to pass a preselection described in Section 12.1 and summarized in Table 12.
 845 Those that pass this preselection are divided into various fit regions described in Section 12.2,
 846 based on the number of jets in the event, and the b-tag score of those jets.

847 12.1 Event Preselection

848 Events are required to include exactly three reconstructed light leptons passing the requirement
 849 described in 11.2, which have a total charge of ± 1 .

850 The leptons are ordered in the analysis code as 0, 1, and 2. Lepton 0 is the lepton whose
 851 charge is opposite the other two. Lepton 1 is the lepton closest to the opposite charge lepton, i.e.
 852 the smallest ΔR , leaving lepton 2 as the lepton further from the opposite charge lepton. Lepton
 853 0 is required to have $p_T > 10 \text{ GeV}$, while the same sign leptons, 1 and 2, are required to have
 854 $p_T > 20 \text{ GeV}$ to reduce the contribution of non-prompt leptons.

855 The invariant mass of at least one pair of opposite sign, same flavor leptons is required
 856 to fall within 10 GeV of the mass of the Z boson, 91.2 GeV. Events where one of the opposite
 857 sign pairs have an invariant mass less than 12 GeV are rejected in order to suppress low mass
 858 resonances.

859 An additional requirement is placed on the missing transverse energy, $E_T^{\text{miss}} > 20 \text{ GeV}$,
 860 and the transverse mass of the W candidate, $m(E_T^{\text{miss}} + l_{\text{other}}) > 30 \text{ GeV}$, where E_T^{miss} is the
 861 missing transverse energy, and l_{other} is the lepton not included in the Z-candidate.

862 Events are required to have one or two reconstructed jets passing the selection described
 863 in Section 11.3. Events with more than two jets are rejected in order to reduce the contribution
 864 of backgrounds such as $t\bar{t}Z$ and $t\bar{t}W$, which tend to have higher jet multiplicity.

Event Selection

Exactly three leptons with charge ± 1
 Two same-charge leptons with $p_T > 20 \text{ GeV}$
 One opposite charge lepton with $p_T > 10 \text{ GeV}$
 $m(l^+l^-)$ within 10 GeV of 91.2 GeV
 Transverse mass of W-candidate, $m_T(E_T^{\text{miss}} + l_{\text{other}}) > 30 \text{ GeV}$
 Missing transverse energy, $E_T^{\text{miss}} > 20 \text{ GeV}$
 One or two jets with $p_T > 25 \text{ GeV}$

Table 12: Summary of the selection applied to events for inclusion in the fit

865 The event yields in the preselection region for both data and Monte Carlo are summarized
 866 in Table 12.1, which shows good agreement between data and Monte Carlo, and demonstrates
 867 that this region consists primarily of WZ events. The WZ events are split into WZ + b, WZ
 868 + c, and WZ + 1 based on the truth flavor of the associated jet in the event. Specifically, this

869 determination is made based on the HadronConeExclTruthLabelID of the jet, as recommended
 870 by the b-tagging working group [25]. In this ordering b-jet supersedes charm, which supersedes
 871 light. That is, WZ + 1 events contain no charm and no b jets at truth level, WZ + c contain at
 872 least one truth charm and no b-jets, and WZ + b contains at least one truth b-jet.

| Process | Events |
|------------|-----------------|
| WZ + b | 167.6 ± 6.5 |
| WZ + c | 1080 ± 40 |
| WZ + l | 7220 ± 310 |
| Other VV | 850 ± 140 |
| t̄tW | 16.8 ± 2.3 |
| t̄tZ | 115 ± 17 |
| rare Top | 2.2 ± 0.1 |
| Single top | 0.10 ± 0.45 |
| Three top | 0.01 ± 0.01 |
| Four top | 0.02 ± 0.01 |
| t̄tWW | 0.23 ± 0.05 |
| Z + jets | 600 ± 260 |
| V + γ | 37 ± 54 |
| tZ | 190 ± 70 |
| tW | 5.5 ± 1.2 |
| WtZ | 25.8 ± 1.1 |
| VVV | 26.2 ± 0.9 |
| VH | 94 ± 7 |
| t̄t | 108.68 ± 8 |
| t̄tH | 4.3 ± 0.5 |
| Total | 10600 ± 530 |
| Data | 10574 |

Table 13: Event yields in the preselection region at 139.0 fb^{-1}

873 Here Other VV represents diboson processes other than WZ, and consists predominantly
 874 of $ZZ \rightarrow ll\bar{l}\bar{l}$ events where one of the leptons is not reconstructed.

875 Simulations are further validated by comparing the kinematic distributions of the Monte

⁸⁷⁶ Carlo with data, which are shown in Figure 12.1. Here, bins with 5% or more WZ+b are

⁸⁷⁷ blinded.

WZ Fit Region - Inclusive

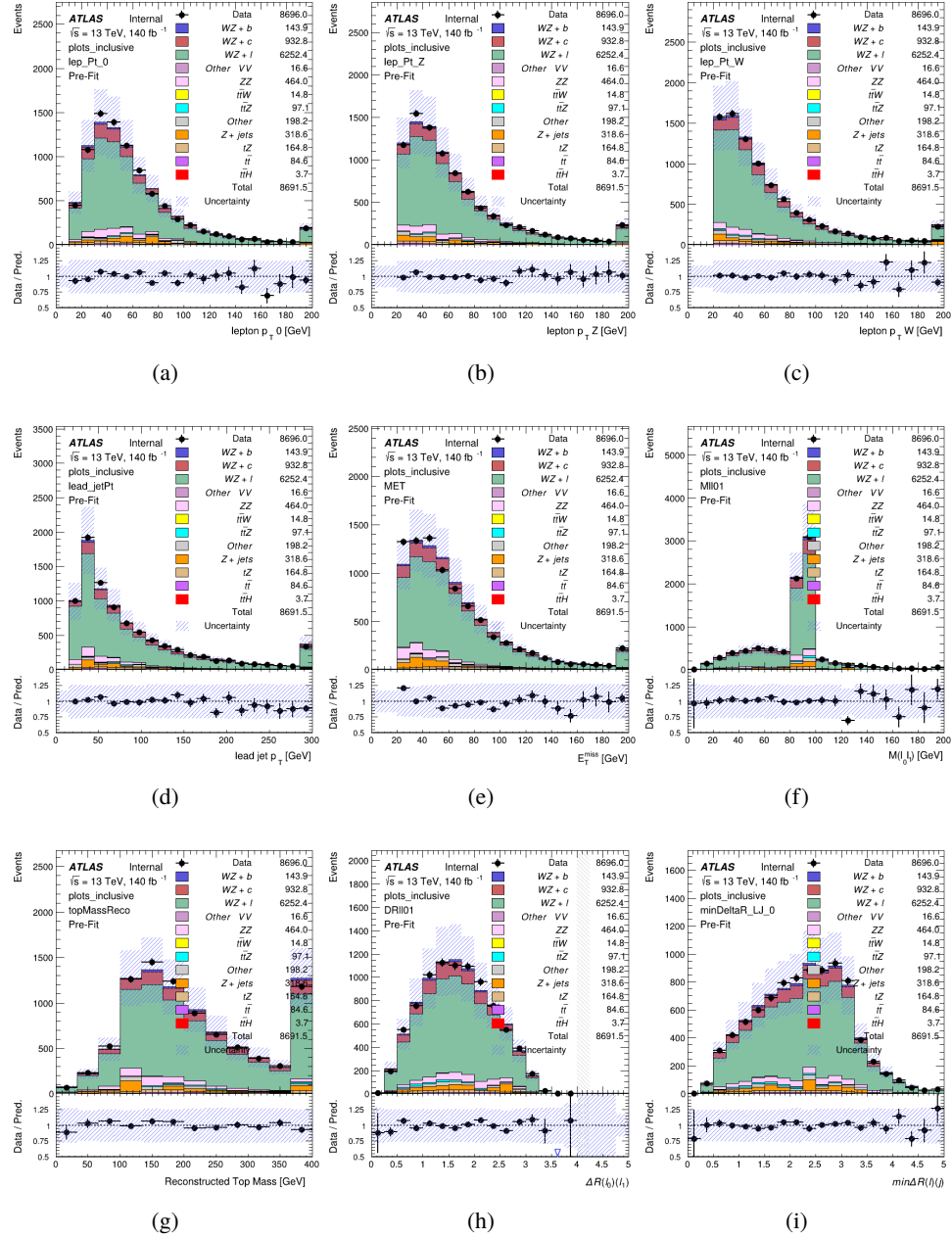


Figure 12.1: Comparisons between the data and MC distributions in the preselection region for (a) the p_T of the opposite sign lepton, (b) the p_T of the other lepton from the Z candidate, (c) the p_T of the lepton from the W candidate, (d) the leading jet p_T , (e) the E_T^{miss} , and (f) the invariant mass of leptons 0 and 1, (g) the reconstructed top mass, (h) $\Delta(R)$ between lepton 0 and 1, (i) the $\Delta(R)$ between the closest lepton and jet.

878 12.2 Fit Regions

879 Once preselection has been applied, the remaining events are categorized into one of twelve
 880 orthogonal regions. The regions used in the fit are summarized in Table 14.

Table 14: A list of the regions used in the fit and the selection used for each.

| Region | Selection |
|-------------|--|
| 1j, <85% | $N_{\text{jets}} = 1, n\text{Jets_DL1r_85} = 0$ |
| 1j, 85%-77% | $N_{\text{jets}} = 1, n\text{Jets_DL1r_85} = 1, n\text{Jets_DL1r_77}=0$ |
| 1j, 77%-70% | $N_{\text{jets}} = 1, n\text{Jets_DL1r_77} = 1, n\text{Jets_DL1r_70}=0$ |
| 1j, 70%-60% | $N_{\text{jets}} = 1, n\text{Jets_DL1r_70} = 1, n\text{Jets_DL1r_60}=0$ |
| 1j, >60% | $N_{\text{jets}} = 1, n\text{Jets_DL1r_60} = 1, tZ \text{ BDT} > 0.725$ |
| 1j tZ CR | $N_{\text{jets}} = 1, n\text{Jets_DL1r_60} = 1, tZ \text{ BDT} < 0.725$ |
| 2j, <85% | $N_{\text{jets}} = 2, n\text{Jets_DL1r_85} = 0$ |
| 2j, 85%-77% | $N_{\text{jets}} = 2, n\text{Jets_DL1r_85} >= 1, n\text{Jets_DL1r_77}=0$ |
| 2j, 77%-70% | $N_{\text{jets}} = 2, n\text{Jets_DL1r_77} >= 1, n\text{Jets_DL1r_70}=0$ |
| 2j, 70%-60% | $N_{\text{jets}} = 2, n\text{Jets_DL1r_70} >= 1, n\text{Jets_DL1r_60}=0$ |
| 2j, >60% | $N_{\text{jets}} = 2, n\text{Jets_DL1r_60} >= 1, tZ \text{ BDT} > 0.725$ |
| 2j tZ CR | $N_{\text{jets}} = 2, n\text{Jets_DL1r_60} >= 1, tZ \text{ BDT} < 0.725$ |

881 The working points discussed in Section 11.4 are used to separate events into fit regions
 882 based on the highest working point reached by a jet in each event. Because the background
 883 composition differs significantly based on the number of b-jets, events are further subdivided
 884 into 1-jet and 2-jet regions in order to minimize the impact of background uncertainties.

885 An unfolding procedure is performed to account for differences in the number of recon-
 886 structed jets compared to the number of truth jets in each event. The `AntiKt4TruthDressedWZJets`
 887 truth jet collection is used to make this determination. In order to account for migration of WZ+1-
 888 jet and WZ+2-jet events between the 1-jet and 2-jet bins at reco level, the signal samples are
 889 separated based on the number of truth jets. Events with 0 jets or more than 3 jets at truth level,

yet fall within one of the categories listed in Table 14, are categorized as WZ + other, and treated as a background. The migration matrix in the number of jets at truth level versus reco level is shown in Figure 12.2. The composition of the number of truth jets in each reco jet bin is taken from MC, with uncertainties in these estimates described in detail in Section 21.

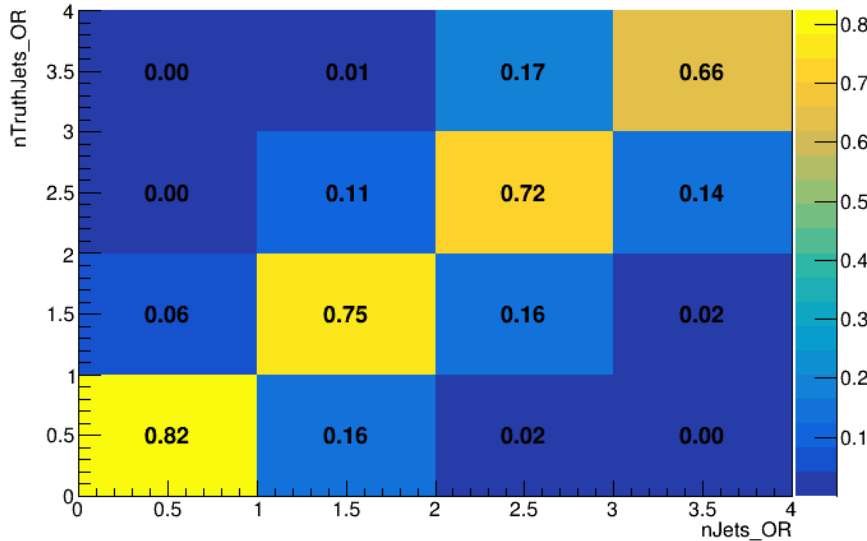


Figure 12.2: Number of truth jets compared to the number of reconstructed jets in each WZ event falling in the preselection region. Each row is normalized to unity.

An additional tZ control region is created based on the BDT described in Section 13. The region with 1-jet passing the 60% working point is split in two - a signal enriched region of events with a BDT score greater than 0.03, and a tZ control region including events with less than 0.03. This cutoff is arrived at by performing an Asimov fit with a variety of cutoffs, and selecting the value that produces the highest significance for the measurement of WZ + b.

The modeling in each region is validated by comparing data and MC predictions for

900 various kinematic distributions. These plot are shown in Figures [12.3-12.16](#).

WZ Fit Region - 1j Inclusive

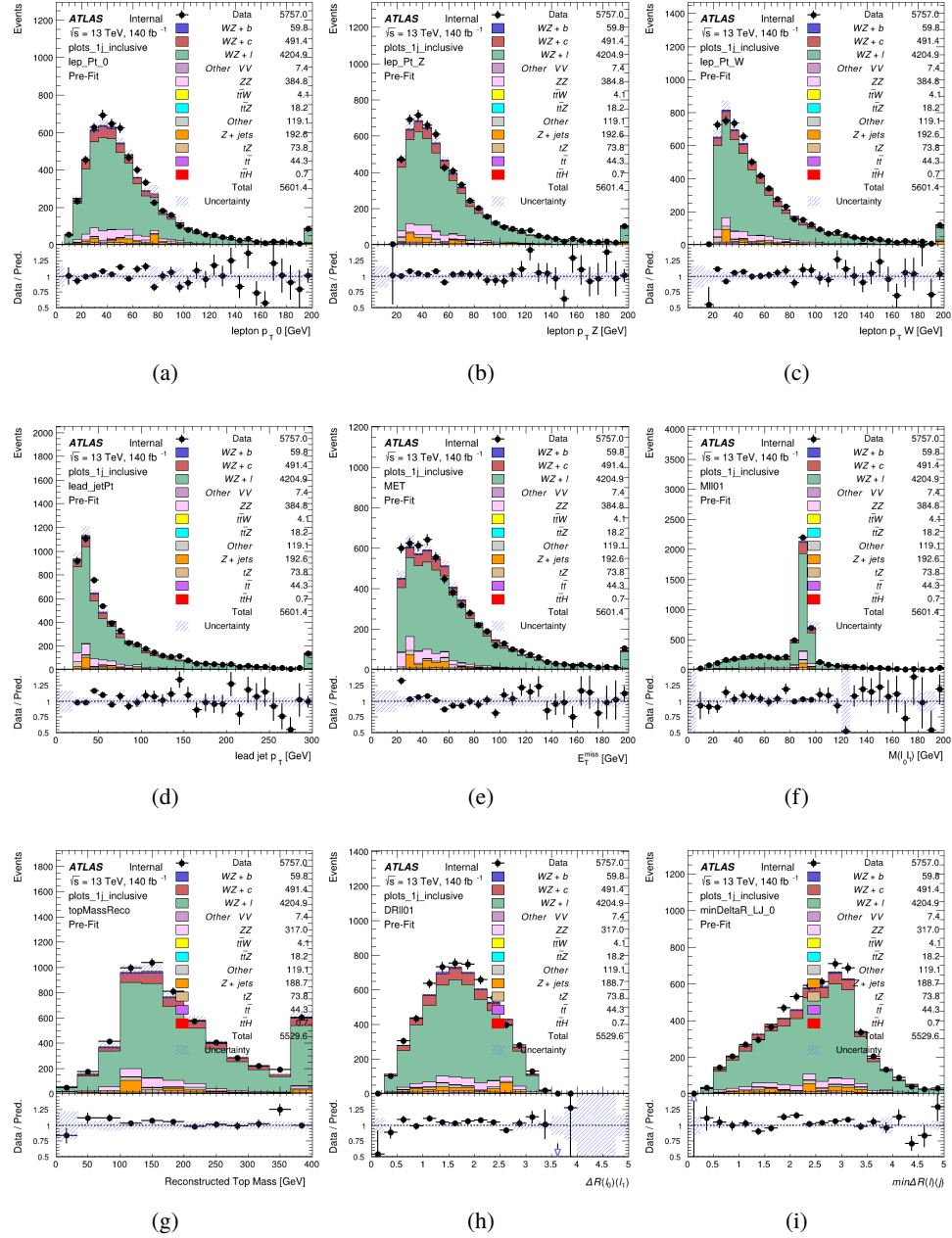


Figure 12.3: Comparisons between the data and MC distributions in the preselection region for (a) the p_T of the opposite sign lepton, (b) the p_T of the other lepton from the Z candidate, (c) the p_T of the lepton from the W candidate, (d) the leading jet p_T , (e) the E_T^{miss} , and (f) the invariant mass of leptons 0 and 1, (g) the reconstructed top mass, (h) $\Delta(R)$ between lepton 0 and 1, (i) the $\Delta(R)$ between the closest lepton and jet.

WZ Fit Region - 1j < 85% WP

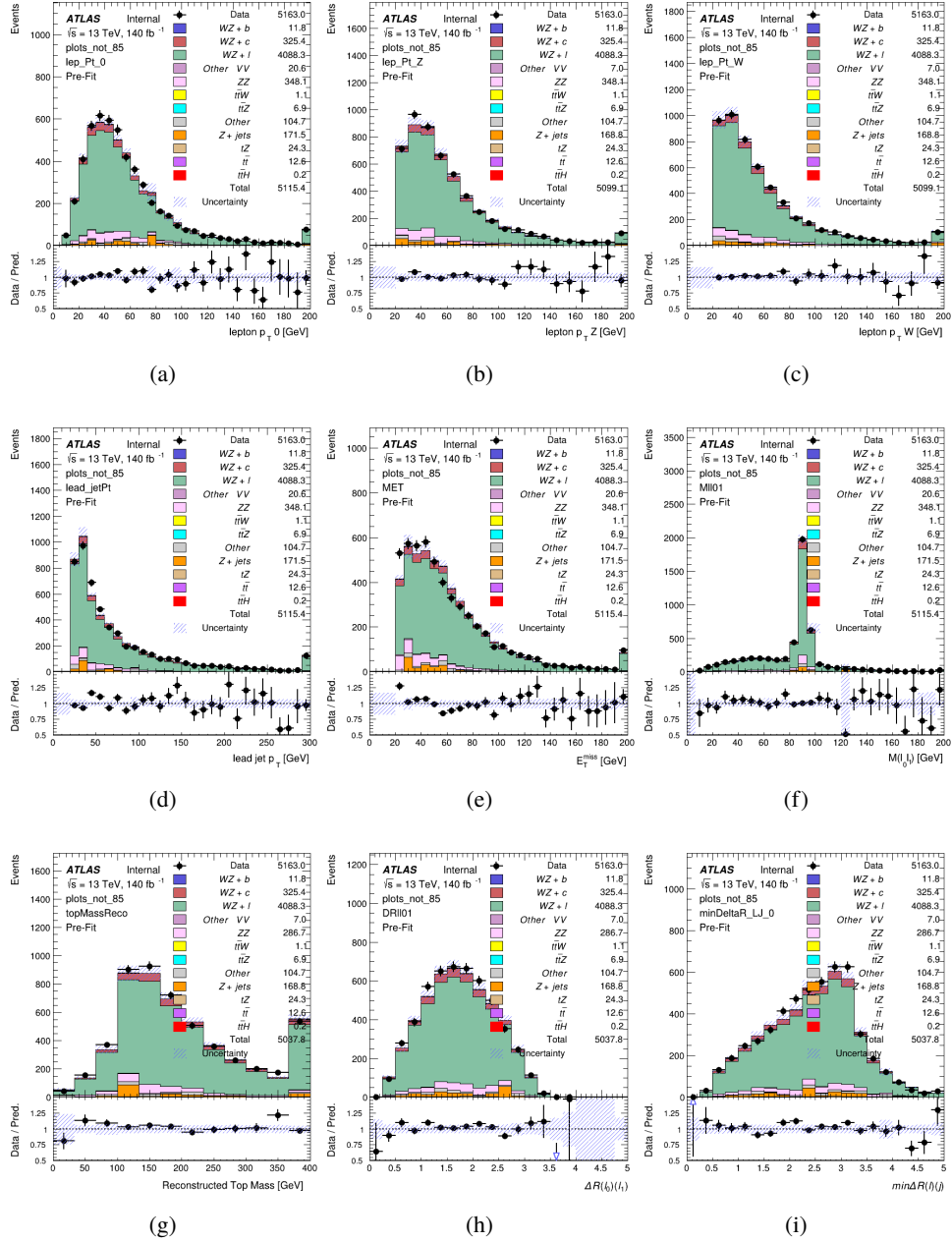


Figure 12.4: Comparisons between the data and MC distributions in the preselection region for (a) the p_T of the opposite sign lepton, (b) the p_T of the other lepton from the Z candidate, (c) the p_T of the lepton from the W candidate, (d) the leading jet p_T , (e) the E_T^{miss} , and (f) the invariant mass of leptons 0 and 1, (g) the reconstructed top mass, (h) $\Delta(R)$ between lepton 0 and 1, (i) the $\Delta(R)$ between the closest lepton and jet.

WZ Fit Region - 1j 77-85% WP

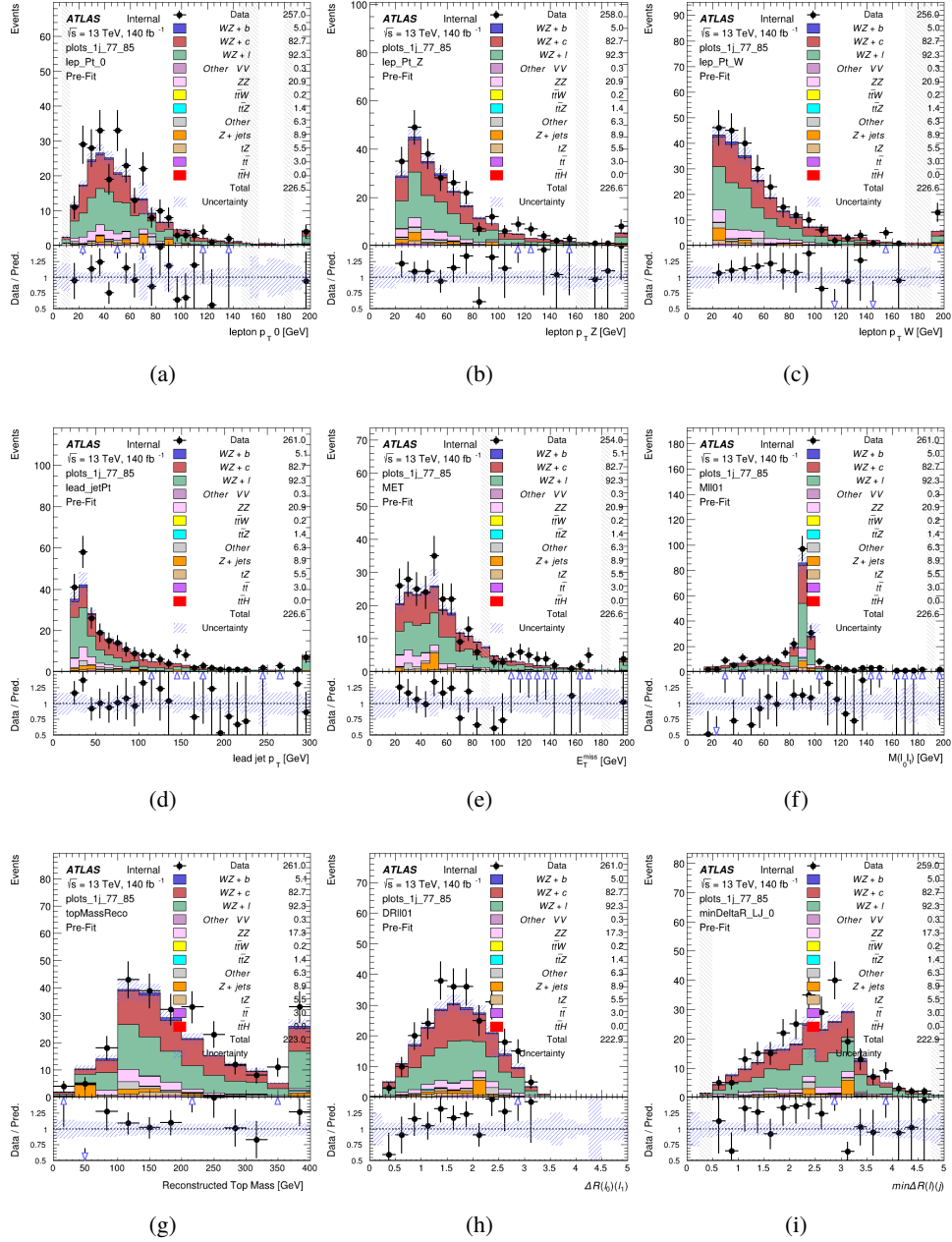


Figure 12.5: Comparisons between the data and MC distributions in the preselection region for (a) the p_T of the opposite sign lepton, (b) the p_T of the other lepton from the Z candidate, (c) the p_T of the lepton from the W candidate, (d) the leading jet p_T , (e) the E_T^{miss} , and (f) the invariant mass of leptons 0 and 1, (g) the reconstructed top mass, (h) $\Delta(R)$ between lepton 0 and 1, (i) the $\Delta(R)$ between the closest lepton and jet.

WZ Fit Region - 1j 70-77% WP

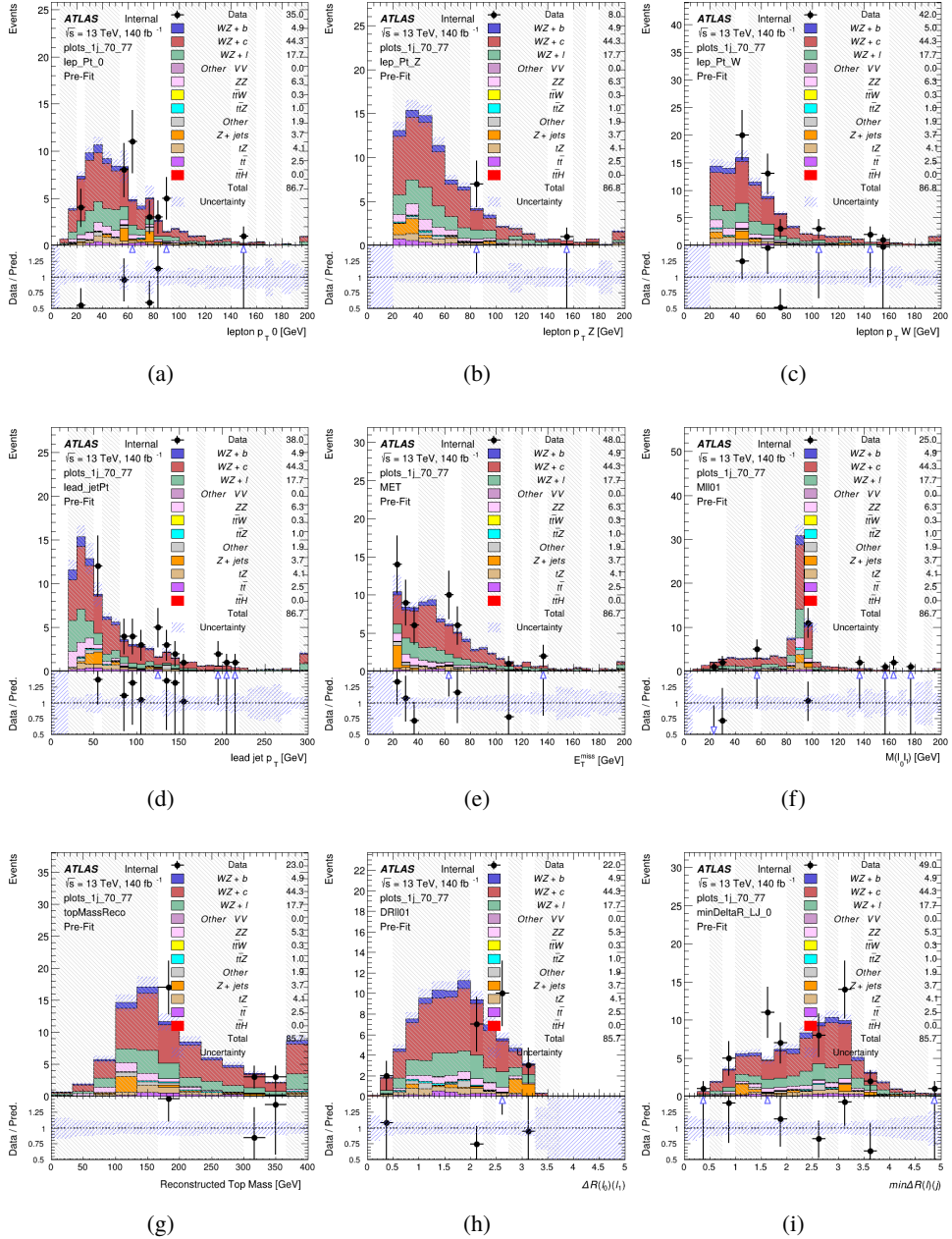


Figure 12.6: Comparisons between the data and MC distributions in the preselection region for (a) the p_T of the opposite sign lepton, (b) the p_T of the other lepton from the Z candidate, (c) the p_T of the lepton from the W candidate, (d) the leading jet p_T , (e) the E_T^{miss} , and (f) the invariant mass of leptons 0 and 1, (g) the reconstructed top mass, (h) $\Delta(R)$ between lepton 0 and 1, (i) the $\Delta(R)$ between the closest lepton and jet.

WZ Fit Region - 1j 60-70% WP

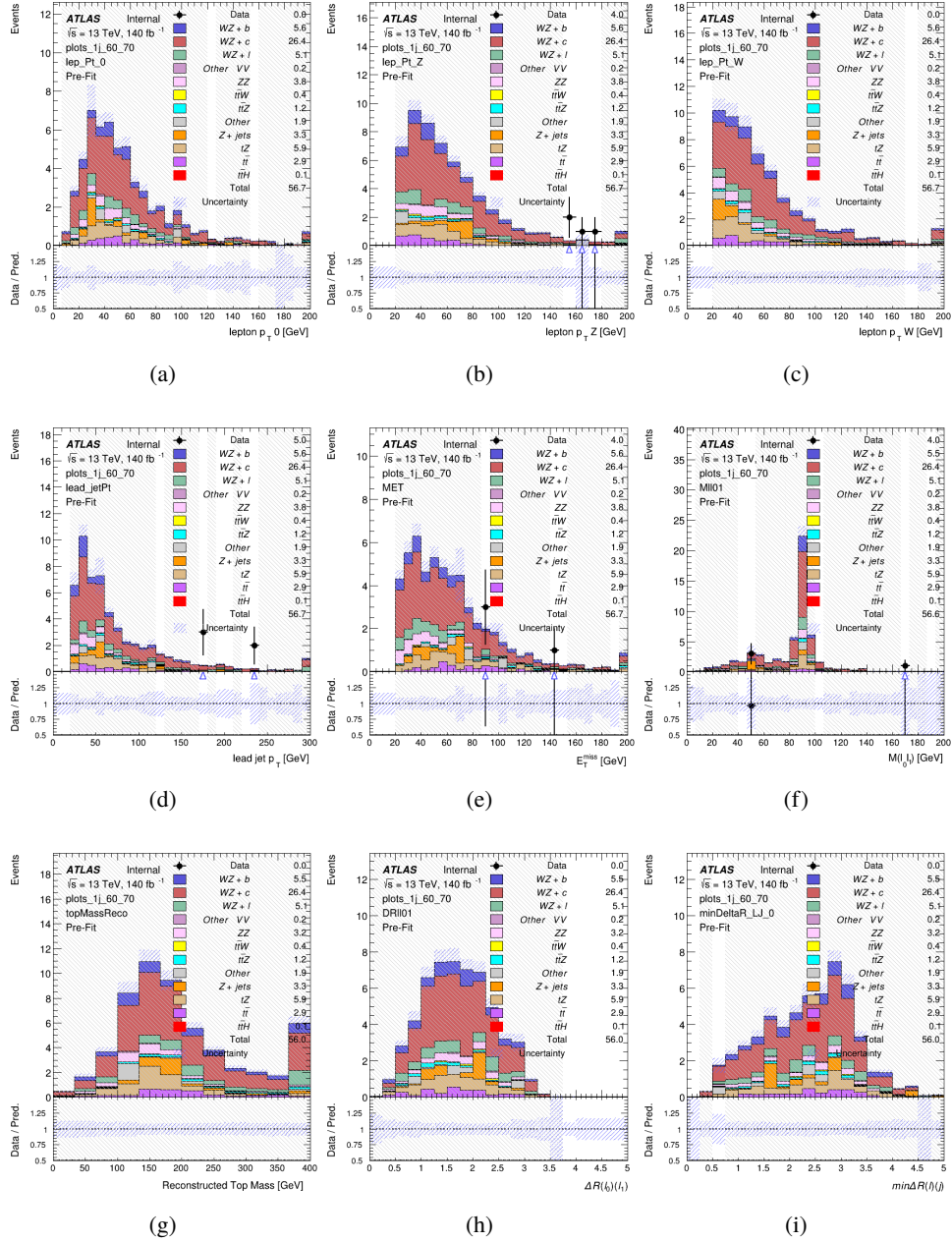


Figure 12.7: Comparisons between the data and MC distributions in the preselection region for (a) the p_T of the opposite sign lepton, (b) the p_T of the other lepton from the Z candidate, (c) the p_T of the lepton from the W candidate, (d) the leading jet p_T , (e) the E_T^{miss} , and (f) the invariant mass of leptons 0 and 1, (g) the reconstructed top mass, (h) $\Delta(R)$ between lepton 0 and 1, (i) the $\Delta(R)$ between the closest lepton and jet.

WZ Fit Region - 1j 60% WP

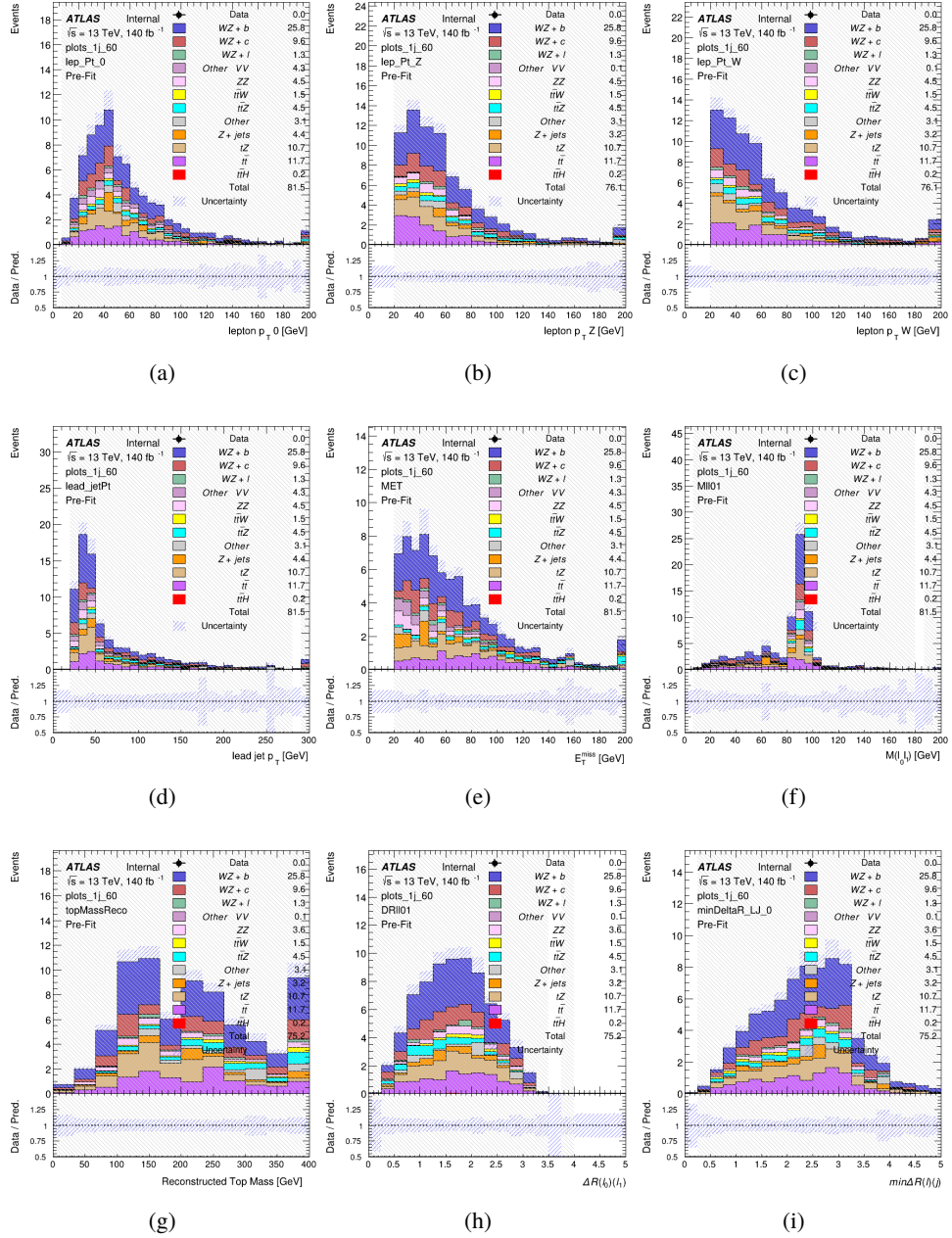


Figure 12.8: Comparisons between the data and MC distributions in the preselection region for (a) the p_T of the opposite sign lepton, (b) the p_T of the other lepton from the Z candidate, (c) the p_T of the lepton from the W candidate, (d) the leading jet p_T , (e) the E_T^{miss} , and (f) the invariant mass of leptons 0 and 1, (g) the reconstructed top mass, (h) $\Delta(R)$ between lepton 0 and 1, (i) the $\Delta(R)$ between the closest lepton and jet.

WZ Fit Region - tZ-CR

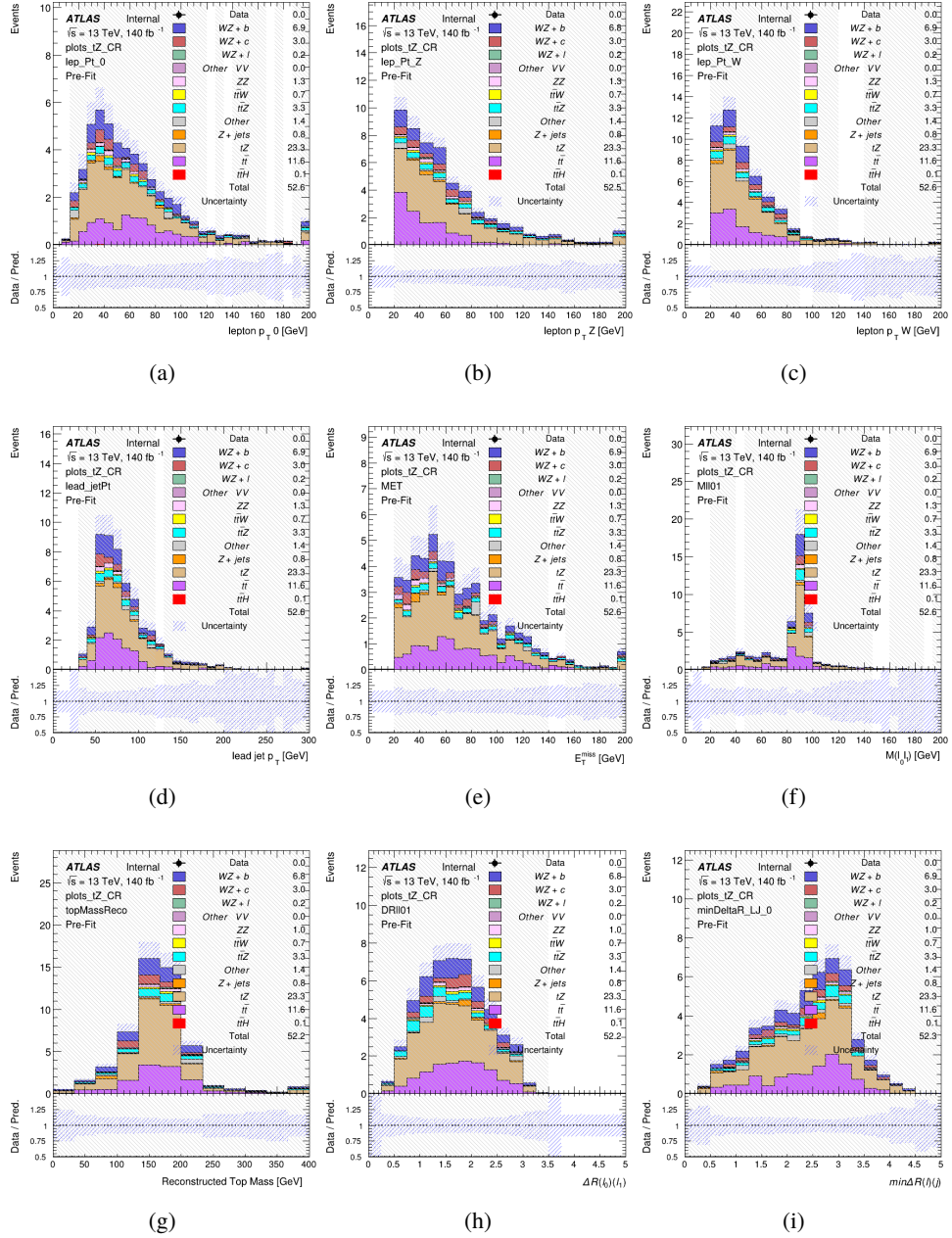


Figure 12.9: Comparisons between the data and MC distributions in the preselection region for (a) the p_T of the opposite sign lepton, (b) the p_T of the other lepton from the Z candidate, (c) the p_T of the lepton from the W candidate, (d) the leading jet p_T , (e) the E_T^{miss} , and (f) the invariant mass of leptons 0 and 1, (g) the reconstructed top mass, (h) $\Delta(R)$ between lepton 0 and 1, (i) the $\Delta(R)$ between the closest lepton and jet.

WZ Fit Region - 2j Inclusive

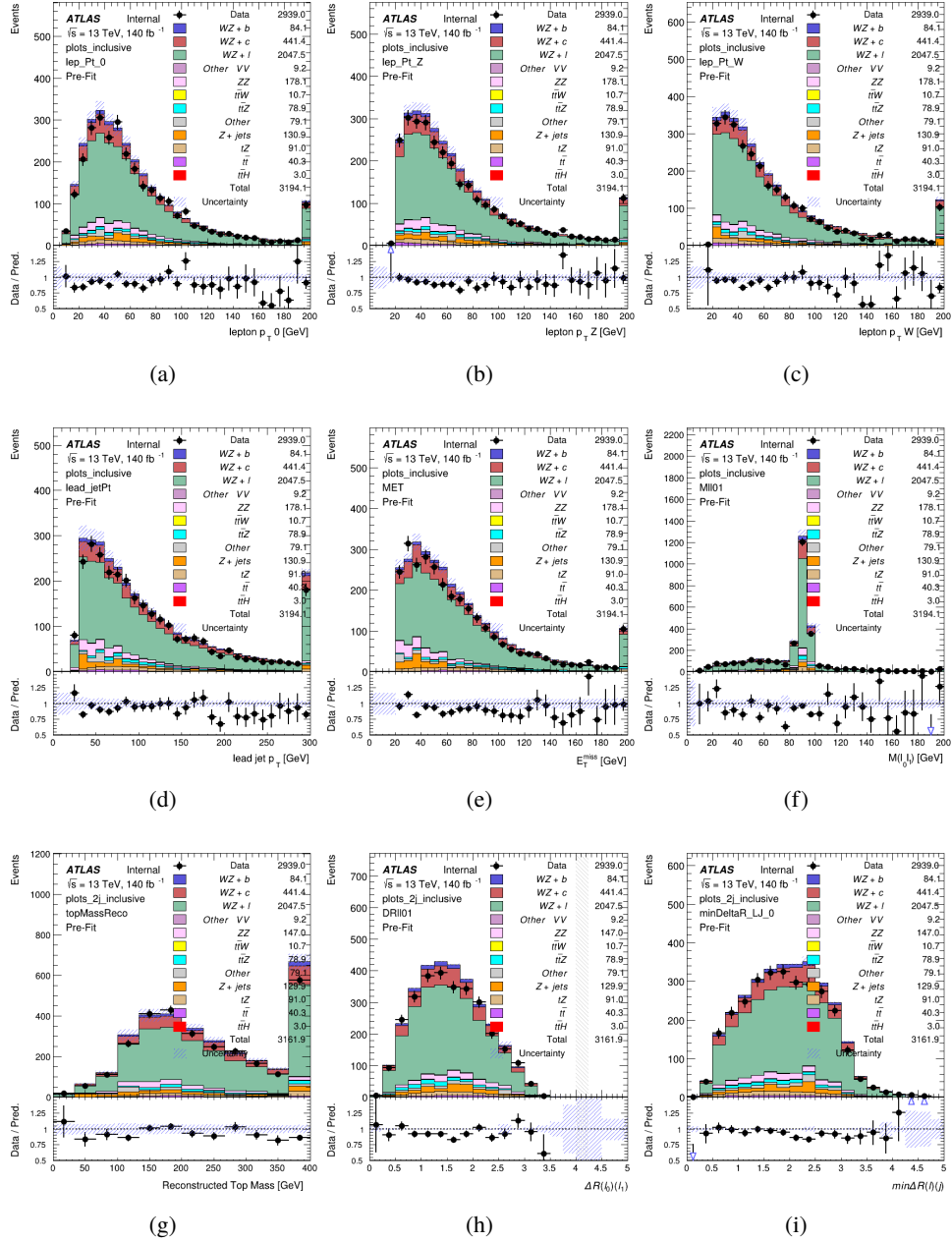


Figure 12.10: Comparisons between the data and MC distributions in the preselection region for (a) the p_T of the opposite sign lepton, (b) the p_T of the other lepton from the Z candidate, (c) the p_T of the lepton from the W candidate, (d) the leading jet p_T , (e) the E_T^{miss} , and (f) the invariant mass of leptons 0 and 1, (g) the reconstructed top mass, (h) $\Delta(R)$ between lepton 0 and 1, (i) the $\Delta(R)$ between the closest lepton and jet.

WZ Fit Region - 2j < 85% WP

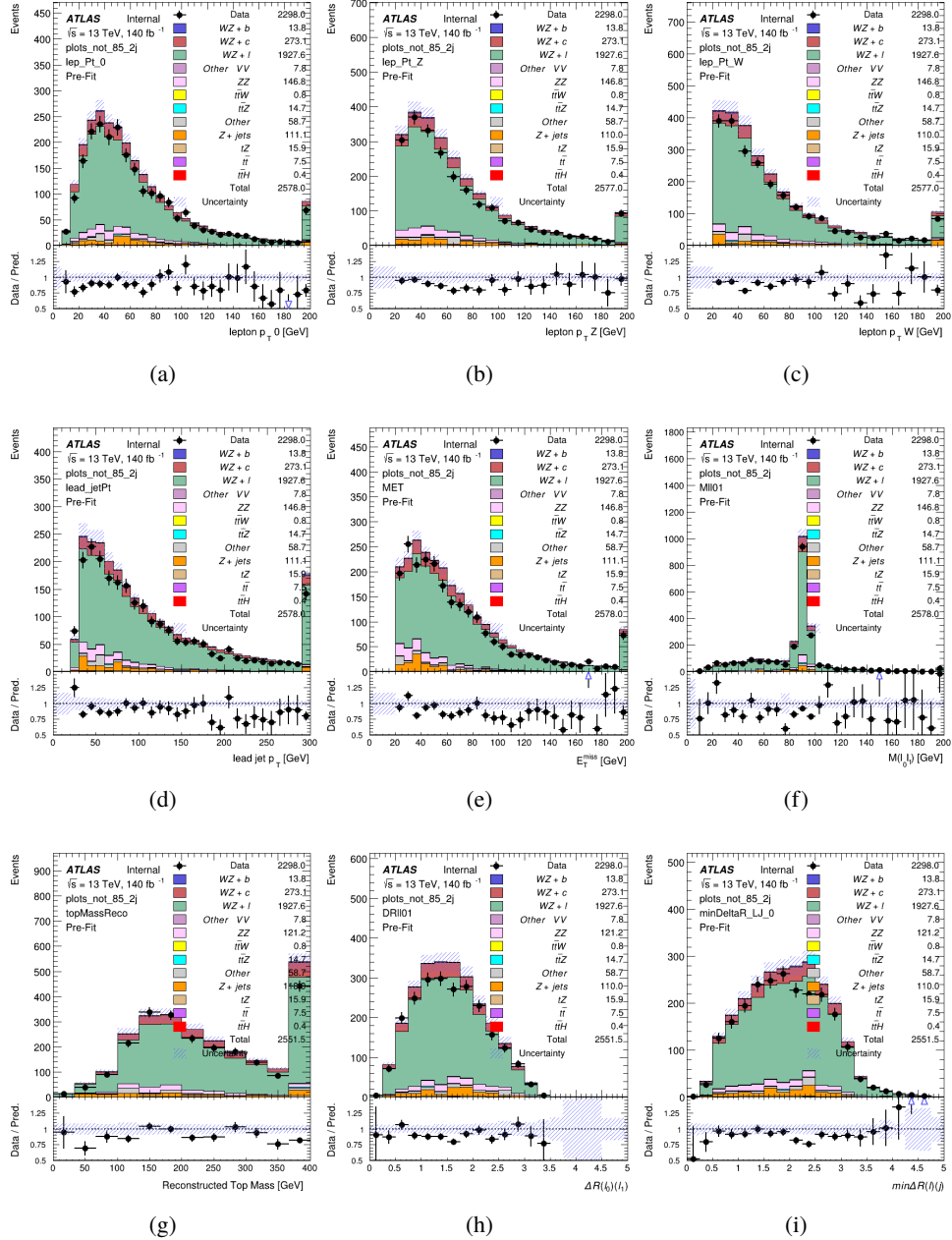


Figure 12.11: Comparisons between the data and MC distributions in the preselection region for (a) the p_T of the opposite sign lepton, (b) the p_T of the other lepton from the Z candidate, (c) the p_T of the lepton from the W candidate, (d) the leading jet p_T , (e) the E_T^{miss} , and (f) the invariant mass of leptons 0 and 1, (g) the reconstructed top mass, (h) $\Delta(R)$ between lepton 0 and 1, (i) the $\Delta(R)$ between the closest lepton and jet.

WZ Fit Region - 2j 77-85% WP

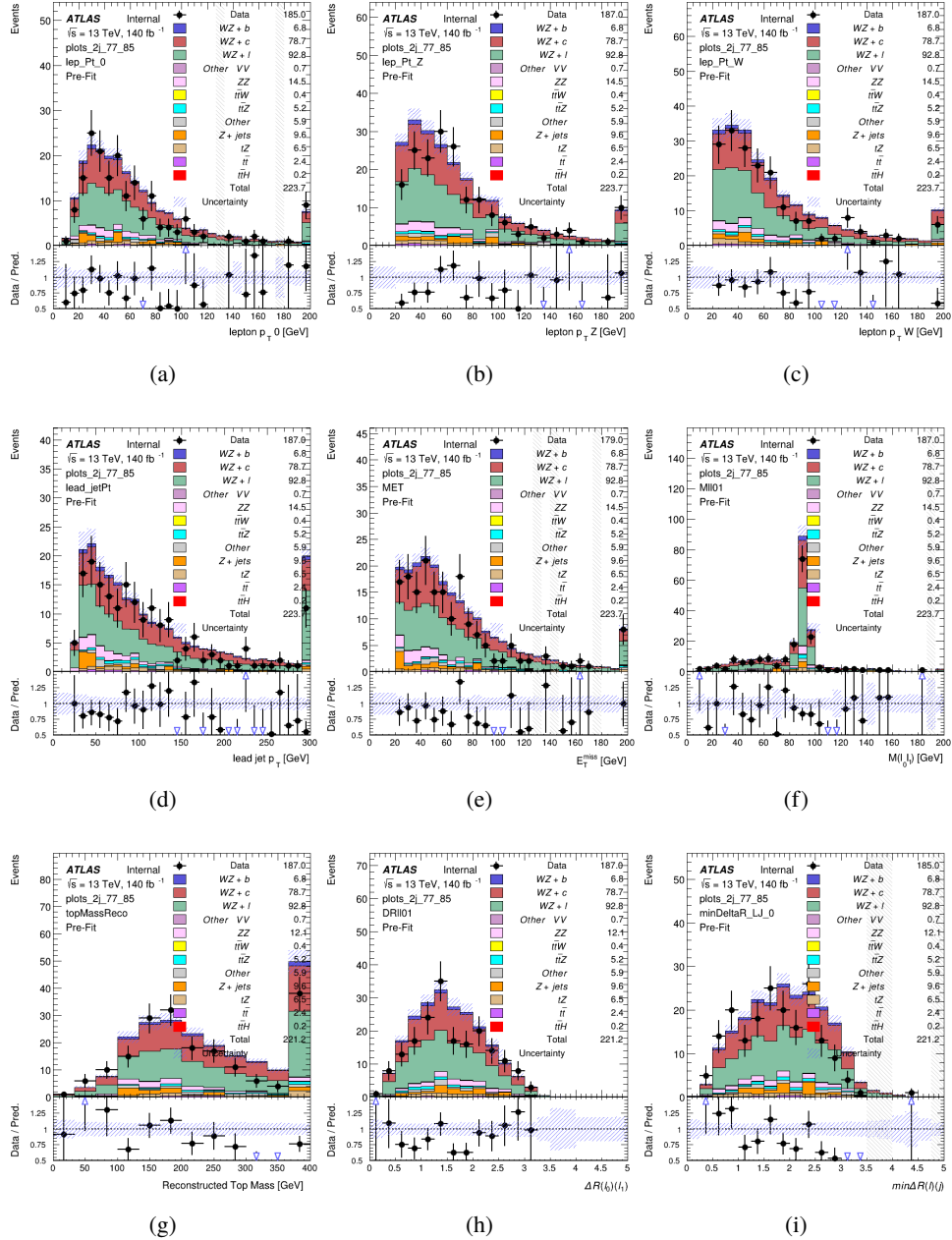


Figure 12.12: Comparisons between the data and MC distributions in the preselection region for (a) the p_T of the opposite sign lepton, (b) the p_T of the other lepton from the Z candidate, (c) the p_T of the lepton from the W candidate, (d) the leading jet p_T , (e) the E_T^{miss} , and (f) the invariant mass of leptons 0 and 1, (g) the reconstructed top mass, (h) $\Delta(R)$ between lepton 0 and 1, (i) the $\Delta(R)$ between the closest lepton and jet.

WZ Fit Region - 2j 70-77% WP

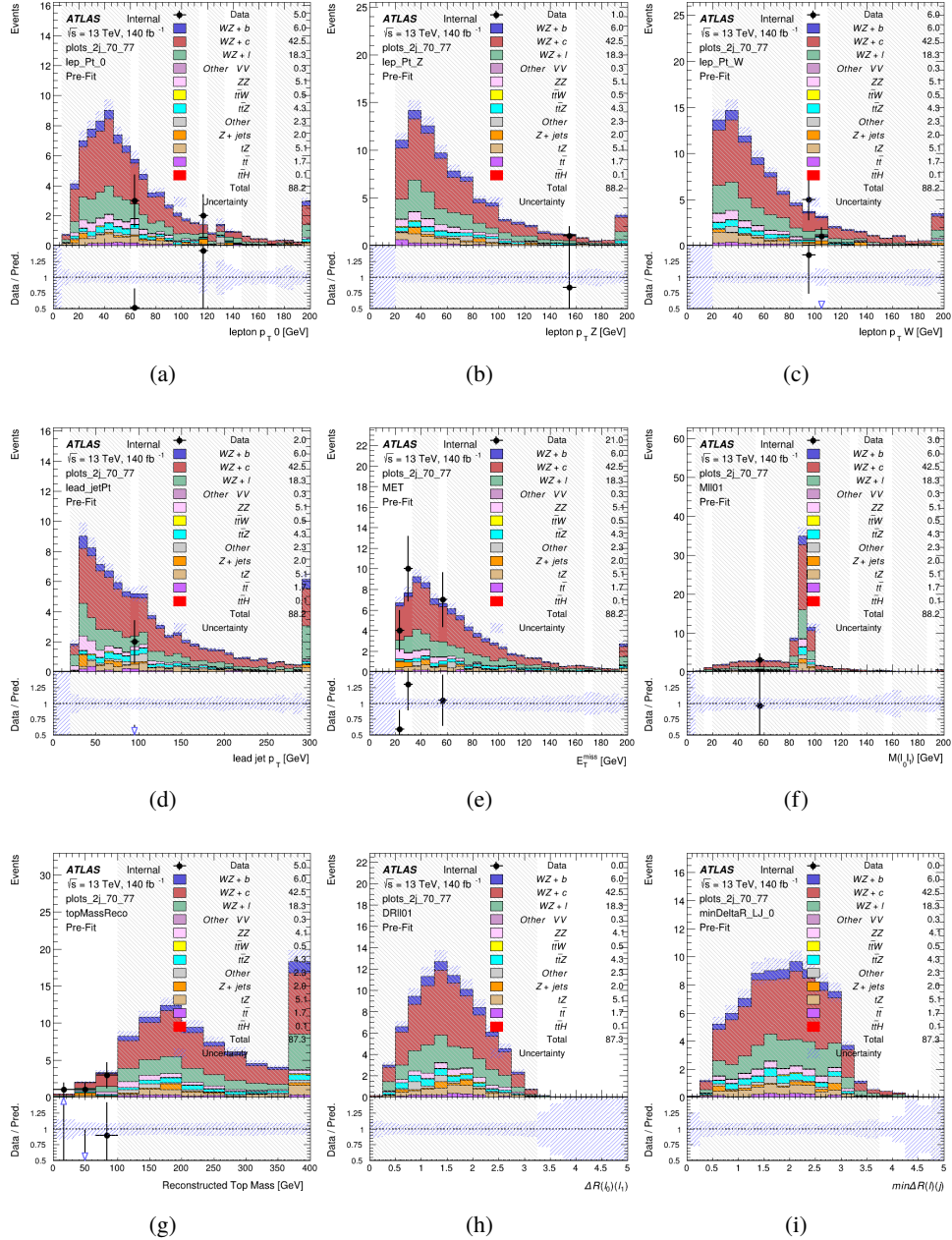


Figure 12.13: Comparisons between the data and MC distributions in the preselection region for (a) the p_T of the opposite sign lepton, (b) the p_T of the other lepton from the Z candidate, (c) the p_T of the lepton from the W candidate, (d) the leading jet p_T , (e) the E_T^{miss} , and (f) the invariant mass of leptons 0 and 1, (g) the reconstructed top mass, (h) $\Delta(R)$ between lepton 0 and 1, (i) the $\Delta(R)$ between the closest lepton and jet.

WZ Fit Region - 2j 60-70% WP

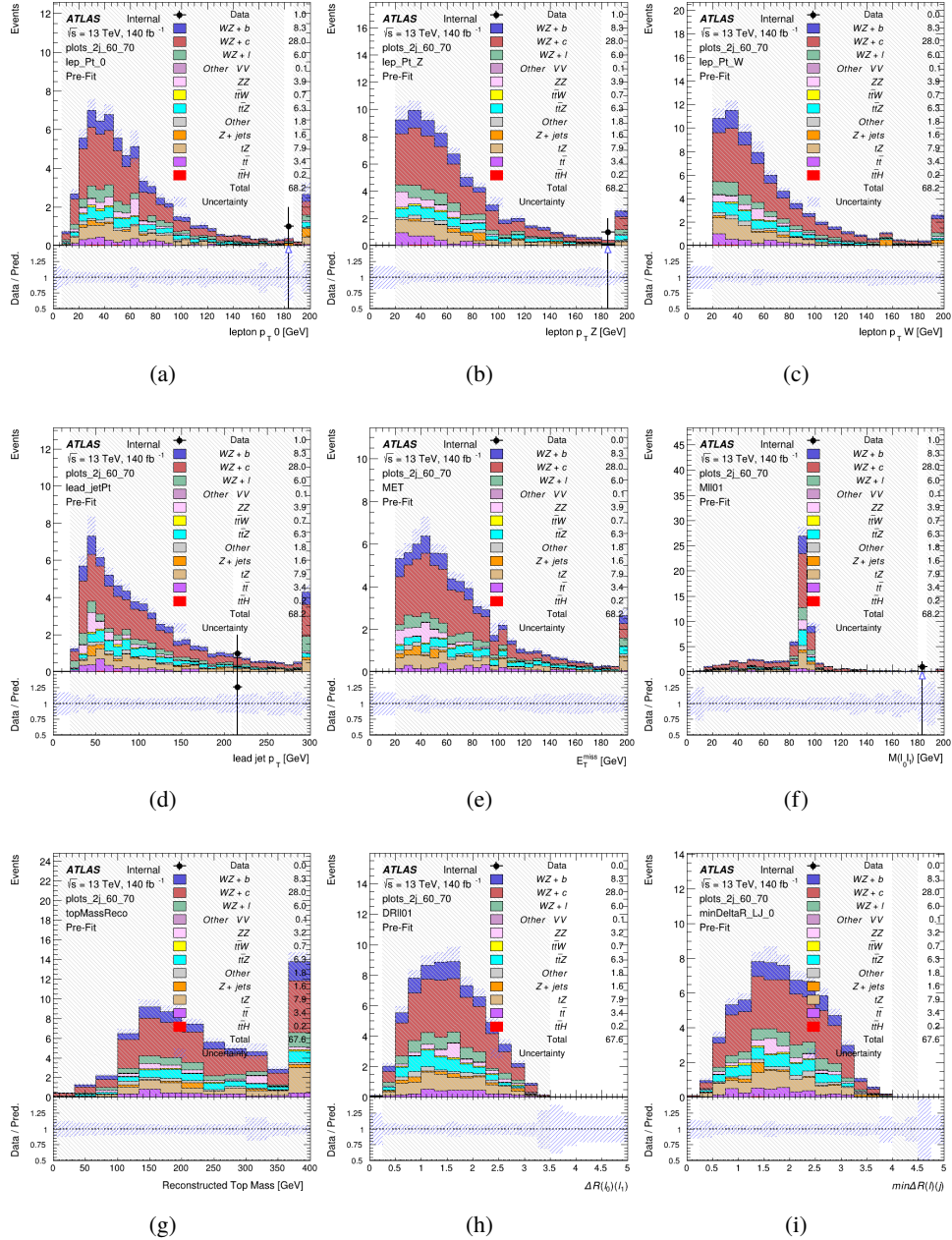


Figure 12.14: Comparisons between the data and MC distributions in the preselection region for (a) the p_T of the opposite sign lepton, (b) the p_T of the other lepton from the Z candidate, (c) the p_T of the lepton from the W candidate, (d) the leading jet p_T , (e) the E_T^{miss} , and (f) the invariant mass of leptons 0 and 1, (g) the reconstructed top mass, (h) $\Delta(R)$ between lepton 0 and 1, (i) the $\Delta(R)$ between the closest lepton and jet.

WZ Fit Region - 2j 60% WP

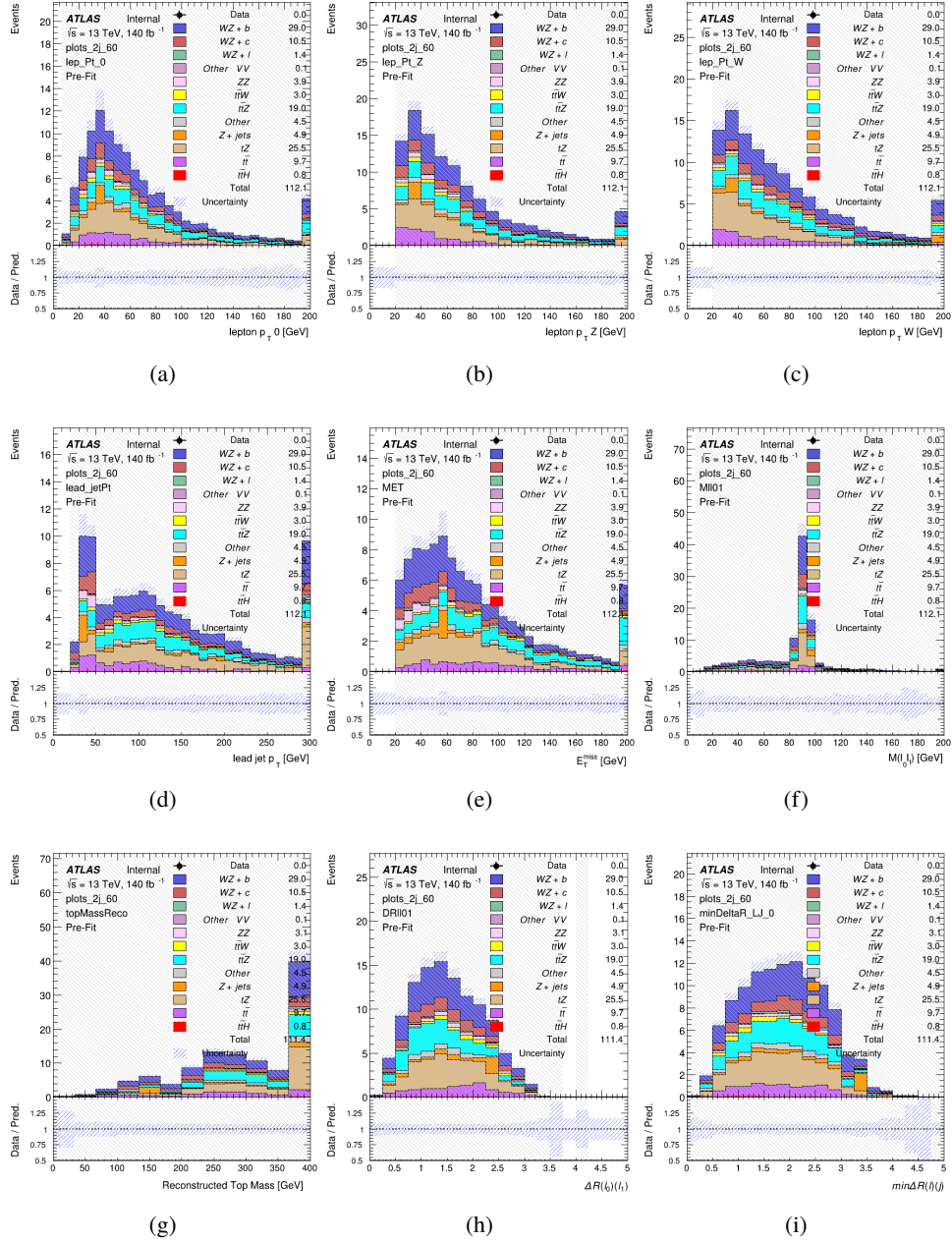


Figure 12.15: Comparisons between the data and MC distributions in the preselection region for (a) the p_T of the opposite sign lepton, (b) the p_T of the other lepton from the Z candidate, (c) the p_T of the lepton from the W candidate, (d) the leading jet p_T , (e) the E_T^{miss} , and (f) the invariant mass of leptons 0 and 1, (g) the reconstructed top mass, (h) $\Delta(R)$ between lepton 0 and 1, (i) the $\Delta(R)$ between the closest lepton and jet.

WZ Fit Region - tZ-CR-2j

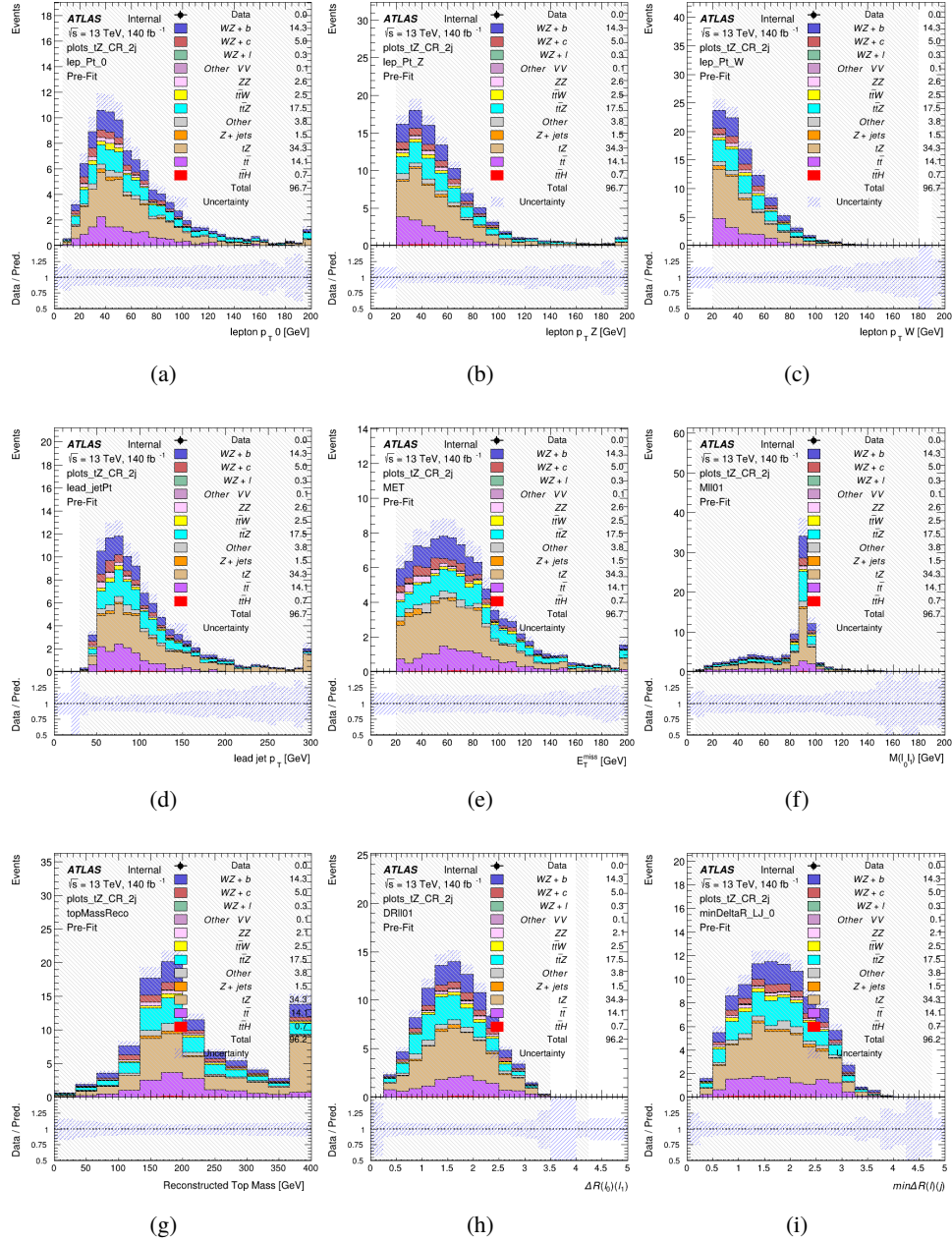


Figure 12.16: Comparisons between the data and MC distributions in the preselection region for (a) the p_T of the opposite sign lepton, (b) the p_T of the other lepton from the Z candidate, (c) the p_T of the lepton from the W candidate, (d) the leading jet p_T , (e) the E_T^{miss} , and (f) the invariant mass of leptons 0 and 1, (g) the reconstructed top mass, (h) $\Delta(R)$ between lepton 0 and 1, (i) the $\Delta(R)$ between the closest lepton and jet.

901 **12.3 Non-Prompt Lepton Estimation**

902 Two processes act as sources of non-prompt leptons appear in the analysis: $t\bar{t}$ and $Z+jet$
 903 production both produce two prompt leptons, and each contribute to the 3l region when an
 904 additional non-prompt lepton appears in the event. The contribution of these processes is
 905 estimated with Monte Carlo simulations, which are validated using enriched control regions.

906 The modelling in the $Z+jets$ and $t\bar{t}$ CRs is further validated for each of the pseudo-
 907 continuous b-tag regions used in the analysis. The relevant lepton p_T spectrum in each b-tag
 908 region is shown in Appendix .2 for these CRs after the correction factors derived below have
 909 been applied.

910 **12.3.1 $t\bar{t}$ Validation**

911 $t\bar{t}$ events can produce two prompt leptons from the decay of each of the tops. These top decays
 912 produce two b-quarks, the decay of which can produce additional non-prompt leptons, which
 913 occasionally pass the event preselection. In order to validate that the Monte Carlo accurately
 914 simulates this process accurately, the MC prediction in a non-prompt $t\bar{t}$ enriched control region
 915 is compared to data.

916 The $t\bar{t}$ control region is similar to the preselection region - three leptons meeting the
 917 criteria described in Section 12 are required, and the requirements on E_T^{miss} remain the same.
 918 However, the selection requiring a lepton pair form a Z-candidate are reversed. Events where the

919 invariant mass of any two opposite sign, same flavor leptons falls within 10 GeV of 91.2 GeV are
920 rejected. This ensures the $t\bar{t}$ control region is orthogonal to the preselection region.

921 Further, because the jet multiplicity of $t\bar{t}$ events tends to be higher than WZ, the number
922 of jets in each event is required to be greater than 1. As b-jets are almost invariably produced
923 from top decays, at least one b-tagged jet passing the 70% DL1r WP in each event is required.

924 Various kinematic plots of this region are shown in Figure 12.17.

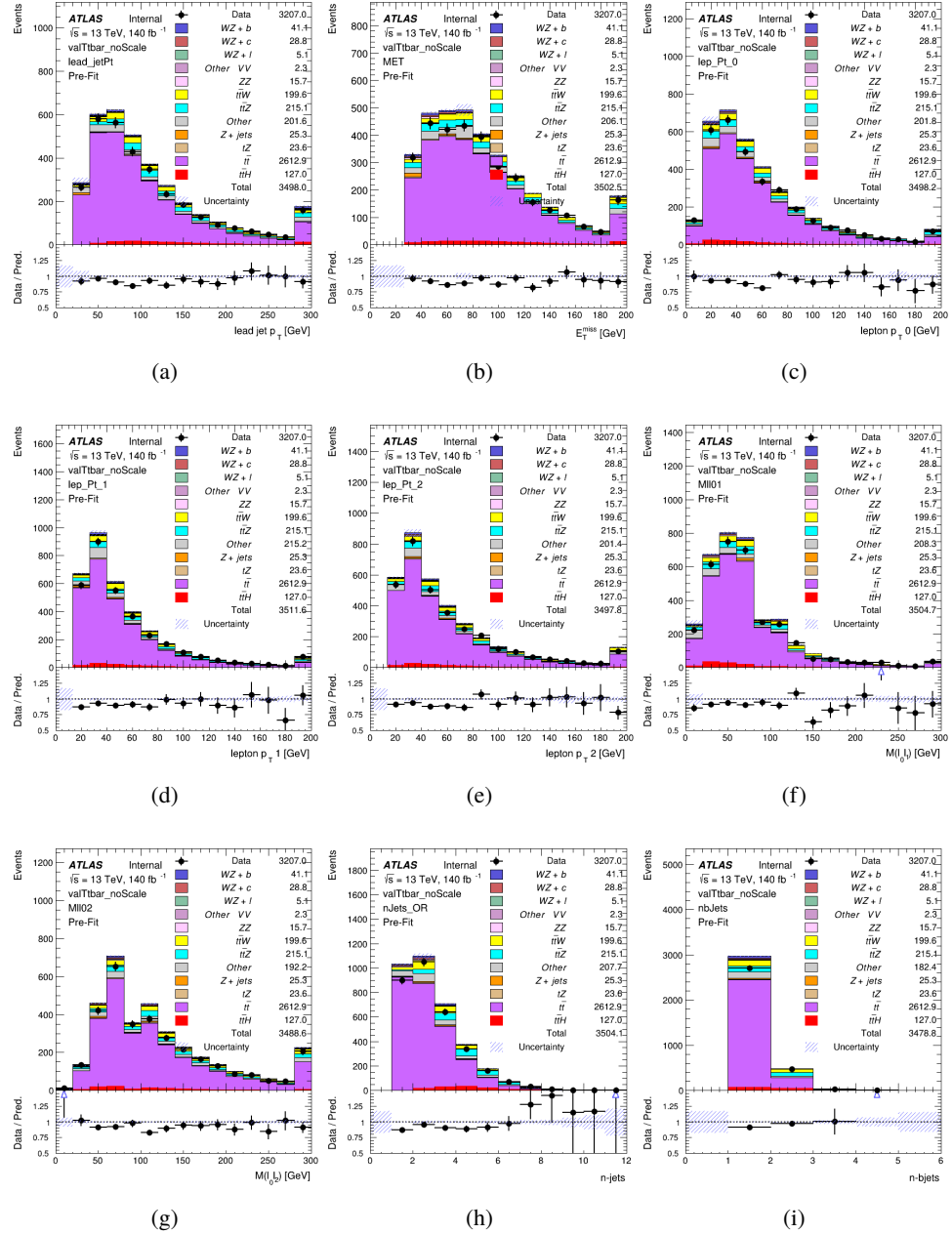


Figure 12.17: Comparisons between the data and MC distributions in the $t\bar{t}$ control region for (a) the p_T of the leading jet, (b) the missing transverse energy, (c) the p_T of lepton 0, (d) p_T of lepton 1, (e) p_T of lepton 2, (f) the invariant mass of leptons 0 and 1, (g) the invariant mass of leptons 0 and 2, (h) the number of jets, (i) the number of b-tagged jets.

925 The shape of each distribution agrees quite well between data and MC, with a constant
926 offset between the two. This is accounted for by applying a constant correction factor of 0.883
927 to the $t\bar{t}$ MC prediction. Plots showing the kinematics of the $t\bar{t}$ VR after this correction factor
928 has been applied are shown in Figure 12.18.

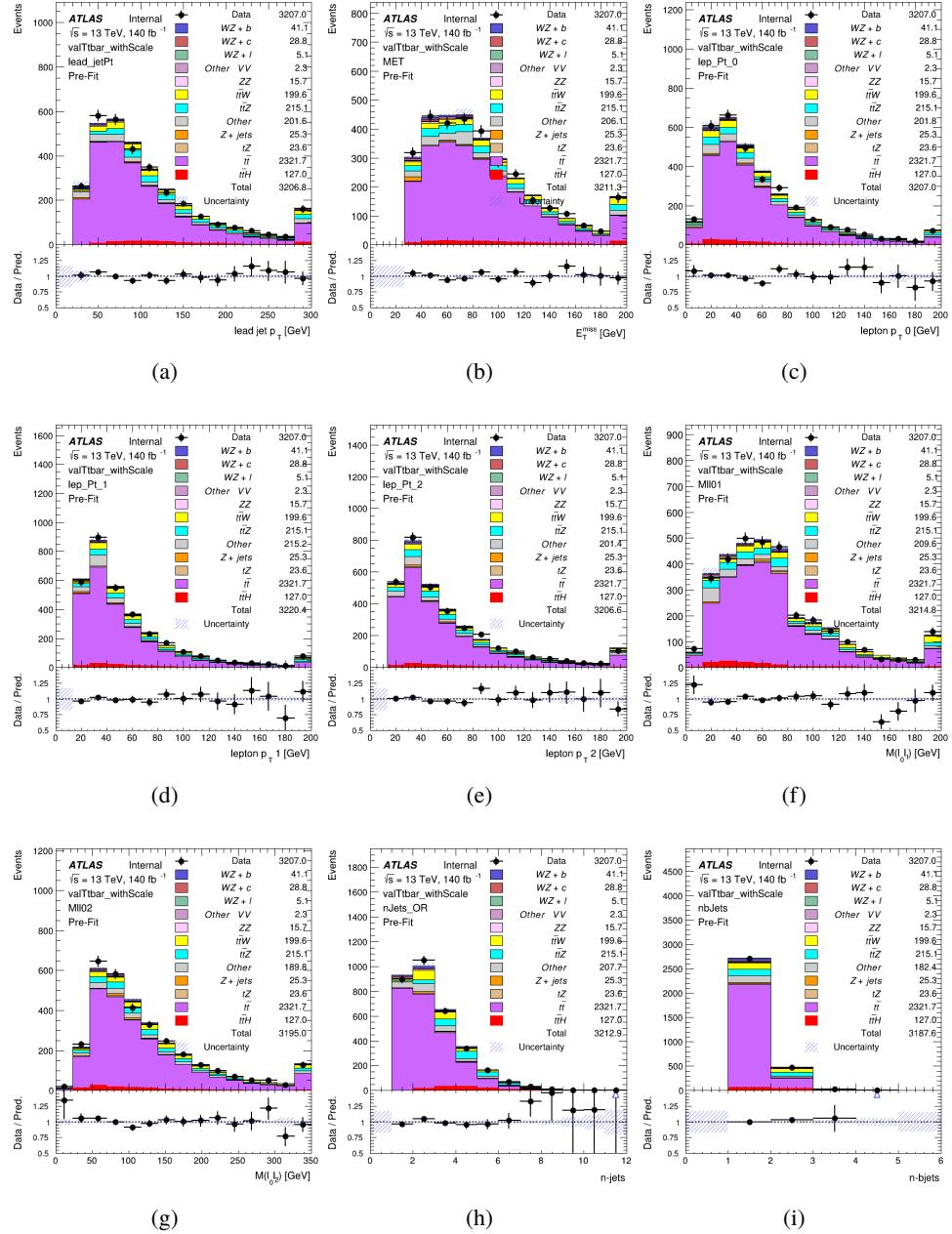


Figure 12.18: Comparisons between the data and MC distributions in the $t\bar{t}$ control region after the correction factor has been applied for (a) the p_T of the leading jet, (b) the missing transverse energy, (c) the p_T of lepton 0, (d) p_T of lepton 1, (e) p_T of lepton 2, (f) the invariant mass of leptons 0 and 1, (g) the invariant mass of leptons 0 and 2, (h) the number of jets, (i) the number of b-tagged jets.

929 The modeling is further validated by looking at the yield in the $t\bar{t}$ VR for each DL1r WP,
 930 giving a clearer correspondence to the signal regions used in the fit. Each region shown in Figure
 931 12.19 requires one or more jets pass the listed WP, with no jets passing the next highest WP.

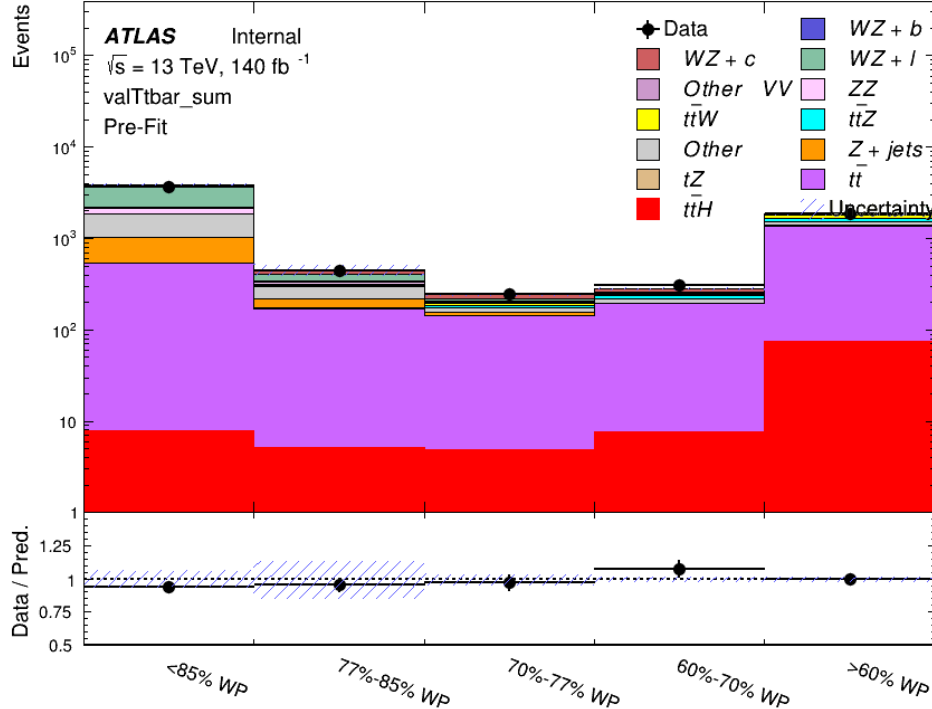


Figure 12.19: Data and MC comparisons for each DL1r WP for both 1-jet and 2-jet regions, after the $t\bar{t}$ VR selection and correction factor have been applied

932 As data and MC are found to agree within 20% for each of these working points, a 20%
 933 systematic uncertainty on the $t\bar{t}$ prediction is included for the analysis.

934 12.3.2 Z+jets Validation

935 Similar to $t\bar{t}$, a non-prompt Z +jets control region is produced in order to validate the MC
936 predictions. The lepton requirements remain the same as the preselection region. Because no
937 neutrinos are present for this process, the E_T^{miss} cut is reversed, requiring $E_T^{\text{miss}} < 30 \text{ GeV}$. This
938 also ensures this control region is orthogonal to the preselection region. Further, the number of
939 jets in each event is required to be greater than or equal to one. Various kinematic plots of this
940 region are shown below. The general agreement between data and MC in each of these suggests
941 that the non-prompt contribution of Z +jets is well modeled by Monte Carlo.

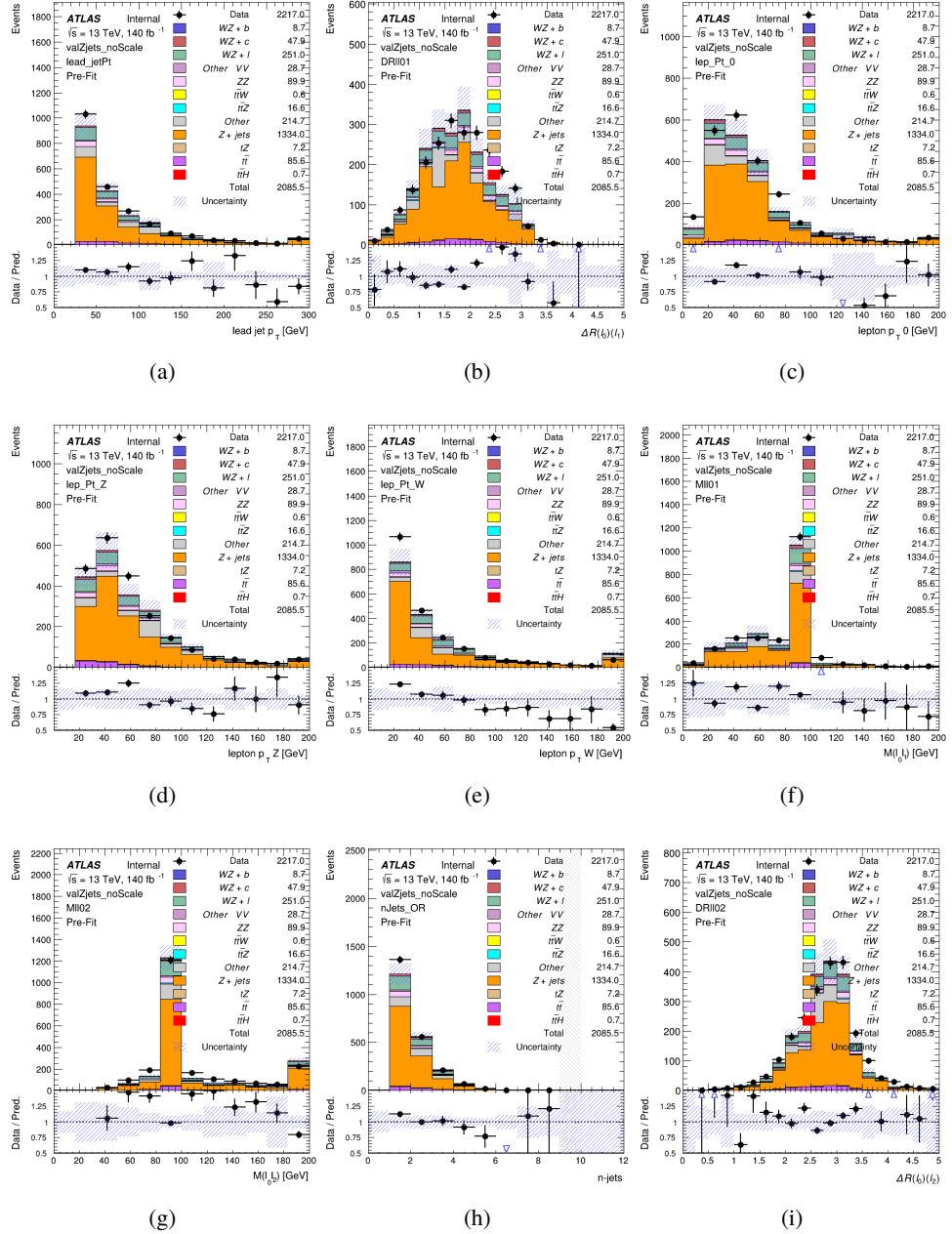


Figure 12.20: Comparisons between the data and MC distributions in the $Z + \text{jets}$ control region for (a) the p_T of the leading jet, (b) ΔR between leptons 0 and 1, (c) the p_T of lepton 0, (d) p_T of SS lepton from the Z candidate, (e) p_T of the SS lepton from the W candidate, (f) the invariant mass of leptons 0 and 1, (g) the invariant mass of leptons 0 and 2, (h) the number of jets, (i) ΔR between leptons 0 and 2. Includes only statistical uncertainties

942 While there is general agreement between data and MC within statistical uncertainty, the
943 shape of the p_T spectrum of the lepton from the W is found to differ. To account for this
944 discrepancy, a variable correction factor is applied to Z+jets. χ^2 minimization of the lepton 2 p_T
945 spectrum is performed to derive a correction factor of $1.53 - 6.6 * 10^{-6}(lep_Pt_W)$. Kinematic
946 plots of the Z + jets control region after this correction factor has been aplied are shown in Figure
947 [12.21](#).

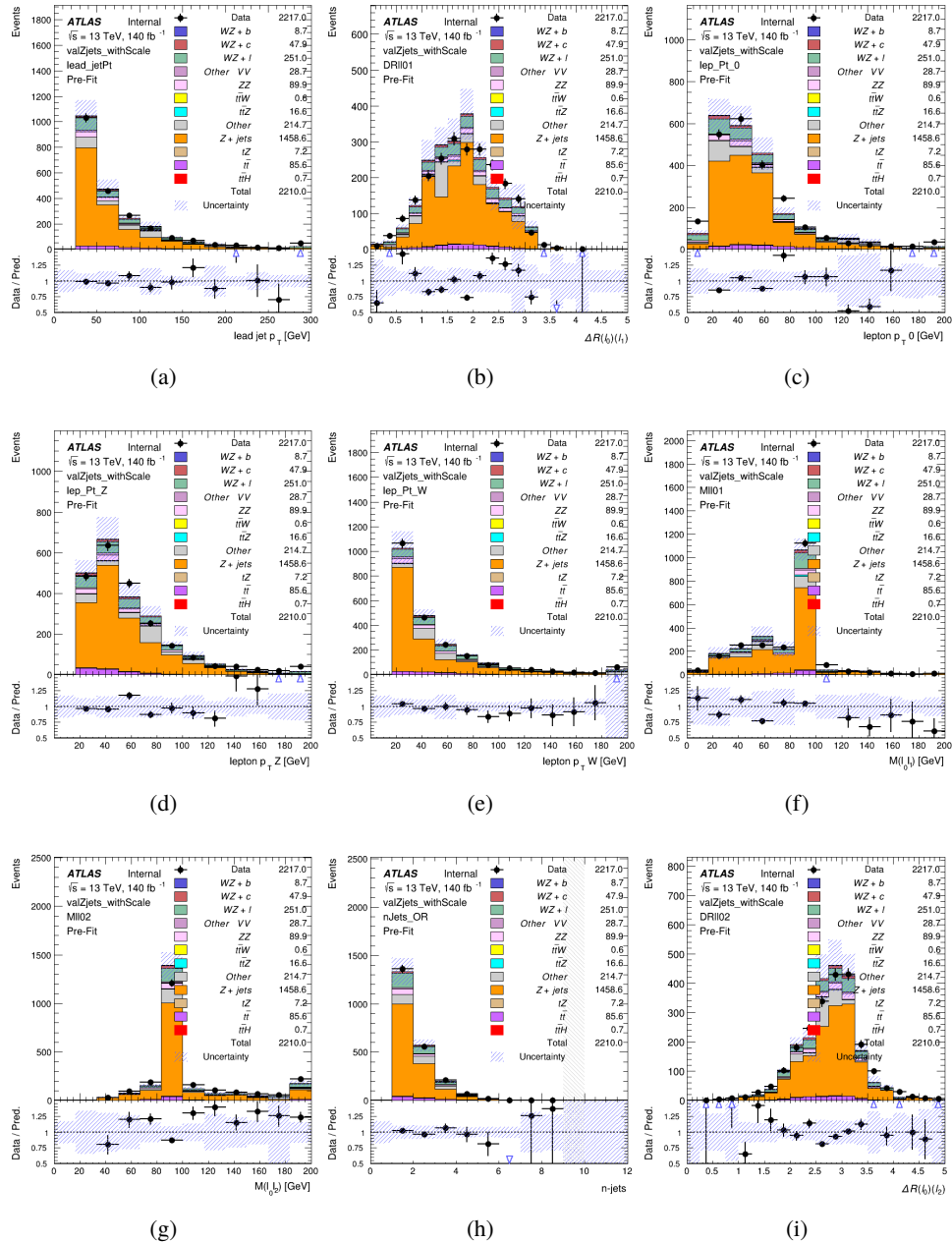


Figure 12.21: Comparisons between the data and MC distributions in the $Z + \text{jets}$ control region after the correction factor has been applied for (a) the p_T of the leading jet, (b) ΔR between leptons 0 and 1, (c) the p_T of lepton 0, (d) p_T of SS lepton from the Z candidate, (e) p_T of the SS lepton from the W candidate, (f) the invariant mass of leptons 0 and 1, (g) the invariant mass of leptons 0 and 2, (h) the number of jets, (i) ΔR between leptons 0 and 2

948 The modeling is further validated by looking at the yield in the Z+jets VR for each DL1r
 949 WP, giving a clearer correspondence to the signal regions used in the fit. Each region shown in
 950 Figure 12.22 requires one or more jets pass the listed WP, with no jets passing the next highest
 951 WP.

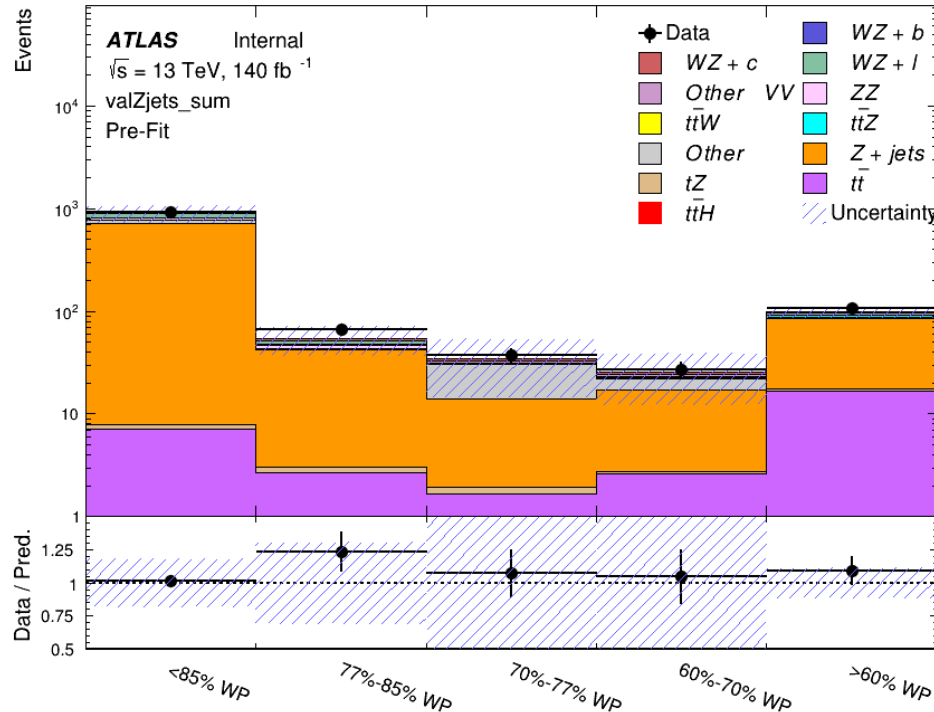


Figure 12.22: Data and MC comparisons for each DL1r WP for both 1-jet and 2-jet regions, after the Z+jets VR selection and correction factor have been applied

952 For each of the b-tagging working points considered, the data falls within 25% of the MC
 953 prediction once this correction factor has been applied. Therefore, a 25% systematic uncertainty
 954 is applied to Z + jets in the analysis.

955 13 tZ Interference Studies and Separation Multivariate Analysis

956 Because tZ produces a final state identical to signal, it represents a predominant background in
957 the most signal enriched regions. That is, the region with one jet passing the 60% DL1r WP.
958 Therefore, a boosted decision tree (BDT) algorithm is trained using TMVA [26] to separate WZ
959 + heavy flavor from tZ.

960 Separation between tZ and WZ + heavy flavor is achieved in part by reconstructing the
961 invariant mass of the top candidate, which clusters more closely to the top mass for tZ than WZ
962 + heavy flavor.

963 The result of this BDT is used to create a tZ enriched region in the fit, reducing its impact
964 on the measurement of WZ + heavy flavor.

965 13.1 Top Mass Reconstruction

966 The reconstruction of the top mass follows the procedure described in detail in section 6.1 of
967 [27]. The mass of the top quark candidate is reconstructed from the jet, the lepton not included
968 in the Z-candidate, and a reconstructed neutrino. In the case that there is one jet in the event,
969 there is only possible b-jet candidate. For events with two jets, the jet with the highest DL1r
970 score is used.

971 The neutrino from the W decay is expected to be the only source of E_T^{miss} . Therefore, the
 972 E_T and ϕ of the neutrino are taken from the E_T^{miss} measurement. This leaves the z-component
 973 of the neutrino momentum, $p_{\nu z}$ as the only unknown.

974 This unknown is solved for by taking the combined invariant mass of the lepton and
 975 neutrino to give the invariant mass of the W boson:

$$976 \quad (p_l + p_\nu)^2 = m_W^2$$

977 Expanding this out into components, this equation gives:

$$978 \quad \sqrt{p_{T\nu}^2 + p_{z\nu}^2} E_l = \frac{m_W^2 - m_l^2}{2} + p_{T\nu}(p_{lx}\cos\phi_\nu + p_{ly}\sin\phi_\nu) + p_{lz}p_{\nu z}$$

979 This equation gives two solutions for $p_{\nu z}$. For cases where only one of these solutions is
 980 real, that is taken as the value of $p_{\nu z}$. For instances with two real solutions, the one which is
 981 shown to be correct in the largest fraction of simulations is taken. For cases when no real solution
 982 is found, often because of detector effects, the value of E_T^{miss} is varied in decreasing increments
 983 of 100 MeV until a real solution is found.

984 The reconstructed top mass distribution for tZ and WZ + b can be seen in figure 13.1.

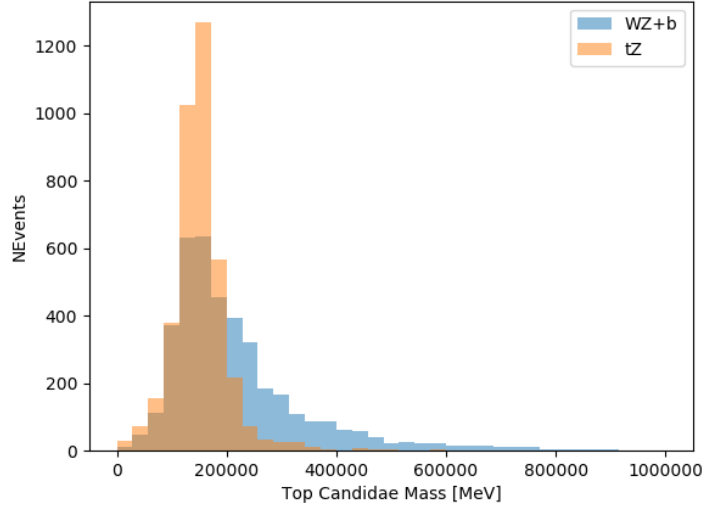


Figure 13.1: Reconstructed top mass distributions for tZ and WZ + b, measured in MeV.

985 13.2 tZ BDT

986 A Boosted Decision Tree (BDT), specifically XGBoost [28], is used to provide separation between
 987 tZ and WZ+b. The following kinematic variables are used as inputs:

- 988 • The invariant mass of the reconstructed top candidate
- 989 • p_T of each of the leptons, jet
- 990 • The invariant mass of each combination of lepton pairs, $M(l\bar{l})$
- 991 • E_T^{miss}
- 992 • Distance between each combination of leptons, $\Delta R(l\bar{l})$

- 993 • Distance between each lepton and the jet, $\Delta R(lj)$

994 The training samples included only events meeting the requirements of the 1-jet, $>60\%$
995 region, i.e. passing all the selection described in section 12 and having exactly one jet which
996 passes the tightest (60%) DL1r working point.

997 The distributions of a few of these features for both signal and background is shown in
998 figure 13.2.

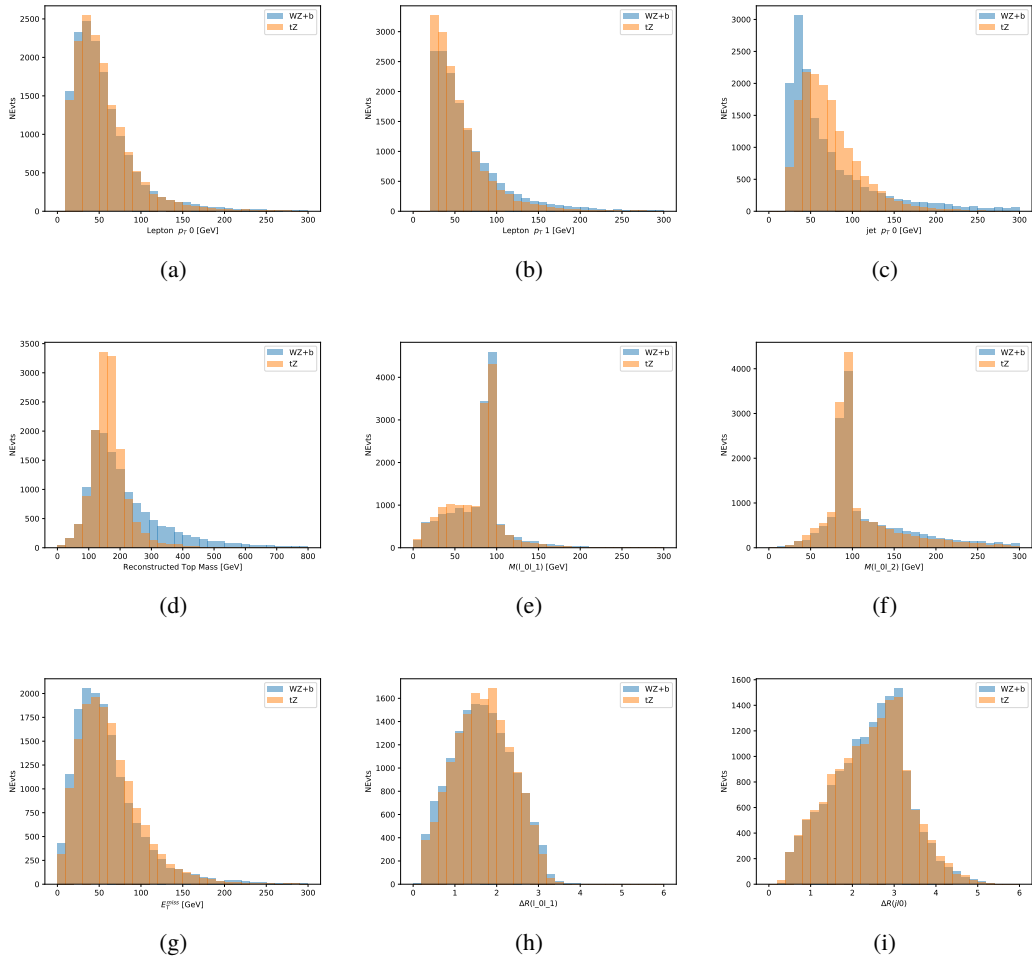


Figure 13.2: Distribution of input features of the BDT for signal (WZ) and background (tZ). Both are scaled to an equal number of events. (a), (b) and (c) show the p_T of lepton 0, lepton 1, and the jet, (d) show the reconstructed top mass, (e) and (f) show the invariant mass of leptons 0 and 1, leptons 0 and 2. (g) shows the E_T^{miss} of each event. (h) and (i) show the ΔR between lepton 0 and lepton 1, and the jet.

999 A sample of 20,000 background (tZ) and signal (WZ+b) Monte Carlo events are used to
 1000 train the BDT. And additional 5,000 events are reserved for testing the model, in order to prevent
 1001 over-fitting. A total of 750 decision trees with a maximum depth of 6 branches are used to build
 1002 the model. These parameters are chosen empirically, by training several models with different

1003 parameters and selecting the one that gave the best separation for the test sample.

1004 The results of the BDT training are shown in figure 13.3. The output scores for both signal
 1005 and background events is shown on the left. The right shows the receiving operating characteristic
 1006 (ROC) curve that results from the MVA. The ROC curve represents the background rejection
 1007 as a function of signal efficiency, where each point on the curve represents a different response
 1008 score. The ROC curve of the BDT is compared to the performance of using an optimal set of flat
 1009 selections on the same set of input variables.

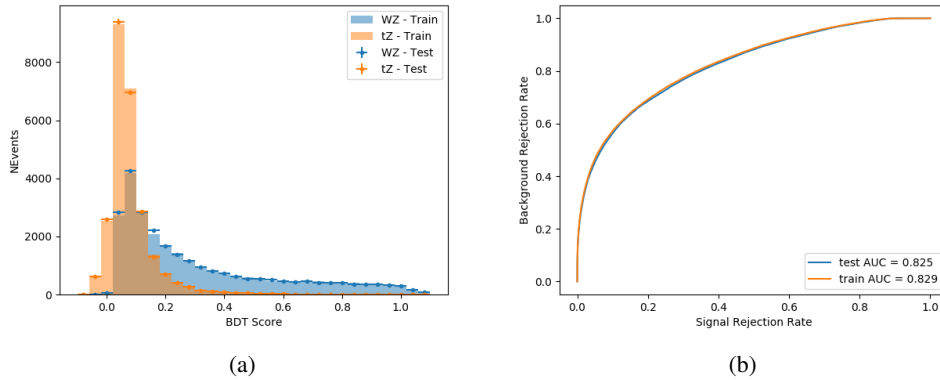


Figure 13.3: Distribution of the BDT response for signal and background events on the left, the ROC curve for the BDT on the right.

1010 The relative important of each input feature in the model, measured by how often they
 1011 appeared in the decision trees, is shown in figure 13.4.

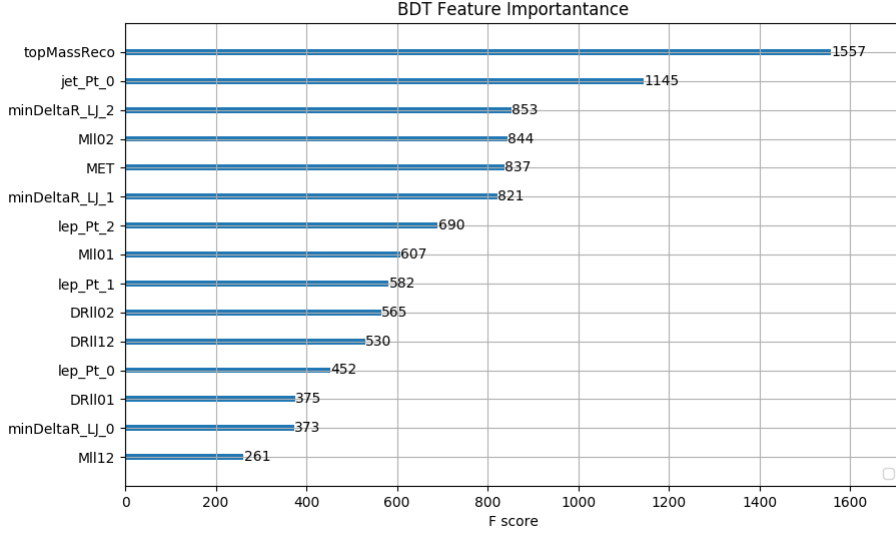


Figure 13.4: Relative importance of each input feature in the model.

1012 These results suggest that some amount of separation can be achieved between these two
 1013 processes, with a high BDT score selecting a set of events that is pure in $WZ + b$. A BDT score
 1014 of 0.725 is selected as a cutoff, where events with scores higher than this form a signal enriched
 1015 region, and events with scores lower than this form a tZ control region. This cutoff is selected by
 1016 varying the value of this cutoff in stat-only Asimov fits, and selecting the value that minimizes
 1017 the statistical uncertainty on $WZ + b$.

1018 14 Systematic Uncertainties

1019 The systematic uncertainties that are considered are summarized in Table 49. These are imple-
 1020 mented in the fit either as a normalization factors or as a shape variation or both in the signal

1021 and background estimations. The numerical impact of each of these uncertainties is outlined in

1022 Section 22.

Table 15: Sources of systematic uncertainty considered in the analysis.

| Systematic uncertainty | Components |
|--|------------|
| Luminosity | 1 |
| Pileup reweighting | 1 |
| Physics Objects | |
| Electron | 6 |
| Muon | 15 |
| Jet energy scale | 28 |
| Jet energy resolution | 8 |
| Jet vertex fraction | 1 |
| Jet flavor tagging | 131 |
| E_T^{miss} | 3 |
| Total (Experimental) | 194 |
| Signal Modeling | |
| Shape modelling | 3 |
| Renormalization and factorization scales | 5 |
| nJet Migration | 5 |
| Background Modeling | |
| Cross section | 15 |
| Renormalization and factorization scales | 12 |
| Total (Signal and background modeling) | 35 |
| Total (Overall) | 230 |

1023 The uncertainty in the combined integrated luminosity is derived from a calibration of the

1024 luminosity scale performed for 13 TeV proton-proton collisions [29], [30].

1025 The experimental uncertainties are related to the reconstruction and identification of light

1026 leptons and b-tagging of jets, and to the reconstruction of E_T^{miss} . The TOTAL electron ID

1027 correlation model is used, corresponding to 1 electron ID systematic. Electron ID is found to be

1028 a subleading systematic that is unconstrained by the fit, making it an appropriate choice for this
1029 analysis.

1030 The sources which contribute to the uncertainty in the jet energy scale (JES) [31] are decom-
1031 posed into uncorrelated components and treated as independent sources in the analysis. The
1032 CategoryReduction model is used to account for JES uncertainties, which decomposes the uncer-
1033 tainties into 30 nuisance parameters included in the fit. The SimpleJER model is used to account
1034 for jet energy resolution (JER) uncertainties, and 8 JER uncertainty components included as
1035 NPs in the fit.

1036 The uncertainties in the b-tagging efficiencies measured in dedicated calibration analyses
1037 [32] are also decomposed into uncorrelated components. The large number of components for
1038 b-tagging is due to the calibration of the distribution of the MVA discriminant.

1039 The full list of systematic uncertainties considered in the analysis is summarized in Tables
1040 50, 51 and 52.

1041

| Experimental Systematics on Leptons and E_T^{miss} | | | |
|---|-------------------------------------|---|-------------------|
| Type | Description | Systematics Name | Application |
| Trigger | | | |
| Scale Factors | Trigger Efficiency | lepSFTrigTight_MU(EL)_SF_Trigger_STAT(SYST) | Event Weight |
| Muons | | | |
| Efficiencies | Reconstruction and Identification | lepSFObjTight_MU_SF_ID_STAT(SYST) | Event Weight |
| | Isolation | lepSFObjTight_MU_SF_Isol_STAT(SYST) | Event Weight |
| | Track To Vertex Association | lepSFObjTight_MU_SF_TTVA_STAT(SYST) | Event Weight |
| p_T Scale | p_T Scale | MUONS_SCALE | p_T Correction |
| Resolution | Inner Detector Energy Resolution | MUONS_ID | p_T Correction |
| | Muon Spectrometer Energy Resolution | MUONS_MS | p_T Correction |
| Electrons | | | |
| Efficiencies | Reconstruction | lepSFObjTight_EL_SF_ID | Event Weight |
| | Identification | lepSFObjTight_EL_SF_Reco | Event Weight |
| | Isolation | lepSFObjTight_EL_SF_Isol | Event Weight |
| Scale Factor | Energy Scale | EG_SCALE_ALL | Energy Correction |
| Resolution | Energy Resolution | EG_RESOLUTION_ALL | Energy Correction |
| E_T^{miss} | | | |
| Soft Tracks Terms | Resolution | MET_SoftTrk_ResoPerp | p_T Correction |
| | Resolution | MET_SoftTrk_ResoPara | p_T Correction |
| | Scale | MET_SoftTrk_ScaleUp | p_T Correction |
| | Scale | MET_SoftTrk_ScaleDown | p_T Correction |

Table 16: Summary of experimental systematics considered for leptons and E_T^{miss} . Includes type, description, name of systematic as used in the fit, and mode of application. The mode of application indicates the systematic evaluation, e.g. as an overall event re-weighting (Event Weight) or rescaling (p_T Correction).

| Experimental Systematics on Jets | | | |
|----------------------------------|--------------------------|--|--|
| Type | Origin | Systematics Name | Application |
| Jet Vertex Tagger | | JVT | Event Weight |
| Energy Scale | Calibration Method | JET_21NP_ JET_EffectiveNP_1-19 | p _T Correction p _T Correction |
| | η inter-calibration | JET_EtaIntercalibration_Modelling JET_EtaIntercalibration_NonClosure JET_EtaIntercalibration_TotalStat | p _T Correction p _T Correction p _T Correction |
| | High p _T jets | JET_SingleParticle_HighPt | p _T Correction |
| | Pile-Up | JET_Pileup_OffsetNPV JET_Pileup_OffsetMu JET_Pileup_PtTerm JET_Pileup_RhoTopology | p _T Correction p _T Correction p _T Correction p _T Correction |
| | Non Closure | JET_PunchThrough_MC15 | p _T Correction |
| | Flavour | JET_Flavor_Response JET_BJES_Response JET_Flavor_Composition | p _T Correction p _T Correction p _T Correction |
| Resolution | | JET_JER_SINGLE_NP | Event Weight |

Table 17: Jet systematics take into account effects of jets calibration method, η inter-calibration, high p_T jets, pile-up, and flavor response. They are all diagonalised into effective parameters.

| Experimental Systematics on b-tagging | | |
|---------------------------------------|---|---|
| Type | Origin | Systematic Name |
| Scale Factors | DL1r b-tagger efficiency on b originated jets in bins of η | DL1r_Continuous_EventWeight_B0-29 |
| | DL1r b-tagger efficiency on c originated jets in bins of η | DL1r_Continuous_EventWeight_C0-19 |
| | DL1r b-tagger efficiency on light flavoured originated jets in bins of η and p_T | DL1r_Continuous_EventWeight_Light0-79 |
| | DL1r b-tagger extrapolation efficiency | DL1r_Continuous_EventWeight_extrapolation DL1r_Continuous_EventWeight_extrapolation_from_charm |

Table 18: Summary of experimental systematics to be included for b-tagging of jets in the analysis, using the continuous DL1r tagging algorithm. All of the b-tagging related systematics are applied as event weights. From left: type, description, and the name of systematic used in the fit.

1042 Theoretical uncertainties applied to MC predictions, including cross section, PDF, and scale
 1043 uncertainties are taken from theory calculations, with the exception of non-prompt and diboson
 1044 backgrounds. The cross-section uncertainty on tZ is taken from [33]. Derivation of the non-
 1045 prompt background uncertainties, Z+jets and t \bar{t} , are explained in detail in Section 12.3. These
 1046 normalization uncertainties are chosen so as to account for the complete uncertainty in the
 1047 non-prompt contribution, and therefore no additional modelling uncertainties are considered for
 1048 Z+jets and t \bar{t} .

1049 The other VV + heavy flavor processes (namely VV+b and VV+charm, which primarily
 1050 consist of ZZ events) are also poorly understood, because these processes involve the same
 1051 physics as WZ + heavy flavor, and have also not been measured. Therefore, a conservative 50%

1052 uncertainty is applied to those samples. While this uncertainty is large, it is found to have little
 1053 impact on the significance of the final result.

1054 The theory uncertainties applied to the predominate background estimates are summarized
 1055 in Table 53.

| Process | X-section [%] |
|--------------------------------|---|
| tZ | X-sec: ± 15.2 QCD Scale: $^{+5.2}_{-1.3}$ PDF($+\alpha_S$): ± 1.2 |
| t̄ H (aMC@NLO+Pythia8) | QCD Scale: $^{+5.8}_{-9.2}$ PDF($+\alpha_S$): ± 3.6 |
| t̄ Z (aMC@NLO+Pythia8) | QCD Scale: $^{+9.6}_{-11.3}$ PDF($+\alpha_S$): ± 4 |
| t̄ W (aMC@NLO+Pythia8) | QCD Scale: $^{+12.9}_{-11.5}$ PDF($+\alpha_S$): ± 3.4 |
| VV + b/charm (Sherpa 2.2.1) | ± 50 |
| VV + light (Sherpa 2.2.1) | ± 6 |
| t̄ t | ± 20 |
| Z + jets | ± 25 |
| Others | ± 50 |

Table 19: Summary of theoretical uncertainties for MC predictions in the analysis.

1056 Additional signal uncertainties are estimated by comparing estimates from the nominal Sherpa
 1057 WZ samples with alternate WZ samples generated with Powheg+PYTHIA8 (DSID 361601).
 1058 MC/MC scale factors are applied to make these comparisons. The shape of the templates used
 1059 in the fit are compared between these two samples for WZ + b, WZ + charm and WZ + light, as
 1060 shown in Figures 14.1 and 14.2. Each of these plots are normalized to unity in order to capture
 1061 differences in shape.

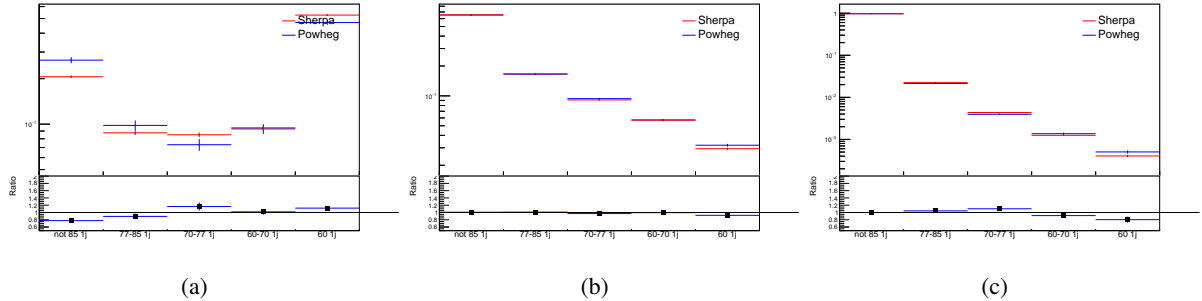


Figure 14.1: Comparison between Sherpa and Powheg predictions of the distribution of (a) $\text{WZ} + \text{b}$, (b) $\text{WZ} + \text{charm}$, and (c) $\text{WZ} + \text{light}$ among the various b-tag WPs used in the 1-jet fit.

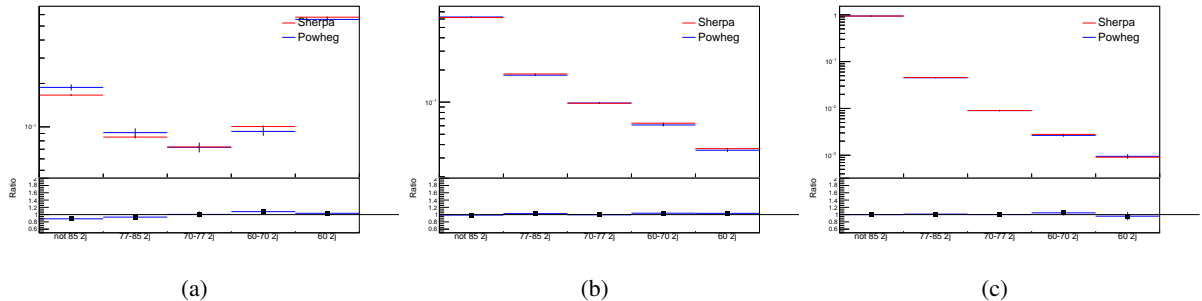


Figure 14.2: Comparison between Sherpa and Powheg predictions of the distribution of (a) $\text{WZ} + \text{b}$, (b) $\text{WZ} + \text{charm}$, and (c) $\text{WZ} + \text{light}$ among the various b-tag WPs used in the 2-jet fit.

1062 Separate systematics are included in the fit for $\text{WZ} + \text{b}$, $\text{WZ} + \text{charm}$ and $\text{WZ} + \text{light}$,
 1063 where the distribution among each of the fit regions is varied based on the prediction of the
 1064 Powheg sample.

1065 A similar approach is taken to account for uncertainties in migrations between the number of
 1066 reco and truth jets. The fraction of events with 1 truth jet which fall into the 1 jet bin versus the
 1067 2 jet bin at reco level is compared for Sherpa and Powheg. The same is done for events with 2
 1068 truth jets. This comparison is shown in figure 14.3.

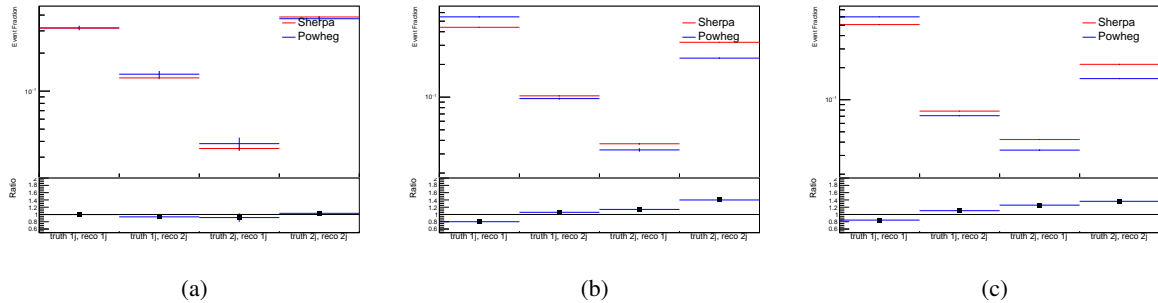


Figure 14.3: Comparison between Sherpa and Powheg predictions for truth jet migrations between the 1 and 2 jet reco bins for (a) WZ + b, (b) WZ + charm, and (c) WZ + light

1069 A systematic is included where events are shifted between the 1-jet and 2-jet regions based
1070 on the differences between these two shapes. This is done independently for each of the WZ +
1071 b, WZ + charm, and WZ + light templates.

Additional systematics are included to account for the uncertainty in the contamination of 0 jet and 3 or more jet events (at truth level) in the 1 and 2 reco jet bins. Because these events fall outside the scope of this measurement, these events are included as a background. As such, a normalization, rather than a shape, uncertainty is applied for this background.

1076 The number of WZ events with 0-jets and ≥ 3 -jets in the reconstructed 1-jet and 2-jet
 1077 regions are compared for Sherpa and Powheg, as seen in figure 14.4. These differences are taken
 1078 as separate normalization systematics on the yield of WZ+0-jet and WZ+ ≥ 3 -jet events.

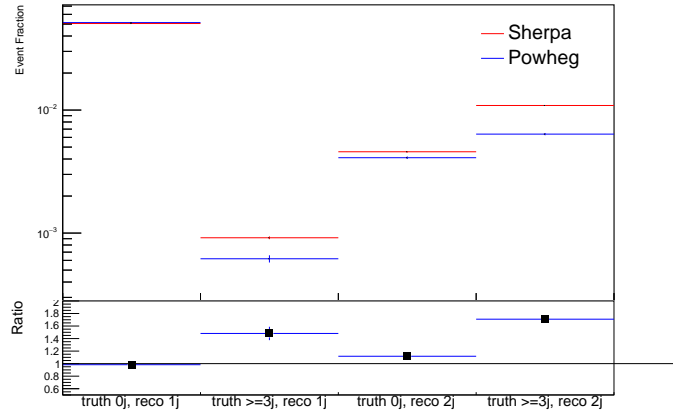


Figure 14.4: Comparison between Sherpa and Powheg predictions for 0 and ≥ 3 truth jet contributions in the 1 and 2 jet reco bins

15 Results

1079 A separate maximum-likelihood fit is performed over the 1-jet and 2-jet fit regions in order to
 1080 extract the best-fit value of the WZ + b-jet and WZ + charm jet contributions. The WZ + b,
 1081 WZ + charm and WZ + light contributions are allowed to float, with the remaining background
 1082 contributions are held fixed. **The current fit strategy treats the WZ + b-jet contribution as**
 1083 **the parameter of interest, with the normalization of the WZ + charm and the WZ + light**
 1084 **contributions taken as systematic uncertainties. This could however be adjusted, depending**
 1085 **on whether it is decided the goal of the analysis should be to measure WZ+b specifically or**
 1086 **WZ + heavy flavor overall.** The result of the fit is used to extract the cross-section of WZ +
 1087 heavy-flavor production.

1088 A maximum likelihood fit to data is performed simultaneously in the regions described

1090 in Section 12. The parameters μ_{WZ+b} , $\mu_{WZ+charm}$, $\mu_{WZ+light}$, where $\mu = \sigma_{\text{observed}}/\sigma_{\text{SM}}$, are
 1091 extracted from the fit.

1092 The Asimov fit for 1-jet events gives an expected μ value of $1.00^{+0.37}_{-0.35}(\text{stat})^{+0.24}_{-0.22}(\text{sys})$ for
 1093 $WZ + b$. The fitted cross-section modifiers for $WZ + \text{charm}$ and $WZ + \text{light}$ are $1.00 \pm 0.17 \pm 0.15$
 1094 and $1.00 \pm 0.04 \pm 0.07$, respectively.

1095 The expected cross-section of $WZ+b$ with 1 associated jet obtained from the fit is
 1096 $1.74^{+0.65}_{-0.61}(\text{stat})^{+0.42}_{-0.37}(\text{sys}) \text{ fb}$ with an expected significance of 2.2σ . The expected cross-section
 1097 of $WZ + \text{charm}$ is measured to be $14.6 \pm 2.5(\text{stat}) \pm 2.1(\text{sys}) \text{ fb}$, with a correlation of -0.23.

1098 For 2-jet events, the fit gives an expected μ value of $1.00^{+0.34}_{-0.33}(\text{stat})^{+0.29}_{-0.28}(\text{sys})$ for $WZ +$
 1099 b . The fitted cross-section modifiers for $WZ + \text{charm}$ and $WZ + \text{light}$ are $1.00 \pm 0.17 \pm 0.15$ and
 1100 $1.00 \pm 0.04 \pm 0.08$, respectively.

1101 The expected $WZ + b$ cross-section in the 2-jet region is $2.46^{+0.83}_{-0.81}(\text{stat})^{+0.073}_{-0.68}(\text{sys}) \text{ fb}$
 1102 with an expected significance of 2.6σ . The 2-jet expected cross-section of $WZ + \text{charm}$ is
 1103 $12.7 \pm 2.2(\text{stat}) \pm 2.0(\text{sys}) \text{ fb}$, and the correlation between $WZ + \text{charm}$ and $WZ + b$ is -0.26.

1104 15.1 1-jet Fit Results

1105 **The results of the fit are currently blinded.**

¹¹⁰⁶ The pre-fit yields in each of the regions used in the fit are shown in Table 15.1, and

¹¹⁰⁷ summarized in Figure 15.1.

¹¹⁰⁸

| Sample | 1j, <85% WP | 1j, 77%-85% WP | 1j, 70%-77% WP | 1j, 60%-70% WP | 1j, >60% WP | tZ CR |
|--------------|-----------------|-----------------|-----------------|-----------------|-----------------|-----------------|
| WZ + b - 1j | 8.1 ± 1.6 | 4.7 ± 0.5 | 4.6 ± 0.4 | 5.1 ± 0.4 | 18.2 ± 2.4 | 4.8 ± 0.6 |
| WZ + c - 1j | 260 ± 22 | 81 ± 6 | 43.1 ± 3.6 | 25.8 ± 2.6 | 9.4 ± 1.8 | 2.9 ± 0.6 |
| WZ + l - 1j | 3090 ± 250 | 91 ± 13 | 17 ± 3 | 4.9 ± 1.6 | 1.3 ± 0.4 | 0.2 ± 0.1 |
| WZ + b - 2j | 1.10 ± 0.37 | 0.44 ± 0.11 | 0.39 ± 0.06 | 0.62 ± 0.14 | 2.1 ± 0.5 | 0.59 ± 0.14 |
| WZ + c - 2j | 21 ± 5 | 5.6 ± 1.2 | 3.0 ± 0.7 | 2.0 ± 0.5 | 0.70 ± 0.20 | 0.30 ± 0.08 |
| WZ + l - 2j | 250 ± 60 | 5.7 ± 1.6 | 0.73 ± 0.53 | 0.31 ± 0.15 | 0.07 ± 0.06 | 0.01 ± 0.01 |
| WZ - Other | 13 ± 5 | 1.4 ± 0.4 | 0.42 ± 0.08 | 0.2 ± 0.01 | 0.30 ± 0.05 | 0.67 ± 0.15 |
| Other VV | 6.2 ± 0.6 | 0.2 ± 0.4 | 0.2 ± 0.04 | 0.07 ± 0.1 | 0.1 ± 0.1 | 0.1 ± 0.2 |
| ZZ | 336 ± 26 | 17.8 ± 2.1 | 4.3 ± 0.6 | 1.7 ± 0.5 | 0.36 ± 0.08 | 0.10 ± 0.03 |
| t̄tW | 1.1 ± 0.2 | 0.2 ± 0.1 | 0.3 ± 0.1 | 0.4 ± 0.1 | 1.5 ± 0.3 | 0.7 ± 0.2 |
| t̄tZ | 6.8 ± 1.2 | 1.4 ± 0.3 | 1.0 ± 0.2 | 1.2 ± 0.2 | 4.4 ± 0.8 | 3.2 ± 0.6 |
| Z + jets | 169 ± 38 | 8.9 ± 1.9 | 3.7 ± 0.8 | 3.3 ± 0.7 | 3.2 ± 0.7 | 0.8 ± 0.17 |
| V + γ | 45 ± 28 | 1.9 ± 2.4 | 0.1 ± 0.1 | 0.02 ± 0.01 | 1.0 ± 0.9 | 0.02 ± 0.03 |
| tZ | 24.3 ± 4.3 | 5.5 ± 1.1 | 4.1 ± 0.8 | 5.9 ± 1.1 | 10.7 ± 2.0 | 23 ± 4 |
| tW | 1.4 ± 0.8 | 0.2 ± 0.5 | 0.0 ± 0.2 | 0.7 ± 0.6 | 0.26 ± 0.42 | 0.39 ± 0.41 |
| WtZ | 2.3 ± 1.2 | 0.6 ± 0.3 | 0.3 ± 0.21 | 0.27 ± 0.2 | 1.1 ± 0.7 | 0.6 ± 0.5 |
| VVV | 12.4 ± 0.5 | 0.93 ± 0.06 | 0.35 ± 0.03 | 0.13 ± 0.02 | 0.14 ± 0.03 | 0.02 ± 0.01 |
| VH | 40 ± 6 | 2.6 ± 1.4 | 0.9 ± 0.8 | 0.7 ± 0.8 | 0.5 ± 0.6 | 0.0 ± 0.0 |
| t̄t | 12.1 ± 1.6 | 2.9 ± 0.6 | 2.5 ± 0.5 | 2.8 ± 0.5 | 11.2 ± 1.4 | 10.9 ± 1.5 |
| t̄tH | 0.24 ± 0.03 | 0.05 ± 0.01 | 0.04 ± 0.01 | 0.06 ± 0.01 | 0.20 ± 0.03 | 0.13 ± 0.02 |
| Total | 5010 ± 260 | 227 ± 24 | 88 ± 12 | 57 ± 8 | 76 ± 16 | 53 ± 8 |

Table 20: Pre-fit yields in each of the 1-jet fit regions.

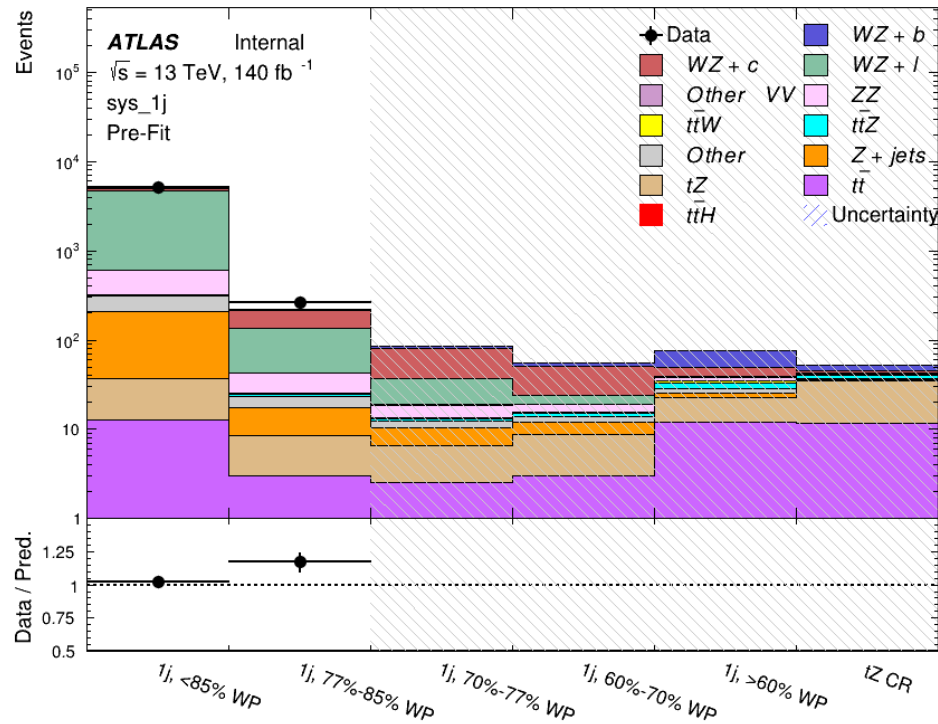


Figure 15.1: Pre-fit summary of the 1-jet fit regions.

1109

The post-fit yields in each region are summarized in Figure 15.1.

1110

| | 1j, <85% WP | 1j, 77%-85% WP | 1j, 70%-77% WP | 1j, 60%-70% WP | 1j, >60% WP | tZ CR |
|-------------|-----------------|-----------------|-----------------|-----------------|-----------------|----------------|
| WZ + b | 8.1 ± 4.9 | 4.7 ± 2.0 | 4.6 ± 2.0 | 5.1 ± 2.1 | 18 ± 10 | 5.0 ± 2.5 |
| WZ + c | 260 ± 60 | 80 ± 14 | 43 ± 7 | 26 ± 5 | 9.4 ± 2.3 | 2.9 ± 0.7 |
| WZ + l | 3090 ± 130 | 90 ± 11 | 17.3 ± 2.8 | 4.9 ± 1.6 | 1.3 ± 0.4 | 0.23 ± 0.1 |
| WZ + b - 2j | 1.10 ± 0.37 | 0.44 ± 0.11 | 0.39 ± 0.06 | 0.62 ± 0.14 | 2.1 ± 0.5 | 0.59 ± 0.1 |
| WZ + c - 2j | 21 ± 5 | 5.6 ± 1.2 | 3.0 ± 0.7 | 2.0 ± 0.5 | 0.70 ± 0.20 | 0.30 ± 0.0 |
| WZ + l - 2j | 250 ± 60 | 5.7 ± 1.6 | 0.73 ± 0.53 | 0.31 ± 0.15 | 0.07 ± 0.06 | 0.01 ± 0.0 |
| WZ - Other | 13 ± 5 | 1.4 ± 0.4 | 0.42 ± 0.08 | 0.2 ± 0.01 | 0.30 ± 0.05 | 0.67 ± 0.1 |
| Other VV | 6.2 ± 0.6 | 0.92 ± 0.07 | 0.02 ± 0.01 | 0.01 ± 0.01 | 0.01 ± 0.01 | 0.01 ± 0.0 |
| ZZ | 346 ± 57 | 19 ± 5 | 4.3 ± 0.8 | 2.7 ± 0.5 | 2.4 ± 0.1 | 2.1 ± 0.6 |
| t̄tW | 1.09 ± 0.21 | 0.2 ± 0.1 | 0.1 ± 0.1 | 0.4 ± 0.1 | 1.5 ± 0.3 | 0.1 ± 0.2 |
| t̄tZ | 6.8 ± 1.2 | 1.4 ± 0.3 | 1.0 ± 0.2 | 1.2 ± 0.2 | 4.4 ± 0.7 | 3.2 ± 0.5 |
| rare Top | 0.14 ± 0.04 | 0.04 ± 0.02 | 0.04 ± 0.0 | 0.1 ± 0.03 | 0.14 ± 0.04 | 0.15 ± 0.0 |
| t̄tWW | 0.04 ± 0.03 | 0.01 ± 0.02 | 0.01 ± 0.01 | 0.01 ± 0.01 | 0.01 ± 0.02 | 0.01 ± 0.0 |
| Z + jets | 169 ± 37 | 8.9 ± 1.9 | 3.7 ± 0.8 | 3.3 ± 0.7 | 3.2 ± 0.7 | 0.8 ± 0.2 |
| W + jets | 0.01 ± 0.01 | 0.01 ± 0.0 |
| V + γ | 46 ± 28 | 1.9 ± 2.4 | 0.1 ± 0.1 | 0.0 ± 0.2 | 1.0 ± 0.9 | 0.0 ± 0.0 |
| tZ | 24 ± 4 | 5.5 ± 1.0 | 4.1 ± 0.8 | 5.9 ± 1.1 | 10.7 ± 1.8 | 23.3 ± 3.7 |
| tW | 1.37 ± 0.82 | 0.18 ± 0.26 | 0.01 ± 0.12 | 0.67 ± 0.64 | 0.26 ± 0.42 | 0.39 ± 0.4 |
| WtZ | 2.3 ± 1.2 | 0.6 ± 0.3 | 0.3 ± 0.2 | 0.3 ± 0.2 | 1.1 ± 0.6 | 0.6 ± 0.3 |
| VVV | 12.4 ± 0.4 | 0.9 ± 0.1 | 0.4 ± 0.1 | 0.13 ± 0.02 | 0.14 ± 0.03 | 0.02 ± 0.0 |
| VH | 40 ± 6 | 2.6 ± 1.4 | 0.9 ± 0.8 | 0.7 ± 0.8 | 0.4 ± 0.6 | 0.01 ± 0.0 |
| t̄t | 12.1 ± 1.6 | 2.9 ± 0.6 | 2.5 ± 0.5 | 2.8 ± 0.5 | 11.2 ± 1.5 | 10.9 ± 1.4 |
| t̄tH | 0.24 ± 0.03 | 0.05 ± 0.01 | 0.04 ± 0.01 | 0.06 ± 0.01 | 0.20 ± 0.03 | 0.13 ± 0.0 |
| Total | 5100 ± 110 | 227 ± 12 | 87 ± 6 | 56.7 ± 4.4 | 76 ± 9 | 52.5 ± 4.2 |

Table 21: Post-fit yields in each of the 1-jet fit regions.

1111

A post-fit summary plot of the 1-jet fitted regions is shown in Figure 15.2:

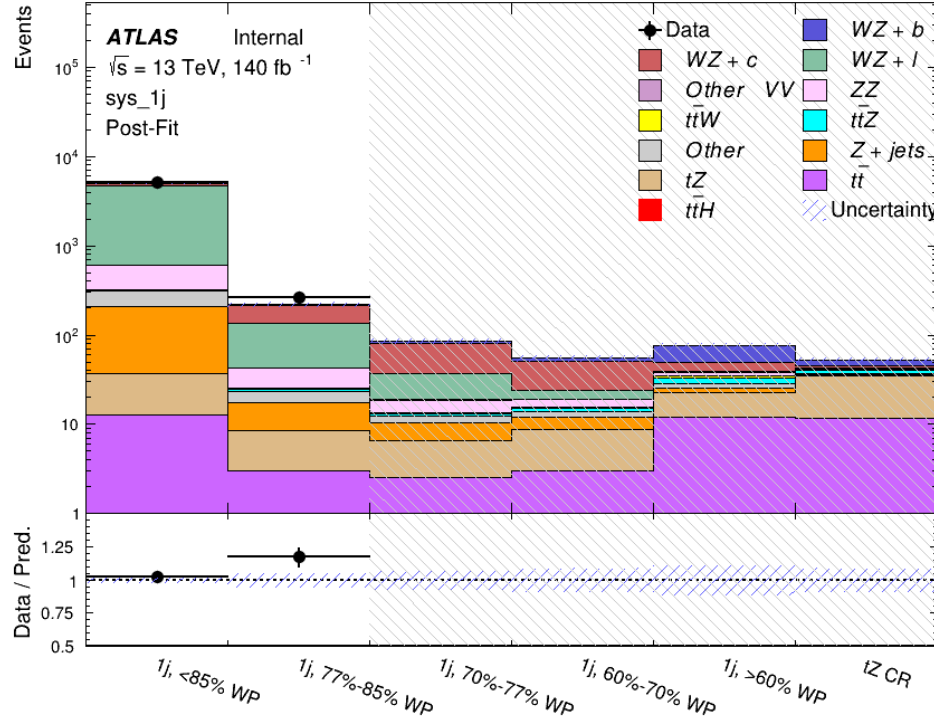


Figure 15.2: Post-fit summary of the 1-jet fit regions.

1112 As described in Section 21, there are 226 systematic uncertainties that are considered
 1113 as NPs in the fit. These NPs are constrained by Gaussian or log-normal probability density
 1114 functions. The latter are used for normalisation factors to ensure that they are always positive.
 1115 The expected number of signal and background events are functions of the likelihood. The prior
 1116 for each NP is added as a penalty term, decreasing the likelihood as it is shifted away from its
 1117 nominal value.

1118 The impact of each NP is calculated by performing the fit with the parameter of interest held
 1119 fixed, varied from its fitted value by its uncertainty, and calculating $\Delta\mu$ relative to the baseline

¹¹²⁰ fit. The impact of the most significant sources of systematic uncertainties is summarized in Table

¹¹²¹ [22.](#)

| Uncertainty Source | $\Delta\mu$ | |
|---------------------------------|-------------|-------|
| WZ + light cross-section | 0.13 | -0.12 |
| WZ + charm cross-section | -0.10 | 0.12 |
| Jet Energy Scale | 0.08 | 0.13 |
| tZ cross-section | -0.10 | 0.10 |
| Jet Energy Resolution | -0.10 | 0.10 |
| Luminosity | -0.08 | 0.09 |
| Other Diboson + b cross-section | -0.07 | 0.07 |
| Flavor tagging | 0.05 | 0.05 |
| t <bar>t</bar> | -0.05 | 0.05 |
| WZ cross-section - QCD scale | -0.04 | 0.03 |
| Total Systematic Uncertainty | 0.28 | 0.32 |

Table 22: Summary of the most significant sources of systematic uncertainty on the measurement of WZ + b with exactly one associated jet.

¹¹²² The ranking and impact of those nuisance parameters with the largest contribution to the

¹¹²³ overall uncertainty is shown in Figure [15.3](#).

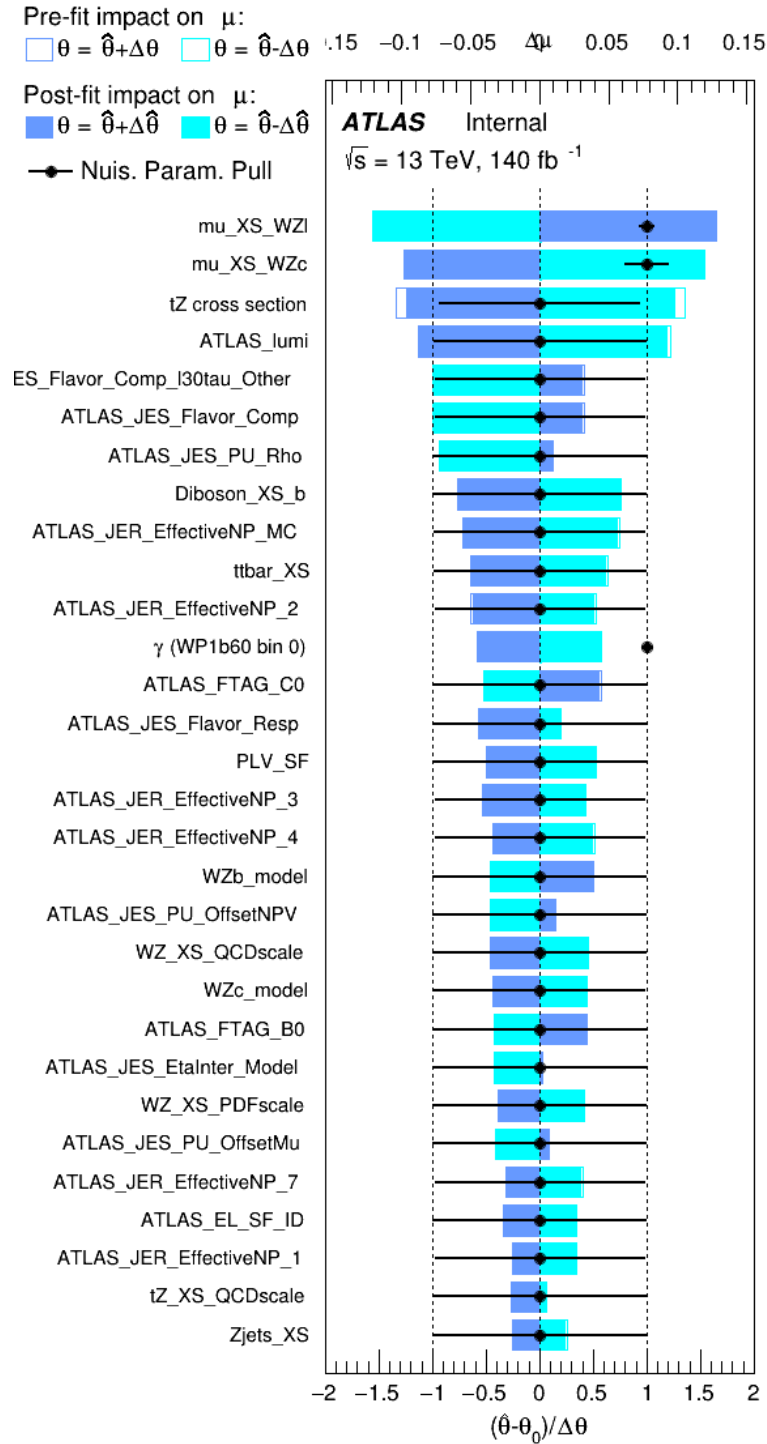


Figure 15.3: Impact of systematic uncertainties on the signal-strength of $WZ + b$ for events with exactly one jet

1124 The large impact of the Jet Energy Scale and Jet Flavor Tagging is unsurprising, as the
1125 shape of the fit regions depends heavily on the modeling of the jets. The other major sources
1126 of uncertainty come from background modelling and cross-section uncertainty. The pie charts
1127 in Figure 15.4 show that for the modelling uncertainties that contribute most correspond to the
1128 most significant backgrounds.

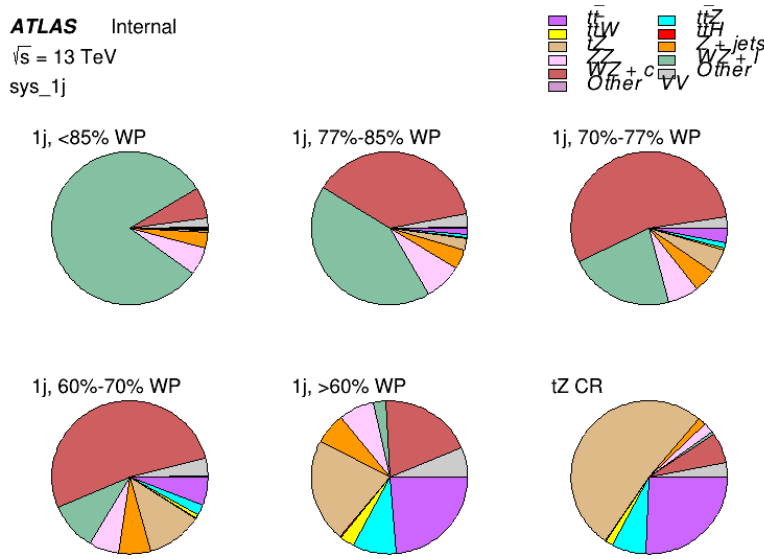


Figure 15.4: Post-fit background composition of the fit regions.

The correlations between these nuisance parameters are summarized in Figure 15.5.

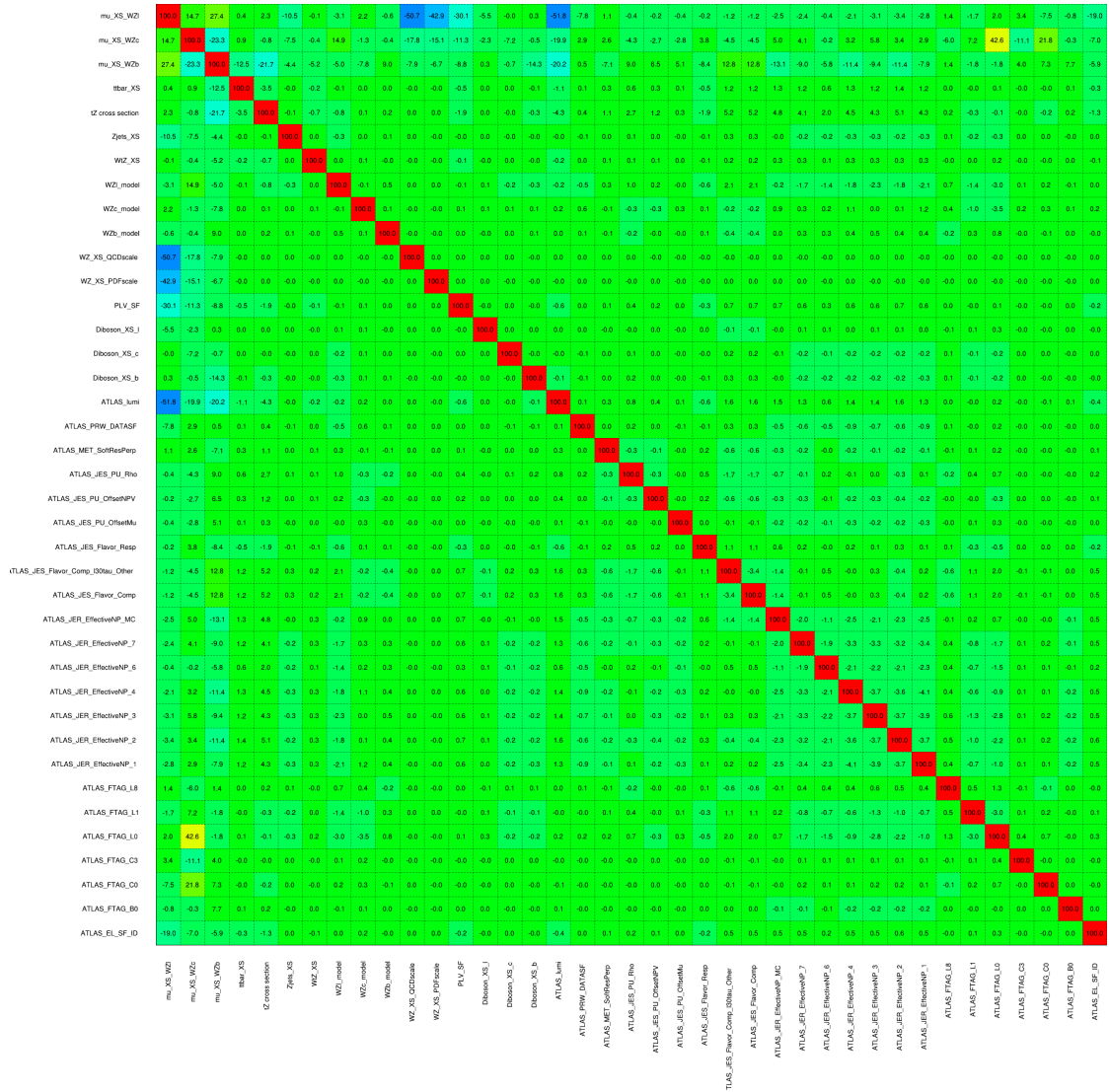


Figure 15.5: Correlations between nuisance parameters

1130 The negative correlations between $\mu_{WZ+charm}$ and μ_{WZ+b} and $\mu_{WZ+light}$ are expected:
1131 WZ + charm is present in both the WZ + b and WZ + light enriched regions, therefore increasing
1132 the fraction of charm requires increasing the fraction of WZ + b and WZ + light. This reasoning
1133 also explains the positive correlation between μ_{WZ+b} and $\mu_{WZ+light}$.

1134 Two of the major backgrounds in the region with the highest purity of WZ + b are tZ and
1135 Other VV + b, explaining the negative correlations between μ_{WZ+b} and the tZ cross section, and
1136 the VV + b cross section.

1137 The high correlation between the luminosity and $\mu_{WZ+light}$ arises from the fact that the
1138 uncertainty on $\mu_{WZ+light}$ is very low (around 4%). Small changes in luminosity cause a change
1139 in the yield of WZ + light that is large compared to its uncertainty, producing a large correlation
1140 between these two parameters.

1141 **15.2 2-jet Fit Results**

1142 **The results of the fit are currently blinded.**

1143 Pre-fit yields in each of the 2-jet fit regions are shown in Figure 15.2.

| | 2j, <85% WP | 2j, 77%-85% WP | 2j, 70%-77% WP | 2j, 60%-70% WP | 2j, >60% WP | tZ CR 2j |
|--------------|------------------|-----------------|-----------------|-----------------|-----------------|----------------|
| WZ + b - 2j | 3.1 ± 1.6 | 6.7 ± 0.5 | 5.6 ± 0.4 | 8.0 ± 0.6 | 31 ± 2 | 14 ± 1 |
| WZ + c - 2j | 180 ± 20 | 54 ± 6 | 41 ± 3 | 24 ± 3 | 11 ± 2 | 4.8 ± 0.6 |
| WZ + l - 2j | 1250 ± 150 | 90 ± 14 | 18 ± 3 | 5.8 ± 1.4 | 1.4 ± 0.4 | 0.25 ± 0.1 |
| WZ + b - 1j | 3.4 ± 0.6 | 1.52 ± 0.35 | 1.58 ± 0.23 | 1.95 ± 0.39 | 6.7 ± 1.1 | 1.9 ± 0.6 |
| WZ + c - 1j | 56 ± 14 | 17.6 ± 4.0 | 8.6 ± 2.2 | 6.3 ± 1.8 | 3.0 ± 0.9 | 0.7 ± 0.2 |
| WZ + l - 1j | 427 ± 120 | 24 ± 7 | 4.7 ± 2.3 | 1.6 ± 0.7 | 0.3 ± 0.2 | 0.01 ± 0.0 |
| WZ - Other | 129 ± 29 | 6.1 ± 4.6 | 1.2 ± 0.3 | 0.3 ± 0.2 | 2.9 ± 0.5 | 3.6 ± 0.6 |
| Other VV | 7.63 ± 0.63 | 0.6 ± 0.5 | 0.16 ± 0.03 | 0.01 ± 0.01 | 0.1 ± 0.1 | 0.1 ± 0.1 |
| ZZ | 135 ± 20 | 14.1 ± 3.2 | 4.7 ± 0.8 | 4.0 ± 0.6 | 4.1 ± 0.7 | 3.1 ± 0.5 |
| t̄tW | 0.8 ± 0.2 | 0.4 ± 0.1 | 0.5 ± 0.1 | 0.7 ± 0.2 | 4.3 ± 0.6 | 3.9 ± 0.6 |
| t̄tZ | 14.7 ± 2.2 | 5.6 ± 0.8 | 4.5 ± 0.7 | 6.5 ± 1.1 | 25.4 ± 4.0 | 21.9 ± 3.4 |
| rare Top | 0.14 ± 0.04 | 0.07 ± 0.03 | 0.03 ± 0.02 | 0.09 ± 0.03 | 0.37 ± 0.07 | 0.6 ± 0.1 |
| t̄tWW | 0.04 ± 0.03 | 0.02 ± 0.02 | 0.01 ± 0.01 | 0.01 ± 0.00 | 0.03 ± 0.03 | 0.01 ± 0.0 |
| Z + jets | 110.0 ± 22.9 | 9.6 ± 2.0 | 2.1 ± 0.50 | 1.6 ± 0.4 | 5.1 ± 1.1 | 1.5 ± 0.3 |
| W + jets | 0.0 ± 0.0 | 0.0 ± 0.0 | 0.0 ± 0.0 | 0.0 ± 0.0 | 0.0 ± 0.0 | 0.0 ± 0.0 |
| V + γ | 25 ± 18 | 0.5 ± 0.2 | 0.1 ± 0.1 | 0.1 ± 0.1 | 0.0 ± 0.02 | 0.05 ± 0.0 |
| tZ | 15.9 ± 2.9 | 6.9 ± 1.3 | 5.1 ± 1.0 | 8.0 ± 1.5 | 18.7 ± 3.2 | 36.4 ± 6.1 |
| tW | 0.9 ± 0.7 | 0.2 ± 0.3 | 0.0 ± 0.1 | 0.0 ± 0.0 | 0.8 ± 0.6 | 0.2 ± 0.2 |
| WtZ | 4.9 ± 2.5 | 1.5 ± 0.8 | 1.1 ± 0.6 | 1.3 ± 0.7 | 4.6 ± 2.4 | 3.3 ± 1.7 |
| VVV | 7.4 ± 0.3 | 1.0 ± 0.1 | 0.4 ± 0.1 | 0.2 ± 0.1 | 0.13 ± 0.03 | 0.04 ± 0.0 |
| VH | 19.5 ± 4.2 | 2.8 ± 1.6 | 0.7 ± 0.7 | 0.1 ± 0.2 | 0.0 ± 0.0 | 0.0 ± 0.0 |
| t̄t | 0.7 ± 0.4 | 0.1 ± 0.1 | 0.05 ± 0.06 | 0.15 ± 0.13 | 0.8 ± 0.5 | 2.3 ± 1.2 |
| t̄t | 6.8 ± 1.0 | 2.4 ± 0.5 | 1.8 ± 0.4 | 3.3 ± 0.6 | 8.4 ± 1.2 | 13.6 ± 1.1 |
| t̄tH | 0.4 ± 0.1 | 0.2 ± 0.1 | 0.16 ± 0.02 | 0.23 ± 0.03 | 0.94 ± 0.11 | 1.03 ± 0.1 |
| Total | 2580 ± 160 | 229 ± 24 | 89 ± 13 | 69 ± 11 | 120 ± 15 | 108 ± 11 |

Table 23: Pre-fit yields in each of the 2-jet fit regions.

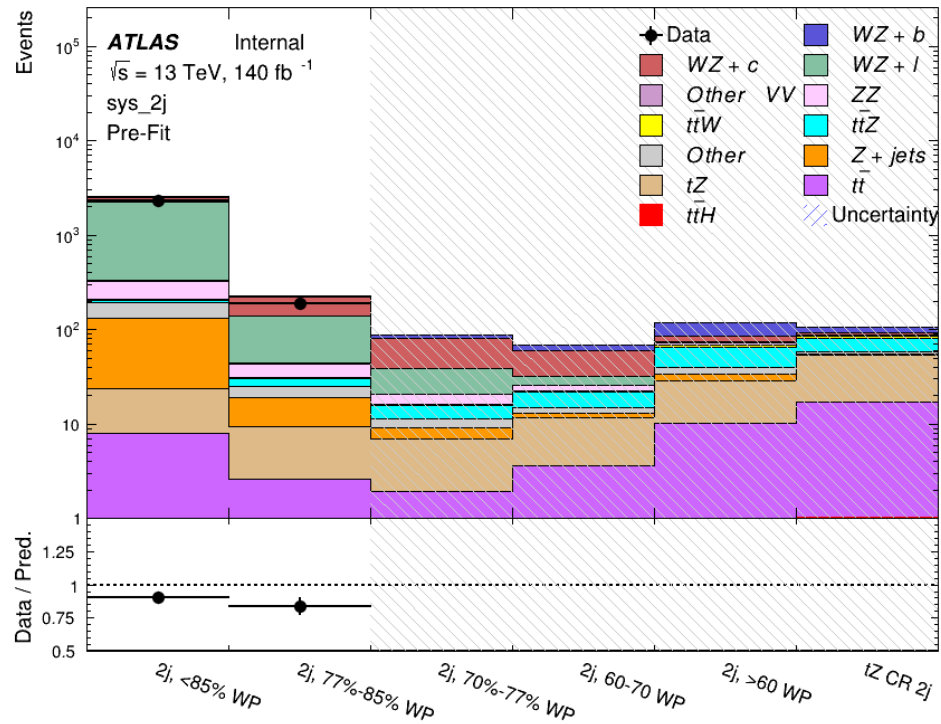


Figure 15.6: Pre-fit summary of the 2-jet fit regions.

1144

The post-fit yields in each region are summarized in Figure 15.2.

| | 2j, <85% WP | 2j, 77%-85% WP | 2j, 70%-77% WP | 2j, 60%-70% WP | 2j, >60% WP | tZ CR 2j |
|-------------|-----------------|-----------------|-----------------|-----------------|-----------------|----------------|
| WZ + b | 13 ± 6 | 6.7 ± 2.9 | 5.8 ± 2.5 | 8.0 ± 3.5 | 31 ± 13 | 14 ± 5 |
| WZ + c | 260 ± 60 | 77 ± 15 | 41 ± 8 | 26 ± 5 | 10.9 ± 2.4 | 4.8 ± 1.1 |
| WZ + l | 1860 ± 90 | 90 ± 12 | 17.6 ± 2.8 | 5.8 ± 1.3 | 1.4 ± 0.4 | 0.3 ± 0.2 |
| WZ + b - 1j | 3.4 ± 0.6 | 1.52 ± 0.35 | 1.58 ± 0.23 | 1.95 ± 0.39 | 6.7 ± 1.1 | 1.9 ± 0.6 |
| WZ + c - 1j | 56 ± 14 | 17.6 ± 4.0 | 8.6 ± 2.2 | 6.3 ± 1.8 | 3.0 ± 0.9 | 0.7 ± 0.2 |
| WZ + l - 1j | 427 ± 120 | 24 ± 7 | 4.7 ± 2.3 | 1.6 ± 0.7 | 0.3 ± 0.2 | 0.01 ± 0.0 |
| WZ - Other | 129 ± 29 | 6.1 ± 4.6 | 1.2 ± 0.3 | 0.3 ± 0.2 | 2.9 ± 0.5 | 3.6 ± 0.6 |
| Other VV | 7.6 ± 0.6 | 0.3 ± 0.3 | 0.3 ± 0.1 | 0.1 ± 0.06 | 0.03 ± 0.02 | 0.1 ± 0.1 |
| ZZ | 145 ± 30 | 11.3 ± 4.4 | 2.7 ± 1.6 | 1.0 ± 0.3 | 4.0 ± 0.1 | 2.4 ± 0.1 |
| t̄tW | 0.8 ± 0.2 | 0.4 ± 0.1 | 0.54 ± 0.12 | 0.74 ± 0.15 | 4.3 ± 0.6 | 3.9 ± 0.6 |
| t̄tZ | 14.7 ± 2.2 | 5.6 ± 0.8 | 4.5 ± 0.7 | 6.5 ± 1.0 | 25.4 ± 3.9 | 21.9 ± 3.0 |
| rare Top | 0.14 ± 0.04 | 0.07 ± 0.03 | 0.03 ± 0.02 | 0.09 ± 0.03 | 0.4 ± 0.1 | 0.6 ± 0.1 |
| t̄tWW | 0.04 ± 0.03 | 0.02 ± 0.02 | 0.01 ± 0.01 | 0.01 ± 0.01 | 0.03 ± 0.03 | 0.01 ± 0.0 |
| Z + jets | 110 ± 23 | 9.6 ± 2.0 | 2.1 ± 0.5 | 1.6 ± 0.4 | 5.1 ± 1.1 | 1.5 ± 0.3 |
| W + jets | 0.0 ± 0.0 | 0.0 ± 0.0 |
| V + γ | 25 ± 19 | 0.5 ± 0.2 | 0.1 ± 0.1 | 0.13 ± 0.14 | 0.0 ± 0.02 | 0.05 ± 0.0 |
| tZ | 15.9 ± 2.7 | 6.9 ± 1.2 | 5.1 ± 0.9 | 8.0 ± 1.4 | 18.7 ± 3.0 | 36 ± 6 |
| tW | 0.1 ± 0.7 | 0.2 ± 0.3 | 0.0 ± 0.1 | 0.0 ± 0.0 | 0.8 ± 0.6 | 0.2 ± 0.2 |
| WtZ | 4.9 ± 2.5 | 1.5 ± 0.8 | 1.1 ± 0.6 | 1.3 ± 0.7 | 4.6 ± 2.3 | 3.3 ± 1.7 |
| VVV | 7.4 ± 0.3 | 1.0 ± 0.1 | 0.36 ± 0.03 | 0.19 ± 0.03 | 0.13 ± 0.03 | 0.04 ± 0.0 |
| VH | 19 ± 4 | 2.8 ± 1.6 | 0.7 ± 0.7 | 0.1 ± 0.2 | 0.0 ± 0.0 | 0.0 ± 0.0 |
| t̄t | 6.8 ± 1.0 | 2.4 ± 0.5 | 1.8 ± 0.4 | 3.3 ± 0.6 | 8.4 ± 1.2 | 13.6 ± 1.7 |
| t̄tH | 0.40 ± 0.05 | 0.19 ± 0.03 | 0.16 ± 0.02 | 0.23 ± 0.03 | 0.94 ± 0.11 | 1.03 ± 0.1 |
| Total | 2580 ± 60 | 229 ± 11 | 89 ± 6 | 69.1 ± 4.1 | 120 ± 10 | 108 ± 6 |

Table 24: Post-fit yields in each of the 2-jet fit regions.

1145

A post-fit summary of the fitted regions is shown in Figure 15.7:

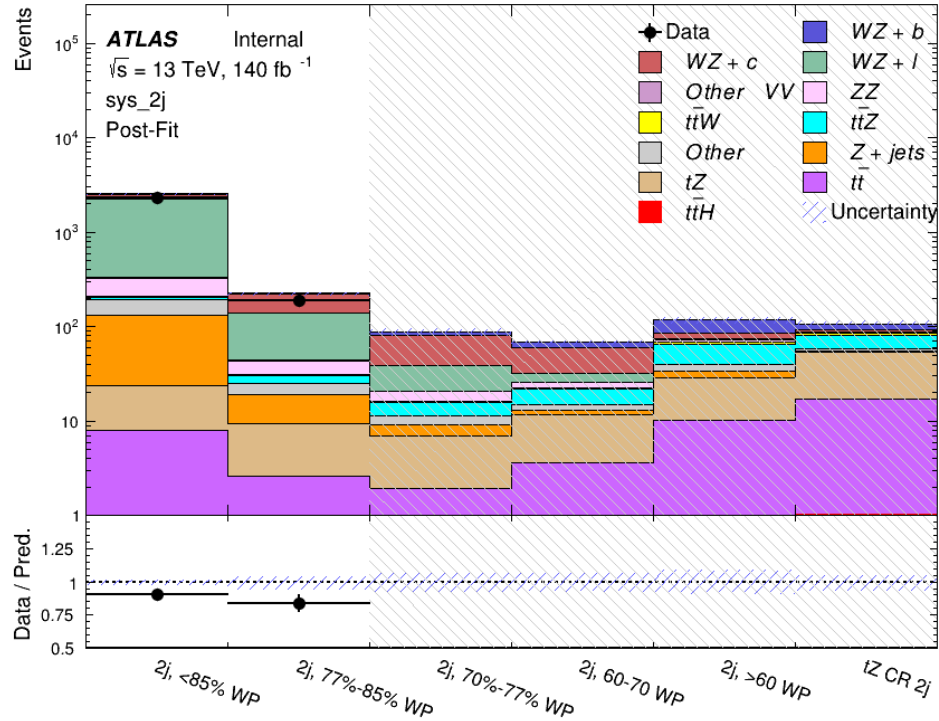


Figure 15.7: Post-fit summary of the fit over 2-jet regions.

1146 The same set of systematic uncertainties consider for the 1-jet fit are included in the 2-jet
 1147 fit as well. The impact of the most significant systematic uncertainties is summarized in Table
 1148 [25](#).

| Uncertainty Source | $\Delta\mu$ | |
|-------------------------------|-------------|-------|
| WZ + c cross-section | -0.1 | 0.14 |
| Luminosity | -0.11 | 0.12 |
| tZ cross-section | -0.11 | 0.11 |
| Jet Energy Scale | -0.11 | 0.11 |
| ttZ cross-section - QCD scale | -0.08 | 0.09 |
| WZ + l cross-section | 0.08 | -0.07 |
| WtZ cross-section | -0.07 | 0.07 |
| Flavor tagging | 0.05 | 0.05 |
| Other VV + b cross-section | -0.05 | 0.05 |
| Jet Energy Resolution | -0.04 | 0.04 |
| Total | 0.29 | 0.31 |

Table 25: Summary of the most significant sources of systematic uncertainty on the measurement of WZ + b 2-jet events.

¹¹⁴⁹ The ranking and impact of those nuisance parameters with the largest contribution to the
¹¹⁵⁰ overall uncertainty is shown in Figure 15.8.

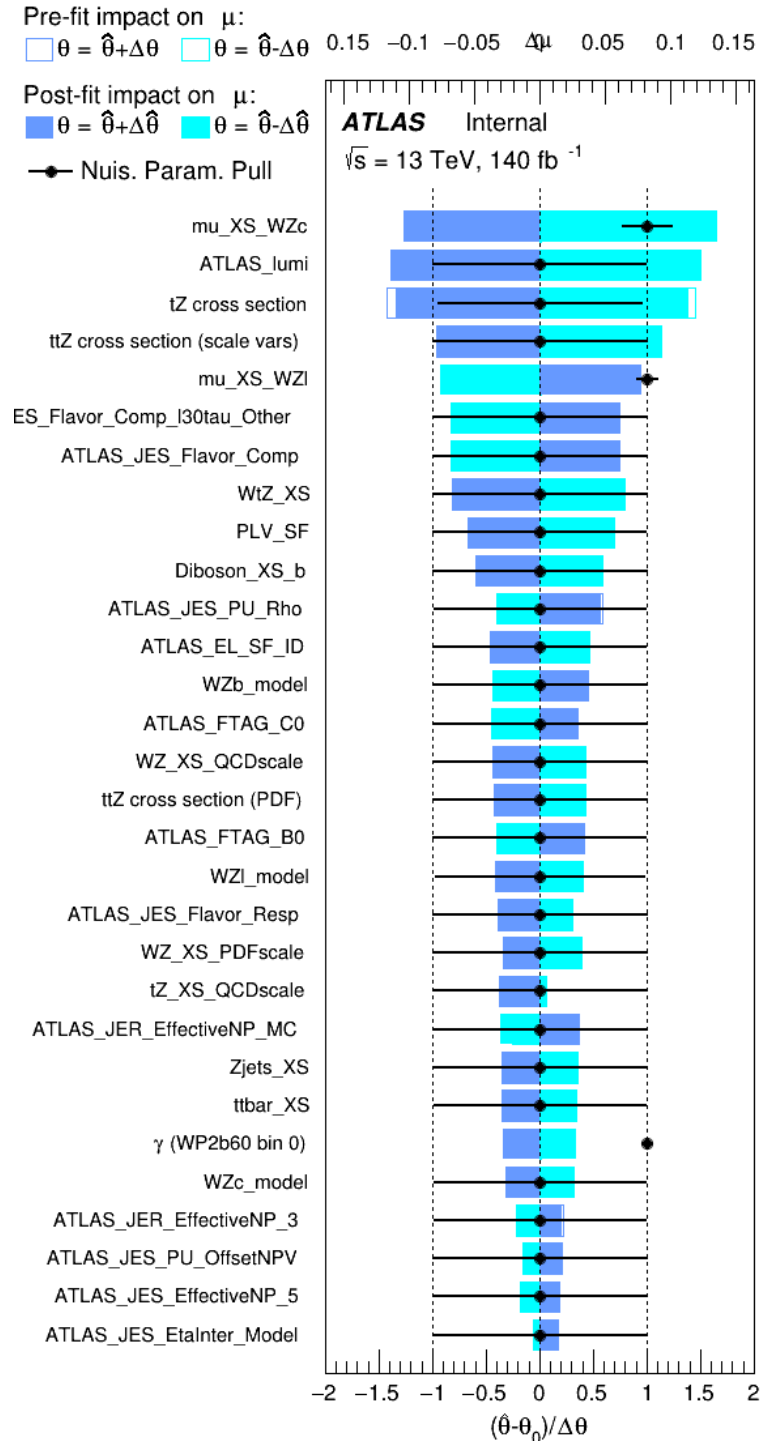


Figure 15.8: Impact of systematic uncertainties on the signal-strength of $WZ + b$ in 2-jet events.

1151 The large impact of the Jet Energy Scale and Jet Flavor Tagging is unsurprising, as the
 1152 shape of the fit regions depends heavily on the modeling of the jets. The other major sources
 1153 of uncertainty come from background modelling and cross-section uncertainty. The pie charts
 1154 in Figure 15.9 show that for the modelling uncertainties that contribute most correspond to the
 1155 most significant backgrounds.

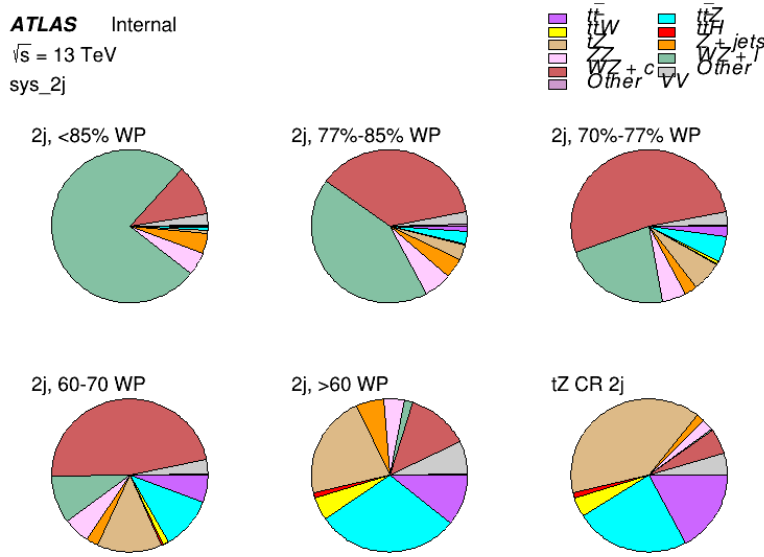


Figure 15.9: Post-fit background composition of the 2-jet fit regions.

1156 The correlations between these nuisance parameters are summarized in Figure 15.10.



Figure 15.10: Correlations between nuisance parameters in the 2-jet fit

As in the 1-jet case, no significant, unexpected correlations are found between nuisance parameters.

Part V**1160 Differential Studies of $t\bar{t}H$ Multilepton****1161 16 Data and Monte Carlo Samples**

1162 For both data and Monte Carlo (MC) simulations, samples were prepared in the `xAOD` format,
1163 which was used to produce a `xAOD` based on the `HIGG8D1` derivation framework. This framework
1164 was designed for the main $t\bar{t}H$ multi-lepton analysis. Because this analysis targets events with
1165 multiple light leptons, as well as tau hadrons, this framework skims the dataset of any events that
1166 do not meet at least one of the following requirements:

- 1167 • at least two light leptons within a range $|\eta| < 2.6$, with leading lepton $p_T > 15$ GeV and
1168 subleading lepton $p_T > 5$ GeV
- 1169 • at least one light lepton with $p_T > 15$ GeV within a range $|\eta| < 2.6$, and at least two hadronic
1170 taus with $p_T > 15$ GeV.

1171 Samples were then generated from these `HIGG8D1` derivations using `AnalysisBase` version
1172 21.2.127. A ptag of `p4133` was used for MC samples, and `p4134` for data.

1173 16.1 Data Samples

1174 The study uses proton-proton collision data collected by the ATLAS detector from 2015 through
1175 2018, which represents an integrated luminosity of 139 fb^{-1} and an energy of $\sqrt{s} = 13 \text{ TeV}$. All
1176 data used in this analysis was included in one of the following Good Run Lists:

- 1177 • data15_13TeV.periodAllYear_DetStatus-v79-repro20-02_DQDefects-00-02-02
1178 _PHYS_StandardGRL_All_Good_25ns.xml

- 1179 • data16_13TeV.periodAllYear_DetStatus-v88-pro20-21_DQDefects-00-02-04
1180 _PHYS_StandardGRL_All_Good_25ns.xml

- 1181 • data17_13TeV.periodAllYear_DetStatus-v97-pro21-13_Unknown_PHYS_StandardGRL
1182 _All_Good_25ns_Triggerno17e33prim.xml

- 1183 • data18_13TeV.periodAllYear_DetStatus-v102-pro22-04_Unknown_PHYS_StandardGRL
1184 _All_Good_25ns_Triggerno17e33prim.xml

1185 16.2 Monte Carlo Samples

1186 Several Monte Carlo (MC) generators were used to simulate both signal and background pro-
1187 cesses. For all of these, the effects of the ATLAS detector are simulated in Geant4. The specific
1188 event generator used for each of these MC samples is listed in Table 26.

Table 26: The configurations used for event generation of signal and background processes, including the event generator, matrix element (ME) order, parton shower algorithm, and parton distribution function (PDF).

| Process | Event generator | ME order | Parton Shower | PDF |
|---------------------------------|---------------------------|----------------------|------------------------|-----------------------------------|
| t̄H | MG5_AMC (MG5_AMC) | NLO (NLO) | PYTHIA 8 (HERWIG++) | NNPDF 3.0 NLO [14] (CT10 [15]) |
| t̄W | MG5_AMC (SHERPA 2.1.1) | NLO (LO multileg) | PYTHIA 8 (SHERPA) | NNPDF 3.0 NLO (NNPDF 3.0 NLO) |
| t̄(Z/γ* → ll) | MG5_AMC | NLO | PYTHIA 8 | NNPDF 3.0 NLO |
| VV | SHERPA 2.2.2 | MEPS NLO | SHERPA | CT10 |
| t̄t | POWHEG-BOX v2 [16] | NLO | PYTHIA 8 | NNPDF 3.0 NLO |
| t̄tγ | MG5_AMC | LO | PYTHIA 8 | NNPDF 2.3 LO |
| tZ | MG5_AMC | LO | PYTHIA 6 | CTEQ6L1 |
| tHqb | MG5_AMC | LO | PYTHIA 8 | CT10 |
| tHW | MG5_AMC (SHERPA 2.1.1) | NLO (LO multileg) | HERWIG++ (SHERPA) | CT10 (NNPDF 3.0 NLO) |
| tWZ | MG5_AMC | NLO | PYTHIA 8 | NNPDF 2.3 LO |
| t̄t̄t, t̄tt̄t̄t̄ | MG5_AMC | LO | PYTHIA 8 | NNPDF 2.3 LO |
| t̄tW+W- | MG5_AMC | LO | PYTHIA 8 | NNPDF 2.3 LO |
| s-, t-channel, Wt single top | POWHEG-BOX v1 [17] | NLO | PYTHIA 6 | CT10 |
| qqVV, VVV | | | | |
| Z → l+l- | SHERPA 2.2.1 | MEPS NLO | SHERPA | NNPDF 3.0 NLO |

1189 While the main t̄H analysis uses a more sophisticated data-driven approach to estimating
 1190 the contribution of events with non-prompt leptons (or "fakes"), at the time of this note this
 1191 strategy has not been completely developed for the full Run-2 dataset. Therefore, the non-
 1192 prompt contribution is estimated with MC, while applying conservative systematic uncertainties
 1193 to these processes, as described in Section 21.

1194 The specific DSIDs used in the analysis are listed below:

| Sample | DSID |
|-------------------|--|
| tH | 345873-5, 346343-5 |
| VV | 364250-364254, 364255, 363355-60, 364890 |
| tW | 410155 |
| tZ | 410156, 410157, 410218-20 |
| low mass tZ | 410276-8 |
| Rare Top | 410397, 410398, 410399 |
| single Top | 410658-9, 410644-5 |
| three Top | 304014 |
| four Top | 410080 |
| tWW | 410081 |
| Z + jets | 364100-41 |
| low mass Z + jets | 364198-215 |
| W + jets | 364156-97 |
| V γ | 364500-35 |
| tZ | 410560 |
| tW | 410013-4 |
| WtZ | 410408 |
| VVV | 364242-9 |
| VH | 342284-5 |
| WtH | 341998 |
| t $\bar{\gamma}$ | 410389 |
| t \bar{t} | 410470 |

Table 27: List of Monte Carlo samples by data set ID used in the analysis.

¹¹⁹⁵ 17 Object Reconstruction

¹¹⁹⁶ All analysis channels considered in this note share a common object selection for leptons and

¹¹⁹⁷ jets, as well as a shared trigger selection.

1198 **17.1 Trigger Requirements**

1199 Events are required to be selected by dilepton triggers, as summarized in Table 28.

| Dilepton triggers (2015) | |
|-------------------------------|----------------------------|
| $\mu\mu$ (asymm.) | HLT_mu18_mu8noL1 |
| ee (symm.) | HLT_2e12_lhloose_L12EM10VH |
| $e\mu, \mu e$ (\sim symm.) | HLT_e17_lhloose_mu14 |
| Dilepton triggers (2016) | |
| $\mu\mu$ (asymm.) | HLT_mu22_mu8noL1 |
| ee (symm.) | HLT_2e17_lhvloose_nod0 |
| $e\mu, \mu e$ (\sim symm.) | HLT_e17_lhloose_nod0_mu14 |
| Dilepton triggers (2017) | |
| $\mu\mu$ (asymm.) | HLT_mu22_mu8noL1 |
| ee (symm.) | HLT_2e24_lhvloose_nod0 |
| $e\mu, \mu e$ (\sim symm.) | HLT_e17_lhloose_nod0_mu14 |
| Dilepton triggers (2018) | |
| $\mu\mu$ (asymm.) | HLT_mu22_mu8noL1 |
| ee (symm.) | HLT_2e24_lhvloose_nod0 |
| $e\mu, \mu e$ (\sim symm.) | HLT_e17_lhloose_nod0_mu14 |

Table 28: List of lowest p_T -threshold, un-prescaled dilepton triggers used for 2015-2018 data taking.

1200 **17.2 Light Leptons**

1201 Electron candidates are reconstructed from energy clusters in the electromagnetic calorimeter
1202 that are associated with charged particle tracks reconstructed in the inner detector [18]. Electron
1203 candidates are required to have $p_T > 10$ GeV and $|\eta_{\text{cluster}}| < 2.47$. Candidates in the transition
1204 region between different electromagnetic calorimeter components, $1.37 < |\eta_{\text{cluster}}| < 1.52$, are
1205 rejected. A multivariate likelihood discriminant combining shower shape and track information

1206 is used to distinguish prompt electrons from nonprompt leptons, such as those originating from
1207 hadronic showers.

1208 To further reduce the non-prompt contribution, the track of each electron is required to
1209 originate from the primary vertex; requirements are imposed on the transverse impact parameter
1210 significance ($|d_0|/\sigma_{d_0}$) and the longitudinal impact parameter ($|\Delta z_0 \sin \theta_\ell|$).

1211 Muon candidates are reconstructed by combining inner detector tracks with track segments
1212 or full tracks in the muon spectrometer [19]. Muon candidates are required to have $p_T > 10$ GeV
1213 and $|\eta| < 2.5$. All leptons are required to be isolated, and pass a non-prompt BDT selection
1214 described in detail in [5].

1215 **17.3 Jets**

1216 Jets are reconstructed from calibrated topological clusters built from energy deposits in the
1217 calorimeters [21], using the anti- k_t algorithm with a radius parameter $R = 0.4$. Jets with energy
1218 contributions likely arising from noise or detector effects are removed from consideration [22],
1219 and only jets satisfying $p_T > 25$ GeV and $|\eta| < 2.5$ are used in this analysis. For jets with
1220 $p_T < 60$ GeV and $|\eta| < 2.4$, a jet-track association algorithm is used to confirm that the jet
1221 originates from the selected primary vertex, in order to reject jets arising from pileup collisions
1222 [23].

1223 17.4 Missing Transverse Energy

1224 Because all $t\bar{t}H - ML$ channels considered include multiple neutrinos, missing transverse
1225 energy (E_T^{miss}) is present in each event. The missing transverse momentum vector is defined as
1226 the inverse of the sum of the transverse momenta of all reconstructed physics objects as well
1227 as remaining unclustered energy, the latter of which is estimated from low- p_T tracks associated
1228 with the primary vertex but not assigned to a hard object [24].

1229 17.5 Overlap removal

1230 To avoid double counting objects and remove leptons originating from decays of hadrons, overlap
1231 removal is performed in the following order: any electron candidate within $\Delta R = 0.1$ of another
1232 electron candidate with higher p_T is removed; any electron candidate within $\Delta R = 0.1$ of a muon
1233 candidate is removed; any jet within $\Delta R = 0.3$ of an electron candidate is removed; if a muon
1234 candidate and a jet lie within $\Delta R = \min(0.4, 0.04 + 10[\text{GeV}] / p_T(\text{muon}))$ of each other, the jet
1235 is kept and the muon is removed.

1236 This algorithm is applied to the preselected objects. The overlap removal procedure is
1237 summarized in Table 29.

| Keep | Remove | Cone size (ΔR) |
|-------------|-----------------------|---|
| electron | electron (low p_T) | 0.1 |
| muon | electron | 0.1 |
| electron | jet | 0.3 |
| jet | muon | $\min(0.4, 0.04 + 10[\text{GeV}]/p_T(\text{muon}))$ |
| electron | tau | 0.2 |

Table 29: Summary of the overlap removal procedure between electrons, muons, and jets.

1238 18 Higgs Momentum Reconstruction

1239 Reconstructing the momentum of the Higgs boson is a particular challenge for channels with
 1240 leptons in the final state: Because all channels include at least two neutrinos in the final state, the
 1241 Higgs can never be fully reconstructed. However, the momentum spectrum can be well predicted
 1242 by a neural network when provided with the four-vectors of the Higgs Boson decay products, as
 1243 shown in Section 18.1. With this in mind, several layers of MVAs are used to reconstruction the
 1244 Higgs momentum.

1245 The first layer is a model designed to select which jets are most likely to be the b-jets that
 1246 came from the top decay, detailed in Section 18.2. As described in Section 18.3, the kinematics
 1247 of these jets are fed into the second layer, which is designed to identify the decay products of
 1248 the Higgs Boson itself. The kinematics of these particles are then fed into yet another neural-
 1249 network, which predicts the momentum of the Higgs (18.4). MVAs are also used in the analysis
 1250 to determine the decay of the Higgs boson in the 3l channel (18.5).

1251 Models are trained on Monte Carlo simulations of $t\bar{t}H$ events generated using MG5_AMC.
 1252 Specifically, events DSIDs 346343-5, 345873-5, and 345672-4 are used for training.

1253 For all of these models, the Keras neural network framework, with Tensorflow as the
1254 backend, is used, and the number of hidden layers and nodes are determined using grid search
1255 optimization. Each neural network uses the LeakyReLU activation function, a learning rate
1256 of 0.01, and the Adam optimization algorithm, as alternatives are found to either decrease or
1257 have no impact on performance. Batch normalization is applied after each layer. For the
1258 classification algorithms (b-jet matching, Higgs reconstruction, and 3l decay identification)
1259 binary-cross entropy is used as the loss function, while the p_T reconstruction algorithm uses
1260 MSE.

1261 The specific inputs features used for each model are arrived at through a process of trial
1262 and error - features considered potentially useful are tried, and those that are found to increase
1263 performance are included. While each model includes a relatively large number of features,
1264 some using upwards of 30, this inclusive approach is found to maximize the performance of each
1265 model while decreasing the variance compared to a reduced number of inputs. Each input feature
1266 is validated by comparing MC simulations to 80 fb^{-1} of data, as shown in the sections below.

1267 **18.1 Decay Candidate Reconstruction**

1268 Machine Learning algorithms are trained to identify the decay products of the Higgs Boson
1269 using MC simulations of $t\bar{t}H$ events. These include light leptons and jets. Reconstructed
1270 physics objects are matched to truth level particles, in order to identify the parents of these

1271 reconstructed objects. The kinematics of the decay product candidates as well as event level
1272 variables are used as inputs.

1273 Leptons considered as possible Higgs and top decay candidates are required to pass the
1274 selection described in Section 17.2. For jets, however, it is found that a large fraction that
1275 originate from either the top decay or the Higgs decay fall outside the selection described in
1276 Section 17.3. Specifically, jets from the Higgs decay tend to be soft, with 32% having $p_T <$
1277 25 GeV. Therefore jets with $p_T < 15$ GeV are considered as possible candidates in the models
1278 described below. By contrast, less than 5% of the jets originating from the Higgs fall below
1279 this p_T . The jets are found to be well modeled even down to this low p_T threshold, as shown in
1280 Section 20.1. The impact of using different p_T selection for the jet candidates is considered in
1281 detail in Section A.5. As they are expected to originate from the primary vertex, jets are also
1282 required to pass a JVT cut.

1283 18.2 b-jet Identification

1284 Including the kinematics of the b-jets that originate from the top decay is found to improve the
1285 identification of the Higgs decay products, and improve the accuracy with which the Higgs
1286 momentum can be reconstructed. Because these b-jets are reconstructed by the detector with
1287 high efficiency (just over 90% of the time), and can be identified relatively consistently, the first
1288 step in reconstructing the Higgs is selecting the b-jets from the top decay.

1289 Exactly two b-jets are expected in the final state of $t\bar{t}H - ML$ events. However, in both
 1290 the 3l and 2lSS channels, only one or more b-tagged jets are required (where the 70% DL1r b-tag
 1291 working point is used). Therefore, for events which have exactly one, or more than two, b-tagged
 1292 jets, deciding which combination of jets correspond to the top decay is non-trivial. Further,
 1293 events with 1 b-tagged jet represent just over half of all $t\bar{t}H - ML$ events. Of those, both b-jets
 1294 are reconstructed by the detector 75% of the time. Therefore, rather than adjusting the selection
 1295 to require exactly 2 b-tagged jets, and losing more than half of the signal events, a neural network
 1296 is used to predict which pair of jets is most likely to correspond to truth b-jets.

1297 Once the network is trained, all possible pairings of jets are fed into the model, and the pair
 1298 of jets with the highest output score are taken to be b-jets in successive steps of the analysis.

1299 18.2.1 2lSS Channel

1300 For the 2lSS channel, the input features shown in Table 30 are used for training. Here j_0 and j_1
 1301 are the two jet candidates, while l_0 and l_1 are the two leptons in the event, both ordered by p_T . jet
 1302 DL1r is an integer corresponding to the calibrated b-tagging working points reached by each jet,
 1303 where 5 represents the tightest working point and 1 represents the loosest. The variables nJets
 1304 DL1r 60% and nJets DL1r 85% represent the number of jets in the event passing the 60% and
 1305 85% b-tag working points, respectively.

| | | |
|--------------------------------------|--|--|
| jet p_T 0 | jet p_T 1 | Lepton p_T 0 |
| Lepton p_T 1 | jet η 0 | jet η 1 |
| $\Delta R(j_0)(j_1)$ | $M(j_0 j_1)$ | $\Delta R(l_0)(j_0)$ |
| $\Delta R(l_0)(j_1)$ | $\Delta R(l_1)(j_0)$ | $\Delta R(l_1)(j_1)$ |
| $M(l_0 j_0)$ | $M(l_0 j_1)$ | $M(l_1 j_0)$ |
| $M(l_1 j_1)$ | jet DL1r 0 | jet DL1r 1 |
| nJets OR DL1r 85 | nJets OR DL1r 60 | $\Delta R(j_0 l_0)(j_1 l_1)$ |
| $\Delta R(j_0 l_1)(j_1 l_0)$ | $p_T(j_0 j_1 l_0 l_1 E_T^{\text{miss}})$ | $M(j_0 j_1 l_0 l_1 E_T^{\text{miss}})$ |
| $\Delta\phi(j_0)(E_T^{\text{miss}})$ | $\Delta\phi(j_1)(E_T^{\text{miss}})$ | HT jets |
| nJets | E_T^{miss} | |

Table 30: Input features used in the b-jet identification algorithm for the 2lSS channel

1306 As there are far more incorrect combinations than correct ones, by a factor of more than
 1307 20:1, the training set is resampled to reduce the fraction of incorrect combinations. A random
 1308 sample of 5 million incorrect entries are used for training, along with close 1 million correct
 1309 entries. 10% of the dataset is set aside for testing, leaving around 5 million datapoints for
 1310 training.

1311 The difference between the distributions for a few of these features for the correct(i.e.
 1312 both jets are truth b-jets), and incorrectcombinations are shown in Figure 18.1. The correct and
 1313 incorrect contributions are scaled to the same integral, so as to better demonstrate the differences
 1314 in the distributions.

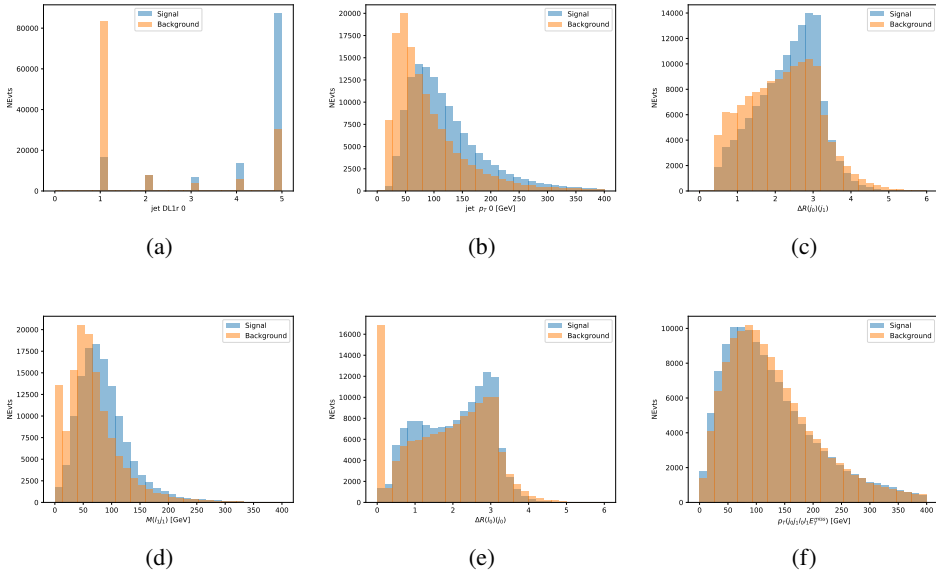


Figure 18.1: Input features for top2lSS training. The signal in blue represents events where both jet candidates are truth b-jets from top decays, and the orange is all other combinations. Each are scaled to the same number of events. (a) shows the DL1r working point of leading jet, (b) shows the p_T of the leading jet, (c) shows the ΔR of the two jets, (d) the invariant mass of lepton 1 and jet 1, (e) the ΔR of lepton 0 and jet 0, and (f) the p_T of both jets, both leptons, and the E_T^{miss} .

1315 The modeling of these inputs is validated against data, with Figure 18.2 showing good
 1316 general agreement between data and MC. Plots for the complete list of features can found in
 1317 Section A.

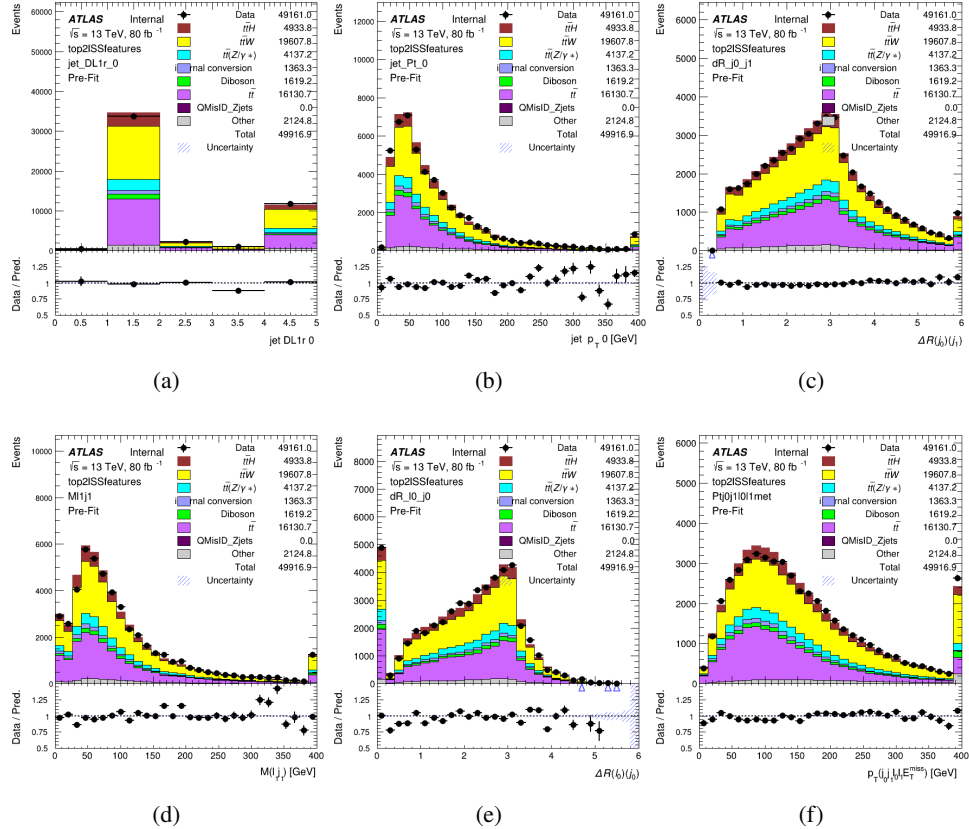


Figure 18.2: Data/MC comparisons of input features for top2ISS training for 80 fb^{-1} of data. (a) shows the DL1r working point of leading jet, (b) shows the p_T of the leading jet, (c) shows the ΔR of the two jets, (d) the invariant mass of lepton 1 and jet 1, (e) the ΔR of lepton 0 and jet 0, and (f) the p_T of both jets, both leptons, and the E_T^{miss} .

1318

Based on the results of grid search evaluation, the optimal architecture is found to include

1319

5 hidden layers with 40 nodes each. No regularizer or dropout is added to the network, as

1320

overfitting is found to not be an issue. The output score distribution as well as the ROC curve for

1321

the trained model are shown in Figure 18.2.1. The model is found to identify the correct pairing

1322

of jets for 73% of 2lSS signal events on test data.

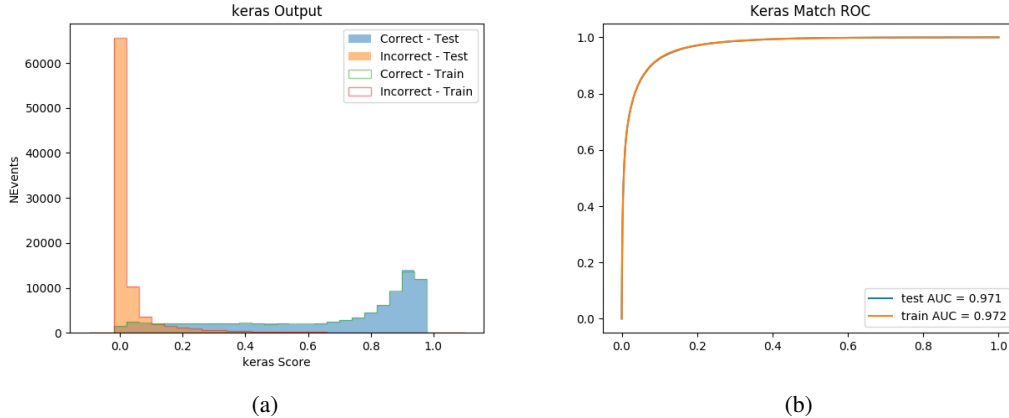


Figure 18.3: Results of the b-jet identification algorithm for the 2lSS channel, showing (a) the output score of the NN for correct and incorrect combinations of jets. (b) the ROC curve of the output, showing background rejection as a function of signal efficiency

1323 For point of comparison, a naïve approach to identify b-jets is used as well: The two jets
 1324 which pass the highest DL1r b-tag working point are assumed to be the b-jets from the top decay.
 1325 In the case that multiple jets meet the same b-tag working point, the jet with higher p_T is used.
 1326 This method identifies the correct jet pair 65% of the time.

1327 The accuracy of the model for different values of n-bjets, compared to this naive approach,
 1328 is shown in Table 31.

| b-jet Selection | Neural Network | Naive |
|-----------------|----------------|-------|
| 1 b-jet | 58.6% | 42.1% |
| 2 b-jets | 88.4% | 87.1% |
| ≥ 3 b-jets | 61.7% | 53.3% |
| Overall | 73.9% | 67.2% |

Table 31: Accuracy of the NN in identifying b-jets from tops in 2lSS events for, compared to the accuracy of taking the two highest b-tagged jets.

¹³²⁹ **18.2.2 3l Channel**

¹³³⁰ The input features used in the 3l channel are listed in Table 32, with the same naming convention
¹³³¹ as the 2lSS channel.

| jet p_T 0 | jet p_T 1 | jet η 0 |
|--|--|--------------------------------------|
| jet η 1 | Lepton p_T 0 | Lepton p_T 1 |
| Lepton p_T 2 | $\Delta R(j_0)(j_1)$ | $M(j_0 j_1)$ |
| $\Delta R(l_0)(j_0)$ | $\Delta R(l_1)(j_0)$ | $\Delta R(l_2)(j_0)$ |
| $\Delta R(l_0)(j_1)$ | $\Delta R(l_1)(j_1)$ | $\Delta R(l_2)(j_1)$ |
| $M(l_0 j_0)$ | $M(l_1 j_0)$ | $M(l_2 j_0)$ |
| $M(l_0 j_1)$ | $M(l_1 j_1)$ | $M(l_2 j_1)$ |
| $\Delta R(j_0 l_0)(j_1 l_1)$ | $\Delta R(j_0 l_0)(j_1 l_2)$ | $\Delta R(j_0 l_1)(j_1 l_0)$ |
| $\Delta R(j_0 l_2)(j_1 l_0)$ | jet DL1r 0 | jet DL1r 1 |
| $p_T(j_0 j_1 l_0 l_1 l_2 E_T^{\text{miss}})$ | $M(t j_0 j_1 l_0 l_1 l_2 E_T^{\text{miss}})$ | $\Delta\phi(j_0)(E_T^{\text{miss}})$ |
| $\Delta\phi(j_1)(E_T^{\text{miss}})$ | HT Lepton | HT jets |
| nJets | E_T^{miss} | nJets OR DL1r 85 |
| nJets OR DL1r 60 | | |

Table 32: Input features for the b-jet identification algorithm in the 3l channel.

¹³³² A few of these features are shown in Figure 18.4, comparing the distributions for correct
¹³³³ and incorrect combinations of jets.

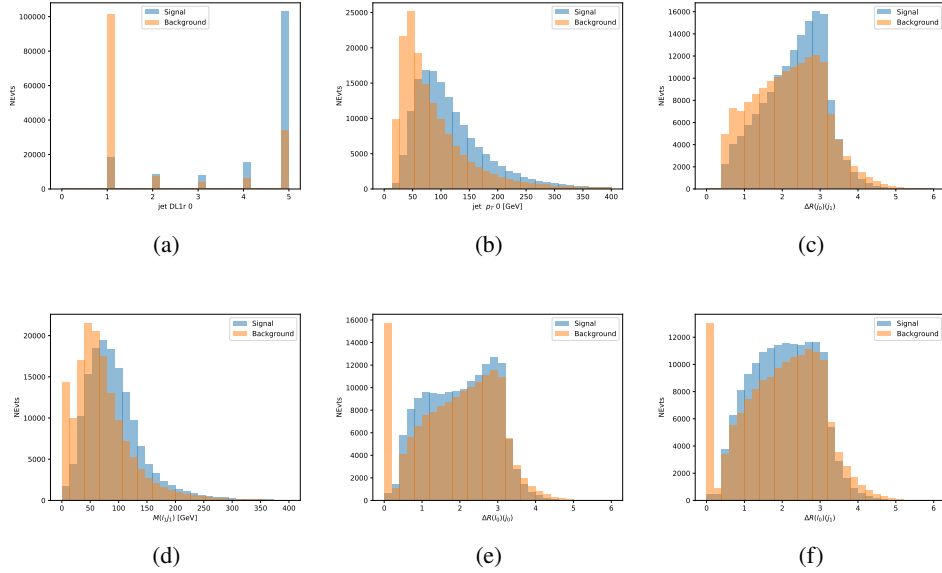


Figure 18.4: Input features for top3l training. The signal in blue represents events where both jet candidates are truth b-jets from top decays, and the orange is all other combinations. Scaled to the same number of events. (a) show the DL1r WP of jet 0, (b) the p_T of jet 0, (c) ΔR between jet 0 and jet 1, (d) the invariant mass of lepton 1 and jet 1, (e) ΔR between lepton 0 and jet 0, and (f) ΔR between lepton 0 and jet 1

1334

The modeling of these inputs is validated against data, with Figure 18.5 showing good

1335

general agreement between data and MC. Plots for the complete list of features can found in

1336

[Section A](#).

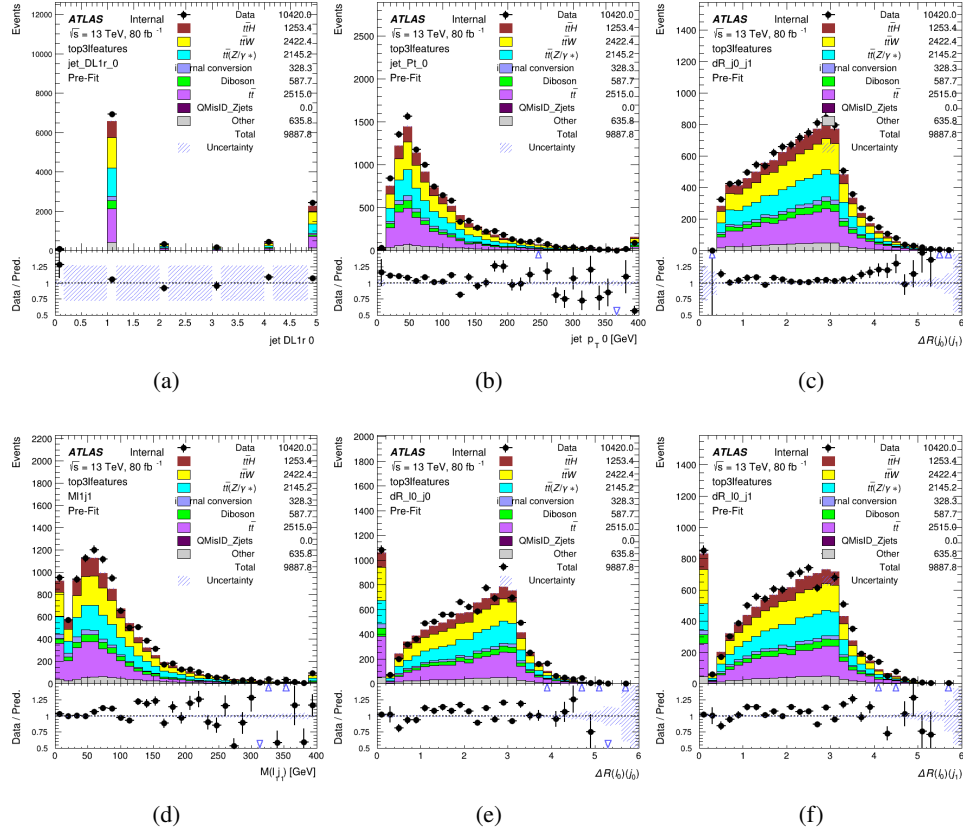


Figure 18.5: Data/MC comparisons of input features for top3l training for 80 fb^{-1} of data. (a) show the DL1r WP of jet 0, (b) the p_T of jet 0, (c) ΔR between jet 0 and jet 1, (d) the invariant mass of lepton 1 and jet 1, (e) ΔR between lepton 0 and jet 0, and (f) ΔR between lepton 0 and jet 1

Again, the dataset is downsized to reduce the ratio of correct and incorrect combination from 20:1, to 5:1. Around 7 million events are used for training, with 10% set aside for testing. Based on the results of grid search evaluation, the optimal architecture is found to include 5 hidden layers with 60 nodes each. The output score distribution as well as the ROC curve for the trained model are shown in Figure 18.2.2.

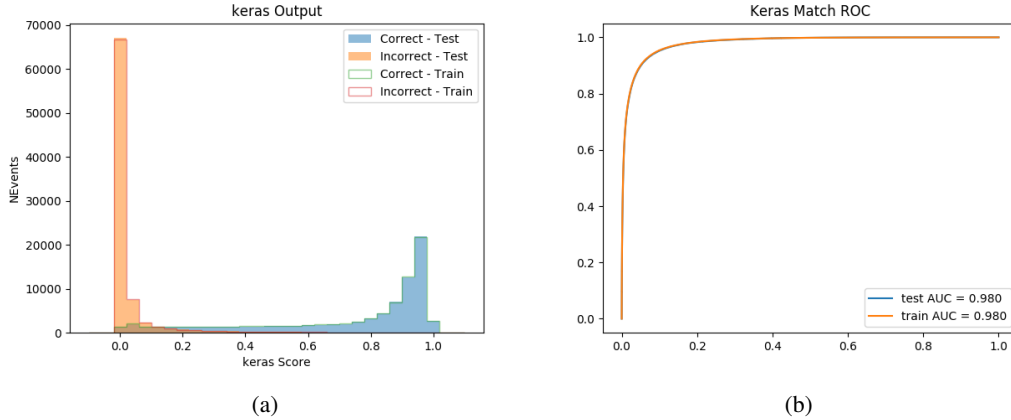


Figure 18.6: Results of the b-jet identification algorithm for the 3l channel, showing (a) the output score of the NN for correct and incorrect combinations of jets. (b) the ROC curve of the output, showing background rejection as a function of signal efficiency

1342 This procedure is found to identify the correct pairing of jets for nearly 80% of 3l signal
 1343 events. The accuracy of the model is summarized in Table 33.

Table 33: Accuracy of the NN in identifying b-jets from tops, compared to the naive method of taking the highest b-tagged jets.

| | NN | Naive |
|-----------------|-------|-------|
| 1 b-jet | 69.0% | 48.9% |
| 2 b-jets | 89.6% | 88.3% |
| ≥ 3 b-jets | 55.7% | 52.3% |
| Overall | 79.8% | 70.2% |

1344 18.3 Higgs Reconstruction

1345 Techniques similar to the b-jet identification algorithms are employed to select the decay products
 1346 of the Higgs: kinematics of all possible combinations of reconstructed objects are fed into a neural
 1347 network to determine which of those is most likely to be the decay products of the Higgs.

1348 Again separate models are used for the 2lSS and 3l channels, while the 3l channel has now
1349 been split into two: $t\bar{t}H$ events with three leptons in the final state include both instances where
1350 the Higgs decays into a lepton (and a neutrino) and a pair of jets, and instances where the Higgs
1351 decays to two leptons.

1352 3l events are therefore categorized as either semi-leptonic (3lS) or fully-leptonic (3lF). In
1353 the semi-leptonic case the reconstructed decay products consist of two jets and a single lepton.
1354 For the fully-leptonic case, the decay products include 2 of the three leptons associated with the
1355 event. For training the models, events are separated into these two categories using truth level
1356 information. A separate MVA, described in Section 18.5, is used to make this distinction at reco
1357 level and determine which model to use.

1358 For all channels, the models described in Section 18.2 are used to identify b-jet candidates,
1359 whose kinematics are used to identify the Higgs decay products. These jets are not considered
1360 as possible candidates for the Higgs decay, justified by the fact that these models are found to
1361 misidentify jets from the Higgs decay as jets from the top decay less than 1% of the time.

1362 18.3.1 2lSS Channel

1363 For the 2lSS channel, the Higgs decay products include one light lepton and two jets. The neural
1364 network is trained on the kinematics of different combinations of leptons and jets, as well as the
1365 b-jets identified in Section 18.2, with the specific input features listed in Table 34.

| Lepton p_T H | Lepton p_T T | jet p_T 0 |
|--|--------------------------|--------------------------|
| jet p_T 1 | top p_T 0 | top p_T 1 |
| top η 0 | top η 1 | jet η 0 |
| jet η 1 | jet Phi 0 | jet Phi 1 |
| Lepton η H | Lepton heta T | $\Delta R(j_0)(j_1)$ |
| $\Delta R(l_H)(j_0)$ | $\Delta R(l_H)(j_1)$ | $M(j_0 j_1)$ |
| $M(l_H j_0)$ | $M(l_H j_1)$ | $\Delta R(l_H)(b_0)$ |
| $\Delta R(l_H)(b_1)$ | $\Delta R(l_T)(b_0)$ | $\Delta R(l_T)(b_1)$ |
| $\Delta R(j_0 j_1)(l_H)$ | $\Delta R(j_0 j_1)(l_T)$ | $\Delta R(j_0 j_1)(b_0)$ |
| $\Delta R(j_0 j_1)(b_1)$ | $\Delta R(j_0)(b_0)$ | $\Delta R(j_0)(b_1)$ |
| $\Delta R(j_1)(b_0)$ | $\Delta R(j_1)(b_1)$ | $M(j_0 j_1 l_H)$ |
| $p_T(j_0 j_1 l_H l_T b_0 b_1 E_T^{\text{miss}})$ | topScore | E_T^{miss} |
| nJets | HT jets | |

Table 34: Input features used to identify the Higgs decay products in 2ISS events

1366 Here j_0 and j_1 , and l_H are the jet and lepton decay candidates, respectively. The other
 1367 lepton in the event is labeled l_T , as it is assumed to have come from the decay of one of the top
 1368 quarks. b_0 and b_1 are the two b-jets identified by the b-jet identification algorithm. The b-jet
 1369 Reco Score is the output of the b-jet reconstruction algorithm.

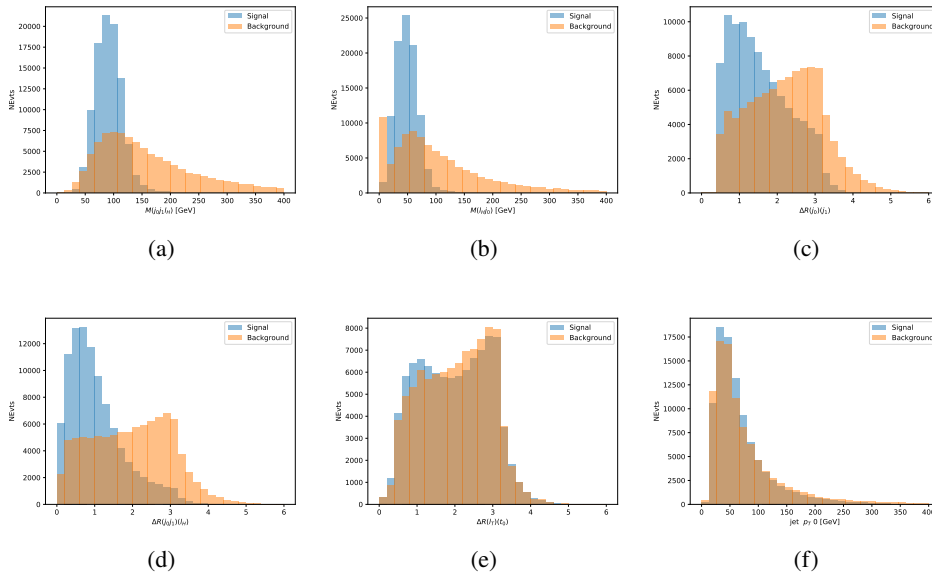


Figure 18.7: Input features for higgs2lSS training. The signal in blue represents events where both jet candidates are truth b-jets from top decays, and the orange is all other combinations. Scaled to the same number of events. (a) shows the invariant mass of the two jet candidates and the lepton candidate, (b) the invariant mass of jet 0 and the lepton candidate, (c) ΔR between the jet candidates, (d) ΔR between jet 0 + jet 1 and the lepton candidate, (e) ΔR between the lepton from the top and the leading b-jet, (f) the p_T of jet 0.

1370 The modeling of these inputs is validated against data, with Figure 18.2 showing good
 1371 general agreement between data and MC. Plots for the complete list of features can found in
 1372 Section A.

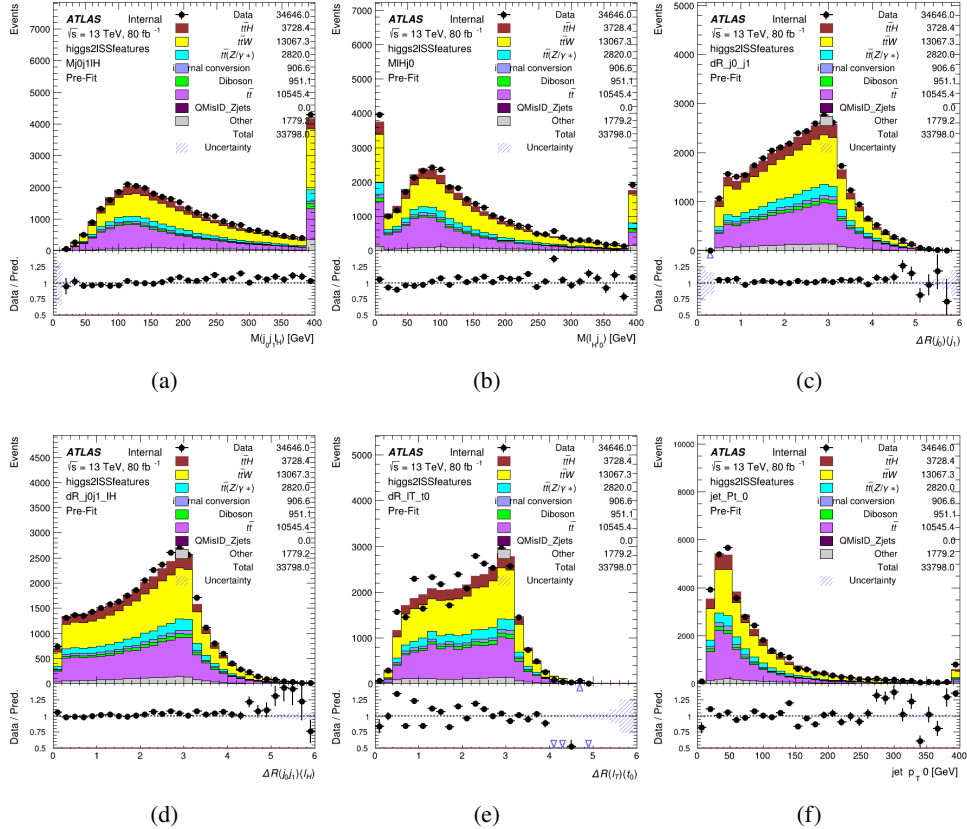


Figure 18.8: Data/MC comparisons of input features for higgs2lSS training for 80 fb^{-1} of data. (a) shows the invariant mass of the two jet candidates and the lepton candidate, (b) the invariant mass of jet 0 and the lepton candidate, (c) ΔR between the jet candidates, (d) ΔR between jet 0 + jet 1 and the lepton candidate, (e) ΔR between the lepton from the top and the leading b-jet, (f) the p_T of jet 0.

1373 A neural network consisting of 7 hidden layers with 60 nodes each is trained on around 2
 1374 million events, with an additional 200,000 reserved for testing the model. In order to compensate
 1375 for large number of incorrect combinations, these have been downsampled such that the correct
 1376 combinations represent over 10% of the training set. The output of the NN is summarized in
 1377 Figure 18.3.1.

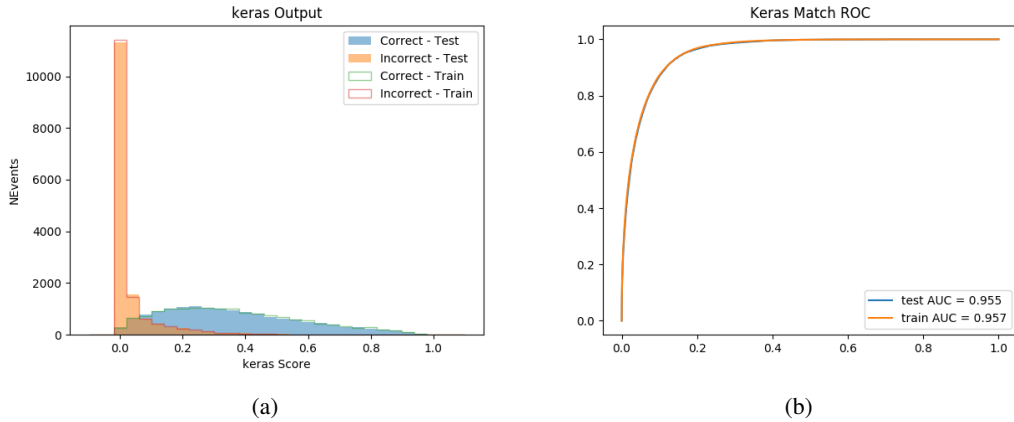


Figure 18.9: Result of the Higgs reconstruction algorithm in the 2lSS channel, showing (a) the output score of the NN for correct and incorrect combinations of jets scaled to an equal number of events, and (b) the ROC curve of the output, showing background rejection as a function of signal efficiency

1378 The neural network identifies the correct combination 55% of the time. It identifies the
 1379 correct lepton 85% of the time, and selects the correct lepton and at least one of the correct jets
 1380 81% of the time.

1381 18.3.2 3l Semi-leptonic Channel

1382 For 3l $t\bar{t}H$ where the Higgs decay semi-leptonically, the decay products include one of the three
 1383 leptons and two jets. In this case, the other two leptons originated from the decay of the tops,
 1384 meaning the opposite-sign (OS) lepton cannot have come from the Higgs. This leaves only the two
 1385 same-sign (SS) leptons as possible Higgs decay products.

| Lepton $p_T H$ | Lepton $p_T T_0$ | Lepton $p_T T_1$ |
|--|--|----------------------------------|
| jet $p_T 0$ | jet $p_T 1$ | top $p_T 0$ |
| top $p_T 1$ | jet $\eta 0$ | jet $\eta 1$ |
| jet $\phi 0$ | jet $\phi 1$ | $\Delta R(j_0)(j_1)$ |
| $M(j_0 j_1)$ | $\Delta R(l_H)(j_0)$ | $\Delta R(l_H)(j_1)$ |
| $\Delta R(j_0 j_1)(l_H)$ | $\Delta R(j_0 j_1)(l_{T_1})$ | $\Delta R(l_{T_0})(l_{T_1})$ |
| $\Delta R(l_H)(l_{T_1})$ | $M(j_0 j_1 l_{T_0})$ | $M(j_0 j_1 l_{T_1})$ |
| $M(j_0 j_1 l_H)$ | $\Delta R(j_0 j_1 l_H)(l_{T_0})$ | $\Delta R(j_0 j_1 l_H)(l_{T_1})$ |
| $\Delta\phi(j_0 j_1 l_H)(E_T^{\text{miss}})$ | $p_T(j_0 j_1 l_H l_{T_0} l_{T_1} b_0 b_1 E_T^{\text{miss}})$ | $M(j_0 j_1 b_0)$ |
| $M(j_0 j_1 b_1)$ | $\Delta R(l_{T_0})(b_0)$ | $\Delta R(l_{T_0})(b_1)$ |
| $\Delta R(l_{T_1})(b_0)$ | $\Delta R(l_{T_1})(b_1)$ | $\Delta R(j_0)(b_0)$ |
| $\Delta R(j_0)(b_1)$ | $\Delta R(j_1)(b_0)$ | $\Delta R(j_1)(b_1)$ |
| topScore | MET | HT jets |
| nJets | | |

Table 35: Input features used to identify the Higgs decay products in 3lS events

1386 Here j_0 and j_1 , and l_H are the jet and lepton decay candidates, respectively. The other
 1387 two leptons in the event are labeled as l_{T0} and l_{T1} . b_0 and b_1 are the two b-jets identified by
 1388 the b-jet identification algorithm. The b-jet Reco Score is the output of the Higgs reconstruction
 1389 algorithm.

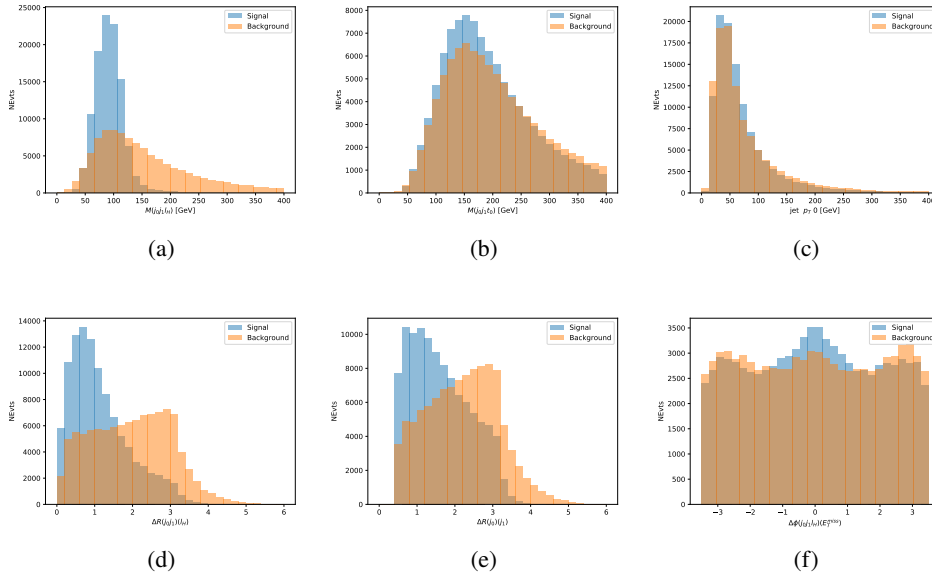


Figure 18.10: Input features for higgs3lS training. The signal in blue represents events where both jet candidates are truth b-jets from top decays, and the orange is all other combinations. Scaled to the same number of events.

1390 The modeling of these inputs is validated against data, with Figure 18.11 showing good
 1391 general agreement between data and MC. Plots for the complete list of features can found in
 1392 appendix A.1.

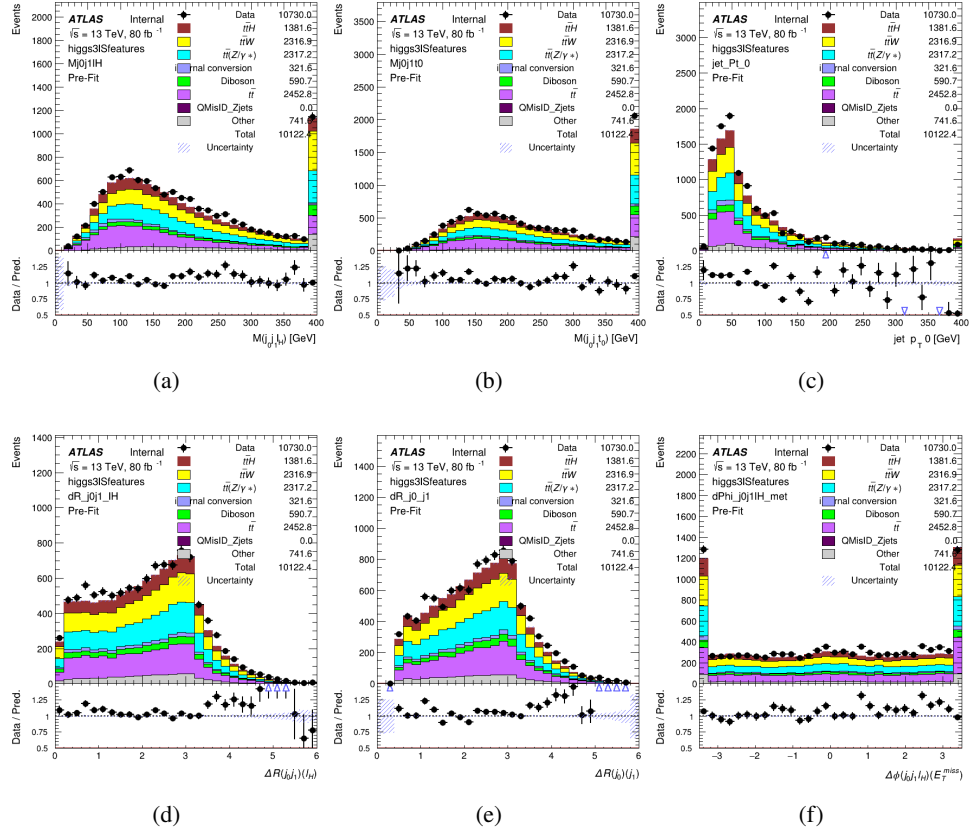


Figure 18.11: Data/MC comparisons of input features for higgs3IS training for 80 fb^{-1} of data.

1393 A neural network of 7 hidden layers with 70 nodes each is trained on 1.8 million events.

1394 Once again, incorrect combinations are downsampled, such that the correct combinations are
 1395 around 10% of the training set. 10% of the dataset is reserved for testing. The output of the NN
 1396 is summarized in Figure 18.3.2.

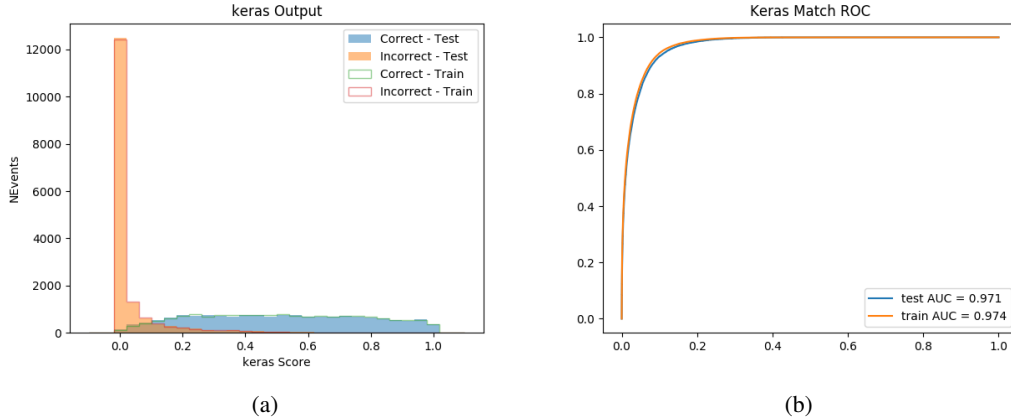


Figure 18.12: Results of the Higgs reconstruction algorithm in the 3lS channel, showing (a) the output score of the NN for correct and incorrect combinations of jets, scaled to an equal number of entries.,. (b) the ROC curve of the output, showing background rejection as a function of signal efficiency

1397 The neural network identifies the correct combination 64% of the time. It identifies the
 1398 correct lepton 85% of the time, and selects the correct lepton and at least one of the correct jets
 1399 83% of the time.

1400 18.3.3 3l Fully-leptonic Channel

1401 In the fully-leptonic 3l case, the goal is identify which two of the three leptons originated from
 1402 the Higgs decay. Since one of these two must be the OS lepton, this problem is reduced to
 1403 determining which of the two SS leptons originated from the Higgs. The kinematics of both
 1404 possibilities are used for training, one where the SS lepton from the Higgs is correctly labeled,
 1405 and one where it is not.

| Lepton $p_T H_1$ | Lepton $p_T H_0$ | Lepton $p_T T$ |
|--------------------------------------|---------------------------------|--|
| top $p_T 0$ | top $p_T 1$ | $\Delta\phi(l_{H_1})(E_T^{\text{miss}})$ |
| $\Delta\phi(l_T)(E_T^{\text{miss}})$ | $M(l_{H_0}l_{H_1})$ | $M(l_{H_1}l_T)$ |
| $M(l_{H_0}l_T)$ | $\Delta R(l_{H_0})(l_{H_1})$ | $\Delta R(l_{H_1})(l_T)$ |
| $\Delta R(l_{H_0})(l_T)$ | $\Delta R(l_{H_0}l_{H_1})(l_T)$ | $\Delta R(l_{H_0}l_T)(l_{H_1})$ |
| $\Delta R(l_{H_0}l_{H_1})(b_0)$ | $\Delta R(l_{H_0}l_{H_1})(b_1)$ | $\Delta R(l_{H_0}b_0)$ |
| $M(l_{H_0}b_0)$ | $\Delta R(l_{H_0}b_1)$ | $M(l_{H_0}b_1)$ |
| $\Delta R(l_{H_1}b_0)$ | $M(l_{H_1}b_0)$ | $\Delta R(l_{H_1}b_1)$ |
| $M(l_{H_1}b_1)$ | E_T^{miss} | topScore |

Table 36: Input features used to identify the Higgs decay products in 3lF events

1406 Here l_{H0} and l_{H1} are the Higgs decay candidates. The other lepton in the event is labeled
 1407 l_T . b_0 and b_1 are the two b-jets identified by the b-jet identification algorithm. The b-jet Reco
 1408 Score is the output of the Higgs reconstruction algorithm.

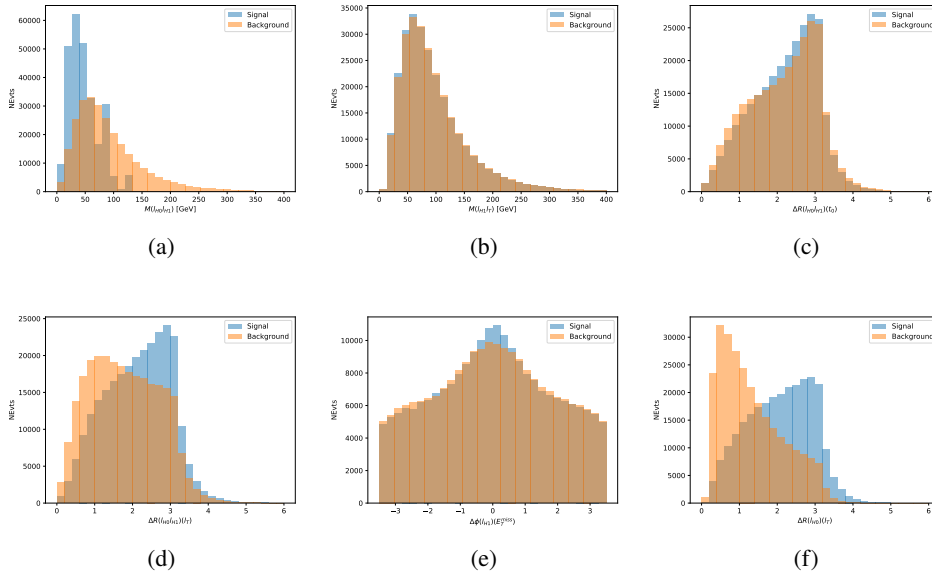


Figure 18.13: Input features for higgs3IF training. The signal in blue represents events where both jet candidates are truth b-jets from top decays, and the orange is all other combinations. Scaled to the same number of events.

1409 The modeling of these inputs is validated against data, with Figure 18.14 showing good
 1410 general agreement between data and MC. Plots for the complete list of features can found in
 1411 Section A.

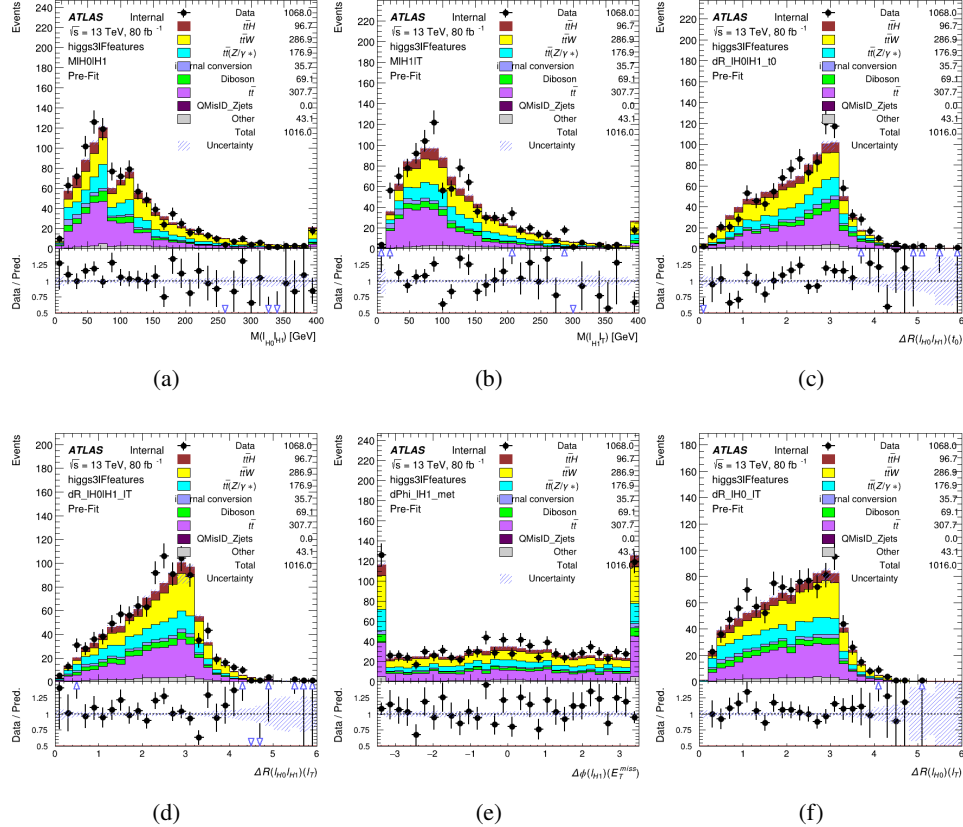


Figure 18.14: Data/MC comparisons of input features for higgs3IF training for 80 fb^{-1} of data.

1412 A neural network consisting of 5 nodes and 60 hidden units is trained on 800,000 events,
 1413 with 10% of the dataset reserved for testing. The output of the model is summarized in Figure
 1414 [18.3.3.](#)

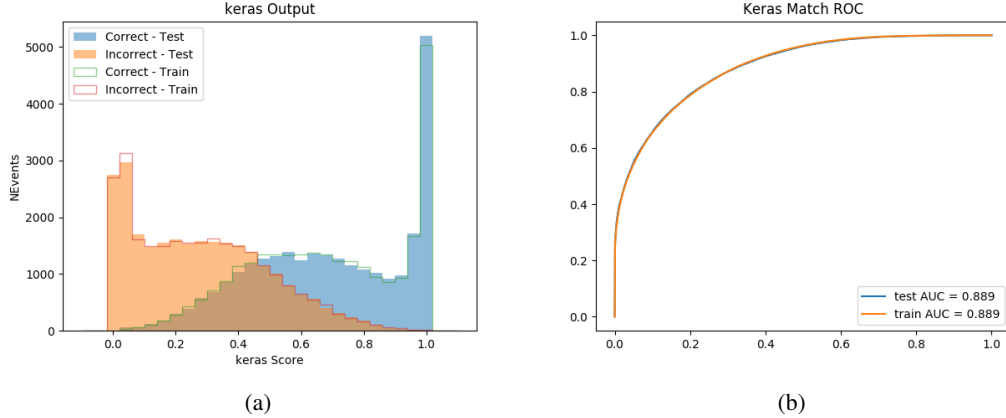


Figure 18.15: (a) the output score of the NN for correct and incorrect combinations of jets. (a) the ROC curve of the output, showing background rejection as a function of signal efficiency

1415 The correct lepton is identified by the model for 80% of events in the testing data set.

1416 **18.4 p_T Prediction**

1417 Once the most probable decay products have been identified, their kinematics are used as inputs
 1418 to a regression model which attempts to predict the momentum of the Higgs Boson. Once again,
 1419 a DNN is used. Input variables representing the b-jets and leptons not from the Higgs decay
 1420 are included as well, as these are found to improve performance. The truth p_T of the Higgs,
 1421 as predicted by MC, are used as labels. Separate models are built for each channel - 2lSS, 3l
 1422 Semi-leptonic and 3l Fully-leptonic.

1423 As a two-bin fit is targeted for the final result, some metrics evaluating the performance
 1424 of the models aim to show how well it distinguished between "high p_T " and "low p_T " events. A

1425 cutoff point of 150 GeV is used to define these two categories.

1426 Because the analysis uses a two bin fit of the Higgs p_T , the momentum reconstruction
1427 could be treated as a binary classification problem, rather than a regression problem. This
1428 approach is explored in detail in Section A.4, and is found not to provide any significant increase
1429 in sensitivity. The regression approach is used because it provides more flexibility for future
1430 analyses, as it is independent of the cutoff between high and low p_T , as well as the number of
1431 bins. Further, a regression allows the output of the neural network to be more clearly understood,
1432 as it can be directly compared to a physics observable.

1433 **18.4.1 2lSS Channel**

1434 The input variables listed in Table 37 are used to predict the Higgs p_T in the 2lSS channel. Here
1435 j_0 and j_1 are the two jets identified as Higgs decay products. The lepton identified as originating
1436 from the Higgs is labeled l_H , while the other lepton is labeled l_T , as it is assumed to have come
1437 from the decay of one of the top quarks. b_0 and b_1 are the two b-jets identified by the b-jet
1438 identification algorithm. The Higgs Reco Score and b-jet Reco Score are the outputs of the Higgs
1439 reconstruction algorithm, and the b-jet identification algorithm, respectively.

| HT | $M(j_0 j_1)$ | $M(j_0 j_1 l_H)$ |
|------------------------------|--|------------------------------|
| $M(l_H j_0)$ | $M(l_H j_1)$ | $p_T(b_0 b_1)$ |
| $p_T(j_0 j_1 l_H)$ | $\Delta\phi(j_0 j_1 l_H)(E_T^{\text{miss}})$ | $\Delta R(j_0)(j_1)$ |
| $\Delta R(j_0 j_1)(l_H)$ | $\Delta R(j_0 j_1 l_H)(l_T)$ | $\Delta R(j_0 j_1 l_H)(b_0)$ |
| $\Delta R(j_0 j_1 l_H)(b_1)$ | $\Delta R(l_H)(j_0)$ | $\Delta R(l_H)(b_0)$ |
| $\Delta R(l_H)(b_1)$ | $\Delta R(l_T)(b_0)$ | $\Delta R(l_T)(b_1)$ |
| $\Delta R(b_0)(b_1)$ | Higgs Reco Score | jet η 0 |
| jet η 1 | jet Phi 0 | jet Phi 1 |
| jet p_T 0 | jet p_T 1 | Lepton η H |
| Lepton ϕ H | Lepton p_T H | Lepton p_T T |
| E_T^{miss} | nJets | b-jet Reco Score |
| b-jet p_T 0 | b-jet p_T 1 | |

Table 37: Input features for reconstructing the Higgs p_T spectrum for 2lSS events

1440 The optimal neural network architecture for this channel is found to consist of 7 hidden
 1441 layers with 60 nodes each. The input data set includes 1.2 million events, 10% of which is used
 1442 for testing, the other 90% for training. Training is found to converge after around 150 epochs.

1443 To evaluate the performance of the model, the predicted p_T spectrum is compared to the
 1444 truth Higgs p_T in Figure 18.16. In order to visualize the model performance more clearly, in (a)
 1445 of that figure, the color of each point is determined by Kernel Density Estimation (KDE). The
 1446 color shown represents the logarithm of the output from KDE, to counteract the large number of
 1447 low p_T events. For that same reason, each column of the histogram shown in (b) of Figure 18.16
 1448 is normalized to unity. This plot therefore demonstrates what the model predicts for each slice
 1449 of truth p_T .

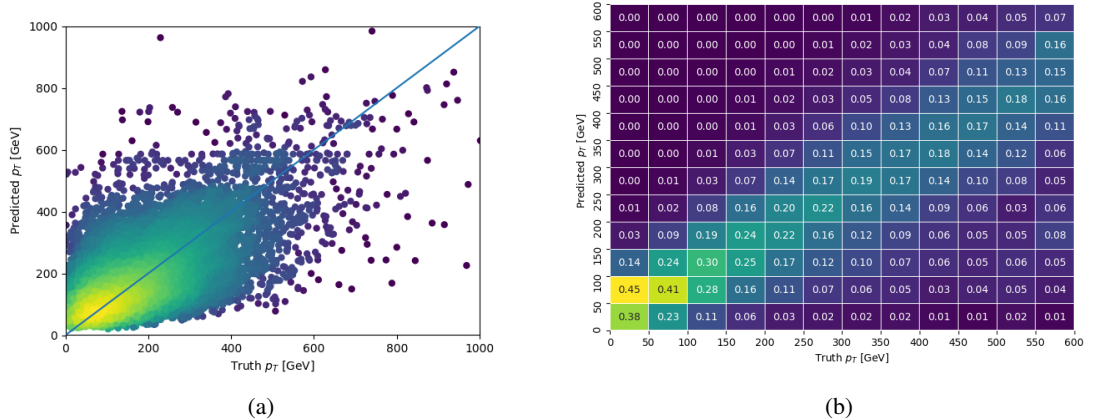


Figure 18.16: The regressed Higgs momentum spectrum as a function of the truth p_T for 2ISS $t\bar{t}H$ events in (a) a scatterplot, where the color of each point represents the log of the point density, based on Gaussian Kernel Density Estimation, and (b) a histogram where each column has been normalized to one.

1450 We are also interested in how well the model distinguishes between events with $p_T < 150$

1451 GeV and >150 GeV. Figure 18.17 demonstrates the NN output for high and low p_T events based
 1452 on this cutoff.

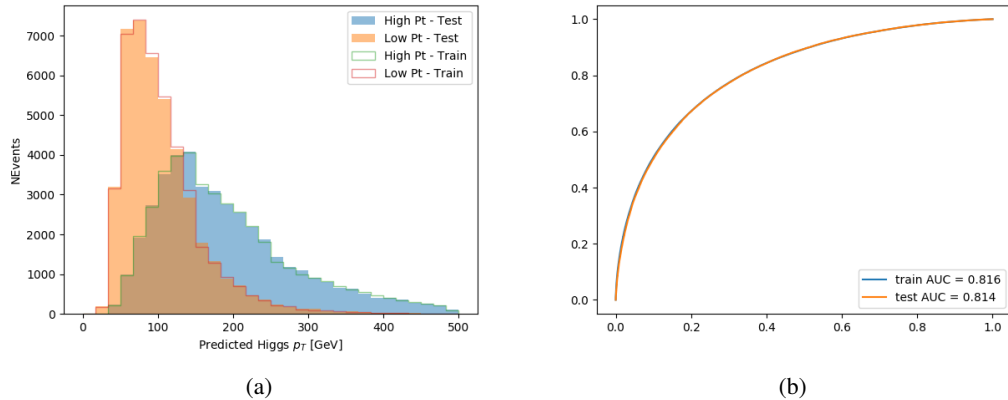


Figure 18.17: (a) shows the reconstructed Higgs p_T for 2lSS events with truth $p_T > 150$ GeV and < 150 GeV, while (b) shows the ROC curve for those two sets of events.

1453 18.4.2 3l Semi-leptonic Channel

1454 The following input features are used to predict the Higgs p_T for events in the 3lS channel:

| HT jets | MET | $M(j_0 j_1)$ |
|--|---------------------------------|------------------------------|
| $M(j_0 j_1 l_H)$ | $M(j_0 j_1 l_{T0})$ | $M(j_0 j_1 l_{T1})$ |
| $M(j_0 j_1 b_0)$ | $M(j_0 j_1 b_1)$ | $M(b_0 l_{T0})$ |
| $M(b_0 l_{T1})$ | $M(b_1 l_{T0})$ | $M(b_1 l_{T1})$ |
| $\Delta\phi(j_0 j_1 l_H)(E_T^{\text{miss}})$ | $\Delta R(j_0)(j_1)$ | $\Delta R(j_0 j_1)(l_H)$ |
| $\Delta R(j_0 j_1)(l_{T1})$ | $\Delta R(j_0 j_1)(b_0)$ | $\Delta R(j_0 j_1)(b_1)$ |
| $\Delta R(j_0 j_1 l_H)(l_{T0})$ | $\Delta R(j_0 j_1 l_H)(l_{T1})$ | $\Delta R(j_0 j_1 l_H)(b_0)$ |
| $\Delta R(j_0 j_1 l_H)(b_1)$ | $\Delta R(l_H)(j_0)$ | $\Delta R(l_H)(j_1)$ |
| $\Delta R(l_H)(l_{T1})$ | $\Delta R(l_{T0})(l_{T1})$ | $\Delta R(l_{T0})(b_0)$ |
| $\Delta R(l_{T0})(b_1)$ | $\Delta R(l_{T1})(b_0)$ | $\Delta R(l_{T1})(b_1)$ |
| higgsScore | jet η 0 | jet η 1 |
| jet ϕ 0 | jet ϕ 1 | jet p_T 0 |
| jet p_T 1 | Lepton η H | Lepton ϕ H |
| Lepton p_T H | Lepton p_T T0 | Lepton p_T T1 |
| nJets | topScore | b-jet p_T 0 |
| b-jet p_T 1 | | |

Table 38: Input features for reconstructing the Higgs p_T spectrum for 3lS events

Again, j_0 and j_1 are the two jets identified as Higgs decay products, ordered by p_T . The lepton identified as originating from the Higgs is labeled l_H , while the other two leptons are labeled l_{T0} and l_{T1} . b_0 and b_1 are the two b-jets identified by the b-jet identification algorithm. The Higgs Reco Score and b-jet Reco Score are the outputs of the Higgs reconstruction algorithm, and the b-jet identification algorithm, respectively.

The optimal neural network architecture for this channel is found to consist of 7 hidden layers with 80 nodes each. The inputdata set includes one million events, 10% of which is used for testing, the other 90% for training. Training is found to converge after around 150 epochs.

To evaluate the performance of the model, the predicted p_T spectrum is compared to the truth Higgs p_T in Figure 18.18. Once again, (a) of 18.18 shows a scatterplots of predicted vs truth p_T , where the color of each point corresponds to the log of the relative KDE at that point. Each column of the the histogram in (b) is normalized to unity, to better demonstrate the output of the NN for each slice of truth p_T .

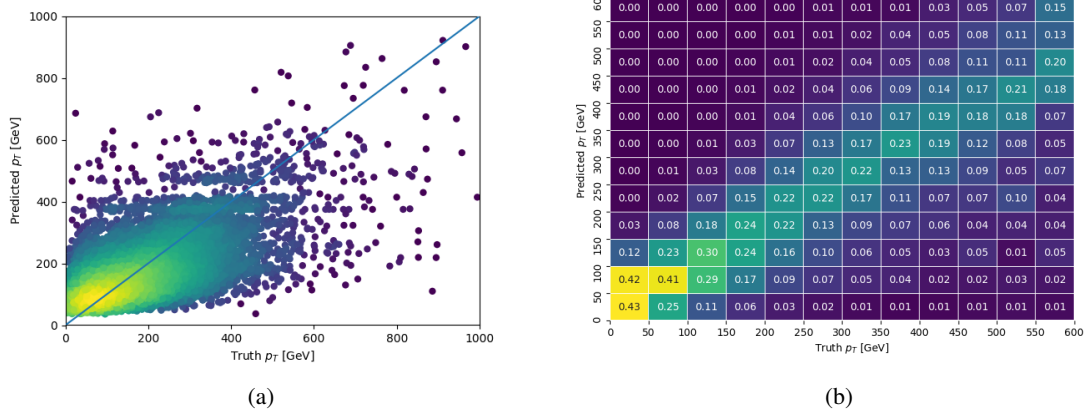


Figure 18.18: The regressed Higgs momentum spectrum as a function of the truth p_T for 3lS $t\bar{t}H$ events in (a) a scatterplot, where the color of each point represents the log of the point density, based on Gaussian Kernel Density Estimation, and (b) a histogram where each column has been normalized to one.

1468 Figure 18.19 shows (a) the output of the NN for events with truth p_T less than and greater
 1469 than 150 GeV and (b) the ROC curve demonstrating how well the NN distinguishes high and low
 1470 p_T events.

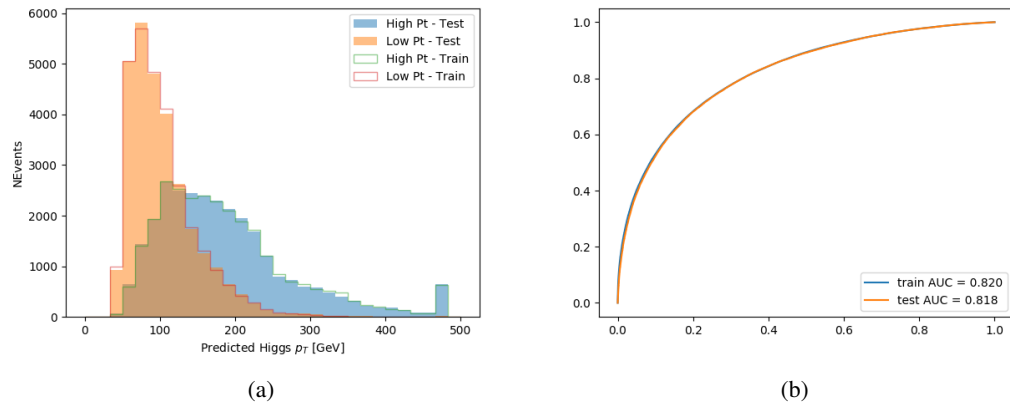


Figure 18.19: (a) shows the reconstructed Higgs p_T for 3lS events with truth $p_T > 150$ GeV and < 150 GeV, while (b) shows the ROC curve for those two sets of events.

18.4.3 3l Fully-leptonic Channel

¹⁴⁷¹ The features listed in 39 are used to construct a model for predictin the Higgs p_T for 3lF events.

¹⁴⁷² The features listed in 39 are used to construct a model for predictin the Higgs p_T for 3lF events.

| HT | $M(l_{H0}l_{H1})$ | $M(l_{H0}l_T)$ |
|-------------------------|-------------------------------|-------------------------------|
| $M(l_{H0}b_0)$ | $M(l_{H0}b_1)$ | $M(l_{H1}l_T)$ |
| $M(l_{H1}b_0)$ | $M(l_{H1}b_1)$ | $\Delta R(l_{H0})(l_{H1})$ |
| $\Delta R(l_{H0})(l_T)$ | $\Delta R(l_{H0}l_{H1})(l_T)$ | $\Delta R(l_{H0}l_T)(l_{H1})$ |
| $\Delta R(l_{H1})(l_T)$ | $\Delta R(l_{H0}b_0)$ | $\Delta R(l_{H0}b_1)$ |
| $\Delta R(l_{H1}b_1)$ | $\Delta R(l_{H1}b_0)$ | higgsScore |
| Lepton η H_0 | Lepton η H_1 | Lepton η T |
| Lepton p_T H_0 | Lepton p_T H_1 | Lepton p_T T |
| E_T^{miss} | topScore | b-jet p_T 0 |
| b-jet p_T 1 | | |

Table 39: Input features for reconstructing the Higgs p_T spectrum for 3lF events

1473 l_{H0} and l_{H1} represent the two leptons identified by the Higgs reconstruction model as
 1474 originating from the Higgs, while l_T is the other lepton in the event. The Higgs Reco Score and
 1475 b-jet Reco Score are the outputs of the Higgs reconstruction algorithm, and b-jet identification
 1476 algorithm, respectively.

1477 The optimal neural network architecture for this channel is found to consist of 5 hidden
 1478 layers with 40 nodes each. The input data set includes 400,000 events, 10% of which is used for
 1479 testing, the other 90% for training. Training is found to converge after around 150 epochs.

1480 The predicted transverse momentum, as a function of the truth p_T , is shown in Figure
 1481 [18.20](#).

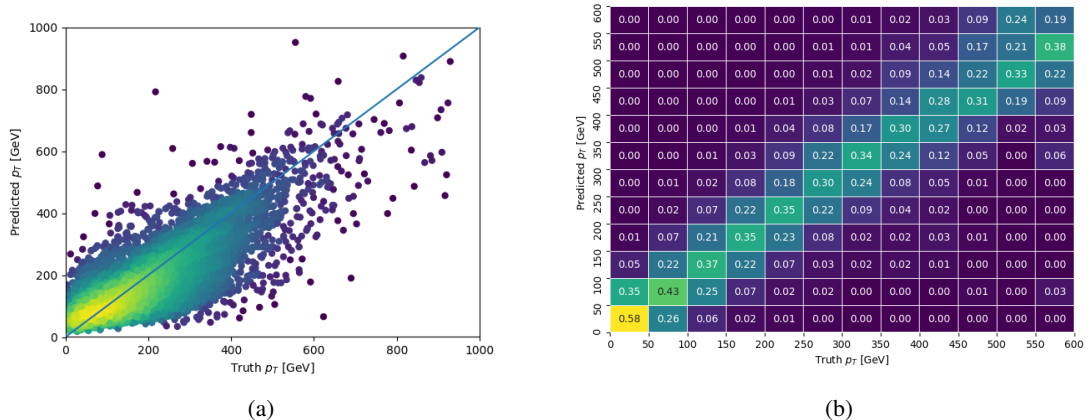


Figure 18.20: The regressed Higgs momentum spectrum as a function of the truth p_T for 3lF $t\bar{t}H$ events in (a) a scatterplot, where the color of each point represents the log of the point density, based on Gaussian Kernel Density Estimation, and (b) a histogram where each column has been normalized to one.

1482 When split into high and low p_T , based on a cutoff of 150 GeV, the

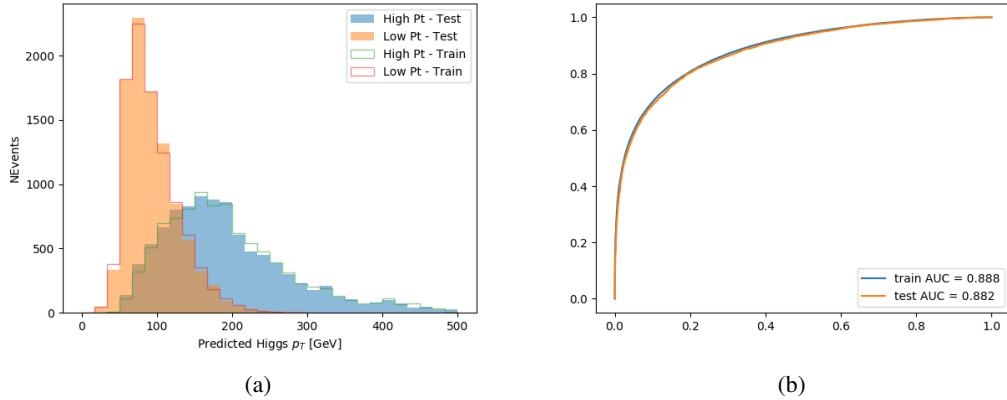


Figure 18.21: (a) shows the reconstructed Higgs p_T for 3lF events with truth $p_T > 150$ GeV and < 150 GeV, while (b) shows the ROC curve for those two sets of events.

1483 18.5 3l Decay Mode

1484 In the 3l channel, there are two possible ways for the Higgs to decay, both involving intermediate
 1485 W boson pairs: Either both W bosons decay leptonically, in which case the reconstructed decay
 1486 consists of two leptons (referred as the fully-leptonic 3l channel), or one W decays leptonically
 1487 and the other hadronically, giving two jets and one lepton in the final state (referred to as the
 1488 semi-leptonic 3l channel). In order to accurately reconstruct the Higgs, it is necessary to identify
 1489 which of these decays took place for each 3l event.

1490 The kinematics of each event, along with the output scores of the Higgs and top recon-
 1491 struction algorithms, are used to distinguish these two possible decay modes. The particular
 1492 inputs used are listed in Table 40.

| | | |
|---------------------|---------------------|---------------------|
| HT jets | $M(l_0 t_0)$ | $M(l_0 t_1)$ |
| $M(l_1 t_0)$ | $M(l_1 t_1)$ | $M(l_0 l_1)$ |
| $M(l_0 l_2)$ | $M(l_1 l_2)$ | $\Delta R(l_0 t_0)$ |
| $\Delta R(l_0 t_1)$ | $\Delta R(l_1 t_0)$ | $\Delta R(l_1 t_1)$ |
| $\Delta R(l l_0 1)$ | $\Delta R(l l_0 2)$ | $\Delta R(l l_1 2)$ |
| Lepton η 0 | Lepton η 1 | Lepton η 2 |
| Lepton ϕ 0 | Lepton ϕ 1 | Lepton ϕ 2 |
| Lepton p_T 0 | Lepton p_T 1 | Lepton p_T 2 |
| E_T^{miss} | nJets | nJets OR DL1r 60 |
| nJets OR DL1r 85 | score3lF | score3lS |
| topScore | total charge | |

Table 40: Input features used to distinguish semi-leptonic and fully-leptonic Higgs decays in the 3l channel.

1493 Here l_0 is the opposite charge lepton, l_1 and l_2 are the two SS leptons order by ΔR
 1494 from lepton 0. score3lF and score3lS are the outputs of the 3lS and 3lF Higgs reconstruction
 1495 algorithms, while topScore is the output of the b-jet identification algorithm.

1496 A neural network with 5 hidden layers, each with 50 nodes, is trained to distinguish these
 1497 two decay modes. The output of the model is summarized in Figure 18.22.

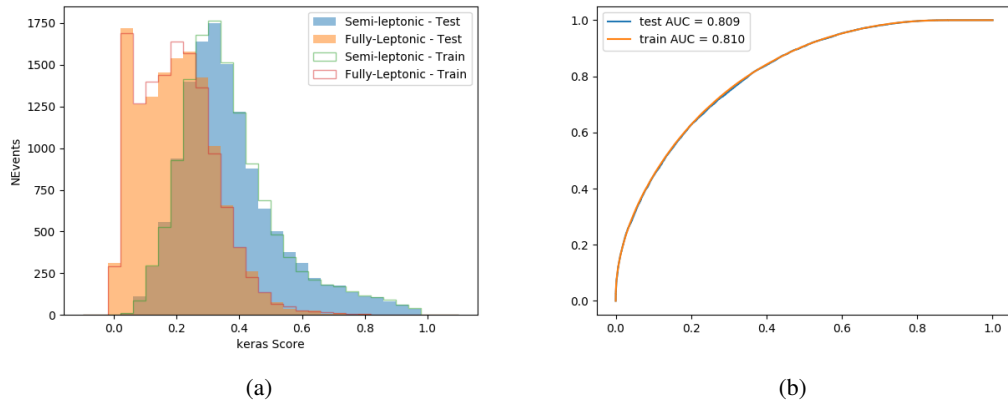


Figure 18.22: (a) shows the output of the decay separation NN for Semi-leptonic (blue) and Fully-leptonic (orange) 3l events, scaled to equal area. (b) shows the ROC curve for those two sets of events.

1498 A cutoff of 0.23 is determined to be optimal for separating 3lS and 3lF in the fit.

1499 19 Signal Region Definitions

1500 Events are divided into two channels based on the number of leptons in the final state: one with
 1501 two same-sign leptons, the other with three leptons. The 3l channel includes events where both
 1502 leptons originated from the Higgs boson as well as events where only one of the leptons

1503 **19.1 Pre-MVA Event Selection**

1504 A preselection is applied to define orthogonal analysis channels based on the number of leptons
1505 in each event. For the 2lSS channel, the following preselection is used:

- 1506
- Two very tight, same-charge, light leptons with $p_T > 20 \text{ GeV}$

1507

 - ≥ 4 reconstructed jets, ≥ 1 b-tagged jets

1508

 - No reconstructed tau candidates

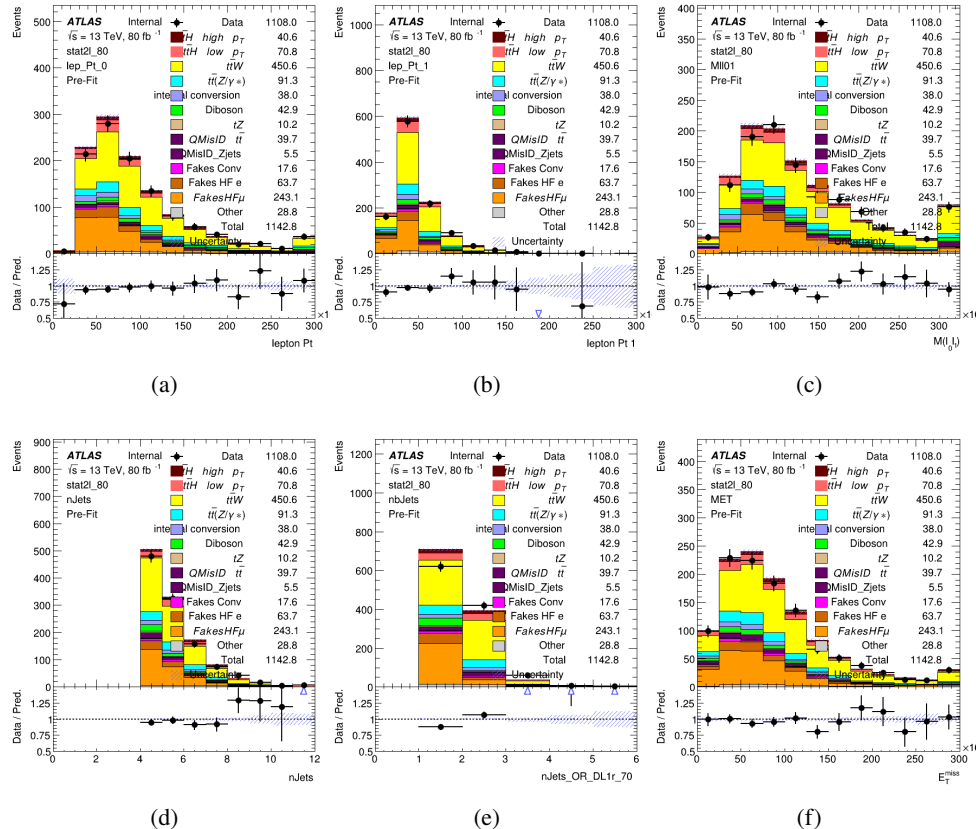
1509 The event yield after the 2lSS preselection has been applied, for MC and data at 80 fb^{-1} ,
1510 is shown in Table 41.

| | Yields |
|-------------------------|------------------|
| t̄H high p _T | 36.19 ± 0.23 |
| t̄H low p _T | 63.58 ± 0.31 |
| t̄W | 440.64 ± 2.32 |
| t̄Z/γ | 91.84 ± 0.79 |
| t̄lllowmass | 8.47 ± 0.28 |
| rareTop | 24.2099 ± 0.40 |
| VV | 38.7927 ± 0.55 |
| tZ | 3e-05 ± 5.47-06 |
| QMISID t̄ | 39.90 ± 2.36 |
| QMISID Zjets | 5.49 ± 0.67 |
| t̄ int. conv. | 12.74 ± 1.40 |
| t̄ + γ int. conv. | 12.09 ± 0.58 |
| t̄ Conv. | 13.55 ± 1.43 |
| t̄ + γ Conv. | 5.35 ± 0.38 |
| t̄ HF e | 59.92 ± 2.89 |
| t̄ + γ HF e | 0.51 ± 0.15 |
| t̄ HF μ | 224.57 ± 5.62 |
| t̄ + γ HF μ | 1.60 ± 0.23 |
| Z + jets internal conv | 3e-05 ± 5.47e-06 |
| Z + jets conv | 0.62 ± 0.21 |
| Z + jets HF e | 0.14 ± 0.13 |
| Z + jets HF μ | 0.82 ± 0.26 |
| Single top Conv | 2.27 ± 0.53 |
| Single top HF e | 2.33 ± 0.50 |
| Single top HF μ | 11.12 ± 1.07 |
| Three top | 2.22 ± 0.02 |
| Four top | 13.09 ± 0.16 |
| t̄WW | 10.985 ± 0.30 |
| tW | 3e-05 ± 5.47-06 |
| WtZ | 9.07 ± 0.44 |
| VVV | 0.30 ± 0.04 |
| VH | 0.59 ± 1.55 |
| Total | 1133.11 ± 7.69 |
| Data | 1108 |

Table 41: Event yield in the 2ISS preselection region.

1511

Figure 20.1. Good general agreement is found.

Figure 19.1: Data/MC comparisons of the 2lSS pre-selection region. (a) and (b) show the p_T of leptons 0 and 1, (c) shows the invariant mass of lepton 0 and 1, (d) shows the jet multiplicity, (e) the b-tagged jet multiplicity, and (f) the missing transverse energy.

1512

For the 3l channel, the following selection is applied:

1513

- Three light leptons with total charge ± 1
- Same charge leptons are required to be very tight, with $p_T > 20 \text{ GeV}$
- Opposite charge lepton must be loose, with $p_T > 10 \text{ GeV}$

1514

- 1516 • ≥ 2 reconstructed jets, ≥ 1 b-tagged jets
- 1517 • No reconstructed tau candidates
- 1518 • $|M(l^+l^-) - 91.2 \text{ GeV}| > 10 \text{ GeV}$ for all opposite-charge, same-flavor lepton pairs
- 1519 The event yield after the 3l preselection has been applied, for MC and data at 80 fb^{-1} , is
- 1520 shown in Table 19.1.

| | Yields |
|-----------------------------|-----------------|
| t̄H high p _T | 18.40 ± 0.13 |
| t̄H low p _T | 29.91 ± 0.16 |
| t̄W | 134.22 ± 1.25 |
| t̄Z/γ | 88.47 ± 0.73 |
| t̄lllowmass | 2.77 ± 0.16 |
| rareTop | 15.05 ± 0.32 |
| VV | 34.54 ± 0.54 |
| tZ | 2e-05 ± 4.47-06 |
| QMisID t̄t | 1.80 ± 0.59 |
| QMisID Zjets | 0.02 ± 0.02 |
| t̄t internal conversion | 4.34 ± 0.43 |
| t̄t + γ internal conversion | 5.83 ± 0.42 |
| t̄t Conv. | 4.71 ± 0.45 |
| t̄t + γ Conv. | 2.64 ± 0.27 |
| t̄t HF e | 27.44 ± 1.05 |
| t̄t + γ HF e | 0.27 ± 0.11 |
| t̄t HF μ | 89.21 ± 1.92 |
| t̄t + γ HF μ | 0.94 ± 0.16 |
| Z + jets conv | 0.09 ± 0.19 |
| Z + jets HF e | 0.25 ± 0.15 |
| Z + jets HF μ | 2.41 ± 0.95 |
| Single top Conv | 0.58 ± 0.61 |
| Single top HF e | 1.50 ± 0.43 |
| Single top HF μ | 4.62 ± 0.85 |
| Three top | 0.96 ± 0.02 |
| Four top | 5.58 ± 0.10 |
| t̄WW | 5.45 ± 0.21 |
| WtZ | 8.71 ± 0.42 |
| VVV | 0.81 ± 0.02 |
| Total | 492.14 ± 3.22 |
| Data | 535 |

Table 42: Yields of the analysis

1521

Comparisons of kinematic distributions for data and MC in this region are shown in Figure

1522 20.2.

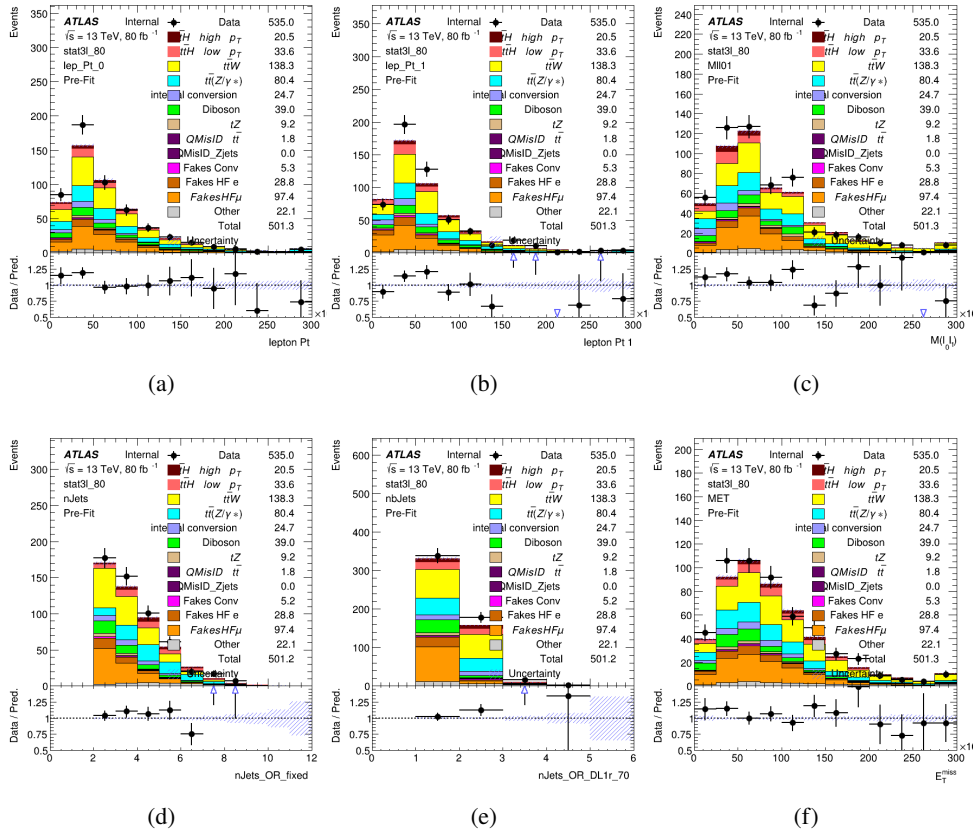


Figure 19.2: Data/MC comparisons of the 3l pre-selection region. (a) and (b) show the p_T of leptons 0 and 1, (c) shows the invariant mass of lepton 0 and 1, (d) shows the jet multiplicity, (e) the b-tagged jet multiplicity, and (f) the missing transverse energy.

1523

19.2 Event MVA

1524

Separate multi-variate analysis techniques (MVAs) are used in order to distinguish signal events

1525

from background for each analysis channel - 2lSS, 3l semi-leptonic (3lS), and 3l fully leptonic

1526

(3lF). In particular, Boosted Decision Tree (BDT) algorithms are produced with XGBoost

1527 [xgboost] are trained using the kinematics of signal and background events derived from Monte
1528 Carlo simulations. Events are weighted in the BDT training by the weight of each Monte Carlo
1529 event.

1530 Because the background composition differs for events with a high reconstructed Higgs p_T
1531 compared to events with low reconstructed Higgs p_T , separate MVAs are produced for high and
1532 low p_T regions. This is found to provide better significance than attempting to build an inclusive
1533 model, as demonstrated in appendix A.2. A cutoff of 150 GeV is used. This gives a total of 6
1534 background rejection MVAs - explicitly, 2lSS high p_T , 2lSS low p_T , 3lS high p_T , 3lS low p_T ,
1535 3lF high p_T , and 3lF low p_T .

1536 The following features are used in both the high and low p_T 2lSS BDTs:

| HT | $M(\text{lep}, E_T^{\text{miss}})$ | $M(l_0 l_1)$ |
|----------------------------------|---|----------------------------------|
| binHiggs p_T 2ISS | $\Delta R(l_0)(l_1)$ | diLepton type |
| higgsRecoScore | jet η 0 | jet η 1 |
| jet ϕ 0 | jet ϕ 1 | jet p_T 0 |
| jet p_T 1 | Lepton η 0 | Lepton η 1 |
| Lepton ϕ 0 | Lepton ϕ 1 | Lepton p_T 0 |
| Lepton p_T 1 | E_T^{miss} | $\min \Delta R(l_0)(\text{jet})$ |
| $\min \Delta R(l_1)(\text{jet})$ | $\min \Delta R(\text{Lepton})(\text{bjet})$ | mjjMax frwdJet |
| nJets | nJets OR DL1r 60 | nJets OR DL1r 70 |
| nJets OR DL1r 85 | topRecoScore | |

Table 43: Input features used to distinguish signal and background events in the 2ISS channel.

1537

While for each of the 31 BDTs, the features listed below are used for training:

| | | |
|------------------------------------|----------------------------------|---|
| $M(\text{lep}, E_T^{\text{miss}})$ | $M(l_0 l_1)$ | $M(l_0 l_1 l_2)$ |
| $M(l_0 l_2)$ | $M(l_1 l_2)$ | $\text{binHiggs } p_T \text{ 3lF}$ |
| $\text{binHiggs } p_T \text{ 3lS}$ | $\Delta R(l_0)(l_1)$ | $\Delta R(l_0)(l_2)$ |
| $\Delta R(l_1)(l_2)$ | decayScore | higgsRecoScore3lF |
| higgsRecoScore3lS | $\text{jet } \eta \text{ 0}$ | $\text{jet } \eta \text{ 1}$ |
| $\text{jet } \phi \text{ 0}$ | $\text{jet } \phi \text{ 1}$ | $\text{jet } p_T \text{ 0}$ |
| $\text{jet } p_T \text{ 1}$ | $\text{Lepton } \eta \text{ 0}$ | $\text{Lepton } \eta \text{ 1}$ |
| $\text{Lepton } \eta \text{ 2}$ | $\text{Lepton } \phi \text{ 0}$ | $\text{Lepton } \phi \text{ 1}$ |
| $\text{Lepton } \phi \text{ 2}$ | $\text{Lepton } p_T \text{ 0}$ | $\text{Lepton } p_T \text{ 1}$ |
| $\text{Lepton } p_T \text{ 2}$ | E_T^{miss} | $\min \Delta R(l_0)(\text{jet})$ |
| $\min \Delta R(l_1)(\text{jet})$ | $\min \Delta R(l_2)(\text{jet})$ | $\min \Delta R(\text{Lepton})(\text{bjet})$ |
| $mjj\text{Max frwdJet}$ | $n\text{Jets}$ | $n\text{Jets OR DL1r 60}$ |
| $n\text{Jets OR DL1r 70}$ | $n\text{Jets OR DL1r 85}$ | topScore |

Table 44: Input features used to distinguish signal and background events in the 3l channel.

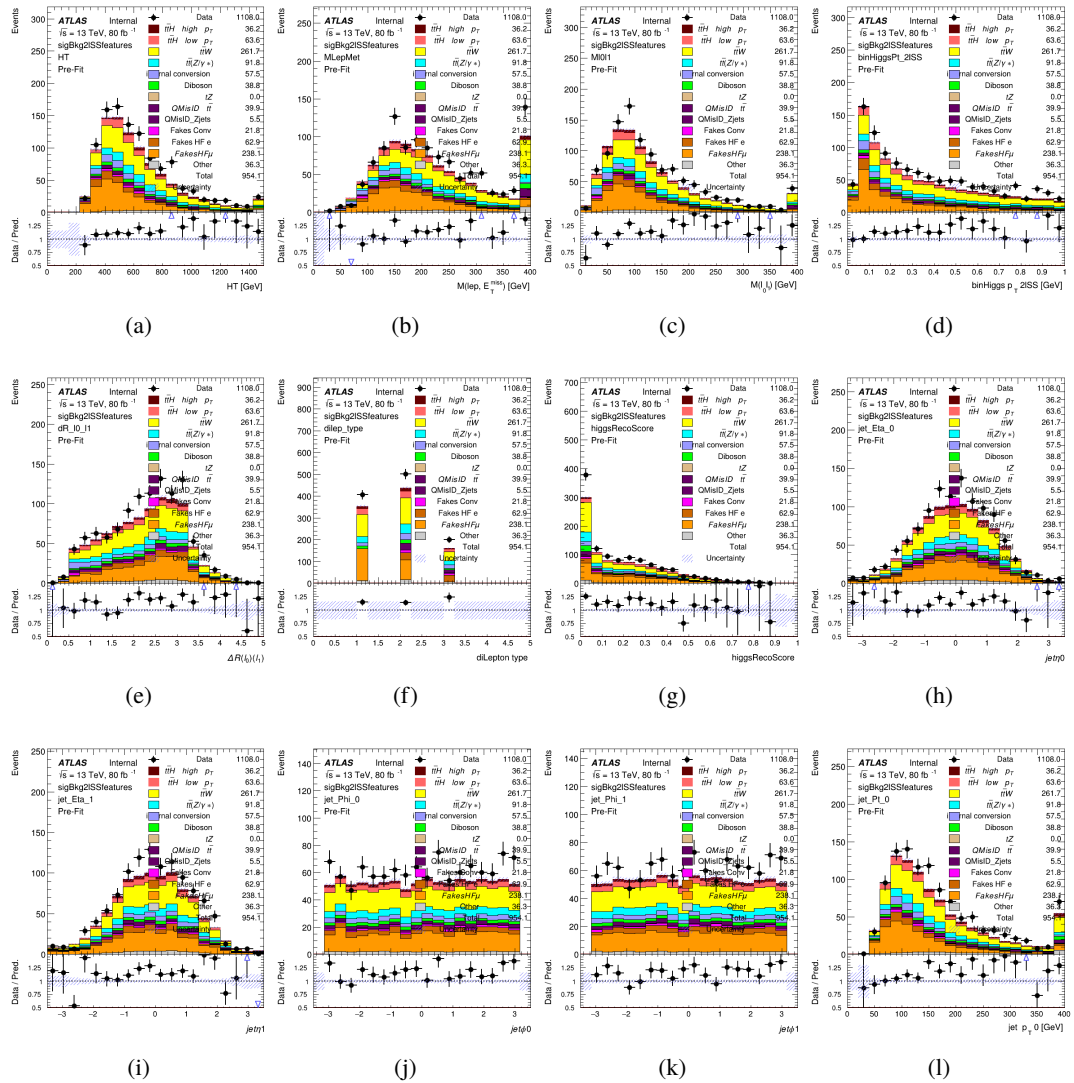


Figure 19.3:

1538

The BDTs are produced with a maximum tree depth of 6, using AUC as the target loss

1539

function.

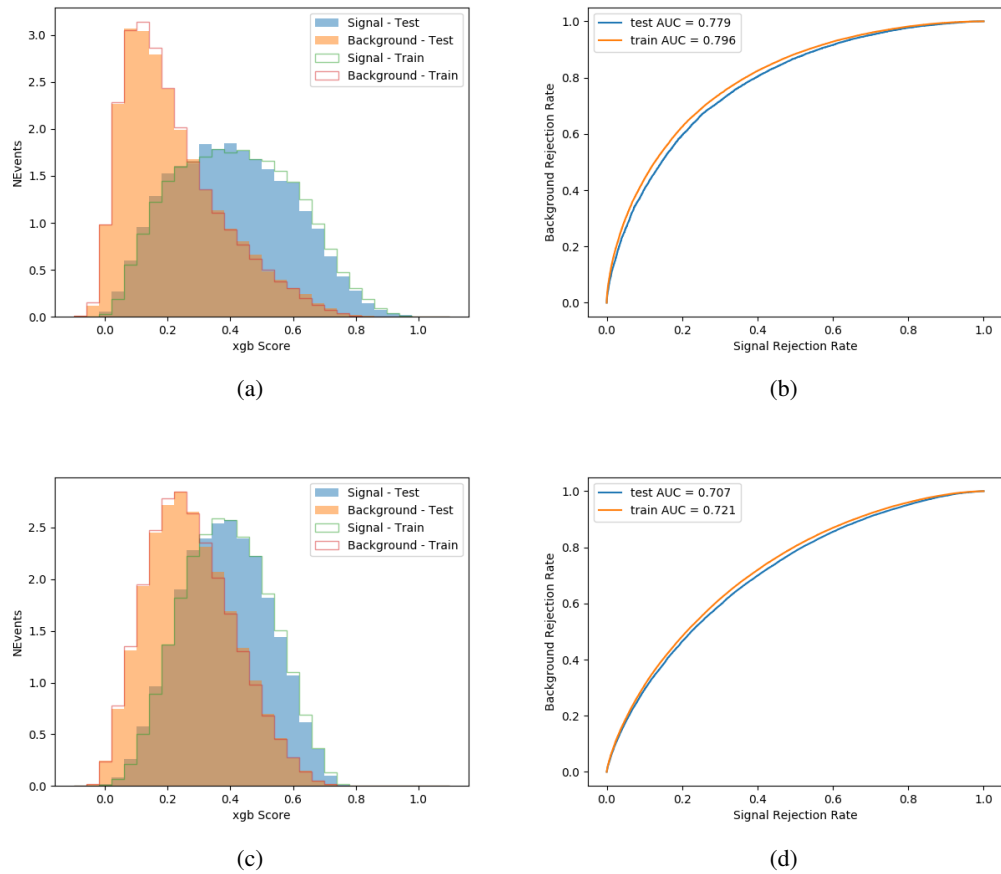


Figure 19.4:

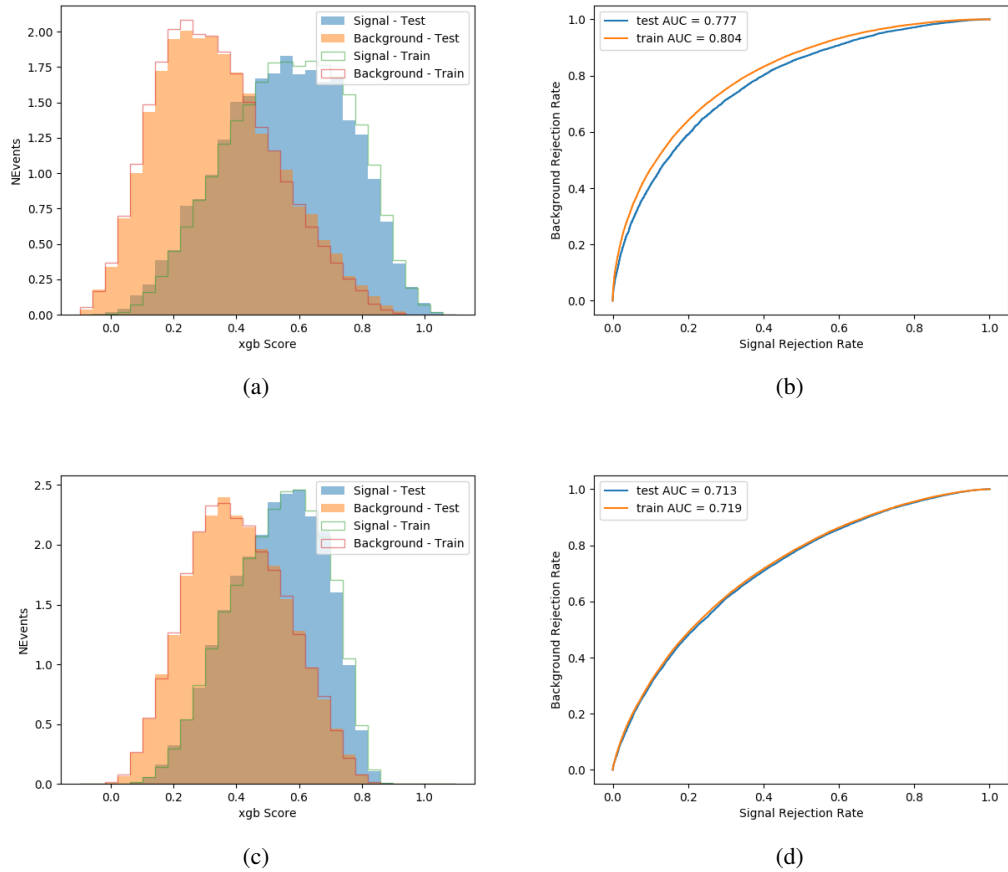


Figure 19.5:

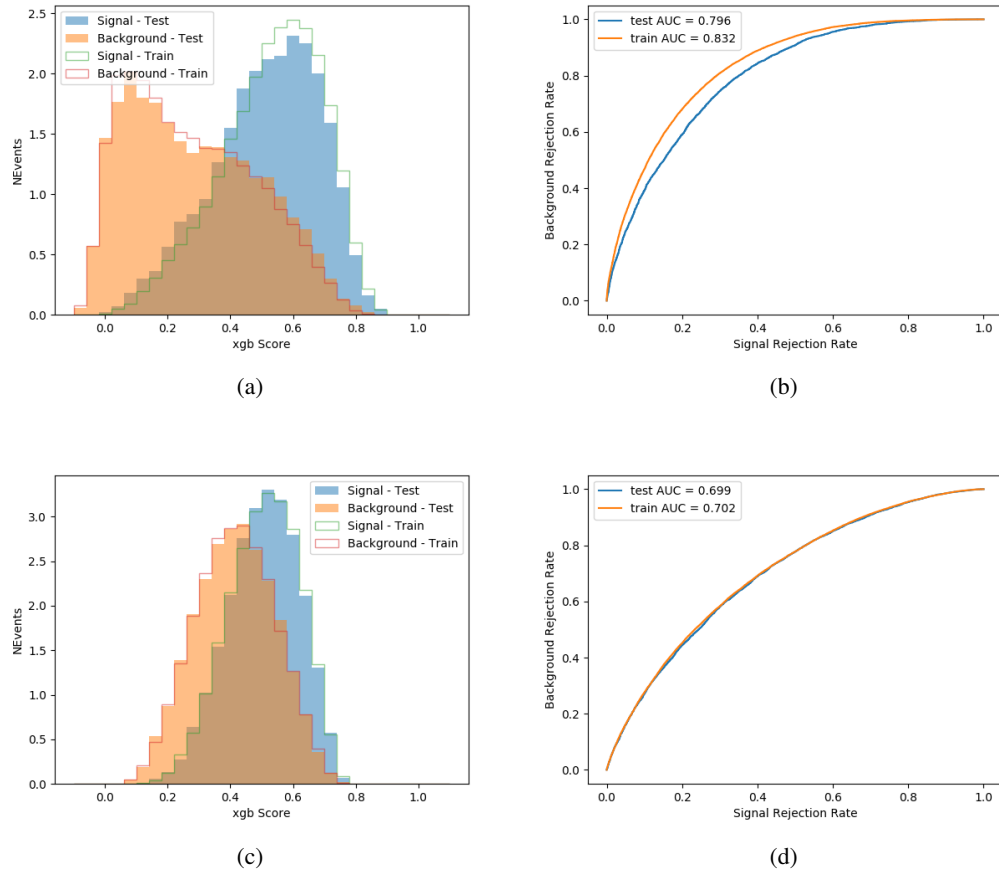


Figure 19.6:

1540 Output distributions of each MVA comparing MC prediction to data at 80 fb^{-1} are shown
 1541 in figures 19.7-19.2.

1542 19.3 Signal Region Definitions

1543 Once pre-selection has been applied, channels are further refined based on the MVAs described
 1544 above. The output of the model described in Section 18.5 is used to separate the three channel

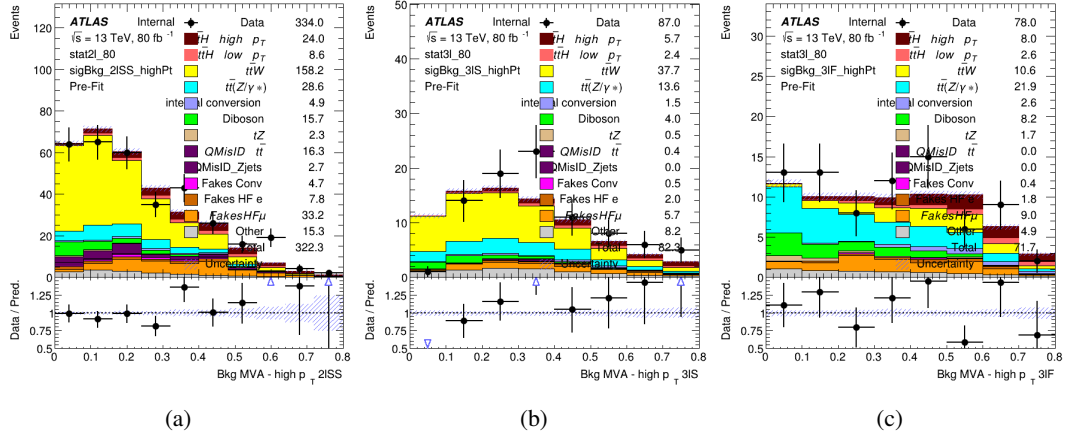


Figure 19.7: Output score of the high p_T BDTs in the (a) 2ISS, (b) 3IS, and (c) 3IF channels

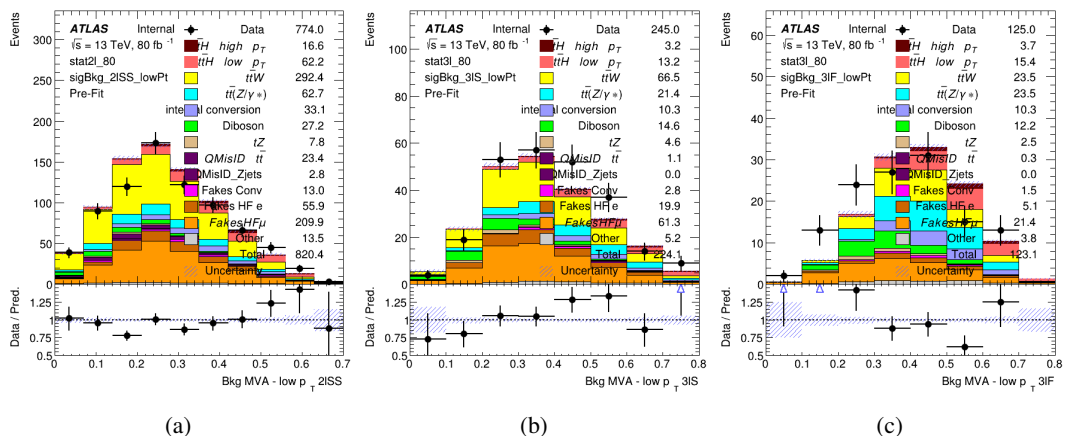


Figure 19.8: Output score of the low p_T BDTs in the (a) 2ISS, (b) 3IS, and (c) 3IF channels

1545 into two - Semi-leptonic and Fully-leptonic - based on the predicted decay mode of the Higgs
 1546 boson. This leaves three orthogonal signal regions - 2lSS, 3lS, and 3lF.

1547 For each event, depending on the number of leptons as well as whether the p_T of the Higgs
 1548 is predicted to be high (> 150 GeV) or low (< 150 GeV), a cut on the appropriate background
 1549 rejection MVA is applied. The particular cut values, listed in Table 45, are determined by
 1550 maximizing S/\sqrt{B} in each region.

| Channel | BDT Score |
|-----------------|-----------|
| 2lSS high p_T | 0.36 |
| 2lSS low p_T | 0.34 |
| 3lS high p_T | 0.51 |
| 3lS low p_T | 0.43 |
| 3lF high p_T | 0.33 |
| 3lF low p_T | 0.41 |

Table 45: Cutoff values on background rejection MVA score applied to signal regions.

1551 The event preselection and MVA selection define the three signal regions. These signal
 1552 region definitions are summarized in Table 46.

| Region | Selection |
|--------|--|
| 2ISS | Two same charge tight leptons with $p_T > 20$ GeV $N_{\text{jets}} \geq 4$, $N_{\text{b-jets}} \geq 1$ b-tagged jets Zero τ_{had} $H_{p_T}^{\text{pred}} > 150$ GeV and BDT score > 0.36 or $H_{p_T}^{\text{pred}} < 150$ GeV and BDT score > 0.34 |
| 3IS | Three light leptons with total charge ± 1 Two tight SS leptons, $p_T > 20$ GeV One loose OS lepton, $p_T > 10$ GeV $N_{\text{jets}} \geq 2$, $N_{\text{b-jets}} \geq 1$ b-tagged jets Zero τ_{had} $ M(l^+l^-) - 91.2 \text{ GeV} > 10 \text{ GeV}$ for all OSSF lepton pairs Decay NN Score < 0.23 $H_{p_T}^{\text{pred}} > 150$ GeV and BDT score > 0.51 or $H_{p_T}^{\text{pred}} > 150$ GeV and BDT score > 0.43 |
| 3IF | Three light leptons with total charge ± 1 Two tight SS leptons, $p_T > 20$ GeV One loose OS lepton, $p_T > 10$ GeV $N_{\text{jets}} \geq 2$, $N_{\text{b-jets}} \geq 1$ b-tagged jets Zero τ_{had} $ M(l^+l^-) - 91.2 \text{ GeV} > 10 \text{ GeV}$ for all OSSF lepton pairs Decay NN Score > 0.23 $H_{p_T}^{\text{pred}} > 150$ GeV and BDT score > 0.33 or $H_{p_T}^{\text{pred}} > 150$ GeV and BDT score > 0.41 |

Table 46: Selection applied to define the three signal regions used in the fit.

20 Background Rejection MVA

1553 Events are divided into two channels based on the number of leptons in the final state: one with
 1554 two same-sign leptons, the other with three leptons. The 3l channel includes events where both
 1555 leptons originated from the Higgs boson as well as events where only one of the leptons

1557 20.1 Pre-MVA Event Selection

1558 A preselection is applied to define orthogonal analysis channels based on the number of leptons
 1559 in each event. For the 2lSS channel, the following preselection is used:

- 1560 • Two very tight, same-charge, light leptons with $p_T > 20$ GeV

- 1561 • ≥ 4 reconstructed jets, ≥ 1 b-tagged jets

- 1562 • No reconstructed tau candidates

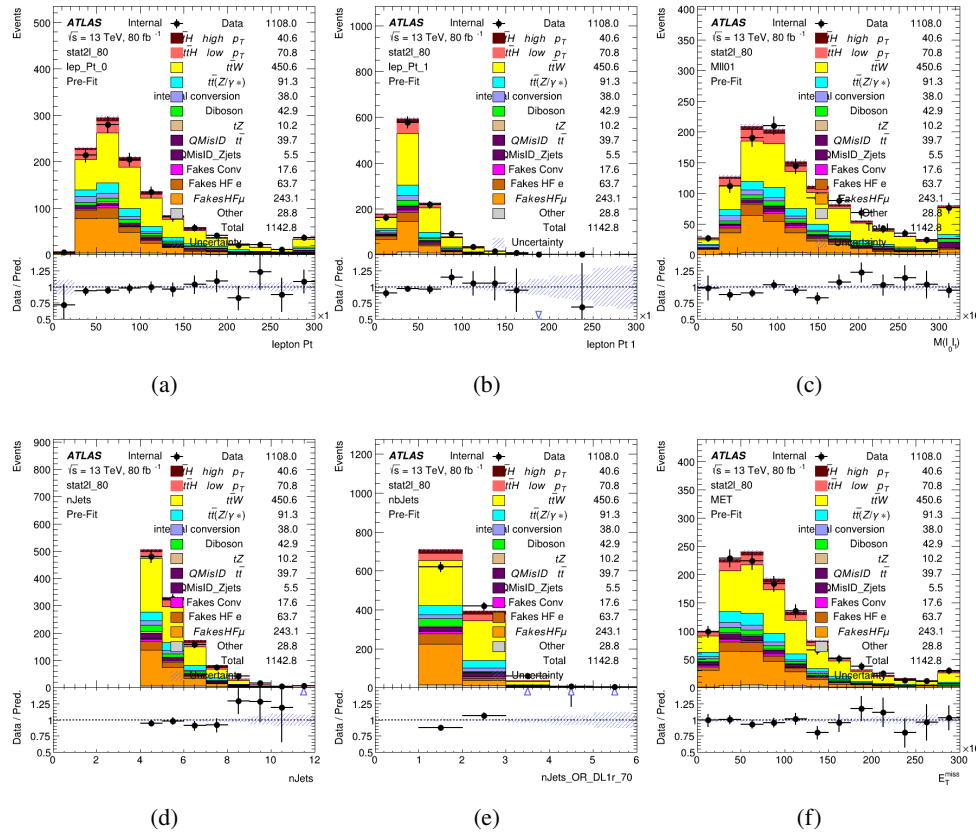


Figure 20.1:

1563 For the 31 channel, the following selection is applied:

1564 • Three light leptons with total charge ± 1

1565 • Same charge leptons are required to be very tight, with $p_T > 20 \text{ GeV}$

1566 • Opposite charge lepton must be loose, with $p_T > 10 \text{ GeV}$

1567 • $>= 2$ reconstructed jets, $>= 1$ b-tagged jets

1568 • No reconstructed tau candidates

1569 • $|M(l^+l^-) - 91.2 \text{ GeV}| > 10 \text{ GeV}$ for all opposite-charge, same-flavor lepton pairs

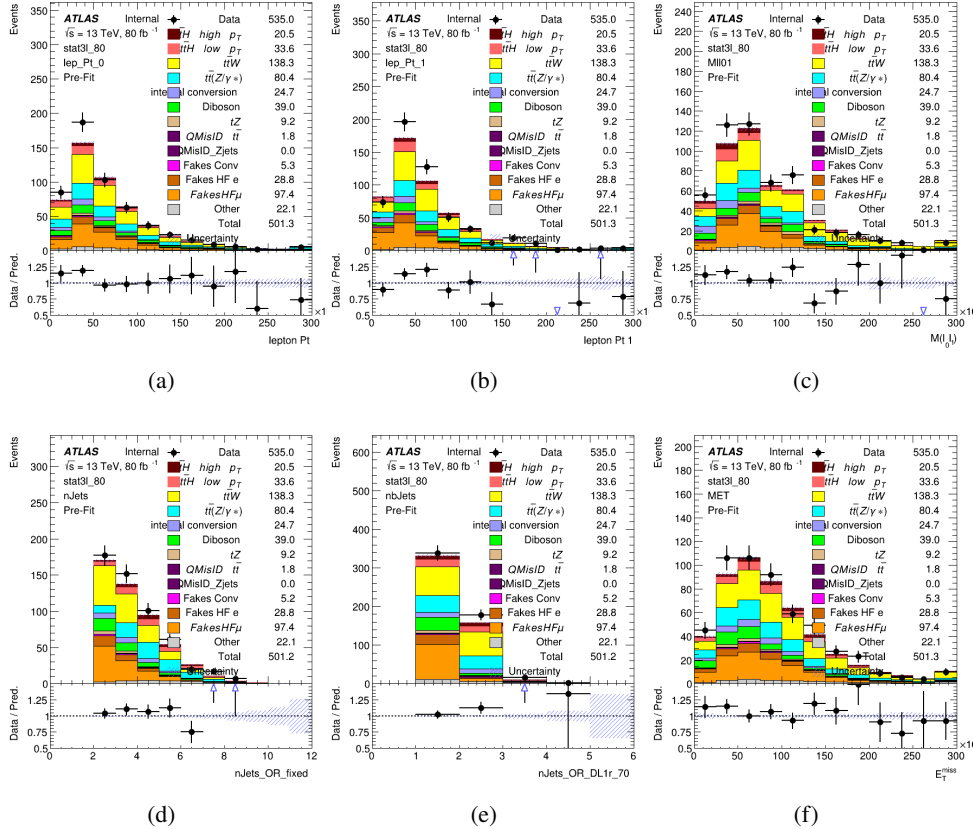


Figure 20.2:

20.2 Event MVA

Separate multi-variate analysis techniques (MVAs) are used in order to distinguish signal events from background for each analysis channel - 2lSS, 3l semi-leptonic (3lS), and 3l fully leptonic (3lF). In particular, Boosted Decision Tree (BDT) algorithms are produced with XGBoost [xgboost] are trained using the kinematics of signal and background events derived from Monte Carlo simulations. Events are weighted in the BDT training by the weight of each Monte Carlo

1576 event.

1577 Because the background composition differs for events with a high reconstructed Higgs p_T
1578 compared to events with low reconstructed Higgs p_T , separate MVAs are produced for high and
1579 low p_T regions. This is found to provide better significance than attempting to build an inclusive
1580 model, as demonstrated in appendix A.2. A cutoff of 150 GeV is used. This gives a total of 6
1581 background rejection MVAs - explicitly, 2lSS high p_T , 2lSS low p_T , 3lS high p_T , 3lS low p_T ,
1582 3lF high p_T , and 3lF low p_T .

1583 The following features are used in both the high and low p_T 2lSS BDTs:

| HT | $M(\text{lep}, E_T^{\text{miss}})$ | $M(l_0 l_1)$ |
|----------------------------------|---|----------------------------------|
| binHiggs p_T 2ISS | $\Delta R(l_0)(l_1)$ | diLepton type |
| higgsRecoScore | jet η 0 | jet η 1 |
| jet ϕ 0 | jet ϕ 1 | jet p_T 0 |
| jet p_T 1 | Lepton η 0 | Lepton η 1 |
| Lepton ϕ 0 | Lepton ϕ 1 | Lepton p_T 0 |
| Lepton p_T 1 | E_T^{miss} | $\min \Delta R(l_0)(\text{jet})$ |
| $\min \Delta R(l_1)(\text{jet})$ | $\min \Delta R(\text{Lepton})(\text{bjet})$ | mjjMax frwdJet |
| nJets | nJets OR DL1r 60 | nJets OR DL1r 70 |
| nJets OR DL1r 85 | topRecoScore | |

Table 47: Input features used to distinguish signal and background events in the 2ISS channel.

1584

While for each of the 31 BDTs, the features listed below are used for training:

| | | |
|------------------------------------|----------------------------------|---|
| $M(\text{lep}, E_T^{\text{miss}})$ | $M(l_0 l_1)$ | $M(l_0 l_1 l_2)$ |
| $M(l_0 l_2)$ | $M(l_1 l_2)$ | $\text{binHiggs } p_T \text{ 3lF}$ |
| $\text{binHiggs } p_T \text{ 3lS}$ | $\Delta R(l_0)(l_1)$ | $\Delta R(l_0)(l_2)$ |
| $\Delta R(l_1)(l_2)$ | decayScore | higgsRecoScore3lF |
| higgsRecoScore3lS | $\text{jet } \eta \text{ 0}$ | $\text{jet } \eta \text{ 1}$ |
| $\text{jet } \phi \text{ 0}$ | $\text{jet } \phi \text{ 1}$ | $\text{jet } p_T \text{ 0}$ |
| $\text{jet } p_T \text{ 1}$ | $\text{Lepton } \eta \text{ 0}$ | $\text{Lepton } \eta \text{ 1}$ |
| $\text{Lepton } \eta \text{ 2}$ | $\text{Lepton } \phi \text{ 0}$ | $\text{Lepton } \phi \text{ 1}$ |
| $\text{Lepton } \phi \text{ 2}$ | $\text{Lepton } p_T \text{ 0}$ | $\text{Lepton } p_T \text{ 1}$ |
| $\text{Lepton } p_T \text{ 2}$ | E_T^{miss} | $\min \Delta R(l_0)(\text{jet})$ |
| $\min \Delta R(l_1)(\text{jet})$ | $\min \Delta R(l_2)(\text{jet})$ | $\min \Delta R(\text{Lepton})(\text{bjet})$ |
| $mjj\text{Max frwdJet}$ | $n\text{Jets}$ | $n\text{Jets OR DL1r 60}$ |
| $n\text{Jets OR DL1r 70}$ | $n\text{Jets OR DL1r 85}$ | topScore |

Table 48: Input features used to distinguish signal and background events in the 3l channel.

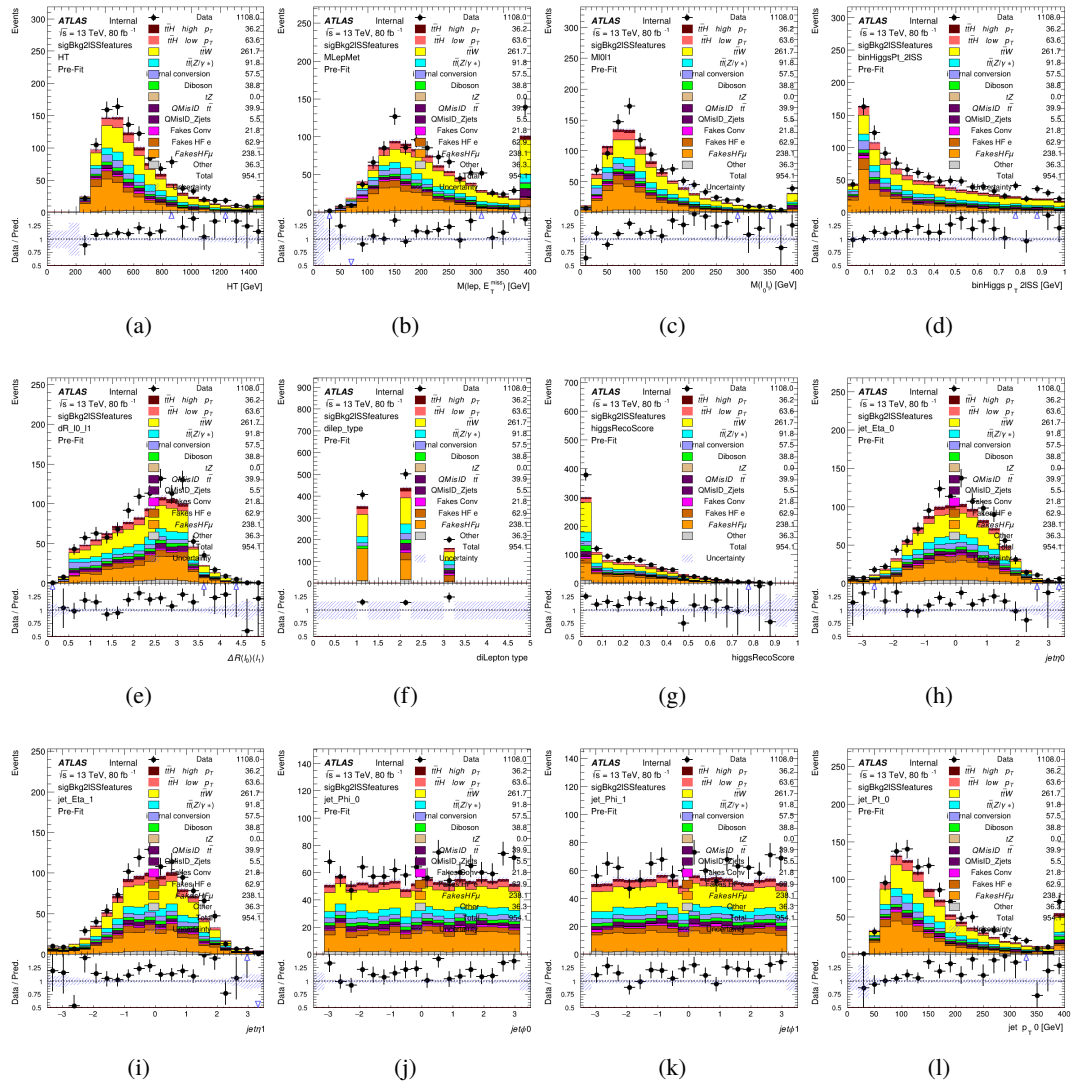


Figure 20.3:

1585

The BDTs are produced with a maximum tree depth of 6, using AUC as the target loss

1586

function.

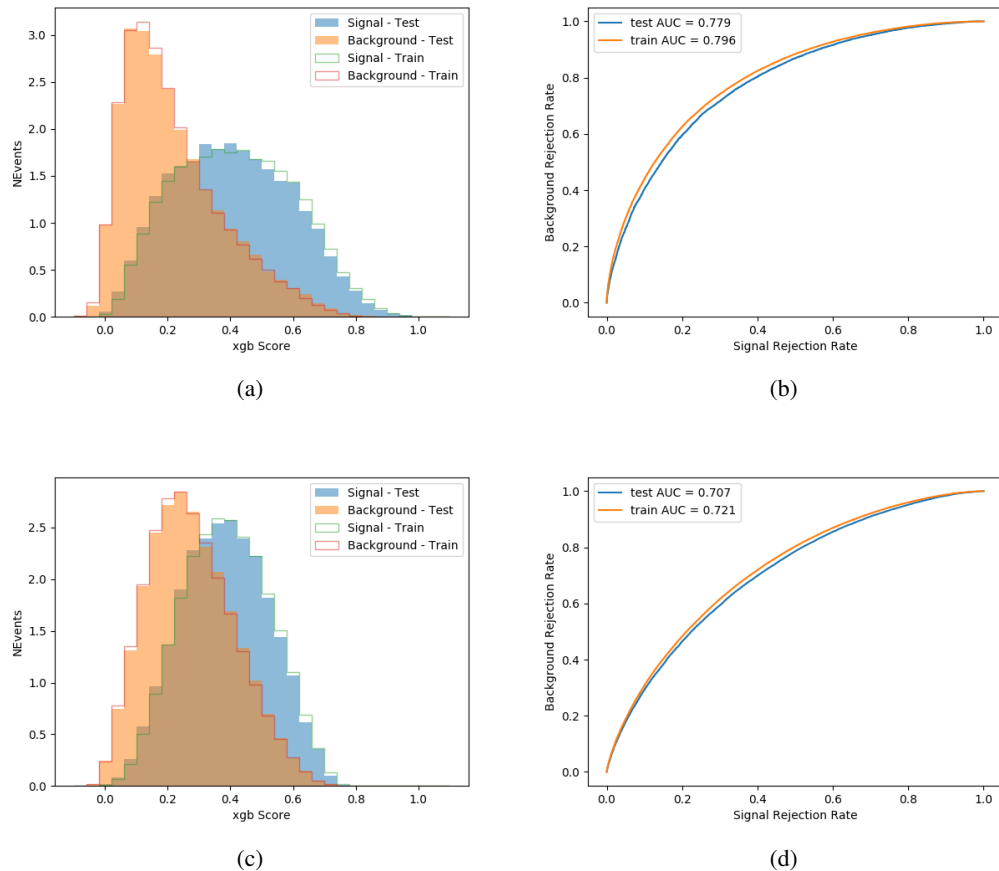


Figure 20.4:

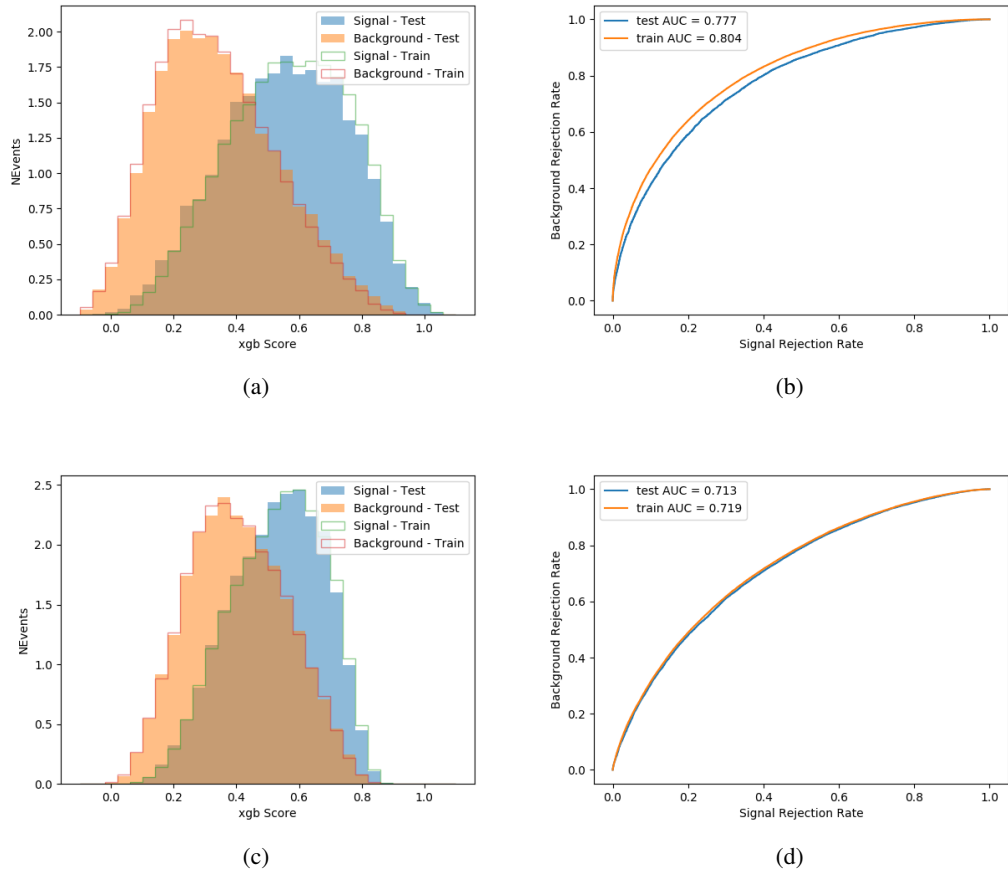


Figure 20.5:

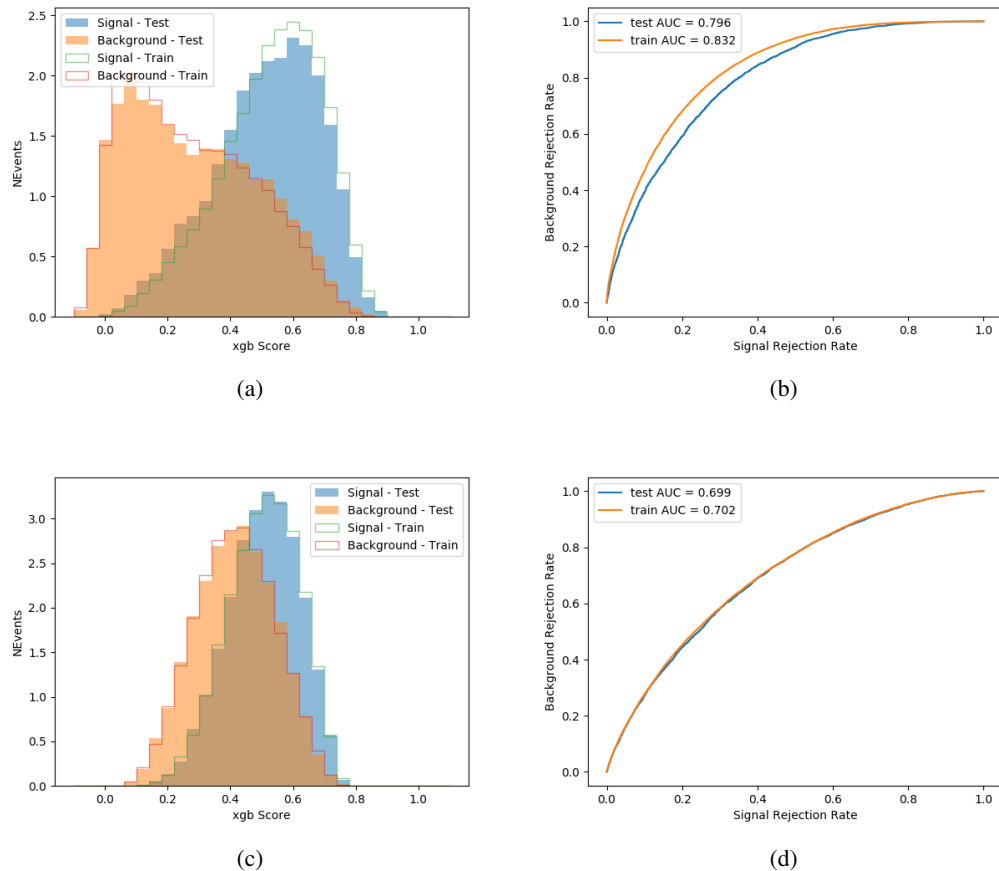


Figure 20.6:

1587

Output distributions of each MVA comparing MC prediction to data at 80 fb^{-1} are shown

1588

in Figure 20.2.

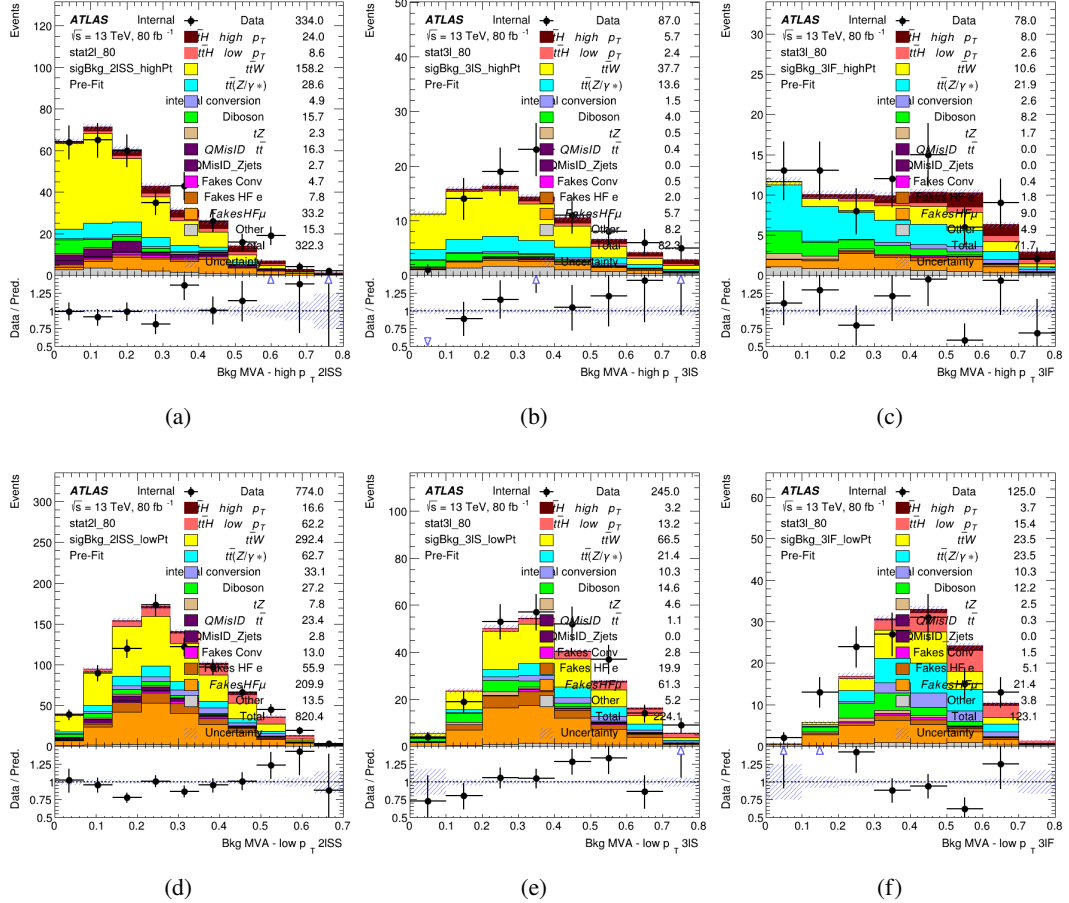


Figure 20.7: scores

1589 20.3 Signal Region Definitions

1590 Once pre-selection has been applied, channels are further refined based on the MVAs described
 1591 above. The output of the model described in Section 18.5 is used to separate the three channel
 1592 into two - Semi-leptonic and Fully-leptonic - based on the predicted decay mode of the Higgs
 1593 boson.

1594 For each event, depending on the channel as well as the predicted p_T of the Higgs derived
1595 from the algorithm described in Section 18.4, a cut on the appropriate background rejection
1596 algorithm is applied. The specific selection used, and the event yield in each channel after this
1597 selection has been applied, is summarized below.

1598 **20.3.1 2lSS**

1599 **20.3.2 3l – Semi – leptonic**

1600 **20.3.3 3l – Fully – leptonic**

1601 **21 Systematic Uncertainties**

1602 The systematic uncertainties that are considered are summarized in Table 49. These are imple-
1603 mented in the fit either as a normalization factors or as a shape variation or both in the signal
1604 and background estimations. The numerical impact of each of these uncertainties is outlined in
1605 section 22.

Table 49: Sources of systematic uncertainty considered in the analysis. Some of the systematic uncertainties are split into several components, as indicated by the number in the rightmost column.

| Systematic uncertainty | Components |
|--|------------|
| Luminosity | 1 |
| Pileup reweighting | 1 |
| Physics Objects | |
| Electron | 6 |
| Muon | 15 |
| Jet energy scale and resolution | 28 |
| Jet vertex fraction | 1 |
| Jet flavor tagging | 131 |
| E_T^{miss} | 3 |
| Total (Experimental) | 186 |
| Background Modeling | |
| Cross section | 24 |
| Renormalization and factorization scales | 10 |
| Parton shower and hadronization model | 2 |
| Shower tune | 4 |
| Total (Signal and background modeling) | 40 |
| Background Modeling | |
| Cross section | 24 |
| Renormalization and factorization scales | 10 |
| Parton shower and hadronization model | 2 |
| Shower tune | 4 |
| Total (Signal and background modeling) | 40 |
| Total (Overall) | 226 |

¹⁶⁰⁶ The uncertainty in the combined 2015+2016 integrated luminosity is derived from a
¹⁶⁰⁷ calibration of the luminosity scale using x-y beam-separation scans performed in August 2015
¹⁶⁰⁸ and May 2016 [29].

¹⁶⁰⁹ The experimental uncertainties are related to the reconstruction and identification of light
¹⁶¹⁰ leptons and b-tagging of jets, and to the reconstruction of E_T^{miss} . The TOTAL electron ID
¹⁶¹¹ correlation model is used, corresponding to 1 electron ID systematic. Electron ID is found to be

1612 a subleading systematic that is unconstrained by the fit, making it an appropriate choice for this
1613 analysis.

1614 The sources which contribute to the uncertainty in the jet energy scale [31] are decom-
1615 posed into uncorrelated components and treated as independent sources in the analysis. The
1616 CategoryReduction model is used to account for JES uncertainties, which decomposes the uncer-
1617 tainties into 30 nuisance parameters included in the fit. The SimpleJER model is used to account
1618 for jet energy resolution (JER) uncertainties, and 8 JER uncertainty components unclued as
1619 NPs in the fit.

1620 The uncertainties in the b-tagging efficiencies measured in dedicated calibration analyses
1621 [32] are also decomposed into uncorrelated components. The large number of components for
1622 b-tagging is due to the calibration of the distribution of the BDT discriminant.

1623 The systematic uncertainties associated with the signal and background processes are
1624 accounted for by varying the cross-section of each process within its uncertainty.

1625 The full list of systematic uncertainties considered in the analysis is summarized in Tables
1626 50, 51 and 52.

1627

| Experimental Systematics on Leptons and E_T^{miss} | | | |
|---|-------------------------------------|---|-------------------|
| Type | Description | Systematics Name | Application |
| Trigger | | | |
| Scale Factors | Trigger Efficiency | lepSFTrigTight_MU(EL)_SF_Trigger_STAT(SYST) | Event Weight |
| Muons | | | |
| Efficiencies | Reconstruction and Identification | lepSFObjTight_MU_SF_ID_STAT(SYST) | Event Weight |
| | Isolation | lepSFObjTight_MU_SF_Isol_STAT(SYST) | Event Weight |
| | Track To Vertex Association | lepSFObjTight_MU_SF_TTVA_STAT(SYST) | Event Weight |
| p_T Scale | p_T Scale | MUONS_SCALE | p_T Correction |
| Resolution | Inner Detector Energy Resolution | MUONS_ID | p_T Correction |
| | Muon Spectrometer Energy Resolution | MUONS_MS | p_T Correction |
| Electrons | | | |
| Efficiencies | Reconstruction | lepSFObjTight_EL_SF_ID | Event Weight |
| | Identification | lepSFObjTight_EL_SF_Reco | Event Weight |
| | Isolation | lepSFObjTight_EL_SF_Isol | Event Weight |
| Scale Factor | Energy Scale | EG_SCALE_ALL | Energy Correction |
| Resolution | Energy Resolution | EG_RESOLUTION_ALL | Energy Correction |
| E_T^{miss} | | | |
| Soft Tracks Terms | Resolution | MET_SoftTrk_ResoPerp | p_T Correction |
| | Resolution | MET_SoftTrk_ResoPara | p_T Correction |
| | Scale | MET_SoftTrk_ScaleUp | p_T Correction |
| | Scale | MET_SoftTrk_ScaleDown | p_T Correction |

Table 50: Summary of experimental systematics considered for leptons and E_T^{miss} . Includes type, description, name of systematic as used in the fit, and mode of application. The mode of application indicates the systematic evaluation, e.g. as an overall event re-weighting (Event Weight) or rescaling (p_T Correction).

| Experimental Systematics on Jets | | | |
|----------------------------------|--------------------------|--|--|
| Type | Origin | Systematics Name | Application |
| Jet Vertex Tagger | | JVT | Event Weight |
| Energy Scale | Calibration Method | JET_21NP_ JET_EffectiveNP_1-19 | p _T Correction p _T Correction |
| | η inter-calibration | JET_EtaIntercalibration_Modelling JET_EtaIntercalibration_NonClosure JET_EtaIntercalibration_TotalStat | p _T Correction p _T Correction p _T Correction |
| | High p _T jets | JET_SingleParticle_HighPt | p _T Correction |
| | Pile-Up | JET_Pileup_OffsetNPV JET_Pileup_OffsetMu JET_Pileup_PtTerm JET_Pileup_RhoTopology | p _T Correction p _T Correction p _T Correction p _T Correction |
| | Non Closure | JET_PunchThrough_MC15 | p _T Correction |
| | Flavour | JET_Flavor_Response JET_BJES_Response JET_Flavor_Composition | p _T Correction p _T Correction p _T Correction |
| Resolution | | JET_JER_SINGLE_NP | Event Weight |

Table 51: Jet systematics take into account effects of jets calibration method, η inter-calibration, high p_T jets, pile-up, and flavor response. They are all diagonalised into effective parameters.

| Experimental Systematics on b-tagging | | |
|---------------------------------------|---|---|
| Type | Origin | Systematic Name |
| Scale Factors | DL1r b-tagger efficiency on b originated jets in bins of η | DL1r_Continuous_EventWeight_B0-29 |
| | DL1r b-tagger efficiency on c originated jets in bins of η | DL1r_Continuous_EventWeight_C0-19 |
| | DL1r b-tagger efficiency on light flavoured originated jets in bins of η and p_T | DL1r_Continuous_EventWeight_Light0-79 |
| | DL1r b-tagger extrapolation efficiency | DL1r_Continuous_EventWeight_extrapolation DL1r_Continuous_EventWeight_extrapolation_from_charm |

Table 52: Summary of experimental systematics to be included for b-tagging of jets in the analysis, using the continuous DL1r tagging algorithm. All of the b-tagging related systematics are applied as event weights. From left: type, description, and the name of systematic used in the fit.

¹⁶²⁸ Theoretical uncertainties applied to MC predictions, including cross section, PDF, and
¹⁶²⁹ scale uncertainties are taken from theory calculations. The theory uncertainties applied to the
¹⁶³⁰ predominate background estimates are summarized in Table 53.

Table 53: Summary of theoretical uncertainties for MC predictions in the analysis.

22 Results

¹⁶³¹ A maximum likelihood fit is performed simultaneously over the reconstructed Higgs p_T spectrum
¹⁶³² in the three signal regions, 2lSS, 3lS, and 3lF. The signal is split into high and low p_T samples,
¹⁶³³ based on whether the truth p_T of the Higgs is above or below 150 GeV. The parameters $\mu_{t\bar{t}Hhighp_T}$
¹⁶³⁴

1635 and $\mu_{t\bar{t}H\text{low}p_T}$, where $\mu = \sigma_{\text{observed}}/\sigma_{\text{SM}}$, are extracted from the fit, signifying the difference
1636 between the observed value and the theory prediction. Unblinded results are shown for the 80
1637 fb^{-1} data set, as well as MC only projections of results using the full Run-2, 140 fb^{-1} dataset.

1638 As described in Section 21, there are 229 systematic uncertainties that are considered
1639 as NPs in the fit. These NPs are constrained by Gaussian or log-normal probability density
1640 functions. The latter are used for normalisation factors to ensure that they are always positive.
1641 The expected number of signal and background events are functions of the likelihood. The prior
1642 for each NP is added as a penalty term, decreasing the likelihood as it is shifted away from its
1643 nominal value.

1644 22.1 Results - 80 fb^{-1}

1645 As the data collected from 2015-2017 has been unblinded for $t\bar{t}H$ —ML channels, representing 80
1646 fb^{-1} , those events are unblinded. The predicted Higgs p_T spectrum is fit to data simultaneously
1647 in each of the three signal regions shown in Figure 22.1.

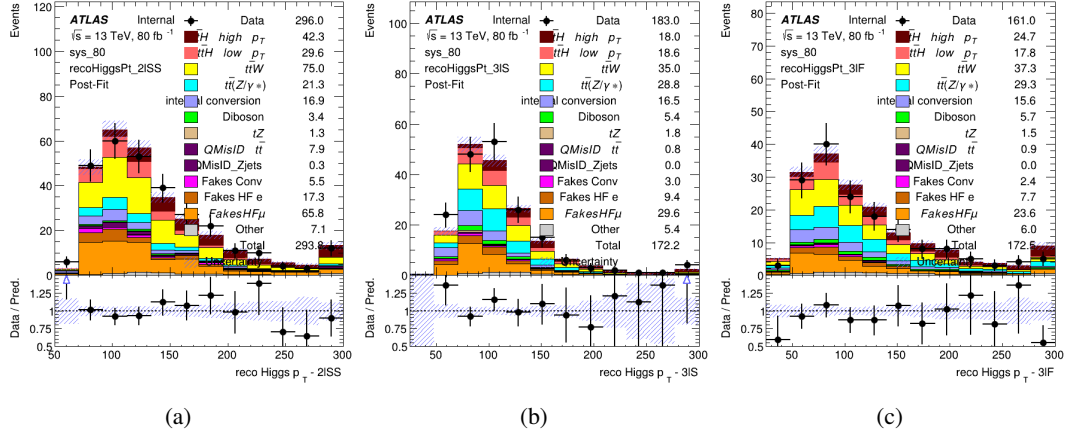


Figure 22.1: Post-fit distributions of the reconstructed Higgs p_T in the three signal regions, (a) 2ISS, (b) 3IS, and (c) 3IF, for 80 fb^{-1} of MC

1648

A post-fit summary of the fitted regions is shown in Figure 22.2.

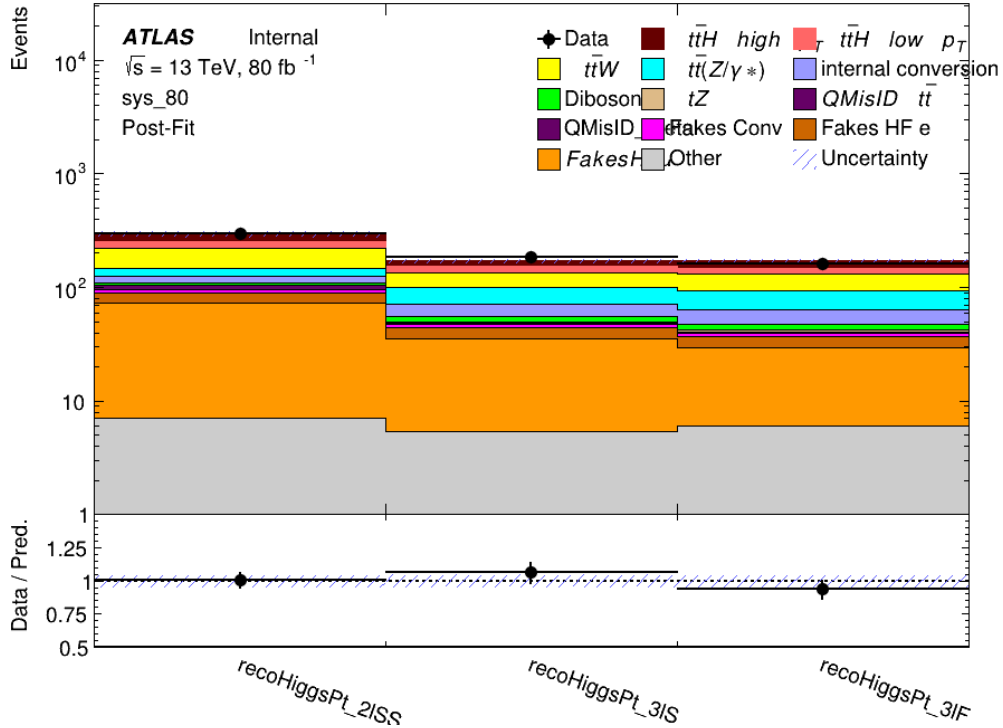


Figure 22.2: Post-fit summary of the yields in each signal region.

1649 The the measured μ values for high and low p_T Higgs production obtained from the fit
 1650 are shown in 54. A significance of 1.7σ is observed for $t\bar{t}H$ high p_T , and 2.1σ is measured for
 1651 $t\bar{t}H$ low p_T .

$$\mu_{t\bar{t}H \text{ high } p_T} = 2.1^{+0.62}_{-0.59}(\text{stat})^{+0.40}_{-0.43}(\text{sys})$$

$$\mu_{t\bar{t}H \text{ low } p_T} = 0.83^{+0.37}_{-0.37}(\text{stat})^{+0.48}_{-0.47}(\text{sys})$$

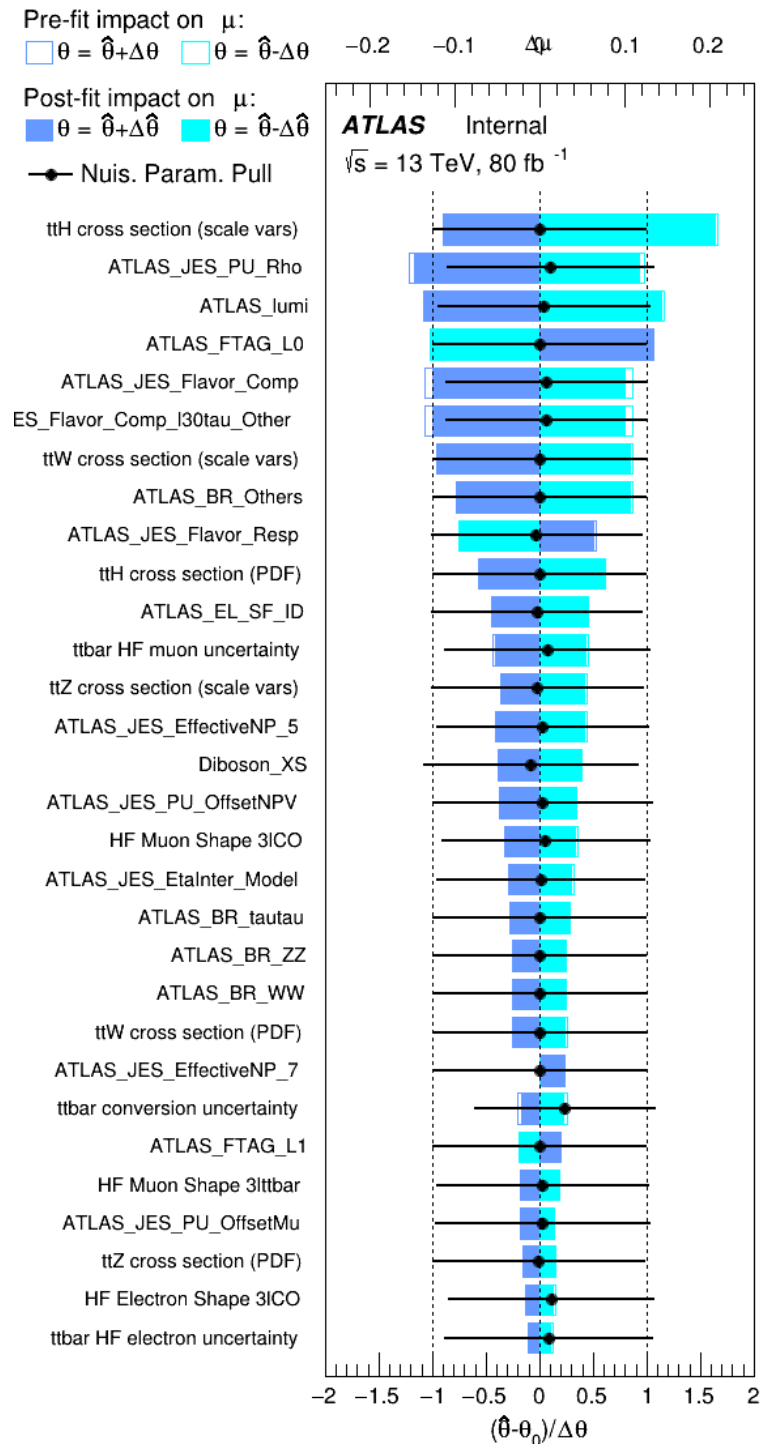
Table 54: Best fit μ values for $t\bar{t}H$ high p_T and $t\bar{t}H$ low p_T , where $\mu = \sigma_{\text{obs}}/\sigma_{\text{pred}}$

1652 The most prominent sources of systematic uncertainty, as measured by their impact on
 1653 $\mu_{t\bar{t}H \text{ high } p_T}$, are summarized in Table 55.

| Uncertainty Source | $\Delta\mu$ | |
|---------------------------------------|-------------|------|
| Jet Energy Scale | 0.25 | 0.23 |
| $t\bar{t}H$ cross-section (QCD Scale) | -0.11 | 0.21 |
| ATLAS Luminosity | -0.13 | 0.14 |
| Jet Flavor Tagging | 0.14 | 0.13 |
| $t\bar{t}W$ cross-section (QCD Scale) | -0.12 | 0.11 |
| Higgs Branching Ratio | -0.1 | 0.11 |
| $t\bar{t}H$ cross-section (PDF) | -0.07 | 0.08 |
| Electron ID | -0.06 | 0.06 |
| $t\bar{t}$ HF Muon Unc. | -0.05 | 0.06 |
| $t\bar{t}Z$ cross-section (QCD Scale) | -0.05 | 0.05 |
| Diboson cross-section | -0.05 | 0.05 |
| HF Muon Shape - 3l | -0.04 | 0.04 |
| Total Systematic Uncertainty | 0.40 | 0.43 |

Table 55: Summary of the most significant sources of systematic uncertainty on the measurement of $t\bar{t}H$ high p_T .

1654 The ranking and impact of those nuisance parameters with the largest contribution to the
 1655 overall uncertainty is shown in Figure 22.3.

Figure 22.3: Impact of systematic uncertainties on the measurement of high p_T $t\bar{t}H$ events

1656

The background composition of each of the fit regions is shown in Figure 22.4.

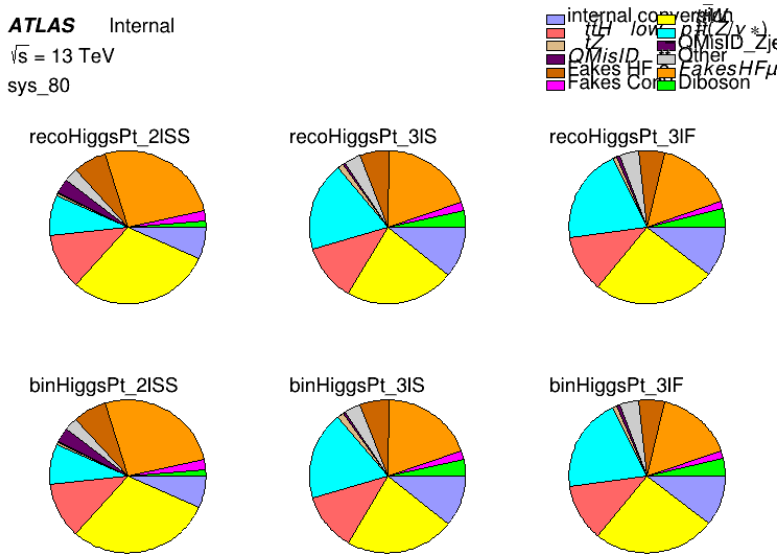


Figure 22.4: Background composition of the fit regions.

1657

22.2 Projected Results - 140 fb^{-1}

1658 As data collected in 2018 has not yet been unblinded for $t\bar{t}H - \text{ML}$ at the time of this note, data
 1659 from that year remains blinded. Instead, an Asimov fit is performed - with the MC prediction
 1660 being used both as the SM prediction as well as the data in the fit - in order to give expected
 1661 results.

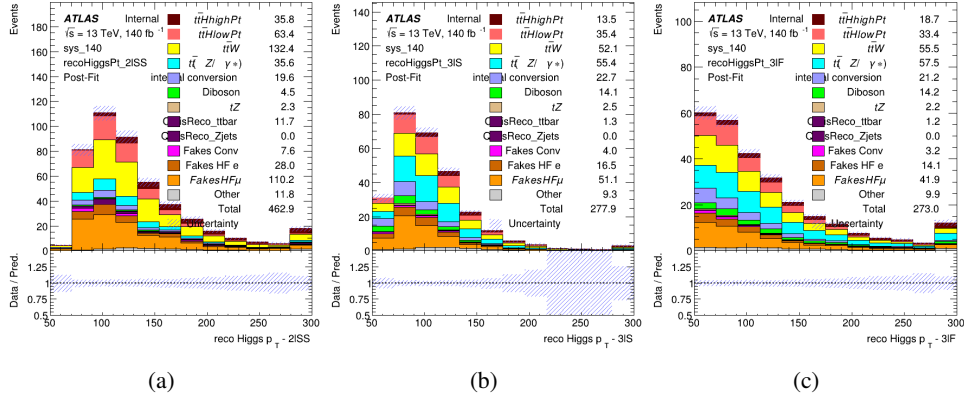


Figure 22.5: Blinded post-fit distributions of the reconstructed Higgs p_T in the three signal regions, (a) 2lSS, (b) 3lS, and (c) 3lF, for 140 fb^{-1} of data

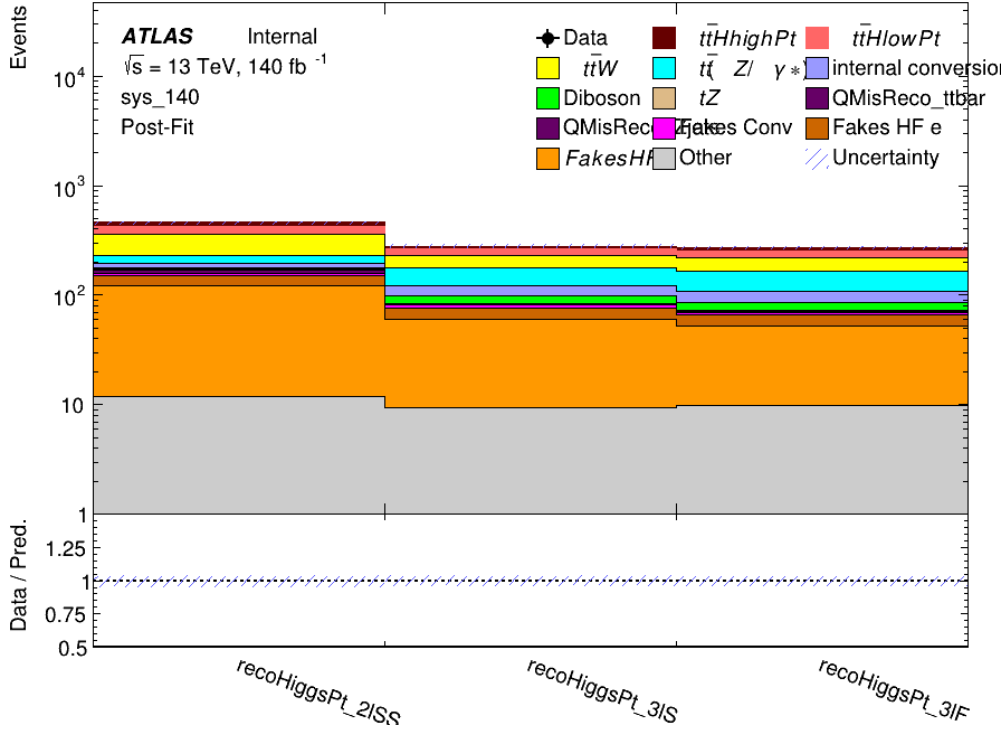


Figure 22.6: Post-fit summary of fit.

¹⁶⁶³ shown in [56](#). A significance of 2.0σ is expected for $t\bar{t}H$ high p_T , and a projected significance

¹⁶⁶⁴ 2.3σ is extracted for $t\bar{t}H$ low p_T .

$$\mu_{t\bar{t}H \text{ high } p_T} = 1.00^{+0.45}_{-0.43} (\text{stat})^{+0.31}_{-0.31} (\text{sys})$$

$$\mu_{t\bar{t}H \text{ low } p_T} = 1.00^{+0.29}_{-0.30} (\text{stat})^{+0.47}_{-0.46} (\text{sys})$$

Table 56: Best fit μ values for $t\bar{t}H$ high p_T and $t\bar{t}H$ low p_T , where $\mu = \sigma_{\text{obs}}/\sigma_{\text{pred}}$

¹⁶⁶⁵ The most prominent sources of systematic uncertainty, as measured by their impact on

¹⁶⁶⁶ $\mu_{t\bar{t}H \text{ high } p_T}$, are summarized in Table [57](#).

| Uncertainty Source | $\Delta\mu$ | |
|---------------------------------------|-------------|------|
| Jet Energy Scale | 0.2 | 0.18 |
| $t\bar{t}W$ cross-section (QCD Scale) | -0.12 | 0.11 |
| ATLAS Luminosity | -0.11 | 0.11 |
| Jet Flavor Tagging | 0.11 | 0.10 |
| $t\bar{t}H$ cross-section (QCD Scale) | -0.06 | 0.06 |
| Higgs Branching Ratio | -0.1 | 0.11 |
| $t\bar{t}H$ cross-section (PDF) | -0.07 | 0.08 |
| Electron ID | -0.05 | 0.05 |
| $t\bar{t}$ HF Muon Unc. | -0.04 | 0.06 |
| $t\bar{t}Z$ cross-section (QCD Scale) | -0.03 | 0.04 |
| Diboson cross-section | -0.03 | 0.03 |
| HF Muon Shape - 3l | -0.02 | 0.02 |
| Total Systematic Uncertainty | 0.31 | 0.31 |

Table 57: Summary of the most significant sources of systematic uncertainty on the measurement of $t\bar{t}H$ high p_T .

¹⁶⁶⁷ The ranking and impact of those nuisance parameters with the largest contribution to the

¹⁶⁶⁸ overall uncertainty is shown in Figure [22.7](#).

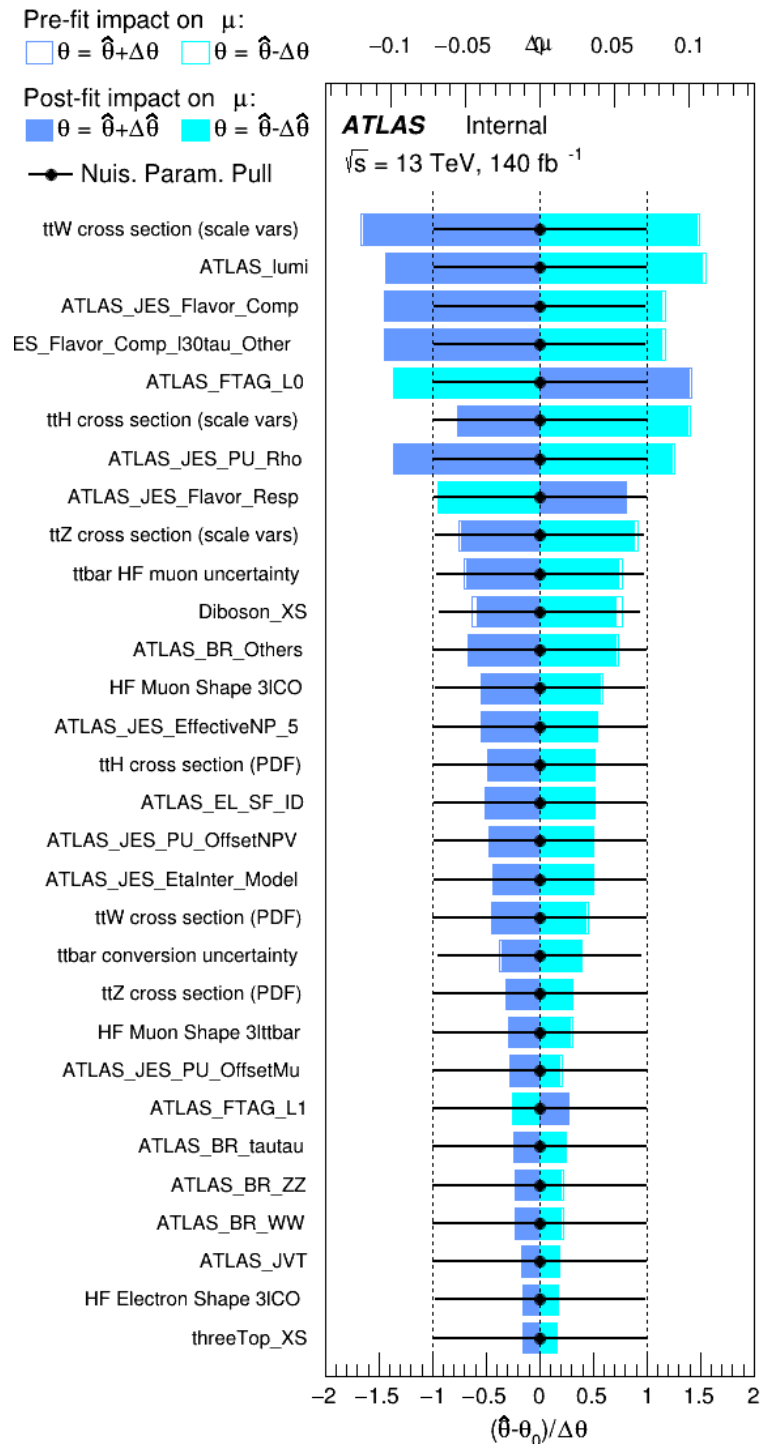


Figure 22.7: Impact of systematic uncertainties on the measurement of high p_T $t\bar{t}H$ events

1669

The background composition of each of the fit regions is shown in Figure 22.8.

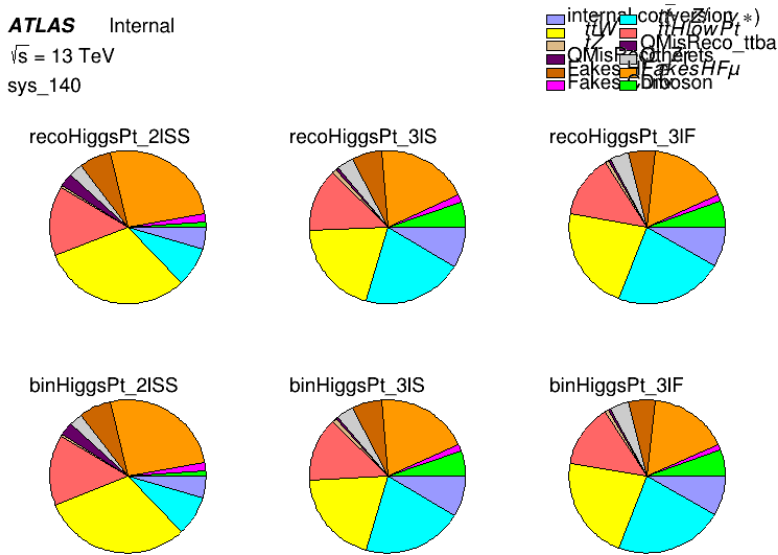


Figure 22.8: Background composition of the fit regions.

1670

Part VI

1671

Conclusion

1672 As search for the effects of dimension-six operators on $t\bar{t}H$ production is performed. An effective
 1673 field theory approached is used to parametrize the effects of high energy physics on the Higgs
 1674 momentum spectrum. The momentum spectrum is reconstructed using various MVA techniques,
 1675 and the limits on dimension-six operators are limited to X.

References

- 1676 [1] R. Oerter, *The theory of almost everything : the Standard Model, the unsung triumph of*
1677 *modern physics*, Pi Press, 2006, ISBN: 978-0-13-236678-6.
- 1679 [2] P. W. Higgs, *Broken Symmetries and the Masses of Gauge Bosons*,
1680 Phys. Rev. Lett. 13 (Oct, 1964) 508-509 ().
- 1681 [3] J. Goldstone, A. Salam and S. Weinberg, *Broken Symmetries*,
1682 Phys. Rev. **127** (3 1962) 965,
1683 URL: <https://link.aps.org/doi/10.1103/PhysRev.127.965>.
- 1684 [4] J. Ellis, *Higgs Physics*,
1685 (2013) 117, 52 pages, 45 figures, Lectures presented at the ESHEP 2013 School of
1686 High-Energy Physics, to appear as part of the proceedings in a CERN Yellow Report,
1687 URL: <https://cds.cern.ch/record/1638469>.
- 1688 [5] *Evidence for the associated production of the Higgs boson and a top quark pair with the*
1689 *ATLAS detector*, tech. rep. ATLAS-CONF-2017-077, CERN, 2017,
1690 URL: <https://cds.cern.ch/record/2291405>.
- 1691 [6] A. M. Sirunyan et al., *Observation of $t\bar{t}H$ Production*,
1692 *Physical Review Letters* **120** (2018), ISSN: 1079-7114,
1693 URL: <http://dx.doi.org/10.1103/PhysRevLett.120.231801>.

- 1694 [7] B. Dumont, S. Fichet and G. von Gersdorff,
 1695 *A Bayesian view of the Higgs sector with higher dimensional operators,*
 1696 *Journal of High Energy Physics* **2013** (2013), ISSN: 1029-8479,
 1697 URL: [http://dx.doi.org/10.1007/JHEP07\(2013\)065](http://dx.doi.org/10.1007/JHEP07(2013)065).
- 1698 [8] S. Banerjee, S. Mukhopadhyay and B. Mukhopadhyaya,
 1699 *Higher dimensional operators and the LHC Higgs data: The role of modified kinematics,*
 1700 *Physical Review D* **89** (2014), ISSN: 1550-2368,
 1701 URL: <http://dx.doi.org/10.1103/PhysRevD.89.053010>.
- 1702 [9] M. Zinser, ‘The Large Hadron Collider’, *Search for New Heavy Charged Bosons and*
 1703 *Measurement of High-Mass Drell-Yan Production in Proton—Proton Collisions,*
 1704 Springer International Publishing, 2018 47, ISBN: 978-3-030-00650-1,
 1705 URL: https://doi.org/10.1007/978-3-030-00650-1_4.
- 1706 [10] *Detector and Technology*, URL: <https://atlas.cern/discover/detector>.
- 1707 [11] M. Marjanovic, *ATLAS Tile calorimeter calibration and monitoring systems*, 2018.
- 1708 [12] M. Aaboud et al., *Observation of electroweak $W^\pm Z$ boson pair production in association*
 1709 *with two jets in pp collisions at $\sqrt{s} = 13$ TeV with the ATLAS detector,*
 1710 *Phys. Lett. B* **793** (2019) 469, arXiv: [1812.09740 \[hep-ex\]](https://arxiv.org/abs/1812.09740).
- 1711 [13] T. Gleisberg et al., *Event generation with SHERPA 1.1*, *JHEP* **02** (2009) 007,
 1712 arXiv: [0811.4622 \[hep-ph\]](https://arxiv.org/abs/0811.4622).
- 1713 [14] R. D. Ball et al., *Parton distributions for the LHC Run II*, *JHEP* **04** (2015) 040,
 1714 arXiv: [1410.8849 \[hep-ph\]](https://arxiv.org/abs/1410.8849).

- 1715 [15] H.-L. Lai et al., *New parton distributions for collider physics*,
1716 [Phys. Rev. D](#) **82** (2010) 074024, arXiv: [1007.2241 \[hep-ph\]](#).
- 1717 [16] S. Frixione, G. Ridolfi and P. Nason,
1718 *A positive-weight next-to-leading-order Monte Carlo for heavy flavour hadroproduction*,
1719 [JHEP](#) **09** (2007) 126, arXiv: [0707.3088 \[hep-ph\]](#).
- 1720 [17] E. Re, *Single-top Wt-channel production matched with parton showers using the*
1721 *POWHEG method*, [Eur. Phys. J. C](#) **71** (2011) 1547, arXiv: [1009.2450 \[hep-ph\]](#).
- 1722 [18] ATLAS Collaboration, *Electron efficiency measurements with the ATLAS detector using*
1723 *the 2015 LHC proton–proton collision data*, ATLAS-CONF-2016-024, 2016,
1724 URL: <https://cds.cern.ch/record/2157687>.
- 1725 [19] ATLAS Collaboration, *Measurement of the muon reconstruction performance of the*
1726 *ATLAS detector using 2011 and 2012 LHC proton–proton collision data*,
1727 [Eur. Phys. J. C](#) **74** (2014) 3130, arXiv: [1407.3935 \[hep-ex\]](#).
- 1728 [20] R. Narayan et al., *Measurement of the total and differential cross sections of a*
1729 *top-quark-antiquark pair in association with a W boson in proton-proton collisions at a*
1730 *centre-of-mass energy of 13 TeV with ATLAS detector at the Large Hadron Collider*,
1731 tech. rep. ATL-COM-PHYS-2020-217, CERN, 2020,
1732 URL: <https://cds.cern.ch/record/2712986>.
- 1733 [21] ATLAS Collaboration, *Jet Calibration and Systematic Uncertainties for Jets*
1734 *Reconstructed in the ATLAS Detector at $\sqrt{s} = 13 \text{ TeV}$* , ATL-PHYS-PUB-2015-015,
1735 2015, URL: <https://cds.cern.ch/record/2037613>.

- 1736 [22] ATLAS Collaboration,
 1737 *Selection of jets produced in 13 TeV proton–proton collisions with the ATLAS detector,*
 1738 ATLAS-CONF-2015-029, 2015, URL: <https://cds.cern.ch/record/2037702>.
- 1739 [23] ATLAS Collaboration, *Performance of pile-up mitigation techniques for jets in pp*
 1740 *collisions at $\sqrt{s} = 8$ TeV using the ATLAS detector*, *Eur. Phys. J. C* **76** (2016) 581,
 1741 arXiv: [1510.03823 \[hep-ex\]](https://arxiv.org/abs/1510.03823).
- 1742 [24] ATLAS Collaboration, *Performance of missing transverse momentum reconstruction*
 1743 *with the ATLAS detector in the first proton–proton collisions at $\sqrt{s} = 13$ TeV,*
 1744 ATL-PHYS-PUB-2015-027, 2015, URL: <https://cds.cern.ch/record/2037904>.
- 1745 [25] 2021, URL: https://twiki.cern.ch/twiki/bin/view/AtlasProtected/BTagCalibrationRecommendationsRelease21#Tools_for_Flavor_Tagging_Calibra.
- 1748 [26] P. S. A. Hoecker, *TMVA 4 Toolkit for Multivariate Data Analysis with ROOT*,
 1749 arXiv:physics/0703039 (2013).
- 1750 [27] F. Cardillo et al., *Measurement of the fiducial and differential cross-section of a top*
 1751 *quark pair in association with a Z boson at 13 TeV with the ATLAS detector*, (2019),
 1752 URL: <https://cds.cern.ch/record/2672207>.
- 1753 [28] T. Chen and C. Guestrin, ‘XGBoost: A Scalable Tree Boosting System’,
 1754 *Proceedings of the 22nd ACM SIGKDD International Conference on Knowledge*
 1755 *Discovery and Data Mining*, KDD ’16, ACM, 2016 785, ISBN: 978-1-4503-4232-2,
 1756 URL: <http://doi.acm.org/10.1145/2939672.2939785>.

- 1757 [29] ATLAS Collaboration, *Luminosity determination in pp collisions at $\sqrt{s} = 7 \text{ TeV}$ using*
1758 *the ATLAS detector at the LHC*, [Eur. Phys. J. C **71** \(2011\) 1630](#),
1759 arXiv: [1101.2185 \[hep-ex\]](#).
- 1760 [30] G. Avoni et al.,
1761 *The new LUCID-2 detector for luminosity measurement and monitoring in ATLAS*,
1762 [JINST **13** \(2018\) P07017](#).
- 1763 [31] G. Aad, T. Abajyan, B. Abbott and etal, *Jet energy resolution in proton-proton collisions*
1764 *at $\sqrt{s} = 7 \text{ TeV}$ recorded in 2010 with the ATLAS detector*,
1765 [The European Physical Journal C **73** \(2013\) 2306](#), ISSN: 1434-6052,
1766 URL: <https://doi.org/10.1140/epjc/s10052-013-2306-0>.
- 1767 [32] A. Collaboration, *Performance of b -jet identification in the ATLAS experiment*,
1768 [Journal of Instrumentation **11** \(2016\) P04008](#),
1769 URL: <http://stacks.iop.org/1748-0221/11/i=04/a=P04008>.
- 1770 [33] *Observation of the associated production of a top quark and a Z boson at 13 TeV with*
1771 *ATLAS*, (2020), URL: <https://cds.cern.ch/record/2722504>.

¹⁷⁷² **List of contributions**

1773

¹⁷⁷⁴ **Appendices**

¹⁷⁷⁵ **.1 Non-prompt lepton MVA**

1776 A lepton MVA has been developed to better reject non-prompt leptons than standard cut
1777 based selections based upon impact parameter, isolation and PID. The name of this MVA is
1778 **PromptLeptonIso**. The full set of studies and detailed explanation can be found in [20].

1779 The decays of W and Z bosons are commonly selected by the identification of one or two
1780 electrons or muons. The negligible lifetimes of these bosons mean that the leptons produced in the
1781 decay originate from the interaction vertex and are thus labelled “prompt”. Analyses using these
1782 light leptons impose strict reconstruction quality, isolation and impact parameter requirements
1783 to remove “fake” leptons. A significant source of the fake light leptons are non-prompt leptons
1784 produced in decays of hadrons that contain bottom (b) or charm (c) quarks. Such hadrons
1785 typically have microscopically significant lifetimes that can be detected experimentally.

1786 These non-prompt leptons can also pass the tight selection criteria. In analyses that
1787 involve top (t) quarks, which decay almost exclusively into a W boson and a b quark, non-
1788 prompt leptons from the semileptonic decay of bottom and charm hadrons can be a significant
1789 source of background events. This is particularly the case in the selection of same-sign dilepton
1790 and multilepton final states.

1791 The main idea is to identify non-prompt light leptons using lifetime information associated
1792 with a track jet that matches the selected light lepton. This lifetime information is computed
1793 using tracks contained within the jet. Typically, lepton lifetime is determined using the impact
1794 parameter of the track reconstructed by the inner tracking detector which is matched to the recon-
1795 structed lepton. Using additional reconstructed charged particle tracks increases the precision of

1796 identifying the displaced decay vertex of bottom or charm hadrons that produced a non-prompt
 1797 light lepton. The MVA also includes information related to the isolation of the lepton to reject
 1798 non-prompt leptons.

1799 **PromptLeptonIso** is a gradient boosted BDT. The training of the BDT is performed on
 1800 leptons selected from the PowHEG+PYTHIA6 non-allhad $t\bar{t}$ MC sample. Eight variables are used
 1801 to train the BDT in order to discriminate between prompt and non-prompt leptons. The track
 1802 jets that are matched to the non-prompt leptons correspond to jets initiated by b or c quarks, and
 1803 may contain a displaced vertex. Consequently, three of the selected variables are used to identify
 1804 b-tag jets by standard ATLAS flavour tagging algorithms. Two variables use the relationship
 1805 between the track jet and lepton: the ratio of the lepton p_T with respect to the track jet p_T and
 1806 ΔR between the lepton and the track jet axis. Finally three additional variables test whether the
 1807 reconstructed lepton is isolated: the number of tracks collected by the track jet and the lepton
 1808 track and calorimeter isolation variables. Table 58 describes the variables used to train the BDT
 1809 algorithm. The choice of input variables has been extensively discussed with Egamma, Muon,
 1810 Tracking, and Flavour Tagging CP groups.

| Variable | Description |
|--|---|
| N_{track} in track jet | Number of tracks collected by the track jet |
| $\text{IP2 log}(P_b/P_{\text{light}})$ | Log-likelihood ratio between the b and light jet hypotheses with the IP2D algorithm |
| $\text{IP3 log}(P_b/P_{\text{light}})$ | Log-likelihood ratio between the b and light jet hypotheses with the IP3D algorithm |
| $N_{\text{TrkAtVtx}} \text{ SV + JF}$ | Number of tracks used in the secondary vertex found by the SV1 algorithm in addition to the number of tracks from secondary vertices found by the JetFitter algorithm with at least two tracks |
| $p_T^{\text{lepton}} / p_T^{\text{track jet}}$ | The ratio of the lepton p_T and the track jet p_T |
| $\Delta R(\text{lepton}, \text{track jet})$ | ΔR between the lepton and the track jet axis |
| $p_T^{\text{VarCone30}} / p_T$ | Lepton track isolation, with track collecting radius of $\Delta R < 0.3$ |
| $E_T^{\text{TopoCone30}} / p_T$ | Lepton calorimeter isolation, with topological cluster collecting radius of $\Delta R < 0.3$ |

Table 58: A table of the variables used in the training of **PromptLeptonIso**.

1811 The output distribution of the BDT is shown in Figure .1.

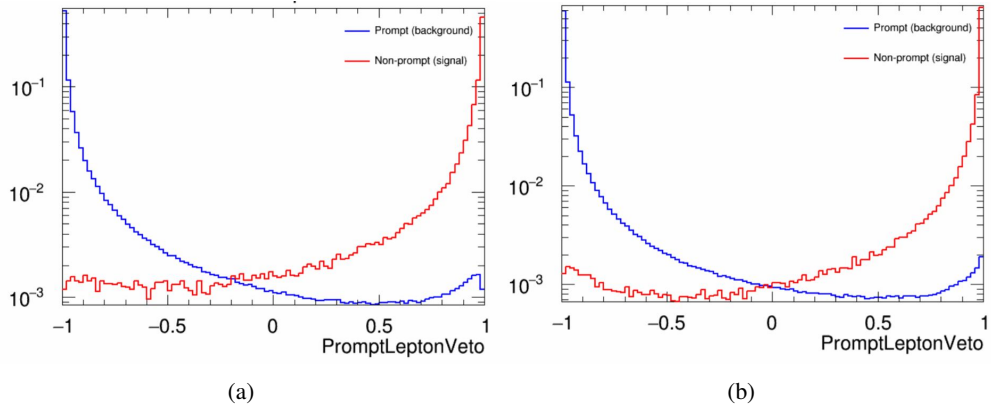


Figure .9: Distribution of the PLV BDT discriminant for (a) electrons and (b) muons

1812 The ROC curve for the BDT response, compared to the standard `FixedCutTight` WP, is
1813 shown in figure .1, which shows a clear improvement when using this alternate training.

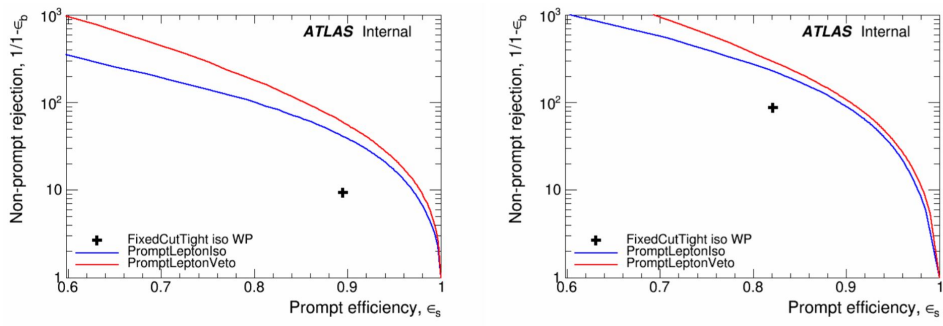


Figure .10: ROC curves for the PLV as well as the performance of the standard FixedCutTight WP for (left) electrons and (right) muons

1814 A cutoff value of -0.7 for electrons and -0.5 for muons are chosen as the WPs for this
 1815 MVA, based on an optimisation of S/\sqrt{B} performed in the preselection regions of the $t\bar{t}H - ML$
 1816 analysis, which have a signature similar to that of this analysis.

1817 The efficiency of the tight `PromptLeptonIso` working point is measured using the tag
1818 and probe method with $Z \rightarrow \ell^+ \ell^-$ events. Such calibration are performed by analysers from
1819 this analysis in communication with the Egamma and Muon combined performance groups. The
1820 scale factor are approximately 0.92 for $10 < p_T < 15$ GeV, and averaging at 0.98 to 0.99 for
1821 higher p_T leptons. An extra systematic is applied to muons within $\Delta R < 0.6$ of a calorimeter
1822 jet, since there is a strong dependence on the scale factor due to the presence of these jets. For
1823 electrons, the dominant systematics is coming from pile-up dependence. Overall the systematics
1824 are a maximum of 3% at low p_T and decreasing at a function of p_T .

1825 **.2 Non-prompt CR Modelling**

1826 In order to further validate the modeling in each of the non-prompt CRs, additional
 1827 kinematic plots are made in the Z+jets CR and $t\bar{t}$ CR in each of the continuous b-tag regions,
 1828 after the correction factors detailed in Section 12.3 have been applied.

1829 In the case of the Z+jets CR, the p_T spectrum of the lepton originating from the W
 1830 candidate is shown, as this is the distribution used to extract the scale factor applied to Z+jets.
 1831 These plots are shown in Figures .11 and .12.

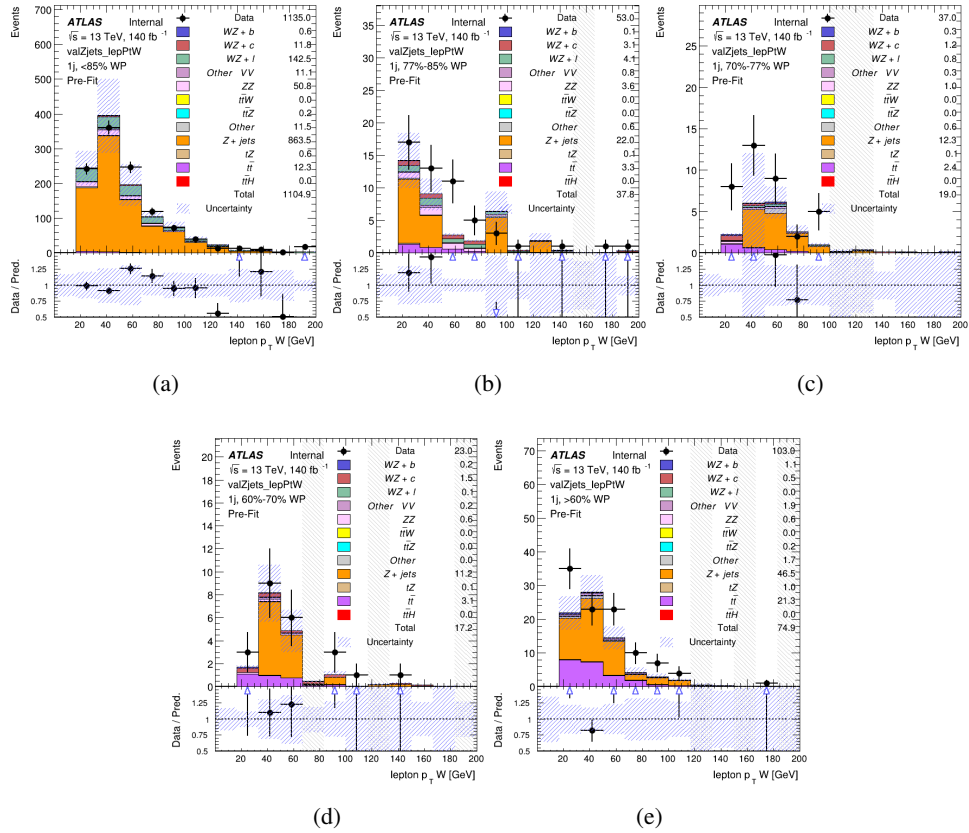


Figure .11: Comparisons between the data and MC distributions of the p_T of the lepton originating from the W-candidate in the Z+jets CR for each of the 1-jet b-tag working point regions

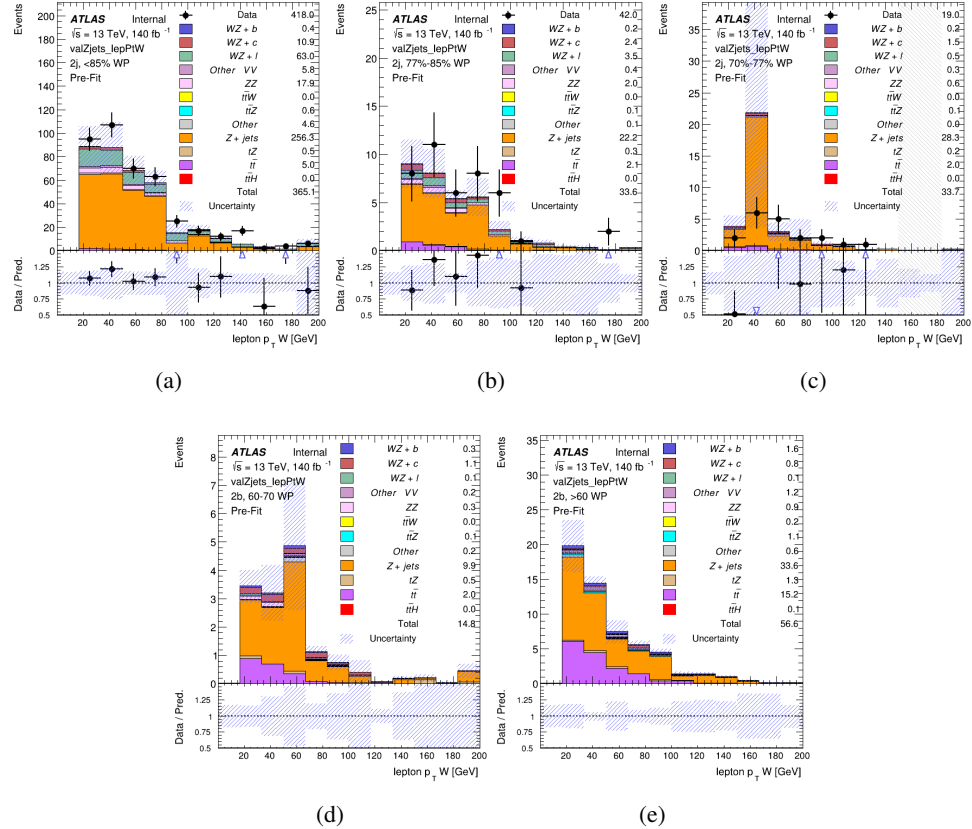


Figure .12: Comparisons between the data and MC distributions of the p_T of the lepton originating from the W-candidate in the Z+jets CR for each of the 2-jet b-tag working point regions

1832 The same is shown for the $t\bar{t}$ CR, but the p_T of the OS lepton is used instead as a
1833 representation of the modeling, as the lepton from the W is not well defined for $t\bar{t}$ events. These
1834 plots are shown in Figures .13 and .14.

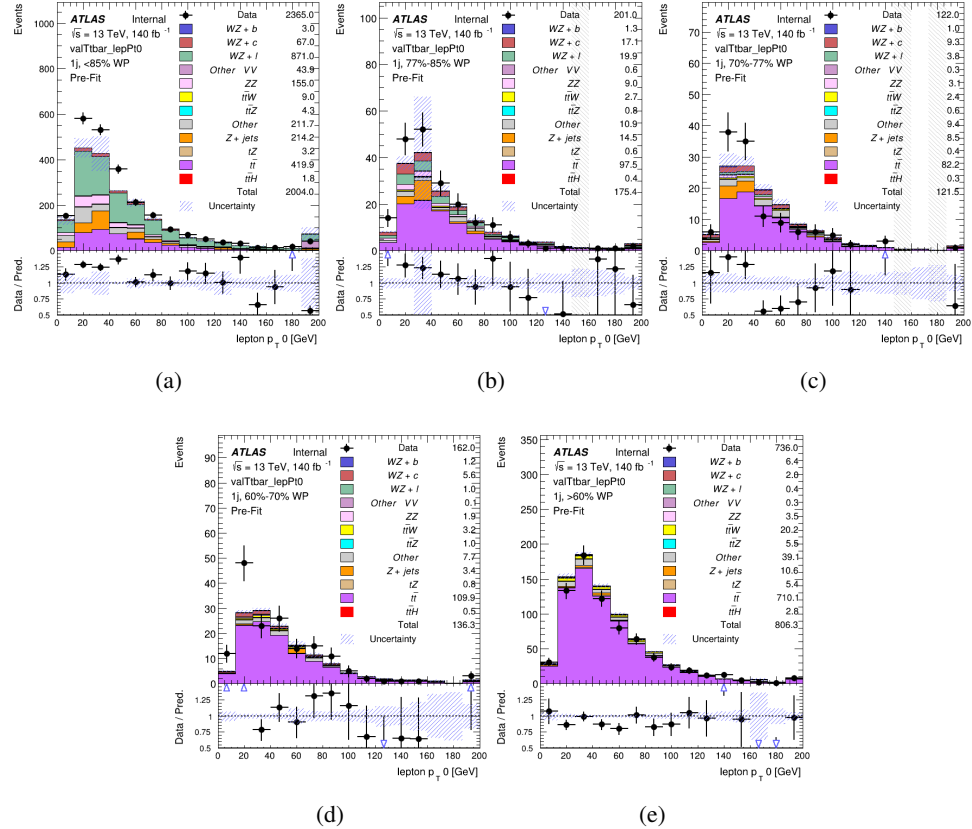


Figure .13: Comparisons between the data and MC distributions of the p_T of the OS lepton in the $t\bar{t}$ CR for each of the 1-jet b-tag working point regions

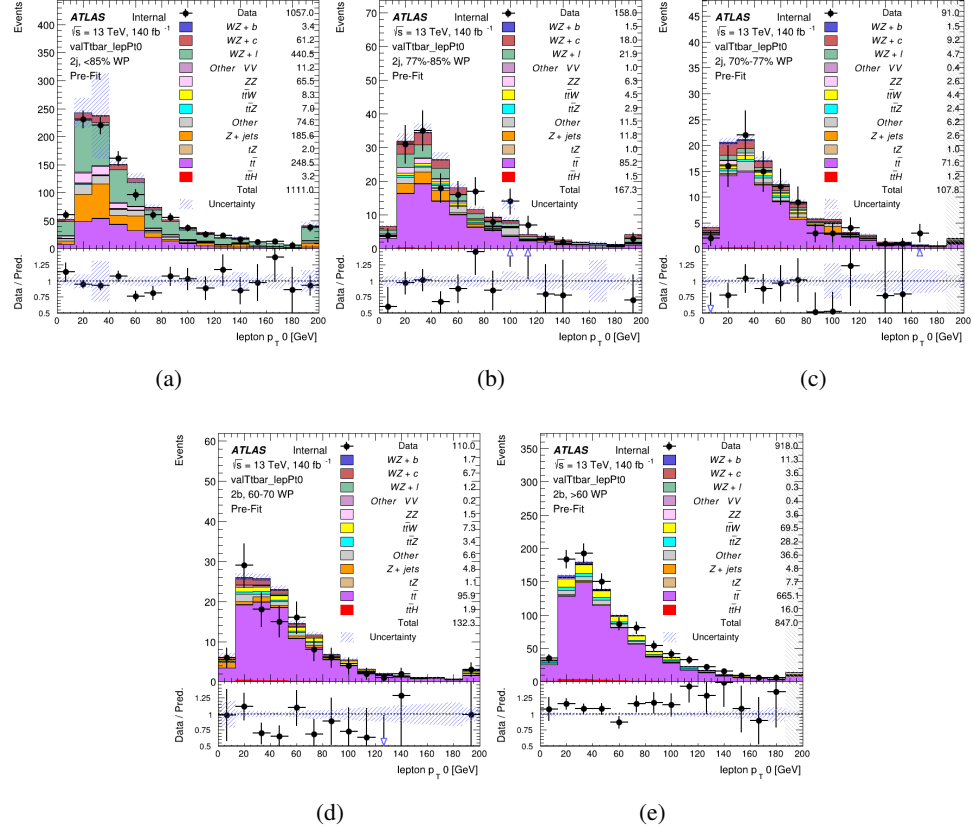


Figure 14: Comparisons between the data and MC distributions of the p_T of the OS lepton in the $t\bar{t}$ CR for each of the 2-jet b-tag working point regions

1835 .3 tZ Interference Studies

1836 Because it includes an on-shell Z boson as well as a b-jet and W from the top decay, tZ
1837 production represents an identical final state to WZ + b-jet. This implies the possibility of matrix
1838 level interference between these two processes not accounted for in the Monte Carlo simulations,
1839 which consider the two processes independently. Truth level studies are performed in order to
1840 estimate the impact of these interference effects.

1841 In order to estimate the matrix level interference effects between tZ and WZ + b-jet, two
1842 different sets of simulations are produced using MadGraph 5 [**Madgraph**] - one which simulates
1843 these two processes independently, and another where they are produced simultaneously, such
1844 that interference effects are present. These two sets of samples are then compared, and the
1845 difference between them can be taken to represent any interference effects.

1846 MadGraph simulations of 10,000 tZ and 10,000 WZ + b-jet events are produced, along
1847 with 20,000 events where both are present, in the fiducial region where three leptons and at least
1848 one jet are produced.

1849 A selection mimicking the preselection used in the main analysis is applied to the samples:
1850 The SS leptons are required to have $p_T > 20$ GeV, and > 10 GeV is required for the OS lepton.
1851 The associated b-jet is required to have $p_T > 25$ GeV, and all physics objects are required to fall
1852 in a range of $|\eta| < 2.5$.

1853 The kinematics of these samples after the selection has been applied are shown below:

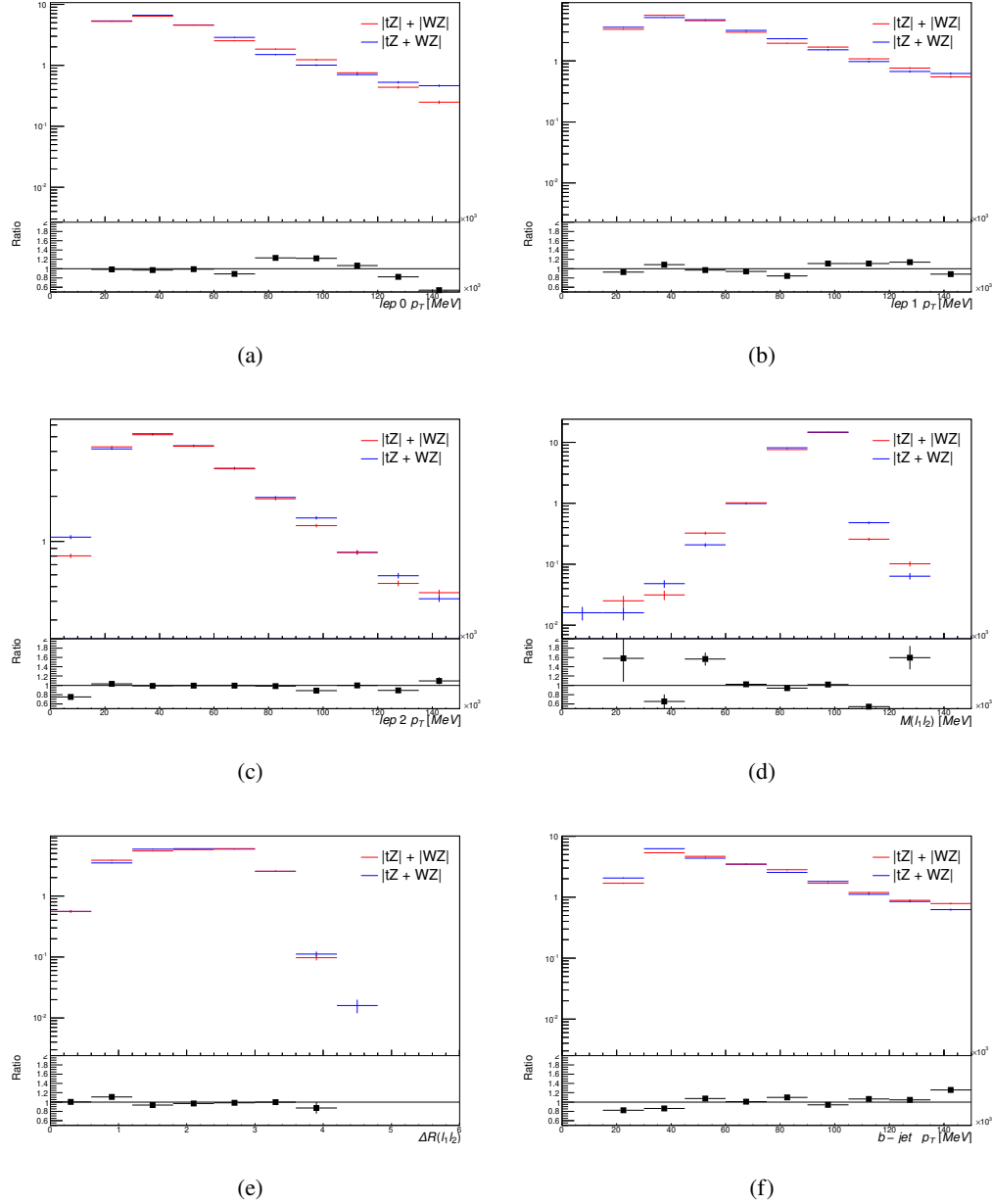


Figure .15: Comparisons between (a) the p_T of the lepton from the W, (b) and (c) show the p_T of the lepton from the Z, (d) the invariant mass of the Z-candidate, (e) ΔR of the leptons from the Z, and (f) the p_T of the b-jet, for WZ and tZ events generated with interference effects (blue) and without interference effects (red).

1854 The overall cross-section of the two methods agree within error, and no significant differ-
1855 ences in the kinematic distributions are seen. It is therefore concluded that interference effects
1856 do not significantly impact the results.

1857 **.4 Alternate tZ Inclusive Fit**

1858 **.4.1 tZ Inclusive Fit**

1859 While tZ is often considered as a distinct process from WZ + b, this could also be considered part
1860 of the signal. Alternate studies are performed where, using the same framework as the nominal
1861 analysis, a measurement of WZ + b is performed that includes tZ as part of WZ+b.

1862 Because of this change, the tZ CR is no longer necessary, and only the five pseudo-
1863 continuous b-tag regions are used in the fit. Further, systematics related to the tZ cross-section
1864 are removed from the fit, as they are now encompassed by the normalization measurement of
1865 WZ + b. All other systematic uncertainties are carried over from the nominal analysis.

1866 An expected WZ + b cross-section of $4.1^{+0.78}_{-0.74}(\text{stat})^{+0.53}_{-0.52}(\text{sys}) \text{ fb}$ is extracted from the fit,
1867 with an expected significance of 4.0σ .

1868 The impact of the predominate systematics are summarized in Table 59.

| Uncertainty Source | $\Delta\mu$ | |
|---------------------------------|-------------|-------|
| WZ + light cross-section | 0.08 | -0.08 |
| Jet Energy Scale | -0.06 | 0.08 |
| Luminosity | -0.05 | 0.06 |
| WZ + charm cross-section | -0.04 | 0.05 |
| Other Diboson + b cross-section | -0.04 | 0.04 |
| WZ cross-section - QCD scale | -0.04 | 0.03 |
| t̄t cross-section | -0.03 | 0.03 |
| Jet Energy Resolution | -0.03 | 0.03 |
| Flavor tagging | -0.03 | 0.03 |
| Z+jets cross section | -0.02 | 0.02 |
| Total Systematic Uncertainty | -0.15 | 0.16 |

Table 59: Summary of the most significant sources of systematic uncertainty on the measurement of WZ + b with exactly one associated jet.

1869 **.4.2 Floating tZ**

1870 In order to quantify the impact of the tZ uncertainty on the fit, an alternate fit strategy is used
1871 where the tZ normalization is allowed to float. This normalization factor replaces the cross-
1872 section uncertainty on tZ, and all other parameters of the fit remain the same.

1873 An uncertainty of 17% on the normalization of tZ is extracted from the fit, compared to a
1874 theory uncertainty of 15% applied to the tZ cross-section. The measured uncertainties on WZ
1875 remain the same.

1876 **.5 DSID list**

Data:

```
data15_13TeV.AllYear.physics_Main.PhysCont.DAOD_HIGG8D1.grp15_v01_p4134
data16_13TeV.AllYear.physics_Main.PhysCont.DAOD_HIGG8D1.grp16_v01_p4134
data17_13TeV.AllYear.physics_Main.PhysCont.DAOD_HIGG8D1.grp17_v01_p4134
data18_13TeV.AllYear.physics_Main.PhysCont.DAOD_HIGG8D1.grp18_v01_p4134
```

mc16a:

```
mc16_13TeV.361603.PowhegPy8EG_CT10nloME_AZNLOCTEQ6L1_ZZllll_mll4.deriv.DAOD_HIGG8D1.e4475_s3126_r9364_r9315_p4133
mc16_13TeV.361602.PowhegPy8EG_CT10nloME_AZNLOCTEQ6L1_WZlvvv_mll4.deriv.DAOD_HIGG8D1.e4054_s3126_r9364_r9315_p4133
mc16_13TeV.361604.PowhegPy8EG_CT10nloME_AZNLOCTEQ6L1_ZZvvll_mll4.deriv.DAOD_HIGG8D1.e4475_s3126_r9364_r9315_p4133
mc16_13TeV.361600.PowhegPy8EG_CT10nloME_AZNLOCTEQ6L1_WWlvvv.deriv.DAOD_HIGG8D1.e4616_s3126_r9364_r9315_p4133
mc16_13TeV.361605.PowhegPy8EG_CT10nloME_AZNLOCTEQ6L1_ZZvvvv_mll4.deriv.DAOD_HIGG8D1.e4054_s3126_s3136_r9364_r9315_p4133
mc16_13TeV.361601.PowhegPy8EG_CT10nloME_AZNLOCTEQ6L1_WZlVll_mll4.deriv.DAOD_HIGG8D1.e4475_s3126_r9364_r9315_p4133
mc16_13TeV.364286.Sherpa_222_NNPDF30NNLO_llvjj_ss_EW4.deriv.DAOD_HIGG8D1.e6055_e5984_s3126_r9364_r9315_p3983 mc16_13TeV.364285.Sherpa_222_NNPDF30NNLO_llvjj_EW6_OFPlus.deriv.DAOD_HIGG8D1.e7421_e5984_s3126_r9364_r9315_p4133
mc16_13TeV.364740.MGPy8EG_NNPDF30NLO_A14NNPDF23LO_lvlljj_EW6_SFPlus.deriv.DAOD_HIGG8D1.e7421_e5984_s3126_r9364_r9315_p4133
mc16_13TeV.364742.MGPy8EG_NNPDF30NLO_A14NNPDF23LO_lvlljj_EW6_SFPlus.deriv.DAOD_HIGG8D1.e7421_e5984_s3126_r9364_r9315_p4133
mc16_13TeV.364253.Sherpa_222_NNPDF30NNLO_llv.deriv.DAOD_HIGG8D1.e5916_s3126_r9364_r9315_p4133
mc16_13TeV.364250.Sherpa_222_NNPDF30NNLO_lll.deriv.DAOD_HIGG8D1.e5894_s3126_r9364_r9315_p4133
mc16_13TeV.364254.Sherpa_222_NNPDF30NNLO_llv.deriv.DAOD_HIGG8D1.e5916_s3126_r9364_r9315_p4133
mc16_13TeV.364255.Sherpa_222_NNPDF30NNLO_lvvv.deriv.DAOD_HIGG8D1.e5916_s3126_r9364_r9315_p4133
mc16_13TeV.410155.aMcAtNloPythia8EvtGen_MEN30NLO_A14N23LO_ttW.deriv.DAOD_HIGG8D1.e5070_s3126_r9364_r9315_p4133
mc16_13TeV.410156.aMcAtNloPythia8EvtGen_MEN30NLO_A14N23LO_ttZnunu.deriv.DAOD_HIGG8D1.e5070_s3126_r9364_r9315_p4133
mc16_13TeV.410157.aMcAtNloPythia8EvtGen_MEN30NLO_A14N23LO_ttZqq.deriv.DAOD_HIGG8D1.e5070_s3126_r9364_r9315_p4133
mc16_13TeV.410218.aMcAtNloPythia8EvtGen_MEN30NLO_A14N23LO_ttee.deriv.DAOD_HIGG8D1.e5070_s3126_r9364_r9315_p4133
mc16_13TeV.410219.aMcAtNloPythia8EvtGen_MEN30NLO_A14N23LO_ttmumu.deriv.DAOD_HIGG8D1.e5070_s3126_r9364_r9315_p4133
mc16_13TeV.410220.aMcAtNloPythia8EvtGen_MEN30NLO_A14N23LO_ttautau.deriv.DAOD_HIGG8D1.e5070_s3126_r9364_r9315_p4133
mc16_13TeV.412063.aMcAtNloPythia8EvtGen_tllq_NNPDF30_nf4_A14.deriv.DAOD_TOPQ1.e7054_e5984_s3126_r9364_r9315_p4174
mc16_13TeV.410276.aMcAtNloPythia8EvtGen_MEN30NLO_A14N23LO_ttee_mll_1_5.deriv.DAOD_HIGG8D1.e6087_e5984_s3126_r9364_r9315_p4133
mc16_13TeV.410277.aMcAtNloPythia8EvtGen_MEN30NLO_A14N23LO_ttmumu_mll_1_5.deriv.DAOD_HIGG8D1.e6087_e5984_s3126_r9364_r9315_p4133
mc16_13TeV.410278.aMcAtNloPythia8EvtGen_MEN30NLO_A14N23LO_ttautau_mll_1_5.deriv.DAOD_HIGG8D1.e6087_e5984_s3126_r9364_r9315_p4133
mc16_13TeV.410397.MadGraphPythia8EvtGen_ttbar_wbee_MEN30LO_A14N23LO.deriv.DAOD_HIGG8D1.e6086_e5984_s3126_r9364_r9315_p4133
```

mc16_13TeV.410398.MadGraphPythia8EvtGen_ttbar_wbmumu_MEN30LO_A14N23LO.deriv.DAOD_HIGG8D1.e6086_e5984_s3126_r9364_r9315_p4133
 mc16_13TeV.410399.MadGraphPythia8EvtGen_ttbar_wbtautau_MEN30LO_A14N23LO.deriv.DAOD_HIGG8D1.e6086_e5984_s3126_r9364_r9315_p4133
 mc16_13TeV.410658.PhPy8EG_A14_tchan_BW50_lept_top.deriv.DAOD_HIGG8D1.e6671_e5984_s3126_r9364_r9315_p4133
 mc16_13TeV.410659.PhPy8EG_A14_tchan_BW50_lept_antitop.deriv.DAOD_HIGG8D1.e6671_e5984_s3126_r9364_r9315_p4133
 mc16_13TeV.410644.PowhegPythia8EvtGen_A14_singletop_schan_lept_top.deriv.DAOD_HIGG8D1.e6527_e5984_s3126_r9364_r9315_p4133
 mc16_13TeV.410645.PowhegPythia8EvtGen_A14_singletop_schan_lept_antitop.deriv.DAOD_HIGG8D1.e6527_e5984_s3126_r9364_r9315_p4133
 mc16_13TeV.304014.MadGraphPythia8EvtGen_A14NNPDF23_3top_SM.deriv.DAOD_HIGG8D1.e4324_s3126_r9364_r9315_p4133
 mc16_13TeV.410080.MadGraphPythia8EvtGen_A14NNPDF23_4topSM.deriv.DAOD_HIGG8D1.e4111_s3126_r9364_r9315_p4133
 mc16_13TeV.410081.MadGraphPythia8EvtGen_A14NNPDF23_ttbarWW.deriv.DAOD_HIGG8D1.e4111_s3126_r9364_r9315_p4133
 mc16_13TeV.364100.Sherpa_221_NNPDF30NNLO_Zmumu_MAXHTPTV0_70_CVetoBVeto.deriv.DAOD_HIGG8D1.e5271_s3126_r9364_r9315_p4133
 mc16_13TeV.364101.Sherpa_221_NNPDF30NNLO_Zmumu_MAXHTPTV0_70_CFilterBVeto.deriv.DAOD_HIGG8D1.e5271_s3126_r9364_r9315_p4133
 mc16_13TeV.364102.Sherpa_221_NNPDF30NNLO_Zmumu_MAXHTPTV0_70_BFilter.deriv.DAOD_HIGG8D1.e5271_s3126_r9364_r9315_p4133
 mc16_13TeV.364103.Sherpa_221_NNPDF30NNLO_Zmumu_MAXHTPTV70_140_CVetoBVeto.deriv.DAOD_HIGG8D1.e5271_s3126_r9364_r9315_p4133
 mc16_13TeV.364104.Sherpa_221_NNPDF30NNLO_Zmumu_MAXHTPTV70_140_CFilterBVeto.deriv.DAOD_HIGG8D1.e5271_s3126_r9364_r9315_p4133
 mc16_13TeV.364106.Sherpa_221_NNPDF30NNLO_Zmumu_MAXHTPTV140_280_CVetoBVeto.deriv.DAOD_HIGG8D1.e5271_s3126_r9364_r9315_p4133
 mc16_13TeV.364107.Sherpa_221_NNPDF30NNLO_Zmumu_MAXHTPTV140_280_CFilterBVeto.deriv.DAOD_HIGG8D1.e5271_s3126_r9364_r9315_p4133
 mc16_13TeV.364108.Sherpa_221_NNPDF30NNLO_Zmumu_MAXHTPTV140_280_BFilter.deriv.DAOD_HIGG8D1.e5271_s3126_r9364_r9315_p4133
 mc16_13TeV.364109.Sherpa_221_NNPDF30NNLO_Zmumu_MAXHTPTV280_500_CVetoBVeto.deriv.DAOD_HIGG8D1.e5271_s3126_r9364_r9315_p4133
 mc16_13TeV.364110.Sherpa_221_NNPDF30NNLO_Zmumu_MAXHTPTV280_500_CFilterBVeto.deriv.DAOD_HIGG8D1.e5271_s3126_r9364_r9315_p4133
 mc16_13TeV.364111.Sherpa_221_NNPDF30NNLO_Zmumu_MAXHTPTV280_500_BFilter.deriv.DAOD_HIGG8D1.e5271_e5984_s3126_r9364_r9315_p4133
 mc16_13TeV.364111.Sherpa_221_NNPDF30NNLO_Zmumu_MAXHTPTV280_500_BFilter.deriv.DAOD_HIGG8D1.e5271_s3126_r9364_r9315_p4133
 mc16_13TeV.364112.Sherpa_221_NNPDF30NNLO_Zmumu_MAXHTPTV500_1000.deriv.DAOD_HIGG8D1.e5271_s3126_r9364_r9315_p4133
 mc16_13TeV.364113.Sherpa_221_NNPDF30NNLO_Zmumu_MAXHTPTV1000_E_CMS.deriv.DAOD_HIGG8D1.e5271_s3126_r9364_r9315_p4133
 mc16_13TeV.364114.Sherpa_221_NNPDF30NNLO_Zee_MAXHTPTV0_70_CVetoBVeto.deriv.DAOD_HIGG8D1.e5299_s3126_r9364_r9315_p4133
 mc16_13TeV.364115.Sherpa_221_NNPDF30NNLO_Zee_MAXHTPTV0_70_CFilterBVeto.deriv.DAOD_HIGG8D1.e5299_s3126_r9364_r9315_p4133
 mc16_13TeV.364116.Sherpa_221_NNPDF30NNLO_Zee_MAXHTPTV0_70_BFilter.deriv.DAOD_HIGG8D1.e5299_s3126_r9364_r9315_p4133
 mc16_13TeV.364117.Sherpa_221_NNPDF30NNLO_Zee_MAXHTPTV70_140_CVetoBVeto.deriv.DAOD_HIGG8D1.e5299_s3126_r9364_r9315_p4133
 mc16_13TeV.364118.Sherpa_221_NNPDF30NNLO_Zee_MAXHTPTV70_140_CFilterBVeto.deriv.DAOD_HIGG8D1.e5299_s3126_r9364_r9315_p4133
 mc16_13TeV.364119.Sherpa_221_NNPDF30NNLO_Zee_MAXHTPTV70_140_BFilter.deriv.DAOD_HIGG8D1.e5299_s3126_r9364_r9315_p4133
 mc16_13TeV.364120.Sherpa_221_NNPDF30NNLO_Zee_MAXHTPTV140_280_CVetoBVeto.deriv.DAOD_HIGG8D1.e5299_s3126_r9364_r9315_p4133
 mc16_13TeV.364121.Sherpa_221_NNPDF30NNLO_Zee_MAXHTPTV140_280_CFilterBVeto.deriv.DAOD_HIGG8D1.e5299_s3126_r9364_r9315_p4133

mc16_13TeV.364122.Sherpa_221_NNPDF30NNLO_Zee_MAXHTPTV140_280_BFilter.deriv.DAOD_HIGG8D1.e5299_s3126_r9364_r9315_p4133
 mc16_13TeV.364123.Sherpa_221_NNPDF30NNLO_Zee_MAXHTPTV280_500_CVetoBVeto.deriv.DAOD_HIGG8D1.e5299_s3126_r9364_r9315_p4133
 mc16_13TeV.364124.Sherpa_221_NNPDF30NNLO_Zee_MAXHTPTV280_500_CFilterBVeto.deriv.DAOD_HIGG8D1.e5299_s3126_r9364_r9315_p4133
 mc16_13TeV.364125.Sherpa_221_NNPDF30NNLO_Zee_MAXHTPTV280_500_BFilter.deriv.DAOD_HIGG8D1.e5299_s3126_r9364_r9315_p4133
 mc16_13TeV.364125.Sherpa_221_NNPDF30NNLO_Zee_MAXHTPTV280_500_BFilter.deriv.DAOD_HIGG8D1.e5299_e5984_s3126_r9364_r9315_p4133
 mc16_13TeV.364126.Sherpa_221_NNPDF30NNLO_Zee_MAXHTPTV500_1000.deriv.DAOD_HIGG8D1.e5299_s3126_r9364_r9315_p4133
 mc16_13TeV.364127.Sherpa_221_NNPDF30NNLO_Zee_MAXHTPTV1000_E_CMS.deriv.DAOD_HIGG8D1.e5299_s3126_r9364_r9315_p4133
 mc16_13TeV.364128.Sherpa_221_NNPDF30NNLO_Ztautau_MAXHTPTV0_70_CVetoBVeto.deriv.DAOD_HIGG8D1.e5307_s3126_r9364_r9315_p4133
 mc16_13TeV.364129.Sherpa_221_NNPDF30NNLO_Ztautau_MAXHTPTV0_70_CFilterBVeto.deriv.DAOD_HIGG8D1.e5307_s3126_r9364_r9315_p4133
 mc16_13TeV.364130.Sherpa_221_NNPDF30NNLO_Ztautau_MAXHTPTV0_70_BFilter.deriv.DAOD_HIGG8D1.e5307_s3126_r9364_r9315_p4133
 mc16_13TeV.364131.Sherpa_221_NNPDF30NNLO_Ztautau_MAXHTPTV70_140_CVetoBVeto.deriv.DAOD_HIGG8D1.e5307_s3126_r9364_r9315_p4133
 mc16_13TeV.364132.Sherpa_221_NNPDF30NNLO_Ztautau_MAXHTPTV70_140_CFilterBVeto.deriv.DAOD_HIGG8D1.e5307_s3126_r9364_r9315_p4133
 mc16_13TeV.364133.Sherpa_221_NNPDF30NNLO_Ztautau_MAXHTPTV70_140_BFilter.deriv.DAOD_HIGG8D1.e5307_s3126_r9364_r9315_p4133
 mc16_13TeV.364134.Sherpa_221_NNPDF30NNLO_Ztautau_MAXHTPTV140_280_CVetoBVeto.deriv.DAOD_HIGG8D1.e5307_s3126_r9364_r9315_p4133
 mc16_13TeV.364135.Sherpa_221_NNPDF30NNLO_Ztautau_MAXHTPTV140_280_CFilterBVeto.deriv.DAOD_HIGG8D1.e5307_s3126_r9364_r9315_p4133
 mc16_13TeV.364136.Sherpa_221_NNPDF30NNLO_Ztautau_MAXHTPTV140_280_BFilter.deriv.DAOD_HIGG8D1.e5307_s3126_r9364_r9315_p4133
 mc16_13TeV.364137.Sherpa_221_NNPDF30NNLO_Ztautau_MAXHTPTV280_500_CVetoBVeto.deriv.DAOD_HIGG8D1.e5307_e5984_s3126_r9364_r9315_p4133
 mc16_13TeV.364137.Sherpa_221_NNPDF30NNLO_Ztautau_MAXHTPTV280_500_CVetoBVeto.deriv.DAOD_HIGG8D1.e5307_s3126_r9364_r9315_p4133
 mc16_13TeV.364138.Sherpa_221_NNPDF30NNLO_Ztautau_MAXHTPTV280_500_CFilterBVeto.deriv.DAOD_HIGG8D1.e5313_s3126_r9364_r9315_p4133
 mc16_13TeV.364139.Sherpa_221_NNPDF30NNLO_Ztautau_MAXHTPTV280_500_BFilter.deriv.DAOD_HIGG8D1.e5313_s3126_r9364_r9315_p4133
 mc16_13TeV.364140.Sherpa_221_NNPDF30NNLO_Ztautau_MAXHTPTV500_1000.deriv.DAOD_HIGG8D1.e5307_s3126_r9364_r9315_p4133
 mc16_13TeV.364141.Sherpa_221_NNPDF30NNLO_Ztautau_MAXHTPTV1000_E_CMS.deriv.DAOD_HIGG8D1.e5307_s3126_r9364_r9315_p4133
 mc16_13TeV.364198.Sherpa_221_NN30NNLO_Zmm_Mll10_40_MAXHTPTV0_70_BVeto.deriv.DAOD_HIGG8D1.e5421_s3126_r9364_r9315_p4133
 mc16_13TeV.364199.Sherpa_221_NN30NNLO_Zmm_Mll10_40_MAXHTPTV0_70_BFilter.deriv.DAOD_HIGG8D1.e5421_s3126_r9364_r9315_p4133
 mc16_13TeV.364200.Sherpa_221_NN30NNLO_Zmm_Mll10_40_MAXHTPTV70_280_BVeto.deriv.DAOD_HIGG8D1.e5421_s3126_r9364_r9315_p4133
 mc16_13TeV.364201.Sherpa_221_NN30NNLO_Zmm_Mll10_40_MAXHTPTV70_280_BFilter.deriv.DAOD_HIGG8D1.e5421_s3126_r9364_r9315_p4133
 mc16_13TeV.364202.Sherpa_221_NN30NNLO_Zmm_Mll10_40_MAXHTPTV280_E_CMS_BVeto.deriv.DAOD_HIGG8D1.e5421_s3126_r9364_r9315_p4133
 mc16_13TeV.364203.Sherpa_221_NN30NNLO_Zmm_Mll10_40_MAXHTPTV280_E_CMS_BFilter.deriv.DAOD_HIGG8D1.e5421_s3126_r9364_r9315_p4133
 mc16_13TeV.364204.Sherpa_221_NN30NNLO_Zee_Mll10_40_MAXHTPTV0_70_BVeto.deriv.DAOD_HIGG8D1.e5421_s3126_r9364_r9315_p4133
 mc16_13TeV.364205.Sherpa_221_NN30NNLO_Zee_Mll10_40_MAXHTPTV0_70_BFilter.deriv.DAOD_HIGG8D1.e5421_s3126_r9364_r9315_p4133
 mc16_13TeV.364206.Sherpa_221_NN30NNLO_Zee_Mll10_40_MAXHTPTV70_280_BVeto.deriv.DAOD_HIGG8D1.e5421_s3126_r9364_r9315_p4133

mc16_13TeV.364207.Sherpa_221_NN30NNLO_Zee_Mll10_40_MAXHTPTV70_280_BFilter.deriv.DAOD_HIGG8D1.e5421_s3126_r9364_r9315_p4133
 mc16_13TeV.364208.Sherpa_221_NN30NNLO_Zee_Mll10_40_MAXHTPTV280_E_CMS_BVeto.deriv.DAOD_HIGG8D1.e5421_s3126_r9364_r9315_p4133
 mc16_13TeV.364209.Sherpa_221_NN30NNLO_Zee_Mll10_40_MAXHTPTV280_E_CMS_BFilter.deriv.DAOD_HIGG8D1.e5421_s3126_r9364_r9315_p4133
 mc16_13TeV.364210.Sherpa_221_NN30NNLO_Ztt_Mll10_40_MAXHTPTV0_70_BVeto.deriv.DAOD_HIGG8D1.e5421_s3126_r9364_r9315_p4133
 mc16_13TeV.364211.Sherpa_221_NN30NNLO_Ztt_Mll10_40_MAXHTPTV0_70_BFilter.deriv.DAOD_HIGG8D1.e5421_s3126_r9364_r9315_p4133
 mc16_13TeV.364212.Sherpa_221_NN30NNLO_Ztt_Mll10_40_MAXHTPTV70_280_BVeto.deriv.DAOD_HIGG8D1.e5421_s3126_r9364_r9315_p4133
 mc16_13TeV.364213.Sherpa_221_NN30NNLO_Ztt_Mll10_40_MAXHTPTV70_280_BFilter.deriv.DAOD_HIGG8D1.e5421_s3126_r9364_r9315_p4133
 mc16_13TeV.364214.Sherpa_221_NN30NNLO_Ztt_Mll10_40_MAXHTPTV280_E_CMS_BVeto.deriv.DAOD_HIGG8D1.e5421_s3126_r9364_r9315_p4133
 mc16_13TeV.364215.Sherpa_221_NN30NNLO_Ztt_Mll10_40_MAXHTPTV280_E_CMS_BFilter.deriv.DAOD_HIGG8D1.e5421_s3126_r9364_r9315_p4133
 mc16_13TeV.364156.Sherpa_221_NNPDF30NNLO_Wmumu_MAXHTPTV0_70_CVetoBVeto.deriv.DAOD_HIGG8D1.e5340_s3126_r9364_r9315_p4133
 mc16_13TeV.364157.Sherpa_221_NNPDF30NNLO_Wmumu_MAXHTPTV0_70_CFilterBVeto.deriv.DAOD_HIGG8D1.e5340_s3126_r9364_r9315_p4133
 mc16_13TeV.364157.Sherpa_221_NNPDF30NNLO_Wmumu_MAXHTPTV0_70_CFilterBVeto.deriv.DAOD_HIGG8D1.e5340_e5984_s3126_r9364_r9315_p4133
 mc16_13TeV.364158.Sherpa_221_NNPDF30NNLO_Wmumu_MAXHTPTV0_70_BFilter.deriv.DAOD_HIGG8D1.e5340_s3126_r9364_r9315_p4133
 mc16_13TeV.364159.Sherpa_221_NNPDF30NNLO_Wmumu_MAXHTPTV70_140_CVetoBVeto.deriv.DAOD_HIGG8D1.e5340_s3126_r9364_r9315_p4133
 mc16_13TeV.364160.Sherpa_221_NNPDF30NNLO_Wmumu_MAXHTPTV70_140_CFilterBVeto.deriv.DAOD_HIGG8D1.e5340_s3126_r9364_r9315_p4133
 mc16_13TeV.364161.Sherpa_221_NNPDF30NNLO_Wmumu_MAXHTPTV70_140_BFilter.deriv.DAOD_HIGG8D1.e5340_s3126_r9364_r9315_p4133
 mc16_13TeV.364162.Sherpa_221_NNPDF30NNLO_Wmumu_MAXHTPTV140_280_CVetoBVeto.deriv.DAOD_HIGG8D1.e5340_s3126_r9364_r9315_p4133
 mc16_13TeV.364163.Sherpa_221_NNPDF30NNLO_Wmumu_MAXHTPTV140_280_CFilterBVeto.deriv.DAOD_HIGG8D1.e5340_s3126_r9364_r9315_p4133
 mc16_13TeV.364163.Sherpa_221_NNPDF30NNLO_Wmumu_MAXHTPTV140_280_CFilterBVeto.deriv.DAOD_HIGG8D1.e5340_e5984_s3126_s3136_r9364_r9315_p4133
 mc16_13TeV.364164.Sherpa_221_NNPDF30NNLO_Wmumu_MAXHTPTV140_280_BFilter.deriv.DAOD_HIGG8D1.e5340_s3126_r9364_r9315_p4133
 mc16_13TeV.364165.Sherpa_221_NNPDF30NNLO_Wmumu_MAXHTPTV280_500_CVetoBVeto.deriv.DAOD_HIGG8D1.e5340_s3126_r9364_r9315_p4133
 mc16_13TeV.364166.Sherpa_221_NNPDF30NNLO_Wmumu_MAXHTPTV280_500_CFilterBVeto.deriv.DAOD_HIGG8D1.e5340_s3126_r9364_r9315_p4133
 mc16_13TeV.364167.Sherpa_221_NNPDF30NNLO_Wmumu_MAXHTPTV280_500_BFilter.deriv.DAOD_HIGG8D1.e5340_e5984_s3126_r9364_r9315_p4133
 mc16_13TeV.364167.Sherpa_221_NNPDF30NNLO_Wmumu_MAXHTPTV280_500_BFilter.deriv.DAOD_HIGG8D1.e5340_s3126_r9364_r9315_p4133
 mc16_13TeV.364168.Sherpa_221_NNPDF30NNLO_Wmumu_MAXHTPTV500_1000.deriv.DAOD_HIGG8D1.e5340_s3126_r9364_r9315_p4133
 mc16_13TeV.364169.Sherpa_221_NNPDF30NNLO_Wmumu_MAXHTPTV1000_E_CMS.deriv.DAOD_HIGG8D1.e5340_s3126_r9364_r9315_p4133
 mc16_13TeV.364170.Sherpa_221_NNPDF30NNLO_Wenu_MAXHTPTV0_70_CVetoBVeto.deriv.DAOD_HIGG8D1.e5340_s3126_r9364_r9315_p4133
 mc16_13TeV.364171.Sherpa_221_NNPDF30NNLO_Wenu_MAXHTPTV0_70_CFilterBVeto.deriv.DAOD_HIGG8D1.e5340_e5984_s3126_r9364_r9315_p4133
 mc16_13TeV.364171.Sherpa_221_NNPDF30NNLO_Wenu_MAXHTPTV0_70_CFilterBVeto.deriv.DAOD_HIGG8D1.e5340_s3126_r9364_r9315_p4133
 mc16_13TeV.364172.Sherpa_221_NNPDF30NNLO_Wenu_MAXHTPTV0_70_BFilter.deriv.DAOD_HIGG8D1.e5340_s3126_r9364_r9315_p4133
 mc16_13TeV.364173.Sherpa_221_NNPDF30NNLO_Wenu_MAXHTPTV70_140_CVetoBVeto.deriv.DAOD_HIGG8D1.e5340_s3126_r9364_r9315_p4133

mc16_13TeV.364174.Sherpa_221_NNPDF30NNLO_Wenu_MAXHTPTV70_140_CFilterBVeto.deriv.DAOD_HIGG8D1.e5340_s3126_r9364_r9315_p4133
 mc16_13TeV.364175.Sherpa_221_NNPDF30NNLO_Wenu_MAXHTPTV70_140_BFilter.deriv.DAOD_HIGG8D1.e5340_e5984_s3126_s3136_r9364_r9315_p4133
 mc16_13TeV.364175.Sherpa_221_NNPDF30NNLO_Wenu_MAXHTPTV70_140_BFilter.deriv.DAOD_HIGG8D1.e5340_s3126_r9364_r9315_p4133
 mc16_13TeV.364176.Sherpa_221_NNPDF30NNLO_Wenu_MAXHTPTV140_280_CVetoBVeto.deriv.DAOD_HIGG8D1.e5340_s3126_r9364_r9315_p4133
 mc16_13TeV.364177.Sherpa_221_NNPDF30NNLO_Wenu_MAXHTPTV140_280_CFilterBVeto.deriv.DAOD_HIGG8D1.e5340_s3126_r9364_r9315_p4133
 mc16_13TeV.364177.Sherpa_221_NNPDF30NNLO_Wenu_MAXHTPTV140_280_CFilterBVeto.deriv.DAOD_HIGG8D1.e5340_e5984_s3126_s3136_r9364_r9315_p4133
 mc16_13TeV.364178.Sherpa_221_NNPDF30NNLO_Wenu_MAXHTPTV140_280_BFilter.deriv.DAOD_HIGG8D1.e5340_s3126_r9364_r9315_p4133
 mc16_13TeV.364179.Sherpa_221_NNPDF30NNLO_Wenu_MAXHTPTV280_500_CVetoBVeto.deriv.DAOD_HIGG8D1.e5340_s3126_r9364_r9315_p4133
 mc16_13TeV.364180.Sherpa_221_NNPDF30NNLO_Wenu_MAXHTPTV280_500_CFilterBVeto.deriv.DAOD_HIGG8D1.e5340_s3126_r9364_r9315_p4133
 mc16_13TeV.364181.Sherpa_221_NNPDF30NNLO_Wenu_MAXHTPTV280_500_BFilter.deriv.DAOD_HIGG8D1.e5340_e5984_s3126_r9364_r9315_p4133
 mc16_13TeV.364181.Sherpa_221_NNPDF30NNLO_Wenu_MAXHTPTV280_500_BFilter.deriv.DAOD_HIGG8D1.e5340_s3126_r9364_r9315_p4133
 mc16_13TeV.364182.Sherpa_221_NNPDF30NNLO_Wenu_MAXHTPTV500_1000.deriv.DAOD_HIGG8D1.e5340_s3126_r9364_r9315_p4133
 mc16_13TeV.364183.Sherpa_221_NNPDF30NNLO_Wenu_MAXHTPTV1000_E_CMS.deriv.DAOD_HIGG8D1.e5340_s3126_r9364_r9315_p4133
 mc16_13TeV.364184.Sherpa_221_NNPDF30NNLO_Wtaunu_MAXHTPTV0_70_CVetoBVeto.deriv.DAOD_HIGG8D1.e5340_s3126_r9364_r9315_p4133
 mc16_13TeV.364185.Sherpa_221_NNPDF30NNLO_Wtaunu_MAXHTPTV0_70_CFilterBVeto.deriv.DAOD_HIGG8D1.e5340_e5984_s3126_r9364_r9315_p4133
 mc16_13TeV.364185.Sherpa_221_NNPDF30NNLO_Wtaunu_MAXHTPTV0_70_CFilterBVeto.deriv.DAOD_HIGG8D1.e5340_s3126_r9364_r9315_p4133
 mc16_13TeV.364186.Sherpa_221_NNPDF30NNLO_Wtaunu_MAXHTPTV0_70_BFilter.deriv.DAOD_HIGG8D1.e5340_s3126_r9364_r9315_p4133
 mc16_13TeV.364187.Sherpa_221_NNPDF30NNLO_Wtaunu_MAXHTPTV70_140_CVetoBVeto.deriv.DAOD_HIGG8D1.e5340_s3126_r9364_r9315_p4133
 mc16_13TeV.364188.Sherpa_221_NNPDF30NNLO_Wtaunu_MAXHTPTV70_140_CFilterBVeto.deriv.DAOD_HIGG8D1.e5340_s3126_r9364_r9315_p4133
 mc16_13TeV.364189.Sherpa_221_NNPDF30NNLO_Wtaunu_MAXHTPTV70_140_BFilter.deriv.DAOD_HIGG8D1.e5340_s3126_r9364_r9315_p4133
 mc16_13TeV.364190.Sherpa_221_NNPDF30NNLO_Wtaunu_MAXHTPTV140_280_CVetoBVeto.deriv.DAOD_HIGG8D1.e5340_e5984_s3126_r9364_r9315_p4133
 mc16_13TeV.364190.Sherpa_221_NNPDF30NNLO_Wtaunu_MAXHTPTV140_280_CVetoBVeto.deriv.DAOD_HIGG8D1.e5340_s3126_r9364_r9315_p4133
 mc16_13TeV.364191.Sherpa_221_NNPDF30NNLO_Wtaunu_MAXHTPTV140_280_CFilterBVeto.deriv.DAOD_HIGG8D1.e5340_s3126_r9364_r9315_p4133
 mc16_13TeV.364191.Sherpa_221_NNPDF30NNLO_Wtaunu_MAXHTPTV140_280_CFilterBVeto.deriv.DAOD_HIGG8D1.e5340_e5984_s3126_s3136_r9364_r9315_p4133
 mc16_13TeV.364192.Sherpa_221_NNPDF30NNLO_Wtaunu_MAXHTPTV140_280_BFilter.deriv.DAOD_HIGG8D1.e5340_s3126_r9364_r9315_p4133
 mc16_13TeV.364193.Sherpa_221_NNPDF30NNLO_Wtaunu_MAXHTPTV280_500_CVetoBVeto.deriv.DAOD_HIGG8D1.e5340_s3126_r9364_r9315_p4133
 mc16_13TeV.364193.Sherpa_221_NNPDF30NNLO_Wtaunu_MAXHTPTV280_500_CVetoBVeto.deriv.DAOD_HIGG8D1.e5340_e5984_s3126_s3136_r9364_r9315_p4133
 mc16_13TeV.364194.Sherpa_221_NNPDF30NNLO_Wtaunu_MAXHTPTV280_500_CFilterBVeto.deriv.DAOD_HIGG8D1.e5340_e5984_s3126_s3136_r9364_r9315_p4133
 mc16_13TeV.364195.Sherpa_221_NNPDF30NNLO_Wtaunu_MAXHTPTV280_500_BFilter.deriv.DAOD_HIGG8D1.e5340_s3126_r9364_r9315_p4133
 mc16_13TeV.364196.Sherpa_221_NNPDF30NNLO_Wtaunu_MAXHTPTV500_1000.deriv.DAOD_HIGG8D1.e5340_s3126_r9364_r9315_p4133

mc16_13TeV.364197.Sherpa_221_NNPDF30NNLO_Wtaunu_MAXHTPTV1000_E_CMS.deriv.DAOD_HIGG8D1.e5340_s3126_r9364_r9315_p4133
 mc16_13TeV.364500.Sherpa_222_NNPDF30NNLO_eegamma_pty_7_15.deriv.DAOD_HIGG8D1.e5928_e5984_s3126_r9364_r9315_p4133
 mc16_13TeV.364501.Sherpa_222_NNPDF30NNLO_eegamma_pty_15_35.deriv.DAOD_HIGG8D1.e5928_e5984_s3126_r9364_r9315_p4133
 mc16_13TeV.364502.Sherpa_222_NNPDF30NNLO_eegamma_pty_35_70.deriv.DAOD_HIGG8D1.e5928_e5984_s3126_r9364_r9315_p4133
 mc16_13TeV.364503.Sherpa_222_NNPDF30NNLO_eegamma_pty_70_140.deriv.DAOD_HIGG8D1.e5928_e5984_s3126_r9364_r9315_p4133
 mc16_13TeV.364504.Sherpa_222_NNPDF30NNLO_eegamma_pty_140_E_CMS.deriv.DAOD_HIGG8D1.e5928_e5984_s3126_r9364_r9315_p4133
 mc16_13TeV.364505.Sherpa_222_NNPDF30NNLO_mumugamma_pty_7_15.deriv.DAOD_HIGG8D1.e5928_e5984_s3126_r9364_r9315_p4133
 mc16_13TeV.364506.Sherpa_222_NNPDF30NNLO_mumugamma_pty_15_35.deriv.DAOD_HIGG8D1.e5988_e5984_s3126_r9364_r9315_p4133
 mc16_13TeV.364507.Sherpa_222_NNPDF30NNLO_mumugamma_pty_35_70.deriv.DAOD_HIGG8D1.e5928_e5984_s3126_r9364_r9315_p4133
 mc16_13TeV.364508.Sherpa_222_NNPDF30NNLO_mumugamma_pty_70_140.deriv.DAOD_HIGG8D1.e5928_e5984_s3126_r9364_r9315_p4133
 mc16_13TeV.364509.Sherpa_222_NNPDF30NNLO_mumugamma_pty_140_E_CMS.deriv.DAOD_HIGG8D1.e5928_e5984_s3126_r9364_r9315_p4133
 mc16_13TeV.364510.Sherpa_222_NNPDF30NNLO_tautaugamma_pty_7_15.deriv.DAOD_HIGG8D1.e5928_s3126_r9364_r9315_p4133
 mc16_13TeV.364511.Sherpa_222_NNPDF30NNLO_tautaugamma_pty_15_35.deriv.DAOD_HIGG8D1.e5928_s3126_r9364_r9315_p4133
 mc16_13TeV.364512.Sherpa_222_NNPDF30NNLO_tautaugamma_pty_35_70.deriv.DAOD_HIGG8D1.e5928_s3126_r9364_r9315_p4133
 mc16_13TeV.364513.Sherpa_222_NNPDF30NNLO_tautaugamma_pty_70_140.deriv.DAOD_HIGG8D1.e5982_s3126_r9364_r9315_p4133
 mc16_13TeV.364514.Sherpa_222_NNPDF30NNLO_tautaugamma_pty_140_E_CMS.deriv.DAOD_HIGG8D1.e5928_s3126_r9364_r9315_p4133
 mc16_13TeV.364521.Sherpa_222_NNPDF30NNLO_enugamma_pty_7_15.deriv.DAOD_HIGG8D1.e5928_s3126_r9364_r9315_p4133
 mc16_13TeV.364522.Sherpa_222_NNPDF30NNLO_enugamma_pty_15_35.deriv.DAOD_HIGG8D1.e5928_s3126_r9364_r9315_p4133
 mc16_13TeV.364523.Sherpa_222_NNPDF30NNLO_enugamma_pty_35_70.deriv.DAOD_HIGG8D1.e5928_s3126_r9364_r9315_p4133
 mc16_13TeV.364524.Sherpa_222_NNPDF30NNLO_enugamma_pty_70_140.deriv.DAOD_HIGG8D1.e5928_s3126_r9364_r9315_p4133
 mc16_13TeV.364525.Sherpa_222_NNPDF30NNLO_enugamma_pty_140_E_CMS.deriv.DAOD_HIGG8D1.e5928_s3126_r9364_r9315_p4133
 mc16_13TeV.364526.Sherpa_222_NNPDF30NNLO_munugamma_pty_7_15.deriv.DAOD_HIGG8D1.e5928_s3126_r9364_r9315_p4133
 mc16_13TeV.364527.Sherpa_222_NNPDF30NNLO_munugamma_pty_15_35.deriv.DAOD_HIGG8D1.e5928_s3126_r9364_r9315_p4133
 mc16_13TeV.364528.Sherpa_222_NNPDF30NNLO_munugamma_pty_35_70.deriv.DAOD_HIGG8D1.e5928_s3126_r9364_r9315_p4133
 mc16_13TeV.364529.Sherpa_222_NNPDF30NNLO_munugamma_pty_70_140.deriv.DAOD_HIGG8D1.e5928_s3126_r9364_r9315_p4133
 mc16_13TeV.364530.Sherpa_222_NNPDF30NNLO_munugamma_pty_140_E_CMS.deriv.DAOD_HIGG8D1.e5928_s3126_r9364_r9315_p4133
 mc16_13TeV.364530.Sherpa_222_NNPDF30NNLO_munugamma_pty_140_E_CMS.deriv.DAOD_HIGG8D1.e5928_e5984_s3126_r9364_r9315_p4133
 mc16_13TeV.364531.Sherpa_222_NNPDF30NNLO_taunugamma_pty_7_15.deriv.DAOD_HIGG8D1.e5928_s3126_r9364_r9315_p4133
 mc16_13TeV.364532.Sherpa_222_NNPDF30NNLO_taunugamma_pty_15_35.deriv.DAOD_HIGG8D1.e5928_s3126_r9364_r9315_p4133
 mc16_13TeV.364533.Sherpa_222_NNPDF30NNLO_taunugamma_pty_35_70.deriv.DAOD_HIGG8D1.e5928_s3126_r9364_r9315_p4133

mc16_13TeV.364534.Sherpa_222_NNPDF30NNLO_taunugamma_pty_70_140.deriv.DAOD_HIGG8D1.e5928_s3126_r9364_r9315_p4133
 mc16_13TeV.364535.Sherpa_222_NNPDF30NNLO_taunugamma_pty_140_E_CMS.deriv.DAOD_HIGG8D1.e5928_s3126_r9364_r9315_p4133
 mc16_13TeV.364535.Sherpa_222_NNPDF30NNLO_taunugamma_pty_140_E_CMS.deriv.DAOD_HIGG8D1.e5928_e5984_s3126_r9364_r9315_p4133
 mc16_13TeV.410560.MadGraphPythia8EvtGen_A14_tZ_4fl_tchan_noAllHad.deriv.DAOD_HIGG8D1.e5803_s3126_r9364_r9315_p4133
 mc16_13TeV.410013.PowhegPythiaEvtGen_P2012_Wt_inclusive_top.deriv.DAOD_HIGG8D1.e3753_s3126_r9364_r9315_p4133
 mc16_13TeV.410014.PowhegPythiaEvtGen_P2012_Wt_inclusive_antitop.deriv.DAOD_HIGG8D1.e3753_s3126_r9364_r9315_p4133
 mc16_13TeV.410408.aMcAtNloPythia8EvtGen_tWZ_Ztoll_minDR1.deriv.DAOD_HIGG8D1.e6423_e5984_s3126_r9364_r9315_p4133
 mc16_13TeV.364242.Sherpa_222_NNPDF30NNLO_WWW_3l3v_EW6.deriv.DAOD_HIGG8D1.e5887_s3126_r9364_r9315_p4133
 mc16_13TeV.364243.Sherpa_222_NNPDF30NNLO_WWZ_4l2v_EW6.deriv.DAOD_HIGG8D1.e5887_s3126_r9364_r9315_p4133
 mc16_13TeV.364244.Sherpa_222_NNPDF30NNLO_WWZ_2l4v_EW6.deriv.DAOD_HIGG8D1.e5887_s3126_r9364_r9315_p4133
 mc16_13TeV.364245.Sherpa_222_NNPDF30NNLO_WZZ_5l1v_EW6.deriv.DAOD_HIGG8D1.e5887_s3126_r9364_r9315_p4133
 mc16_13TeV.364246.Sherpa_222_NNPDF30NNLO_WZZ_3l3v_EW6.deriv.DAOD_HIGG8D1.e5887_s3126_r9364_r9315_p4133
 mc16_13TeV.364247.Sherpa_222_NNPDF30NNLO_ZZZ_6l0v_EW6.deriv.DAOD_HIGG8D1.e5887_s3126_r9364_r9315_p4133
 mc16_13TeV.364248.Sherpa_222_NNPDF30NNLO_ZZZ_4l2v_EW6.deriv.DAOD_HIGG8D1.e5887_s3126_r9364_r9315_p4133
 mc16_13TeV.364249.Sherpa_222_NNPDF30NNLO_ZZZ_2l4v_EW6.deriv.DAOD_HIGG8D1.e5887_s3126_r9364_r9315_p4133
 mc16_13TeV.342284.Pythia8EvtGen_A14NNPDF23LO_WH125_inc.deriv.DAOD_HIGG8D1.e4246_s3126_r9364_r9315_p4133
 mc16_13TeV.342285.Pythia8EvtGen_A14NNPDF23LO_ZH125_inc.deriv.DAOD_HIGG8D1.e4246_s3126_r9364_r9315_p4133
 mc16_13TeV.341998.aMcAtNloHppEG_UEEE5_CTEQ6L1_CT10ME_tWH125_gamgam_yt_plus1.deriv.DAOD_HIGG8D1.e4394_e5984_s3126_r9364_r9315_p4133
 mc16_13TeV.410389.MadGraphPythia8EvtGen_A14NNPDF23_ttgamma_nonallhadronic.deriv.DAOD_HIGG8D1.e6155_e5984_s3126_r9364_r9315_p4133
 mc16_13TeV.410470.PhPy8EG_A14_ttbar_hdamp258p75_nonallhad.deriv.DAOD_HIGG8D1.e6337_e5984_s3126_r9364_r9315_p4133
 mc16_13TeV.410472.PhPy8EG_A14_ttbar_hdamp258p75_dil.deriv.DAOD_HIGG8D1.e6348_e5984_s3126_r9364_r9315_p4133
 mc16_13TeV.346343.PhPy8EG_A14NNPDF23_NNPDF30ME_ttH125_allhad.deriv.DAOD_HIGG8D1.e7148_e5984_s3126_r9364_r9315_p4133
 mc16_13TeV.346344.PhPy8EG_A14NNPDF23_NNPDF30ME_ttH125_semilep.deriv.DAOD_HIGG8D1.e7148_e5984_s3126_r9364_r9315_p4133
 mc16_13TeV.346345.PhPy8EG_A14NNPDF23_NNPDF30ME_ttH125_dilep.deriv.DAOD_HIGG8D1.e7148_e5984_s3126_r9364_r9315_p4133

mc16d:

mc16_13TeV.364253.Sherpa_222_NNPDF30NNLO_lllv.deriv.DAOD_HIGG8D1.e5916_e5984_s3126_r10201_r10210_p4133
 mc16_13TeV.364250.Sherpa_222_NNPDF30NNLO_llll.deriv.DAOD_HIGG8D1.e5894_e5984_s3126_r10201_r10210_p4133
 mc16_13TeV.364254.Sherpa_222_NNPDF30NNLO_llvv.deriv.DAOD_HIGG8D1.e5916_e5984_s3126_r10201_r10210_p4133
 mc16_13TeV.364255.Sherpa_222_NNPDF30NNLO_lvvv.deriv.DAOD_HIGG8D1.e5916_e5984_s3126_r10201_r10210_p4133
 mc16_13TeV.410155.aMcAtNloPythia8EvtGen_MEN30NLO_A14N23LO_ttW.deriv.DAOD_HIGG8D1.e5070_e5984_s3126_r10201_r10210_p4133

mc16_13TeV.410156.aMcAtNloPythia8EvtGen_MEN30NLO_A14N23LO_ttZnunu.deriv.DAOD_HIGG8D1.e5070_e5984_s3126_r10201_r10210_p4133
 mc16_13TeV.410157.aMcAtNloPythia8EvtGen_MEN30NLO_A14N23LO_ttZqq.deriv.DAOD_HIGG8D1.e5070_e5984_s3126_r10201_r10210_p4133
 mc16_13TeV.410218.aMcAtNloPythia8EvtGen_MEN30NLO_A14N23LO_ttee.deriv.DAOD_HIGG8D1.e5070_e5984_s3126_r10201_r10210_p4133
 mc16_13TeV.410219.aMcAtNloPythia8EvtGen_MEN30NLO_A14N23LO_ttmumu.deriv.DAOD_HIGG8D1.e5070_e5984_s3126_r10201_r10210_p4133
 mc16_13TeV.410220.aMcAtNloPythia8EvtGen_MEN30NLO_A14N23LO_ttautau.deriv.DAOD_HIGG8D1.e5070_e5984_s3126_r10201_r10210_p4133
 mc16_13TeV.410276.aMcAtNloPythia8EvtGen_MEN30NLO_A14N23LO_ttee_mll_1_5.deriv.DAOD_HIGG8D1.e6087_e5984_s3126_r10201_r10210_p4133
 mc16_13TeV.410277.aMcAtNloPythia8EvtGen_MEN30NLO_A14N23LO_ttmumu_mll_1_5.deriv.DAOD_HIGG8D1.e6087_e5984_s3126_r10201_r10210_p4133
 mc16_13TeV.410278.aMcAtNloPythia8EvtGen_MEN30NLO_A14N23LO_ttautau_mll_1_5.deriv.DAOD_HIGG8D1.e6087_e5984_s3126_r10201_r10210_p4133
 mc16_13TeV.410397.MadGraphPythia8EvtGen_ttbar_wbee_MEN30LO_A14N23LO.deriv.DAOD_HIGG8D1.e6086_e5984_s3126_r10201_r10210_p4133
 mc16_13TeV.410398.MadGraphPythia8EvtGen_ttbar_wbmumu_MEN30LO_A14N23LO.deriv.DAOD_HIGG8D1.e6086_e5984_s3126_r10201_r10210_p4133
 mc16_13TeV.410399.MadGraphPythia8EvtGen_ttbar_wbttau_MEN30LO_A14N23LO.deriv.DAOD_HIGG8D1.e6086_e5984_s3126_r10201_r10210_p4133
 mc16_13TeV.410658.PhPy8EG_A14_tchan_BW50_lept_top.deriv.DAOD_HIGG8D1.e6671_e5984_s3126_r10201_r10210_p4133
 mc16_13TeV.410659.PhPy8EG_A14_tchan_BW50_lept_antitop.deriv.DAOD_HIGG8D1.e6671_e5984_s3126_r10201_r10210_p4133
 mc16_13TeV.410644.PowhegPythia8EvtGen_A14_singletop_schan_lept_top.deriv.DAOD_HIGG8D1.e6527_e5984_s3126_r10201_r10210_p4133
 mc16_13TeV.410645.PowhegPythia8EvtGen_A14_singletop_schan_lept_antitop.deriv.DAOD_HIGG8D1.e6527_s3126_r10201_r10210_p4133
 mc16_13TeV.412063.aMcAtNloPythia8EvtGen_tllq_NNPDF30_nf4_A14.deriv.DAOD_TOPQ1.e7054_e5984_s3126_r10201_r10210_p4174
 mc16_13TeV.304014.MadGraphPythia8EvtGen_A14NNPDF23_3top_SM.deriv.DAOD_HIGG8D1.e4324_e5984_s3126_r10201_r10210_p4133
 mc16_13TeV.410080.MadGraphPythia8EvtGen_A14NNPDF23_4topSM.deriv.DAOD_HIGG8D1.e4111_e5984_s3126_r10201_r10210_p4133
 mc16_13TeV.410081.MadGraphPythia8EvtGen_A14NNPDF23_ttbarWW.deriv.DAOD_HIGG8D1.e4111_e5984_s3126_r10201_r10210_p4133
 mc16_13TeV.364100.Sherpa_221_NNPDF30NNLO_Zmumu_MAXHTPTV0_70_CVetoBVeto.deriv.DAOD_HIGG8D1.e5271_s3126_r10201_r10210_p4133
 mc16_13TeV.364101.Sherpa_221_NNPDF30NNLO_Zmumu_MAXHTPTV0_70_CFfilterBVeto.deriv.DAOD_HIGG8D1.e5271_s3126_r10201_r10210_p4133
 mc16_13TeV.364101.Sherpa_221_NNPDF30NNLO_Zmumu_MAXHTPTV0_70_CFfilterBVeto.deriv.DAOD_HIGG8D1.e5271_e5984_s3126_r10201_r10210_p4133
 mc16_13TeV.364102.Sherpa_221_NNPDF30NNLO_Zmumu_MAXHTPTV0_70_BFilter.deriv.DAOD_HIGG8D1.e5271_s3126_r10201_r10210_p4133
 mc16_13TeV.364103.Sherpa_221_NNPDF30NNLO_Zmumu_MAXHTPTV70_140_CVetoBVeto.deriv.DAOD_HIGG8D1.e5271_s3126_r10201_r10210_p4133
 mc16_13TeV.364104.Sherpa_221_NNPDF30NNLO_Zmumu_MAXHTPTV70_140_CFfilterBVeto.deriv.DAOD_HIGG8D1.e5271_s3126_r10201_r10210_p4133
 mc16_13TeV.364106.Sherpa_221_NNPDF30NNLO_Zmumu_MAXHTPTV140_280_CVetoBVeto.deriv.DAOD_HIGG8D1.e5271_s3126_r10201_r10210_p4133
 mc16_13TeV.364107.Sherpa_221_NNPDF30NNLO_Zmumu_MAXHTPTV140_280_CFfilterBVeto.deriv.DAOD_HIGG8D1.e5271_s3126_r10201_r10210_p4133
 mc16_13TeV.364108.Sherpa_221_NNPDF30NNLO_Zmumu_MAXHTPTV140_280_BFilter.deriv.DAOD_HIGG8D1.e5271_e5984_s3126_r10201_r10210_p4133
 mc16_13TeV.364109.Sherpa_221_NNPDF30NNLO_Zmumu_MAXHTPTV280_500_CVetoBVeto.deriv.DAOD_HIGG8D1.e5271_e5984_s3126_r10201_r10210_p4133
 mc16_13TeV.364109.Sherpa_221_NNPDF30NNLO_Zmumu_MAXHTPTV280_500_CVetoBVeto.deriv.DAOD_HIGG8D1.e5271_s3126_r10201_r10210_p4133

mc16_13TeV.364110.Sherpa_221_NNPDF30NNLO_Zmumu_MAXHTPTV280_500_CFilterBVeto.deriv.DAOD_HIGG8D1.e5271_s3126_r10201_r10210_p4133
 mc16_13TeV.364111.Sherpa_221_NNPDF30NNLO_Zmumu_MAXHTPTV280_500_BFilter.deriv.DAOD_HIGG8D1.e5271_e5984_s3126_r10201_r10210_p4133
 mc16_13TeV.364111.Sherpa_221_NNPDF30NNLO_Zmumu_MAXHTPTV280_500_BFilter.deriv.DAOD_HIGG8D1.e5271_s3126_r10201_r10210_p4133
 mc16_13TeV.364112.Sherpa_221_NNPDF30NNLO_Zmumu_MAXHTPTV500_1000.deriv.DAOD_HIGG8D1.e5271_e5984_s3126_r10201_r10210_p4133
 mc16_13TeV.364112.Sherpa_221_NNPDF30NNLO_Zmumu_MAXHTPTV500_1000.deriv.DAOD_HIGG8D1.e5271_s3126_r10201_r10210_p4133
 mc16_13TeV.364113.Sherpa_221_NNPDF30NNLO_Zmumu_MAXHTPTV1000_E_CMS.deriv.DAOD_HIGG8D1.e5271_s3126_r10201_r10210_p4133
 mc16_13TeV.364114.Sherpa_221_NNPDF30NNLO_Zee_MAXHTPTV0_70_CVetoBVeto.deriv.DAOD_HIGG8D1.e5299_s3126_r10201_r10210_p4133
 mc16_13TeV.364115.Sherpa_221_NNPDF30NNLO_Zee_MAXHTPTV0_70_CFilterBVeto.deriv.DAOD_HIGG8D1.e5299_e5984_s3126_r10201_r10210_p4133
 mc16_13TeV.364116.Sherpa_221_NNPDF30NNLO_Zee_MAXHTPTV0_70_BFilter.deriv.DAOD_HIGG8D1.e5299_e5984_s3126_r10201_r10210_p4133
 mc16_13TeV.364117.Sherpa_221_NNPDF30NNLO_Zee_MAXHTPTV70_140_CVetoBVeto.deriv.DAOD_HIGG8D1.e5299_e5984_s3126_r10201_r10210_p4133
 mc16_13TeV.364118.Sherpa_221_NNPDF30NNLO_Zee_MAXHTPTV70_140_CFilterBVeto.deriv.DAOD_HIGG8D1.e5299_e5984_s3126_r10201_r10210_p4133
 mc16_13TeV.364119.Sherpa_221_NNPDF30NNLO_Zee_MAXHTPTV70_140_BFilter.deriv.DAOD_HIGG8D1.e5299_e5984_s3126_r10201_r10210_p4133
 mc16_13TeV.364120.Sherpa_221_NNPDF30NNLO_Zee_MAXHTPTV140_280_CVetoBVeto.deriv.DAOD_HIGG8D1.e5299_e5984_s3126_r10201_r10210_p4133
 mc16_13TeV.364121.Sherpa_221_NNPDF30NNLO_Zee_MAXHTPTV140_280_CFilterBVeto.deriv.DAOD_HIGG8D1.e5299_e5984_s3126_r10201_r10210_p4133
 mc16_13TeV.364122.Sherpa_221_NNPDF30NNLO_Zee_MAXHTPTV140_280_BFilter.deriv.DAOD_HIGG8D1.e5299_e5984_s3126_r10201_r10210_p4133
 mc16_13TeV.364123.Sherpa_221_NNPDF30NNLO_Zee_MAXHTPTV280_500_CVetoBVeto.deriv.DAOD_HIGG8D1.e5299_e5984_s3126_r10201_r10210_p4133
 mc16_13TeV.364124.Sherpa_221_NNPDF30NNLO_Zee_MAXHTPTV280_500_CFilterBVeto.deriv.DAOD_HIGG8D1.e5299_e5984_s3126_r10201_r10210_p4133
 mc16_13TeV.364125.Sherpa_221_NNPDF30NNLO_Zee_MAXHTPTV280_500_BFilter.deriv.DAOD_HIGG8D1.e5299_e5984_s3126_r10201_r10210_p4133
 mc16_13TeV.364126.Sherpa_221_NNPDF30NNLO_Zee_MAXHTPTV500_1000.deriv.DAOD_HIGG8D1.e5299_e5984_s3126_r10201_r10210_p4133
 mc16_13TeV.364127.Sherpa_221_NNPDF30NNLO_Zee_MAXHTPTV1000_E_CMS.deriv.DAOD_HIGG8D1.e5299_e5984_s3126_r10201_r10210_p4133
 mc16_13TeV.364128.Sherpa_221_NNPDF30NNLO_Ztautau_MAXHTPTV0_70_CVetoBVeto.deriv.DAOD_HIGG8D1.e5307_e5984_s3126_r10201_r10210_p4133
 mc16_13TeV.364129.Sherpa_221_NNPDF30NNLO_Ztautau_MAXHTPTV0_70_CFilterBVeto.deriv.DAOD_HIGG8D1.e5307_e5984_s3126_r10201_r10210_p4133
 mc16_13TeV.364130.Sherpa_221_NNPDF30NNLO_Ztautau_MAXHTPTV0_70_BFilter.deriv.DAOD_HIGG8D1.e5307_e5984_s3126_r10201_r10210_p4133
 mc16_13TeV.364131.Sherpa_221_NNPDF30NNLO_Ztautau_MAXHTPTV70_140_CVetoBVeto.deriv.DAOD_HIGG8D1.e5307_e5984_s3126_r10201_r10210_p4133
 mc16_13TeV.364132.Sherpa_221_NNPDF30NNLO_Ztautau_MAXHTPTV70_140_CFilterBVeto.deriv.DAOD_HIGG8D1.e5307_e5984_s3126_r10201_r10210_p4133
 mc16_13TeV.364133.Sherpa_221_NNPDF30NNLO_Ztautau_MAXHTPTV70_140_BFilter.deriv.DAOD_HIGG8D1.e5307_e5984_s3126_r10201_r10210_p4133
 mc16_13TeV.364134.Sherpa_221_NNPDF30NNLO_Ztautau_MAXHTPTV140_280_CVetoBVeto.deriv.DAOD_HIGG8D1.e5307_e5984_s3126_r10201_r10210_p4133
 mc16_13TeV.364135.Sherpa_221_NNPDF30NNLO_Ztautau_MAXHTPTV140_280_CFilterBVeto.deriv.DAOD_HIGG8D1.e5307_e5984_s3126_r10201_r10210_p4133
 mc16_13TeV.364136.Sherpa_221_NNPDF30NNLO_Ztautau_MAXHTPTV140_280_BFilter.deriv.DAOD_HIGG8D1.e5307_e5984_s3126_r10201_r10210_p4133
 mc16_13TeV.364137.Sherpa_221_NNPDF30NNLO_Ztautau_MAXHTPTV280_500_CVetoBVeto.deriv.DAOD_HIGG8D1.e5307_e5984_s3126_r10201_r10210_p4133
 mc16_13TeV.364138.Sherpa_221_NNPDF30NNLO_Ztautau_MAXHTPTV280_500_CFilterBVeto.deriv.DAOD_HIGG8D1.e5313_e5984_s3126_r10201_r10210_p4133

mc16_13TeV.364139.Sherpa_221_NNPDF30NNLO_Ztautau_MAXHTPTV280_500_BFilter.deriv.DAOD_HIGG8D1.e5313_e5984_s3126_r10201_r10210_p4133
 mc16_13TeV.364140.Sherpa_221_NNPDF30NNLO_Ztautau_MAXHTPTV500_1000.deriv.DAOD_HIGG8D1.e5307_e5984_s3126_r10201_r10210_p4133
 mc16_13TeV.364141.Sherpa_221_NNPDF30NNLO_Ztautau_MAXHTPTV1000_E_CMS.deriv.DAOD_HIGG8D1.e5307_e5984_s3126_r10201_r10210_p4133
 mc16_13TeV.364198.Sherpa_221_NN30NNLO_Zmm_Mll10_40_MAXHTPTV0_70_BVeto.deriv.DAOD_HIGG8D1.e5421_e5984_s3126_r10201_r10210_p4133
 mc16_13TeV.364199.Sherpa_221_NN30NNLO_Zmm_Mll10_40_MAXHTPTV0_70_BFilter.deriv.DAOD_HIGG8D1.e5421_e5984_s3126_r10201_r10210_p4133
 mc16_13TeV.364200.Sherpa_221_NN30NNLO_Zmm_Mll10_40_MAXHTPTV70_280_BVeto.deriv.DAOD_HIGG8D1.e5421_e5984_s3126_r10201_r10210_p4133
 mc16_13TeV.364201.Sherpa_221_NN30NNLO_Zmm_Mll10_40_MAXHTPTV70_280_BFilter.deriv.DAOD_HIGG8D1.e5421_e5984_s3126_r10201_r10210_p4133
 mc16_13TeV.364202.Sherpa_221_NN30NNLO_Zmm_Mll10_40_MAXHTPTV280_E_CMS_BVeto.deriv.DAOD_HIGG8D1.e5421_e5984_s3126_r10201_r10210_p4133
 mc16_13TeV.364203.Sherpa_221_NN30NNLO_Zmm_Mll10_40_MAXHTPTV280_E_CMS_BFilter.deriv.DAOD_HIGG8D1.e5421_e5984_s3126_r10201_r10210_p4133
 mc16_13TeV.364204.Sherpa_221_NN30NNLO_Zee_Mll10_40_MAXHTPTV0_70_BVeto.deriv.DAOD_HIGG8D1.e5421_e5984_s3126_r10201_r10210_p4133
 mc16_13TeV.364205.Sherpa_221_NN30NNLO_Zee_Mll10_40_MAXHTPTV0_70_BFilter.deriv.DAOD_HIGG8D1.e5421_e5984_s3126_r10201_r10210_p4133
 mc16_13TeV.364206.Sherpa_221_NN30NNLO_Zee_Mll10_40_MAXHTPTV70_280_BVeto.deriv.DAOD_HIGG8D1.e5421_e5984_s3126_r10201_r10210_p4133
 mc16_13TeV.364207.Sherpa_221_NN30NNLO_Zee_Mll10_40_MAXHTPTV70_280_BFilter.deriv.DAOD_HIGG8D1.e5421_e5984_s3126_r10201_r10210_p4133
 mc16_13TeV.364208.Sherpa_221_NN30NNLO_Zee_Mll10_40_MAXHTPTV280_E_CMS_BVeto.deriv.DAOD_HIGG8D1.e5421_e5984_s3126_r10201_r10210_p4133
 mc16_13TeV.364209.Sherpa_221_NN30NNLO_Zee_Mll10_40_MAXHTPTV280_E_CMS_BFilter.deriv.DAOD_HIGG8D1.e5421_e5984_s3126_r10201_r10210_p4133
 mc16_13TeV.364210.Sherpa_221_NN30NNLO_Ztt_Mll10_40_MAXHTPTV0_70_BVeto.deriv.DAOD_HIGG8D1.e5421_e5984_s3126_r10201_r10210_p4133
 mc16_13TeV.364211.Sherpa_221_NN30NNLO_Ztt_Mll10_40_MAXHTPTV0_70_BFilter.deriv.DAOD_HIGG8D1.e5421_e5984_s3126_r10201_r10210_p4133
 mc16_13TeV.364212.Sherpa_221_NN30NNLO_Ztt_Mll10_40_MAXHTPTV70_280_BVeto.deriv.DAOD_HIGG8D1.e5421_e5984_s3126_r10201_r10210_p4133
 mc16_13TeV.364213.Sherpa_221_NN30NNLO_Ztt_Mll10_40_MAXHTPTV70_280_BFilter.deriv.DAOD_HIGG8D1.e5421_e5984_s3126_r10201_r10210_p4133
 mc16_13TeV.364214.Sherpa_221_NN30NNLO_Ztt_Mll10_40_MAXHTPTV280_E_CMS_BVeto.deriv.DAOD_HIGG8D1.e5421_e5984_s3126_r10201_r10210_p4133
 mc16_13TeV.364215.Sherpa_221_NN30NNLO_Ztt_Mll10_40_MAXHTPTV280_E_CMS_BFilter.deriv.DAOD_HIGG8D1.e5421_e5984_s3126_r10201_r10210_p4133
 mc16_13TeV.364156.Sherpa_221_NNPDF30NNLO_Wmunu_MAXHTPTV0_70_CVetoBVeto.deriv.DAOD_HIGG8D1.e5340_s3126_r10201_r10210_p4133
 mc16_13TeV.364156.Sherpa_221_NNPDF30NNLO_Wmunu_MAXHTPTV0_70_CVetoBVeto.deriv.DAOD_HIGG8D1.e5340_e5984_s3126_s3136_r10201_r10210_p4133
 mc16_13TeV.364157.Sherpa_221_NNPDF30NNLO_Wmunu_MAXHTPTV0_70_CFilterBVeto.deriv.DAOD_HIGG8D1.e5340_e5984_s3126_s3136_r10201_r10210_p4133
 mc16_13TeV.364157.Sherpa_221_NNPDF30NNLO_Wmunu_MAXHTPTV0_70_CFilterBVeto.deriv.DAOD_HIGG8D1.e5340_s3126_r10201_r10210_p4133
 mc16_13TeV.364158.Sherpa_221_NNPDF30NNLO_Wmunu_MAXHTPTV0_70_BFilter.deriv.DAOD_HIGG8D1.e5340_e5984_s3126_s3136_r10201_r10210_p4133
 mc16_13TeV.364158.Sherpa_221_NNPDF30NNLO_Wmunu_MAXHTPTV0_70_BFilter.deriv.DAOD_HIGG8D1.e5340_s3126_r10201_r10210_p4133
 mc16_13TeV.364159.Sherpa_221_NNPDF30NNLO_Wmunu_MAXHTPTV70_140_CVetoBVeto.deriv.DAOD_HIGG8D1.e5340_s3126_r10201_r10210_p4133
 mc16_13TeV.364159.Sherpa_221_NNPDF30NNLO_Wmunu_MAXHTPTV70_140_CVetoBVeto.deriv.DAOD_HIGG8D1.e5340_e5984_s3126_r10201_r10210_p4133
 mc16_13TeV.364159.Sherpa_221_NNPDF30NNLO_Wmunu_MAXHTPTV70_140_CVetoBVeto.deriv.DAOD_HIGG8D1.e5340_e5984_s3126_s3136_r10201_r10210_p4133

mc16_13TeV.364160.Sherpa_221_NNPDF30NNLO_Wmunu_MAXHTPTV70_140_CFilterBVeto.deriv.DAOD_HIGG8D1.e5340_e5984_s3126_r10201_r10210_p4133
 mc16_13TeV.364160.Sherpa_221_NNPDF30NNLO_Wmunu_MAXHTPTV70_140_CFilterBVeto.deriv.DAOD_HIGG8D1.e5340_s3126_r10201_r10210_p4133
 mc16_13TeV.364161.Sherpa_221_NNPDF30NNLO_Wmunu_MAXHTPTV70_140_BFilter.deriv.DAOD_HIGG8D1.e5340_s3126_r10201_r10210_p4133
 mc16_13TeV.364161.Sherpa_221_NNPDF30NNLO_Wmunu_MAXHTPTV70_140_BFilter.deriv.DAOD_HIGG8D1.e5340_e5984_s3126_s3136_r10201_r10210_p4133
 mc16_13TeV.364162.Sherpa_221_NNPDF30NNLO_Wmunu_MAXHTPTV140_280_CVetoBVeto.deriv.DAOD_HIGG8D1.e5340_s3126_r10201_r10210_p4133
 mc16_13TeV.364162.Sherpa_221_NNPDF30NNLO_Wmunu_MAXHTPTV140_280_CVetoBVeto.deriv.DAOD_HIGG8D1.e5340_e5984_s3126_s3136_r10201_r10210_p4133
 mc16_13TeV.364163.Sherpa_221_NNPDF30NNLO_Wmunu_MAXHTPTV140_280_CFilterBVeto.deriv.DAOD_HIGG8D1.e5340_s3126_r10201_r10210_p4133
 mc16_13TeV.364163.Sherpa_221_NNPDF30NNLO_Wmunu_MAXHTPTV140_280_CFilterBVeto.deriv.DAOD_HIGG8D1.e5340_e5984_s3126_s3136_r10201_r10210_p4133
 mc16_13TeV.364163.Sherpa_221_NNPDF30NNLO_Wmunu_MAXHTPTV140_280_CFilterBVeto.deriv.DAOD_HIGG8D1.e5340_e5984_s3126_r10201_r10210_p4133
 mc16_13TeV.364164.Sherpa_221_NNPDF30NNLO_Wmunu_MAXHTPTV140_280_BFilter.deriv.DAOD_HIGG8D1.e5340_s3126_r10201_r10210_p4133
 mc16_13TeV.364164.Sherpa_221_NNPDF30NNLO_Wmunu_MAXHTPTV140_280_BFilter.deriv.DAOD_HIGG8D1.e5340_e5984_s3126_s3136_r10201_r10210_p4133
 mc16_13TeV.364165.Sherpa_221_NNPDF30NNLO_Wmunu_MAXHTPTV280_500_CVetoBVeto.deriv.DAOD_HIGG8D1.e5340_e5984_s3126_s3136_r10201_r10210_p4133
 mc16_13TeV.364166.Sherpa_221_NNPDF30NNLO_Wmunu_MAXHTPTV280_500_CFilterBVeto.deriv.DAOD_HIGG8D1.e5340_s3126_r10201_r10210_p4133
 mc16_13TeV.364166.Sherpa_221_NNPDF30NNLO_Wmunu_MAXHTPTV280_500_CFilterBVeto.deriv.DAOD_HIGG8D1.e5340_e5984_s3126_s3136_r10201_r10210_p4133
 mc16_13TeV.364167.Sherpa_221_NNPDF30NNLO_Wmunu_MAXHTPTV280_500_BFilter.deriv.DAOD_HIGG8D1.e5340_s3126_r10201_r10210_p4133
 mc16_13TeV.364167.Sherpa_221_NNPDF30NNLO_Wmunu_MAXHTPTV280_500_BFilter.deriv.DAOD_HIGG8D1.e5340_e5984_s3126_r10201_r10210_p4133
 mc16_13TeV.364168.Sherpa_221_NNPDF30NNLO_Wmunu_MAXHTPTV500_1000.deriv.DAOD_HIGG8D1.e5340_s3126_r10201_r10210_p4133
 mc16_13TeV.364168.Sherpa_221_NNPDF30NNLO_Wmunu_MAXHTPTV500_1000.deriv.DAOD_HIGG8D1.e5340_e5984_s3126_s3136_r10201_r10210_p4133
 mc16_13TeV.364169.Sherpa_221_NNPDF30NNLO_Wmunu_MAXHTPTV1000_E_CMS.deriv.DAOD_HIGG8D1.e5340_s3126_r10201_r10210_p4133
 mc16_13TeV.364169.Sherpa_221_NNPDF30NNLO_Wmunu_MAXHTPTV1000_E_CMS.deriv.DAOD_HIGG8D1.e5340_e5984_s3126_s3136_r10201_r10210_p4133
 mc16_13TeV.364170.Sherpa_221_NNPDF30NNLO_Wenu_MAXHTPTV0_70_CVetoBVeto.deriv.DAOD_HIGG8D1.e5340_e5984_s3126_s3136_r10201_r10210_p4133
 mc16_13TeV.364170.Sherpa_221_NNPDF30NNLO_Wenu_MAXHTPTV0_70_CVetoBVeto.deriv.DAOD_HIGG8D1.e5340_s3126_r10201_r10210_p4133
 mc16_13TeV.364171.Sherpa_221_NNPDF30NNLO_Wenu_MAXHTPTV0_70_CFilterBVeto.deriv.DAOD_HIGG8D1.e5340_e5984_s3126_r10201_r10210_p4133
 mc16_13TeV.364171.Sherpa_221_NNPDF30NNLO_Wenu_MAXHTPTV0_70_CFilterBVeto.deriv.DAOD_HIGG8D1.e5340_s3126_r10201_r10210_p4133
 mc16_13TeV.364171.Sherpa_221_NNPDF30NNLO_Wenu_MAXHTPTV0_70_CFilterBVeto.deriv.DAOD_HIGG8D1.e5340_e5984_s3126_s3136_r10201_r10210_p4133
 mc16_13TeV.364172.Sherpa_221_NNPDF30NNLO_Wenu_MAXHTPTV0_70_BFilter.deriv.DAOD_HIGG8D1.e5340_e5984_s3126_s3136_r10201_r10210_p4133
 mc16_13TeV.364172.Sherpa_221_NNPDF30NNLO_Wenu_MAXHTPTV0_70_BFilter.deriv.DAOD_HIGG8D1.e5340_e5984_s3126_r10201_r10210_p4133
 mc16_13TeV.364173.Sherpa_221_NNPDF30NNLO_Wenu_MAXHTPTV70_140_CVetoBVeto.deriv.DAOD_HIGG8D1.e5340_s3126_r10201_r10210_p4133
 mc16_13TeV.364173.Sherpa_221_NNPDF30NNLO_Wenu_MAXHTPTV70_140_CVetoBVeto.deriv.DAOD_HIGG8D1.e5340_e5984_s3126_r10201_r10210_p4133

mc16_13TeV.364174.Sherpa_221_NNPDF30NNLO_Wenu_MAXHTPTV70_140_CFilterBVeto.deriv.DAOD_HIGG8D1.e5340_s3126_r10201_r10210_p4133
 mc16_13TeV.364174.Sherpa_221_NNPDF30NNLO_Wenu_MAXHTPTV70_140_CFilterBVeto.deriv.DAOD_HIGG8D1.e5340_e5984_s3126_r10201_r10210_p4133
 mc16_13TeV.364175.Sherpa_221_NNPDF30NNLO_Wenu_MAXHTPTV70_140_BFilter.deriv.DAOD_HIGG8D1.e5340_e5984_s3126_r10201_r10210_p4133
 mc16_13TeV.364175.Sherpa_221_NNPDF30NNLO_Wenu_MAXHTPTV70_140_BFilter.deriv.DAOD_HIGG8D1.e5340_e5984_s3126_s3136_r10201_r10210_p4133
 mc16_13TeV.364175.Sherpa_221_NNPDF30NNLO_Wenu_MAXHTPTV70_140_BFilter.deriv.DAOD_HIGG8D1.e5340_s3126_r10201_r10210_p4133
 mc16_13TeV.364176.Sherpa_221_NNPDF30NNLO_Wenu_MAXHTPTV140_280_CVetoBVeto.deriv.DAOD_HIGG8D1.e5340_e5984_s3126_s3136_r10201_r10210_p4133
 mc16_13TeV.364176.Sherpa_221_NNPDF30NNLO_Wenu_MAXHTPTV140_280_CVetoBVeto.deriv.DAOD_HIGG8D1.e5340_s3126_r10201_r10210_p4133
 mc16_13TeV.364177.Sherpa_221_NNPDF30NNLO_Wenu_MAXHTPTV140_280_CFilterBVeto.deriv.DAOD_HIGG8D1.e5340_s3126_r10201_r10210_p4133
 mc16_13TeV.364177.Sherpa_221_NNPDF30NNLO_Wenu_MAXHTPTV140_280_CFilterBVeto.deriv.DAOD_HIGG8D1.e5340_e5984_s3126_s3136_r10201_r10210_p4133
 mc16_13TeV.364177.Sherpa_221_NNPDF30NNLO_Wenu_MAXHTPTV140_280_CFilterBVeto.deriv.DAOD_HIGG8D1.e5340_e5984_s3126_s3136_r10201_r10210_p4133
 mc16_13TeV.364177.Sherpa_221_NNPDF30NNLO_Wenu_MAXHTPTV140_280_CFilterBVeto.deriv.DAOD_HIGG8D1.e5340_e5984_s3126_r10201_r10210_p4133
 mc16_13TeV.364178.Sherpa_221_NNPDF30NNLO_Wenu_MAXHTPTV140_280_BFilter.deriv.DAOD_HIGG8D1.e5340_s3126_r10201_r10210_p4133
 mc16_13TeV.364179.Sherpa_221_NNPDF30NNLO_Wenu_MAXHTPTV280_500_CVetoBVeto.deriv.DAOD_HIGG8D1.e5340_s3126_r10201_r10210_p4133
 mc16_13TeV.364179.Sherpa_221_NNPDF30NNLO_Wenu_MAXHTPTV280_500_CVetoBVeto.deriv.DAOD_HIGG8D1.e5340_e5984_s3126_r10201_r10210_p4133
 mc16_13TeV.364180.Sherpa_221_NNPDF30NNLO_Wenu_MAXHTPTV280_500_CFilterBVeto.deriv.DAOD_HIGG8D1.e5340_e5984_s3126_s3136_r10201_r10210_p4133
 mc16_13TeV.364180.Sherpa_221_NNPDF30NNLO_Wenu_MAXHTPTV280_500_CFilterBVeto.deriv.DAOD_HIGG8D1.e5340_s3126_r10201_r10210_p4133
 mc16_13TeV.364181.Sherpa_221_NNPDF30NNLO_Wenu_MAXHTPTV280_500_BFilter.deriv.DAOD_HIGG8D1.e5340_e5984_s3126_r10201_r10210_p4133
 mc16_13TeV.364181.Sherpa_221_NNPDF30NNLO_Wenu_MAXHTPTV280_500_BFilter.deriv.DAOD_HIGG8D1.e5340_s3126_r10201_r10210_p4133
 mc16_13TeV.364182.Sherpa_221_NNPDF30NNLO_Wenu_MAXHTPTV500_1000.deriv.DAOD_HIGG8D1.e5340_s3126_r10201_r10210_p4133
 mc16_13TeV.364182.Sherpa_221_NNPDF30NNLO_Wenu_MAXHTPTV500_1000.deriv.DAOD_HIGG8D1.e5340_e5984_s3126_s3136_r10201_r10210_p4133
 mc16_13TeV.364183.Sherpa_221_NNPDF30NNLO_Wenu_MAXHTPTV1000_E_CMS.deriv.DAOD_HIGG8D1.e5340_e5984_s3126_r10201_r10210_p4133
 mc16_13TeV.364184.Sherpa_221_NNPDF30NNLO_Wtaunu_MAXHTPTV0_70_CVetoBVeto.deriv.DAOD_HIGG8D1.e5340_e5984_s3126_r10201_r10210_p4133
 mc16_13TeV.364184.Sherpa_221_NNPDF30NNLO_Wtaunu_MAXHTPTV0_70_CVetoBVeto.deriv.DAOD_HIGG8D1.e5340_s3126_r10201_r10210_p4133
 mc16_13TeV.364185.Sherpa_221_NNPDF30NNLO_Wtaunu_MAXHTPTV0_70_CFilterBVeto.deriv.DAOD_HIGG8D1.e5340_e5984_s3126_r10201_r10210_p4133
 mc16_13TeV.364186.Sherpa_221_NNPDF30NNLO_Wtaunu_MAXHTPTV0_70_BFilter.deriv.DAOD_HIGG8D1.e5340_e5984_s3126_r10201_r10210_p4133
 mc16_13TeV.364187.Sherpa_221_NNPDF30NNLO_Wtaunu_MAXHTPTV70_140_CVetoBVeto.deriv.DAOD_HIGG8D1.e5340_e5984_s3126_r10201_r10210_p4133
 mc16_13TeV.364188.Sherpa_221_NNPDF30NNLO_Wtaunu_MAXHTPTV70_140_CFilterBVeto.deriv.DAOD_HIGG8D1.e5340_e5984_s3126_r10201_r10210_p4133
 mc16_13TeV.364189.Sherpa_221_NNPDF30NNLO_Wtaunu_MAXHTPTV70_140_BFilter.deriv.DAOD_HIGG8D1.e5340_s3126_r10201_r10210_p4133
 mc16_13TeV.364190.Sherpa_221_NNPDF30NNLO_Wtaunu_MAXHTPTV140_280_CVetoBVeto.deriv.DAOD_HIGG8D1.e5340_s3126_r10201_r10210_p4133
 mc16_13TeV.364190.Sherpa_221_NNPDF30NNLO_Wtaunu_MAXHTPTV140_280_CVetoBVeto.deriv.DAOD_HIGG8D1.e5340_e5984_s3126_s3136_r10201_r10210_p4133

mc16_13TeV.364191.Sherpa_221_NNPDF30NNLO_Wtaunu_MAXHTPTV140_280_CFilterBVeto.deriv.DAOD_HIGG8D1.e5340_e5984_s3126_s3136_r10201_r10210_p4133
 mc16_13TeV.364191.Sherpa_221_NNPDF30NNLO_Wtaunu_MAXHTPTV140_280_CFilterBVeto.deriv.DAOD_HIGG8D1.e5340_s3126_r10201_r10210_p4133
 mc16_13TeV.364192.Sherpa_221_NNPDF30NNLO_Wtaunu_MAXHTPTV140_280_BFilter.deriv.DAOD_HIGG8D1.e5340_e5984_s3126_r10201_r10210_p4133
 mc16_13TeV.364193.Sherpa_221_NNPDF30NNLO_Wtaunu_MAXHTPTV280_500_CVetoBVeto.deriv.DAOD_HIGG8D1.e5340_e5984_s3126_r10201_r10210_p4133
 mc16_13TeV.364193.Sherpa_221_NNPDF30NNLO_Wtaunu_MAXHTPTV280_500_CVetoBVeto.deriv.DAOD_HIGG8D1.e5340_e5984_s3126_s3136_r10201_r10210_p4133
 mc16_13TeV.364194.Sherpa_221_NNPDF30NNLO_Wtaunu_MAXHTPTV280_500_CFilterBVeto.deriv.DAOD_HIGG8D1.e5340_e5984_s3126_r10201_r10210_p4133
 mc16_13TeV.364194.Sherpa_221_NNPDF30NNLO_Wtaunu_MAXHTPTV280_500_CFilterBVeto.deriv.DAOD_HIGG8D1.e5340_s3126_r10201_r10210_p4133
 mc16_13TeV.364194.Sherpa_221_NNPDF30NNLO_Wtaunu_MAXHTPTV280_500_BFilter.deriv.DAOD_HIGG8D1.e5340_e5984_s3126_r10201_r10210_p4133
 mc16_13TeV.364194.Sherpa_221_NNPDF30NNLO_Wtaunu_MAXHTPTV280_500_BFilter.deriv.DAOD_HIGG8D1.e5340_s3126_s3136_r10201_r10210_p4133
 mc16_13TeV.364195.Sherpa_221_NNPDF30NNLO_Wtaunu_MAXHTPTV280_500_BFilter.deriv.DAOD_HIGG8D1.e5340_e5984_s3126_r10201_r10210_p4133
 mc16_13TeV.364195.Sherpa_221_NNPDF30NNLO_Wtaunu_MAXHTPTV280_500_BFilter.deriv.DAOD_HIGG8D1.e5340_s3126_r10201_r10210_p4133
 mc16_13TeV.364196.Sherpa_221_NNPDF30NNLO_Wtaunu_MAXHTPTV500_1000.deriv.DAOD_HIGG8D1.e5340_e5984_s3126_s3136_r10201_r10210_p4133
 mc16_13TeV.364196.Sherpa_221_NNPDF30NNLO_Wtaunu_MAXHTPTV500_1000.deriv.DAOD_HIGG8D1.e5340_s3126_r10201_r10210_p4133
 mc16_13TeV.364197.Sherpa_221_NNPDF30NNLO_Wtaunu_MAXHTPTV1000_E_CMS.deriv.DAOD_HIGG8D1.e5340_e5984_s3126_r10201_r10210_p4133
 mc16_13TeV.364500.Sherpa_222_NNPDF30NNLO_eegamma_pty_7_15.deriv.DAOD_HIGG8D1.e5928_e5984_s3126_r10201_r10210_p4133
 mc16_13TeV.364501.Sherpa_222_NNPDF30NNLO_eegamma_pty_15_35.deriv.DAOD_HIGG8D1.e5928_e5984_s3126_r10201_r10210_p4133
 mc16_13TeV.364502.Sherpa_222_NNPDF30NNLO_eegamma_pty_35_70.deriv.DAOD_HIGG8D1.e5928_e5984_s3126_r10201_r10210_p4133
 mc16_13TeV.364503.Sherpa_222_NNPDF30NNLO_eegamma_pty_70_140.deriv.DAOD_HIGG8D1.e5928_e5984_s3126_r10201_r10210_p4133
 mc16_13TeV.364504.Sherpa_222_NNPDF30NNLO_eegamma_pty_140_E_CMS.deriv.DAOD_HIGG8D1.e5928_e5984_s3126_r10201_r10210_p4133
 mc16_13TeV.364505.Sherpa_222_NNPDF30NNLO_mumugamma_pty_7_15.deriv.DAOD_HIGG8D1.e5928_e5984_s3126_r10201_r10210_p4133
 mc16_13TeV.364506.Sherpa_222_NNPDF30NNLO_mumugamma_pty_15_35.deriv.DAOD_HIGG8D1.e5928_e5984_s3126_r10201_r10210_p4133
 mc16_13TeV.364507.Sherpa_222_NNPDF30NNLO_mumugamma_pty_35_70.deriv.DAOD_HIGG8D1.e5928_e5984_s3126_r10201_r10210_p4133
 mc16_13TeV.364508.Sherpa_222_NNPDF30NNLO_mumugamma_pty_70_140.deriv.DAOD_HIGG8D1.e5928_e5984_s3126_r10201_r10210_p4133
 mc16_13TeV.364509.Sherpa_222_NNPDF30NNLO_mumugamma_pty_140_E_CMS.deriv.DAOD_HIGG8D1.e5928_e5984_s3126_r10201_r10210_p4133
 mc16_13TeV.364510.Sherpa_222_NNPDF30NNLO_tautaugamma_pty_7_15.deriv.DAOD_HIGG8D1.e5928_e5984_s3126_r10201_r10210_p4133
 mc16_13TeV.364511.Sherpa_222_NNPDF30NNLO_tautaugamma_pty_15_35.deriv.DAOD_HIGG8D1.e5928_e5984_s3126_r10201_r10210_p4133
 mc16_13TeV.364512.Sherpa_222_NNPDF30NNLO_tautaugamma_pty_35_70.deriv.DAOD_HIGG8D1.e5928_e5984_s3126_r10201_r10210_p4133
 mc16_13TeV.364513.Sherpa_222_NNPDF30NNLO_tautaugamma_pty_70_140.deriv.DAOD_HIGG8D1.e5982_e5984_s3126_r10201_r10210_p4133
 mc16_13TeV.364513.Sherpa_222_NNPDF30NNLO_tautaugamma_pty_70_140.deriv.DAOD_HIGG8D1.e5928_e5984_s3126_r10201_r10210_p4133
 mc16_13TeV.364514.Sherpa_222_NNPDF30NNLO_tautaugamma_pty_140_E_CMS.deriv.DAOD_HIGG8D1.e5928_e5984_s3126_r10201_r10210_p4133
 mc16_13TeV.364521.Sherpa_222_NNPDF30NNLO_enugamma_pty_7_15.deriv.DAOD_HIGG8D1.e5928_e5984_s3126_r10201_r10210_p4133
 mc16_13TeV.364522.Sherpa_222_NNPDF30NNLO_enugamma_pty_15_35.deriv.DAOD_HIGG8D1.e5928_e5984_s3126_r10201_r10210_p4133

mc16_13TeV.364523.Sherpa_222_NNPDF30NNLO_enugamma_pty_35_70.deriv.DAOD_HIGG8D1.e5928_e5984_s3126_r10201_r10210_p4133
 mc16_13TeV.364524.Sherpa_222_NNPDF30NNLO_enugamma_pty_70_140.deriv.DAOD_HIGG8D1.e5928_e5984_s3126_r10201_r10210_p4133
 mc16_13TeV.364525.Sherpa_222_NNPDF30NNLO_enugamma_pty_140_E_CMS.deriv.DAOD_HIGG8D1.e5928_e5984_s3126_r10201_r10210_p4133
 mc16_13TeV.364526.Sherpa_222_NNPDF30NNLO_munugamma_pty_7_15.deriv.DAOD_HIGG8D1.e5928_e5984_s3126_r10201_r10210_p4133
 mc16_13TeV.364527.Sherpa_222_NNPDF30NNLO_munugamma_pty_15_35.deriv.DAOD_HIGG8D1.e5928_e5984_s3126_r10201_r10210_p4133
 mc16_13TeV.364528.Sherpa_222_NNPDF30NNLO_munugamma_pty_35_70.deriv.DAOD_HIGG8D1.e5928_e5984_s3126_r10201_r10210_p4133
 mc16_13TeV.364529.Sherpa_222_NNPDF30NNLO_munugamma_pty_70_140.deriv.DAOD_HIGG8D1.e5928_e5984_s3126_r10201_r10210_p4133
 mc16_13TeV.364530.Sherpa_222_NNPDF30NNLO_munugamma_pty_140_E_CMS.deriv.DAOD_HIGG8D1.e5928_e5984_s3126_r10201_r10210_p4133
 mc16_13TeV.364531.Sherpa_222_NNPDF30NNLO_taunugamma_pty_7_15.deriv.DAOD_HIGG8D1.e5928_e5984_s3126_r10201_r10210_p4133
 mc16_13TeV.364532.Sherpa_222_NNPDF30NNLO_taunugamma_pty_15_35.deriv.DAOD_HIGG8D1.e5928_e5984_s3126_r10201_r10210_p4133
 mc16_13TeV.364533.Sherpa_222_NNPDF30NNLO_taunugamma_pty_35_70.deriv.DAOD_HIGG8D1.e5928_e5984_s3126_r10201_r10210_p4133
 mc16_13TeV.364534.Sherpa_222_NNPDF30NNLO_taunugamma_pty_70_140.deriv.DAOD_HIGG8D1.e5928_e5984_s3126_r10201_r10210_p4133
 mc16_13TeV.364535.Sherpa_222_NNPDF30NNLO_taunugamma_pty_140_E_CMS.deriv.DAOD_HIGG8D1.e5928_e5984_s3126_r10201_r10210_p4133
 mc16_13TeV.410560.MadGraphPythia8EvtGen_A14_tZ_4fl_tchan_noAllHad.deriv.DAOD_HIGG8D1.e5803_e5984_s3126_r10201_r10210_p4133
 mc16_13TeV.410013.PowhegPythiaEvtGen_P2012_Wt_inclusive_top.deriv.DAOD_HIGG8D1.e3753_s3126_r10201_r10210_p4133
 mc16_13TeV.410014.PowhegPythiaEvtGen_P2012_Wt_inclusive_antitop.deriv.DAOD_HIGG8D1.e3753_s3126_r10201_r10210_p4133
 mc16_13TeV.410408.aMcAtNloPythia8EvtGen_tWZ_Ztoll_minDR1.deriv.DAOD_HIGG8D1.e6423_e5984_s3126_r10201_r10210_p4133
 mc16_13TeV.364242.Sherpa_222_NNPDF30NNLO_WWW_3l3v_EW6.deriv.DAOD_HIGG8D1.e5887_e5984_s3126_r10201_r10210_p4133
 mc16_13TeV.364243.Sherpa_222_NNPDF30NNLO_WWZ_4l2v_EW6.deriv.DAOD_HIGG8D1.e5887_e5984_s3126_r10201_r10210_p4133
 mc16_13TeV.364244.Sherpa_222_NNPDF30NNLO_WWZ_2l4v_EW6.deriv.DAOD_HIGG8D1.e5887_e5984_s3126_r10201_r10210_p4133
 mc16_13TeV.364245.Sherpa_222_NNPDF30NNLO_WZZ_5l1v_EW6.deriv.DAOD_HIGG8D1.e5887_e5984_s3126_r10201_r10210_p4133
 mc16_13TeV.364246.Sherpa_222_NNPDF30NNLO_WZZ_3l3v_EW6.deriv.DAOD_HIGG8D1.e5887_e5984_s3126_r10201_r10210_p4133
 mc16_13TeV.364247.Sherpa_222_NNPDF30NNLO_ZZZ_6l0v_EW6.deriv.DAOD_HIGG8D1.e5887_e5984_s3126_r10201_r10210_p4133
 mc16_13TeV.364248.Sherpa_222_NNPDF30NNLO_ZZZ_4l2v_EW6.deriv.DAOD_HIGG8D1.e5887_e5984_s3126_r10201_r10210_p4133
 mc16_13TeV.364249.Sherpa_222_NNPDF30NNLO_ZZZ_2l4v_EW6.deriv.DAOD_HIGG8D1.e5887_e5984_s3126_r10201_r10210_p4133
 mc16_13TeV.342284.Pythia8EvtGen_A14NNPDF23LO_WH125_inc.deriv.DAOD_HIGG8D1.e4246_e5984_s3126_r10201_r10210_p4133
 mc16_13TeV.342285.Pythia8EvtGen_A14NNPDF23LO_ZH125_inc.deriv.DAOD_HIGG8D1.e4246_e5984_s3126_r10201_r10210_p4133
 mc16_13TeV.341998.aMcAtNloHppEG_UEEE5_CTEQ6L1_CT10ME_tWH125_gamgam_yt_plus1.deriv.DAOD_HIGG8D1.e4394_e5984_s3126_r10201_r10210_p4133
 mc16_13TeV.410470.PhPy8EG_A14_ttbar_hdamp258p75_nonallhad.deriv.DAOD_HIGG8D1.e6337_e5984_s3126_r10201_r10210_p4133
 mc16_13TeV.410472.PhPy8EG_A14_ttbar_hdamp258p75_dil.deriv.DAOD_HIGG8D1.e6348_e5984_s3126_r10201_r10210_p4133
 mc16_13TeV.346343.PhPy8EG_A14NNPDF23_NNPDF30ME_ttH125_allhad.deriv.DAOD_HIGG8D1.e7148_e5984_s3126_r10201_r10210_p4133

mc16_13TeV.346344.PhPy8EG_A14NNPDF23_NNPDF30ME_ttH125_semilep.deriv.DAOD_HIGG8D1.e7148_e5984_a875_r10201_r10210_p4133

mc16_13TeV.346345.PhPy8EG_A14NNPDF23_NNPDF30ME_ttH125_dilep.deriv.DAOD_HIGG8D1.e7148_e5984_a875_r10201_r10210_p4133

mc16e:

mc16_13TeV.361605.PowhegPy8EG_CT10nloME_AZNLOCTEQ6L1_ZZvvvv_mll4.deriv.DAOD_HIGG8D1.e4054_e5984_s3126_r10724_r10726_p4133

mc16_13TeV.361602.PowhegPy8EG_CT10nloME_AZNLOCTEQ6L1_WZlvvv_mll4.deriv.DAOD_HIGG8D1.e4054_e5984_s3126_r10724_r10726_p4133

mc16_13TeV.361601.PowhegPy8EG_CT10nloME_AZNLOCTEQ6L1_WZlvlL_mll4.deriv.DAOD_HIGG8D1.e4475_e5984_s3126_r10724_r10726_p4133

mc16_13TeV.361600.PowhegPy8EG_CT10nloME_AZNLOCTEQ6L1_WWlvvv.deriv.DAOD_HIGG8D1.e4616_e5984_s3126_r10724_r10726_p4133

mc16_13TeV.361603.PowhegPy8EG_CT10nloME_AZNLOCTEQ6L1_ZZllll_mll4.deriv.DAOD_HIGG8D1.e4475_e5984_s3126_r10724_r10726_p4133

mc16_13TeV.361604.PowhegPy8EG_CT10nloME_AZNLOCTEQ6L1_ZZvvll_mll4.deriv.DAOD_HIGG8D1.e4475_e5984_s3126_r10724_r10726_p4133

mc16_13TeV.364288.Sherpa_222_NNPDF30NNLO_llll_lowMllPtComplement.deriv.DAOD_HIGG8D1.e6096_s3126_r10724_p3983 mc16_13TeV.364287.Sherpa_222_NNPDF

mc16_13TeV.364285.Sherpa_222_NNPDF30NNLO_llvjj_EW6.deriv.DAOD_HIGG8D1.e6055_e5984_s3126_r10724_r10726_p3983

mc16_13TeV.364284.Sherpa_222_NNPDF30NNLO_llvjj_EW6.deriv.DAOD_HIGG8D1.e6055_s3126_r10724_p3983

mc16_13TeV.364283.Sherpa_222_NNPDF30NNLO_lllljj_EW6.deriv.DAOD_HIGG8D1.e6055_s3126_r10724_p3983

mc16_13TeV.364739.MGPy8EG_NNPDF30NLO_A14NNPDF23LO_lvlljjEW6_OFMinus.deriv.DAOD_HIGG8D1.e7421_e5984_s3126_r10724_r10726_p4133

mc16_13TeV.364742.MGPy8EG_NNPDF30NLO_A14NNPDF23LO_lvlljjEW6_SFPlus.deriv.DAOD_HIGG8D1.e7421_e5984_s3126_r10724_r10726_p4133

mc16_13TeV.364740.MGPy8EG_NNPDF30NLO_A14NNPDF23LO_lvlljjEW6_OFPlus.deriv.DAOD_HIGG8D1.e7421_e5984_s3126_r10724_r10726_p4133

mc16_13TeV.364741.MGPy8EG_NNPDF30NLO_A14NNPDF23LO_lvlljjEW6_SFMinus.deriv.DAOD_HIGG8D1.e7421_e5984_s3126_r10724_r10726_p4133

mc16_13TeV.364253.Sherpa_222_NNPDF30NNLO_llv.deriv.DAOD_HIGG8D1.e5916_e5984_s3126_r10724_r10726_p4133

mc16_13TeV.364250.Sherpa_222_NNPDF30NNLO_llll.deriv.DAOD_HIGG8D1.e5894_e5984_s3126_r10724_r10726_p4133

mc16_13TeV.364254.Sherpa_222_NNPDF30NNLO_llv.deriv.DAOD_HIGG8D1.e5916_e5984_s3126_r10724_r10726_p4133

mc16_13TeV.364255.Sherpa_222_NNPDF30NNLO_lvvv.deriv.DAOD_HIGG8D1.e5916_e5984_s3126_r10724_r10726_p4133

mc16_13TeV.410155.aMcAtNloPythia8EvtGen_MEN30NLO_A14N23LO_ttW.deriv.DAOD_HIGG8D1.e5070_e5984_s3126_r10724_r10726_p4133

mc16_13TeV.410156.aMcAtNloPythia8EvtGen_MEN30NLO_A14N23LO_ttZnunu.deriv.DAOD_HIGG8D1.e5070_e5984_s3126_r10724_r10726_p4133

mc16_13TeV.410157.aMcAtNloPythia8EvtGen_MEN30NLO_A14N23LO_ttZqq.deriv.DAOD_HIGG8D1.e5070_e5984_s3126_r10724_r10726_p4133

mc16_13TeV.410218.aMcAtNloPythia8EvtGen_MEN30NLO_A14N23LO_ttee.deriv.DAOD_HIGG8D1.e5070_e5984_s3126_r10724_r10726_p4133

mc16_13TeV.410219.aMcAtNloPythia8EvtGen_MEN30NLO_A14N23LO_ttmumu.deriv.DAOD_HIGG8D1.e5070_e5984_s3126_r10724_r10726_p4133

mc16_13TeV.410220.aMcAtNloPythia8EvtGen_MEN30NLO_A14N23LO_ttautau.deriv.DAOD_HIGG8D1.e5070_e5984_s3126_r10724_r10726_p4133

mc16_13TeV.410276.aMcAtNloPythia8EvtGen_MEN30NLO_A14N23LO_ttee_mll_1_5.deriv.DAOD_HIGG8D1.e6087_e5984_s3126_r10724_r10726_p4133

mc16_13TeV.410277.aMcAtNloPythia8EvtGen_MEN30NLO_A14N23LO_ttmumu_mll_1_5.deriv.DAOD_HIGG8D1.e6087_e5984_s3126_r10724_r10726_p4133

mc16_13TeV.410278.aMcAtNloPythia8EvtGen_MEN30NLO_A14N23LO_ttautau_mll_1_5.deriv.DAOD_HIGG8D1.e6087_e5984_s3126_r10724_r10726_p4133

mc16_13TeV.410397.MadGraphPythia8EvtGen_ttbar_wbee_MEN30LO_A14N23LO.deriv.DAOD_HIGG8D1.e6086_e5984_s3126_r10724_r10726_p4133
 mc16_13TeV.410398.MadGraphPythia8EvtGen_ttbar_wbmumu_MEN30LO_A14N23LO.deriv.DAOD_HIGG8D1.e6086_e5984_s3126_r10724_r10726_p4133
 mc16_13TeV.410399.MadGraphPythia8EvtGen_ttbar_wbttau_MEN30LO_A14N23LO.deriv.DAOD_HIGG8D1.e6086_e5984_s3126_r10724_r10726_p4133
 mc16_13TeV.410658.PhPy8EG_A14_tchan_BW50_lept_top.deriv.DAOD_HIGG8D1.e6671_e5984_s3126_s3136_r10724_r10726_p4133
 mc16_13TeV.410659.PhPy8EG_A14_tchan_BW50_lept_antitop.deriv.DAOD_HIGG8D1.e6671_e5984_s3126_s3136_r10724_r10726_p4133
 mc16_13TeV.410644.PowhegPythia8EvtGen_A14_singletop_schan_lept_top.deriv.DAOD_HIGG8D1.e6527_e5984_s3126_r10724_r10726_p4133
 mc16_13TeV.410645.PowhegPythia8EvtGen_A14_singletop_schan_lept_antitop.deriv.DAOD_HIGG8D1.e6527_e5984_s3126_r10724_r10726_p4133
 mc16_13TeV.412063.aMcAtNloPythia8EvtGen_llq_NNPDF30_nf4_A14.deriv.DAOD_TOPQ1.e7054_e5984_s3126_r10724_r10726_p4174
 mc16_13TeV.304014.MadGraphPythia8EvtGen_A14NNPDF23_3top_SM.deriv.DAOD_HIGG8D1.e4324_e5984_s3126_r10724_r10726_p4133
 mc16_13TeV.410080.MadGraphPythia8EvtGen_A14NNPDF23_4topSM.deriv.DAOD_HIGG8D1.e4111_e5984_s3126_r10724_r10726_p4133
 mc16_13TeV.410081.MadGraphPythia8EvtGen_A14NNPDF23_ttbarWW.deriv.DAOD_HIGG8D1.e4111_e5984_s3126_r10724_r10726_p4133
 mc16_13TeV.364100.Sherpa_221_NNPDF30NNLO_Zmumu_MAXHTPTV0_70_CVetoBVeto.deriv.DAOD_HIGG8D1.e5271_e5984_s3126_s3136_r10724_r10726_p4133
 mc16_13TeV.364100.Sherpa_221_NNPDF30NNLO_Zmumu_MAXHTPTV0_70_CVetoBVeto.deriv.DAOD_HIGG8D1.e5271_e5984_s3126_r10724_r10726_p4133
 mc16_13TeV.364101.Sherpa_221_NNPDF30NNLO_Zmumu_MAXHTPTV0_70_CFilterBVeto.deriv.DAOD_HIGG8D1.e5271_e5984_s3126_r10724_r10726_p4133
 mc16_13TeV.364102.Sherpa_221_NNPDF30NNLO_Zmumu_MAXHTPTV0_70_BFilter.deriv.DAOD_HIGG8D1.e5271_e5984_s3126_s3136_r10724_r10726_p4133
 mc16_13TeV.364102.Sherpa_221_NNPDF30NNLO_Zmumu_MAXHTPTV0_70_BFilter.deriv.DAOD_HIGG8D1.e5271_e5984_s3126_r10724_r10726_p4133
 mc16_13TeV.364103.Sherpa_221_NNPDF30NNLO_Zmumu_MAXHTPTV70_140_CVetoBVeto.deriv.DAOD_HIGG8D1.e5271_e5984_s3126_r10724_r10726_p4133
 mc16_13TeV.364103.Sherpa_221_NNPDF30NNLO_Zmumu_MAXHTPTV70_140_CVetoBVeto.deriv.DAOD_HIGG8D1.e5271_e5984_s3126_s3136_r10724_r10726_p4133
 mc16_13TeV.364104.Sherpa_221_NNPDF30NNLO_Zmumu_MAXHTPTV70_140_CFilterBVeto.deriv.DAOD_HIGG8D1.e5271_e5984_s3126_r10724_r10726_p4133
 mc16_13TeV.364104.Sherpa_221_NNPDF30NNLO_Zmumu_MAXHTPTV70_140_CFilterBVeto.deriv.DAOD_HIGG8D1.e5271_e5984_s3126_s3136_r10724_r10726_p4133
 mc16_13TeV.364106.Sherpa_221_NNPDF30NNLO_Zmumu_MAXHTPTV140_280_CVetoBVeto.deriv.DAOD_HIGG8D1.e5271_e5984_s3126_s3136_r10724_r10726_p4133
 mc16_13TeV.364107.Sherpa_221_NNPDF30NNLO_Zmumu_MAXHTPTV140_280_CFilterBVeto.deriv.DAOD_HIGG8D1.e5271_e5984_s3126_r10724_r10726_p4133
 mc16_13TeV.364107.Sherpa_221_NNPDF30NNLO_Zmumu_MAXHTPTV140_280_CFilterBVeto.deriv.DAOD_HIGG8D1.e5271_e5984_s3126_s3136_r10724_r10726_p4133
 mc16_13TeV.364108.Sherpa_221_NNPDF30NNLO_Zmumu_MAXHTPTV140_280_BFilter.deriv.DAOD_HIGG8D1.e5271_e5984_s3126_r10724_r10726_p4133
 mc16_13TeV.364109.Sherpa_221_NNPDF30NNLO_Zmumu_MAXHTPTV280_500_CVetoBVeto.deriv.DAOD_HIGG8D1.e5271_e5984_s3126_r10724_r10726_p4133
 mc16_13TeV.364110.Sherpa_221_NNPDF30NNLO_Zmumu_MAXHTPTV280_500_CFilterBVeto.deriv.DAOD_HIGG8D1.e5271_e5984_s3126_r10724_r10726_p4133
 mc16_13TeV.364110.Sherpa_221_NNPDF30NNLO_Zmumu_MAXHTPTV280_500_CFilterBVeto.deriv.DAOD_HIGG8D1.e5271_e5984_s3126_s3136_r10724_r10726_p4133
 mc16_13TeV.364111.Sherpa_221_NNPDF30NNLO_Zmumu_MAXHTPTV280_500_BFilter.deriv.DAOD_HIGG8D1.e5271_e5984_s3126_s3136_r10724_r10726_p4133
 mc16_13TeV.364111.Sherpa_221_NNPDF30NNLO_Zmumu_MAXHTPTV280_500_BFilter.deriv.DAOD_HIGG8D1.e5271_e5984_s3126_r10724_r10726_p4133
 mc16_13TeV.364112.Sherpa_221_NNPDF30NNLO_Zmumu_MAXHTPTV500_1000.deriv.DAOD_HIGG8D1.e5271_e5984_s3126_r10724_r10726_p4133

mc16_13TeV.364113.Sherpa_221_NNPDF30NNLO_Zmumu_MAXHTPTV1000_E_CMS.deriv.DAOD_HIGG8D1.e5271_e5984_s3126_r10724_r10726_p4133
 mc16_13TeV.364113.Sherpa_221_NNPDF30NNLO_Zmumu_MAXHTPTV1000_E_CMS.deriv.DAOD_HIGG8D1.e5271_e5984_s3126_s3136_r10724_r10726_p4133
 mc16_13TeV.364114.Sherpa_221_NNPDF30NNLO_Zee_MAXHTPTV0_70_CVetoBVeto.deriv.DAOD_HIGG8D1.e5299_e5984_s3126_s3136_r10724_r10726_p4133
 mc16_13TeV.364114.Sherpa_221_NNPDF30NNLO_Zee_MAXHTPTV0_70_CVetoBVeto.deriv.DAOD_HIGG8D1.e5299_e5984_s3126_r10724_r10726_p4133
 mc16_13TeV.364115.Sherpa_221_NNPDF30NNLO_Zee_MAXHTPTV0_70_CFilterBVeto.deriv.DAOD_HIGG8D1.e5299_e5984_s3126_s3136_r10724_r10726_p4133
 mc16_13TeV.364115.Sherpa_221_NNPDF30NNLO_Zee_MAXHTPTV0_70_CFilterBVeto.deriv.DAOD_HIGG8D1.e5299_e5984_s3126_r10724_r10726_p4133
 mc16_13TeV.364116.Sherpa_221_NNPDF30NNLO_Zee_MAXHTPTV0_70_BFilter.deriv.DAOD_HIGG8D1.e5299_e5984_s3126_r10724_r10726_p4133
 mc16_13TeV.364117.Sherpa_221_NNPDF30NNLO_Zee_MAXHTPTV70_140_CVetoBVeto.deriv.DAOD_HIGG8D1.e5299_e5984_s3126_s3136_r10724_r10726_p4133
 mc16_13TeV.364117.Sherpa_221_NNPDF30NNLO_Zee_MAXHTPTV70_140_CVetoBVeto.deriv.DAOD_HIGG8D1.e5299_e5984_s3126_r10724_r10726_p4133
 mc16_13TeV.364118.Sherpa_221_NNPDF30NNLO_Zee_MAXHTPTV70_140_CFilterBVeto.deriv.DAOD_HIGG8D1.e5299_e5984_s3126_s3136_r10724_r10726_p4133
 mc16_13TeV.364118.Sherpa_221_NNPDF30NNLO_Zee_MAXHTPTV70_140_CFilterBVeto.deriv.DAOD_HIGG8D1.e5299_e5984_s3126_r10724_r10726_p4133
 mc16_13TeV.364119.Sherpa_221_NNPDF30NNLO_Zee_MAXHTPTV70_140_BFilter.deriv.DAOD_HIGG8D1.e5299_e5984_s3126_r10724_r10726_p4133
 mc16_13TeV.364120.Sherpa_221_NNPDF30NNLO_Zee_MAXHTPTV140_280_CVetoBVeto.deriv.DAOD_HIGG8D1.e5299_e5984_s3126_r10724_r10726_p4133
 mc16_13TeV.364121.Sherpa_221_NNPDF30NNLO_Zee_MAXHTPTV140_280_CFilterBVeto.deriv.DAOD_HIGG8D1.e5299_e5984_s3126_r10724_r10726_p4133
 mc16_13TeV.364122.Sherpa_221_NNPDF30NNLO_Zee_MAXHTPTV140_280_BFilter.deriv.DAOD_HIGG8D1.e5299_e5984_s3126_s3136_r10724_r10726_p4133
 mc16_13TeV.364122.Sherpa_221_NNPDF30NNLO_Zee_MAXHTPTV140_280_BFilter.deriv.DAOD_HIGG8D1.e5299_e5984_s3126_r10724_r10726_p4133
 mc16_13TeV.364123.Sherpa_221_NNPDF30NNLO_Zee_MAXHTPTV280_500_CVetoBVeto.deriv.DAOD_HIGG8D1.e5299_e5984_s3126_r10724_r10726_p4133
 mc16_13TeV.364124.Sherpa_221_NNPDF30NNLO_Zee_MAXHTPTV280_500_CFilterBVeto.deriv.DAOD_HIGG8D1.e5299_e5984_s3126_r10724_r10726_p4133
 mc16_13TeV.364125.Sherpa_221_NNPDF30NNLO_Zee_MAXHTPTV280_500_BFilter.deriv.DAOD_HIGG8D1.e5299_e5984_s3126_s3136_r10724_r10726_p4133
 mc16_13TeV.364125.Sherpa_221_NNPDF30NNLO_Zee_MAXHTPTV280_500_BFilter.deriv.DAOD_HIGG8D1.e5299_e5984_s3126_r10724_r10726_p4133
 mc16_13TeV.364126.Sherpa_221_NNPDF30NNLO_Zee_MAXHTPTV500_1000.deriv.DAOD_HIGG8D1.e5299_e5984_s3126_r10724_r10726_p4133
 mc16_13TeV.364126.Sherpa_221_NNPDF30NNLO_Zee_MAXHTPTV500_1000.deriv.DAOD_HIGG8D1.e5299_e5984_s3126_s3136_r10724_r10726_p4133
 mc16_13TeV.364127.Sherpa_221_NNPDF30NNLO_Zee_MAXHTPTV1000_E_CMS.deriv.DAOD_HIGG8D1.e5299_e5984_s3126_s3136_r10724_r10726_p4133
 mc16_13TeV.364127.Sherpa_221_NNPDF30NNLO_Zee_MAXHTPTV1000_E_CMS.deriv.DAOD_HIGG8D1.e5299_e5984_s3126_r10724_r10726_p4133
 mc16_13TeV.364128.Sherpa_221_NNPDF30NNLO_Ztautau_MAXHTPTV0_70_CVetoBVeto.deriv.DAOD_HIGG8D1.e5307_e5984_s3126_s3136_r10724_r10726_p4133
 mc16_13TeV.364128.Sherpa_221_NNPDF30NNLO_Ztautau_MAXHTPTV0_70_CVetoBVeto.deriv.DAOD_HIGG8D1.e5307_e5984_s3126_r10724_r10726_p4133
 mc16_13TeV.364129.Sherpa_221_NNPDF30NNLO_Ztautau_MAXHTPTV0_70_CFilterBVeto.deriv.DAOD_HIGG8D1.e5307_e5984_s3126_r10724_r10726_p4133
 mc16_13TeV.364129.Sherpa_221_NNPDF30NNLO_Ztautau_MAXHTPTV0_70_CFilterBVeto.deriv.DAOD_HIGG8D1.e5307_e5984_s3126_s3136_r10724_r10726_p4133
 mc16_13TeV.364130.Sherpa_221_NNPDF30NNLO_Ztautau_MAXHTPTV0_70_BFilter.deriv.DAOD_HIGG8D1.e5307_e5984_s3126_s3136_r10724_r10726_p4133
 mc16_13TeV.364130.Sherpa_221_NNPDF30NNLO_Ztautau_MAXHTPTV0_70_BFilter.deriv.DAOD_HIGG8D1.e5307_e5984_s3126_r10724_r10726_p4133
 mc16_13TeV.364131.Sherpa_221_NNPDF30NNLO_Ztautau_MAXHTPTV70_140_CVetoBVeto.deriv.DAOD_HIGG8D1.e5307_e5984_s3126_r10724_r10726_p4133

mc16_13TeV.364132.Sherpa_221_NNPDF30NNLO_Ztautau_MAXHTPTV70_140_CFilterBVeto.deriv.DAOD_HIGG8D1.e5307_e5984_s3126_r10724_r10726_p4133
 mc16_13TeV.364132.Sherpa_221_NNPDF30NNLO_Ztautau_MAXHTPTV70_140_CFilterBVeto.deriv.DAOD_HIGG8D1.e5307_e5984_s3126_s3136_r10724_r10726_p4133
 mc16_13TeV.364133.Sherpa_221_NNPDF30NNLO_Ztautau_MAXHTPTV70_140_BFilter.deriv.DAOD_HIGG8D1.e5307_e5984_s3126_r10724_r10726_p4133
 mc16_13TeV.364134.Sherpa_221_NNPDF30NNLO_Ztautau_MAXHTPTV140_280_CVetoBVeto.deriv.DAOD_HIGG8D1.e5307_e5984_s3126_r10724_r10726_p4133
 mc16_13TeV.364135.Sherpa_221_NNPDF30NNLO_Ztautau_MAXHTPTV140_280_CFilterBVeto.deriv.DAOD_HIGG8D1.e5307_e5984_s3126_r10724_r10726_p4133
 mc16_13TeV.364135.Sherpa_221_NNPDF30NNLO_Ztautau_MAXHTPTV140_280_CFilterBVeto.deriv.DAOD_HIGG8D1.e5307_e5984_s3126_s3136_r10724_r10726_p4133
 mc16_13TeV.364136.Sherpa_221_NNPDF30NNLO_Ztautau_MAXHTPTV140_280_BFilter.deriv.DAOD_HIGG8D1.e5307_e5984_s3126_r10724_r10726_p4133
 mc16_13TeV.364137.Sherpa_221_NNPDF30NNLO_Ztautau_MAXHTPTV280_500_CVetoBVeto.deriv.DAOD_HIGG8D1.e5307_e5984_s3126_r10724_r10726_p4133
 mc16_13TeV.364138.Sherpa_221_NNPDF30NNLO_Ztautau_MAXHTPTV280_500_CFilterBVeto.deriv.DAOD_HIGG8D1.e5313_e5984_s3126_s3136_r10724_r10726_p4133
 mc16_13TeV.364138.Sherpa_221_NNPDF30NNLO_Ztautau_MAXHTPTV280_500_CFilterBVeto.deriv.DAOD_HIGG8D1.e5313_e5984_s3126_r10724_r10726_p4133
 mc16_13TeV.364139.Sherpa_221_NNPDF30NNLO_Ztautau_MAXHTPTV280_500_BFilter.deriv.DAOD_HIGG8D1.e5313_e5984_s3126_r10724_r10726_p4133
 mc16_13TeV.364139.Sherpa_221_NNPDF30NNLO_Ztautau_MAXHTPTV280_500_BFilter.deriv.DAOD_HIGG8D1.e5313_e5984_s3126_s3136_r10724_r10726_p4133
 mc16_13TeV.364140.Sherpa_221_NNPDF30NNLO_Ztautau_MAXHTPTV500_1000.deriv.DAOD_HIGG8D1.e5307_e5984_s3126_r10724_r10726_p4133
 mc16_13TeV.364140.Sherpa_221_NNPDF30NNLO_Ztautau_MAXHTPTV500_1000.deriv.DAOD_HIGG8D1.e5307_e5984_s3126_s3136_r10724_r10726_p4133
 mc16_13TeV.364141.Sherpa_221_NNPDF30NNLO_Ztautau_MAXHTPTV1000_E_CMS.deriv.DAOD_HIGG8D1.e5307_e5984_s3126_s3136_r10724_r10726_p4133
 mc16_13TeV.364141.Sherpa_221_NNPDF30NNLO_Ztautau_MAXHTPTV1000_E_CMS.deriv.DAOD_HIGG8D1.e5307_e5984_s3126_r10724_r10726_p4133
 mc16_13TeV.364198.Sherpa_221_NN30NNLO_Zmm_Mll10_40_MAXHTPTV0_70_BVeto.deriv.DAOD_HIGG8D1.e5421_e5984_s3126_r10724_r10726_p4133
 mc16_13TeV.364199.Sherpa_221_NN30NNLO_Zmm_Mll10_40_MAXHTPTV0_70_BFilter.deriv.DAOD_HIGG8D1.e5421_e5984_s3126_r10724_r10726_p4133
 mc16_13TeV.364200.Sherpa_221_NN30NNLO_Zmm_Mll10_40_MAXHTPTV70_280_BVeto.deriv.DAOD_HIGG8D1.e5421_e5984_s3126_r10724_r10726_p4133
 mc16_13TeV.364201.Sherpa_221_NN30NNLO_Zmm_Mll10_40_MAXHTPTV70_280_BFilter.deriv.DAOD_HIGG8D1.e5421_e5984_s3126_r10724_r10726_p4133
 mc16_13TeV.364202.Sherpa_221_NN30NNLO_Zmm_Mll10_40_MAXHTPTV280_E_CMS_BVeto.deriv.DAOD_HIGG8D1.e5421_e5984_s3126_r10724_r10726_p4133
 mc16_13TeV.364203.Sherpa_221_NN30NNLO_Zmm_Mll10_40_MAXHTPTV280_E_CMS_BFilter.deriv.DAOD_HIGG8D1.e5421_e5984_s3126_r10724_r10726_p4133
 mc16_13TeV.364204.Sherpa_221_NN30NNLO_Zee_Mll10_40_MAXHTPTV0_70_BVeto.deriv.DAOD_HIGG8D1.e5421_e5984_s3126_r10724_r10726_p4133
 mc16_13TeV.364205.Sherpa_221_NN30NNLO_Zee_Mll10_40_MAXHTPTV0_70_BFilter.deriv.DAOD_HIGG8D1.e5421_e5984_s3126_r10724_r10726_p4133
 mc16_13TeV.364206.Sherpa_221_NN30NNLO_Zee_Mll10_40_MAXHTPTV70_280_BVeto.deriv.DAOD_HIGG8D1.e5421_e5984_s3126_r10724_r10726_p4133
 mc16_13TeV.364207.Sherpa_221_NN30NNLO_Zee_Mll10_40_MAXHTPTV70_280_BFilter.deriv.DAOD_HIGG8D1.e5421_e5984_s3126_r10724_r10726_p4133
 mc16_13TeV.364208.Sherpa_221_NN30NNLO_Zee_Mll10_40_MAXHTPTV280_E_CMS_BVeto.deriv.DAOD_HIGG8D1.e5421_e5984_s3126_r10724_r10726_p4133
 mc16_13TeV.364209.Sherpa_221_NN30NNLO_Zee_Mll10_40_MAXHTPTV280_E_CMS_BFilter.deriv.DAOD_HIGG8D1.e5421_e5984_s3126_r10724_r10726_p4133
 mc16_13TeV.364210.Sherpa_221_NN30NNLO_Ztt_Mll10_40_MAXHTPTV0_70_BVeto.deriv.DAOD_HIGG8D1.e5421_e5984_s3126_r10724_r10726_p4133
 mc16_13TeV.364211.Sherpa_221_NN30NNLO_Ztt_Mll10_40_MAXHTPTV0_70_BFilter.deriv.DAOD_HIGG8D1.e5421_e5984_s3126_r10724_r10726_p4133
 mc16_13TeV.364212.Sherpa_221_NN30NNLO_Ztt_Mll10_40_MAXHTPTV70_280_BVeto.deriv.DAOD_HIGG8D1.e5421_e5984_s3126_r10724_r10726_p4133

mc16_13TeV.364213.Sherpa_221_NN30NNLO_Ztt_Mll10_40_MAXHTPTV70_280_BFilter.deriv.DAOD_HIGG8D1.e5421_e5984_s3126_r10724_r10726_p4133
 mc16_13TeV.364214.Sherpa_221_NN30NNLO_Ztt_Mll10_40_MAXHTPTV280_E_CMS_BVeto.deriv.DAOD_HIGG8D1.e5421_e5984_s3126_r10724_r10726_p4133
 mc16_13TeV.364215.Sherpa_221_NN30NNLO_Ztt_Mll10_40_MAXHTPTV280_E_CMS_BFilter.deriv.DAOD_HIGG8D1.e5421_e5984_s3126_r10724_r10726_p4133
 mc16_13TeV.364156.Sherpa_221_NNPDF30NNLO_Wmunu_MAXHTPTV0_70_CVetoBVeto.deriv.DAOD_HIGG8D1.e5340_e5984_s3126_r10724_r10726_p4133
 mc16_13TeV.364157.Sherpa_221_NNPDF30NNLO_Wmunu_MAXHTPTV0_70_CFilterBVeto.deriv.DAOD_HIGG8D1.e5340_e5984_s3126_r10724_r10726_p4133
 mc16_13TeV.364158.Sherpa_221_NNPDF30NNLO_Wmunu_MAXHTPTV0_70_BFilter.deriv.DAOD_HIGG8D1.e5340_e5984_s3126_s3136_r10724_r10726_p4133
 mc16_13TeV.364158.Sherpa_221_NNPDF30NNLO_Wmunu_MAXHTPTV0_70_BFilter.deriv.DAOD_HIGG8D1.e5340_e5984_s3126_r10724_r10726_p4133
 mc16_13TeV.364159.Sherpa_221_NNPDF30NNLO_Wmunu_MAXHTPTV70_140_CVetoBVeto.deriv.DAOD_HIGG8D1.e5340_e5984_s3126_s3136_r10724_r10726_p4133
 mc16_13TeV.364160.Sherpa_221_NNPDF30NNLO_Wmunu_MAXHTPTV70_140_CFilterBVeto.deriv.DAOD_HIGG8D1.e5340_e5984_s3126_s3136_r10724_r10726_p4133
 mc16_13TeV.364160.Sherpa_221_NNPDF30NNLO_Wmunu_MAXHTPTV70_140_CFilterBVeto.deriv.DAOD_HIGG8D1.e5340_e5984_s3126_r10724_r10726_p4133
 mc16_13TeV.364161.Sherpa_221_NNPDF30NNLO_Wmunu_MAXHTPTV70_140_BFilter.deriv.DAOD_HIGG8D1.e5340_e5984_s3126_r10724_r10726_p4133
 mc16_13TeV.364162.Sherpa_221_NNPDF30NNLO_Wmunu_MAXHTPTV140_280_CVetoBVeto.deriv.DAOD_HIGG8D1.e5340_e5984_s3126_r10724_r10726_p4133
 mc16_13TeV.364163.Sherpa_221_NNPDF30NNLO_Wmunu_MAXHTPTV140_280_CFilterBVeto.deriv.DAOD_HIGG8D1.e5340_e5984_s3126_s3136_r10724_r10726_p4133
 mc16_13TeV.364163.Sherpa_221_NNPDF30NNLO_Wmunu_MAXHTPTV140_280_CFilterBVeto.deriv.DAOD_HIGG8D1.e5340_e5984_s3126_r10724_r10726_p4133
 mc16_13TeV.364164.Sherpa_221_NNPDF30NNLO_Wmunu_MAXHTPTV140_280_BFilter.deriv.DAOD_HIGG8D1.e5340_e5984_s3126_r10724_r10726_p4133
 mc16_13TeV.364165.Sherpa_221_NNPDF30NNLO_Wmunu_MAXHTPTV280_500_CVetoBVeto.deriv.DAOD_HIGG8D1.e5340_e5984_s3126_r10724_r10726_p4133
 mc16_13TeV.364165.Sherpa_221_NNPDF30NNLO_Wmunu_MAXHTPTV280_500_CVetoBVeto.deriv.DAOD_HIGG8D1.e5340_e5984_s3126_s3136_r10724_r10726_p4133
 mc16_13TeV.364166.Sherpa_221_NNPDF30NNLO_Wmunu_MAXHTPTV280_500_CFilterBVeto.deriv.DAOD_HIGG8D1.e5340_e5984_s3126_s3136_r10724_r10726_p4133
 mc16_13TeV.364166.Sherpa_221_NNPDF30NNLO_Wmunu_MAXHTPTV280_500_CFilterBVeto.deriv.DAOD_HIGG8D1.e5340_e5984_s3126_r10724_r10726_p4133
 mc16_13TeV.364167.Sherpa_221_NNPDF30NNLO_Wmunu_MAXHTPTV280_500_BFilter.deriv.DAOD_HIGG8D1.e5340_e5984_s3126_r10724_r10726_p4133
 mc16_13TeV.364167.Sherpa_221_NNPDF30NNLO_Wmunu_MAXHTPTV280_500_BFilter.deriv.DAOD_HIGG8D1.e5340_e5984_s3126_s3136_r10724_r10726_p4133
 mc16_13TeV.364168.Sherpa_221_NNPDF30NNLO_Wmunu_MAXHTPTV500_1000.deriv.DAOD_HIGG8D1.e5340_e5984_s3126_r10724_r10726_p4133
 mc16_13TeV.364168.Sherpa_221_NNPDF30NNLO_Wmunu_MAXHTPTV500_1000.deriv.DAOD_HIGG8D1.e5340_e5984_s3126_s3136_r10724_r10726_p4133
 mc16_13TeV.364169.Sherpa_221_NNPDF30NNLO_Wmunu_MAXHTPTV1000_E_CMS.deriv.DAOD_HIGG8D1.e5340_e5984_s3126_s3136_r10724_r10726_p4133
 mc16_13TeV.364169.Sherpa_221_NNPDF30NNLO_Wmunu_MAXHTPTV1000_E_CMS.deriv.DAOD_HIGG8D1.e5340_e5984_s3126_r10724_r10726_p4133
 mc16_13TeV.364170.Sherpa_221_NNPDF30NNLO_Wenu_MAXHTPTV0_70_CVetoBVeto.deriv.DAOD_HIGG8D1.e5340_e5984_s3126_r10724_r10726_p4133
 mc16_13TeV.364171.Sherpa_221_NNPDF30NNLO_Wenu_MAXHTPTV0_70_CFilterBVeto.deriv.DAOD_HIGG8D1.e5340_e5984_s3126_r10724_r10726_p4133
 mc16_13TeV.364172.Sherpa_221_NNPDF30NNLO_Wenu_MAXHTPTV0_70_BFilter.deriv.DAOD_HIGG8D1.e5340_e5984_s3126_r10724_r10726_p4133
 mc16_13TeV.364173.Sherpa_221_NNPDF30NNLO_Wenu_MAXHTPTV70_140_CVetoBVeto.deriv.DAOD_HIGG8D1.e5340_e5984_s3126_s3136_r10724_r10726_p4133
 mc16_13TeV.364174.Sherpa_221_NNPDF30NNLO_Wenu_MAXHTPTV70_140_CFilterBVeto.deriv.DAOD_HIGG8D1.e5340_e5984_s3126_r10724_r10726_p4133
 mc16_13TeV.364175.Sherpa_221_NNPDF30NNLO_Wenu_MAXHTPTV70_140_BFilter.deriv.DAOD_HIGG8D1.e5340_e5984_s3126_s3136_r10724_r10726_p4133

mc16_13TeV.364176.Sherpa_221_NNPDF30NNLO_Wenu_MAXHTPTV140_280_CVetoBVeto.deriv.DAOD_HIGG8D1.e5340_e5984_s3126_r10724_r10726_p4133
 mc16_13TeV.364177.Sherpa_221_NNPDF30NNLO_Wenu_MAXHTPTV140_280_CFilterBVeto.deriv.DAOD_HIGG8D1.e5340_e5984_s3126_r10724_r10726_p4133
 mc16_13TeV.364177.Sherpa_221_NNPDF30NNLO_Wenu_MAXHTPTV140_280_CFilterBVeto.deriv.DAOD_HIGG8D1.e5340_e5984_s3126_s3136_r10724_r10726_p4133
 mc16_13TeV.364178.Sherpa_221_NNPDF30NNLO_Wenu_MAXHTPTV140_280_BFilter.deriv.DAOD_HIGG8D1.e5340_e5984_s3126_r10724_r10726_p4133
 mc16_13TeV.364179.Sherpa_221_NNPDF30NNLO_Wenu_MAXHTPTV280_500_CVetoBVeto.deriv.DAOD_HIGG8D1.e5340_e5984_s3126_r10724_r10726_p4133
 mc16_13TeV.364179.Sherpa_221_NNPDF30NNLO_Wenu_MAXHTPTV280_500_CVetoBVeto.deriv.DAOD_HIGG8D1.e5340_e5984_s3126_s3136_r10724_r10726_p4133
 mc16_13TeV.364180.Sherpa_221_NNPDF30NNLO_Wenu_MAXHTPTV280_500_CFilterBVeto.deriv.DAOD_HIGG8D1.e5340_e5984_s3126_s3136_r10724_r10726_p4133
 mc16_13TeV.364180.Sherpa_221_NNPDF30NNLO_Wenu_MAXHTPTV280_500_CFilterBVeto.deriv.DAOD_HIGG8D1.e5340_e5984_s3126_r10724_r10726_p4133
 mc16_13TeV.364181.Sherpa_221_NNPDF30NNLO_Wenu_MAXHTPTV280_500_BFilter.deriv.DAOD_HIGG8D1.e5340_e5984_s3126_s3136_r10724_r10726_p4133
 mc16_13TeV.364181.Sherpa_221_NNPDF30NNLO_Wenu_MAXHTPTV280_500_BFilter.deriv.DAOD_HIGG8D1.e5340_e5984_s3126_r10724_r10726_p4133
 mc16_13TeV.364182.Sherpa_221_NNPDF30NNLO_Wenu_MAXHTPTV500_1000.deriv.DAOD_HIGG8D1.e5340_e5984_s3126_s3136_r10724_r10726_p4133
 mc16_13TeV.364182.Sherpa_221_NNPDF30NNLO_Wenu_MAXHTPTV500_1000.deriv.DAOD_HIGG8D1.e5340_e5984_s3126_r10724_r10726_p4133
 mc16_13TeV.364183.Sherpa_221_NNPDF30NNLO_Wenu_MAXHTPTV1000_E_CMS.deriv.DAOD_HIGG8D1.e5340_e5984_s3126_r10724_r10726_p4133
 mc16_13TeV.364183.Sherpa_221_NNPDF30NNLO_Wenu_MAXHTPTV1000_E_CMS.deriv.DAOD_HIGG8D1.e5340_e5984_s3126_s3136_r10724_r10726_p4133
 mc16_13TeV.364184.Sherpa_221_NNPDF30NNLO_Wtaunu_MAXHTPTV0_70_CVetoBVeto.deriv.DAOD_HIGG8D1.e5340_e5984_s3126_r10724_r10726_p4133
 mc16_13TeV.364185.Sherpa_221_NNPDF30NNLO_Wtaunu_MAXHTPTV0_70_CFilterBVeto.deriv.DAOD_HIGG8D1.e5340_e5984_s3126_r10724_r10726_p4133
 mc16_13TeV.364186.Sherpa_221_NNPDF30NNLO_Wtaunu_MAXHTPTV0_70_BFilter.deriv.DAOD_HIGG8D1.e5340_e5984_s3126_s3136_r10724_r10726_p4133
 mc16_13TeV.364186.Sherpa_221_NNPDF30NNLO_Wtaunu_MAXHTPTV0_70_BFilter.deriv.DAOD_HIGG8D1.e5340_e5984_s3126_r10724_r10726_p4133
 mc16_13TeV.364187.Sherpa_221_NNPDF30NNLO_Wtaunu_MAXHTPTV70_140_CVetoBVeto.deriv.DAOD_HIGG8D1.e5340_e5984_s3126_r10724_r10726_p4133
 mc16_13TeV.364188.Sherpa_221_NNPDF30NNLO_Wtaunu_MAXHTPTV70_140_CFilterBVeto.deriv.DAOD_HIGG8D1.e5340_e5984_s3126_r10724_r10726_p4133
 mc16_13TeV.364189.Sherpa_221_NNPDF30NNLO_Wtaunu_MAXHTPTV70_140_BFilter.deriv.DAOD_HIGG8D1.e5340_e5984_s3126_r10724_r10726_p4133
 mc16_13TeV.364189.Sherpa_221_NNPDF30NNLO_Wtaunu_MAXHTPTV70_140_BFilter.deriv.DAOD_HIGG8D1.e5340_e5984_s3126_s3136_r10724_r10726_p4133
 mc16_13TeV.364190.Sherpa_221_NNPDF30NNLO_Wtaunu_MAXHTPTV140_280_CVetoBVeto.deriv.DAOD_HIGG8D1.e5340_e5984_s3126_r10724_r10726_p4133
 mc16_13TeV.364190.Sherpa_221_NNPDF30NNLO_Wtaunu_MAXHTPTV140_280_CVetoBVeto.deriv.DAOD_HIGG8D1.e5340_e5984_s3126_s3136_r10724_r10726_p4133
 mc16_13TeV.364191.Sherpa_221_NNPDF30NNLO_Wtaunu_MAXHTPTV140_280_CFilterBVeto.deriv.DAOD_HIGG8D1.e5340_e5984_s3126_r10724_r10726_p4133
 mc16_13TeV.364191.Sherpa_221_NNPDF30NNLO_Wtaunu_MAXHTPTV140_280_CFilterBVeto.deriv.DAOD_HIGG8D1.e5340_e5984_s3126_s3136_r10724_r10726_p4133
 mc16_13TeV.364192.Sherpa_221_NNPDF30NNLO_Wtaunu_MAXHTPTV140_280_BFilter.deriv.DAOD_HIGG8D1.e5340_e5984_s3126_s3136_r10724_r10726_p4133
 mc16_13TeV.364192.Sherpa_221_NNPDF30NNLO_Wtaunu_MAXHTPTV140_280_BFilter.deriv.DAOD_HIGG8D1.e5340_e5984_s3126_r10724_r10726_p4133
 mc16_13TeV.364193.Sherpa_221_NNPDF30NNLO_Wtaunu_MAXHTPTV280_500_CVetoBVeto.deriv.DAOD_HIGG8D1.e5340_e5984_s3126_r10724_r10726_p4133
 mc16_13TeV.364193.Sherpa_221_NNPDF30NNLO_Wtaunu_MAXHTPTV280_500_CVetoBVeto.deriv.DAOD_HIGG8D1.e5340_e5984_s3126_s3136_r10724_r10726_p4133
 mc16_13TeV.364194.Sherpa_221_NNPDF30NNLO_Wtaunu_MAXHTPTV280_500_CFilterBVeto.deriv.DAOD_HIGG8D1.e5340_e5984_s3126_s3136_r10724_r10726_p4133

mc16_13TeV.364194.Sherpa_221_NNPDF30NNLO_Wtaunu_MAXHTPTV280_500_CFilterBVeto.deriv.DAOD_HIGG8D1.e5340_e5984_s3126_r10724_r10726_p4133
 mc16_13TeV.364195.Sherpa_221_NNPDF30NNLO_Wtaunu_MAXHTPTV280_500_BFilter.deriv.DAOD_HIGG8D1.e5340_e5984_s3126_s3136_r10724_r10726_p4133
 mc16_13TeV.364195.Sherpa_221_NNPDF30NNLO_Wtaunu_MAXHTPTV280_500_BFilter.deriv.DAOD_HIGG8D1.e5340_e5984_s3126_r10724_r10726_p4133
 mc16_13TeV.364196.Sherpa_221_NNPDF30NNLO_Wtaunu_MAXHTPTV500_1000.deriv.DAOD_HIGG8D1.e5340_e5984_s3126_s3136_r10724_r10726_p4133
 mc16_13TeV.364196.Sherpa_221_NNPDF30NNLO_Wtaunu_MAXHTPTV500_1000.deriv.DAOD_HIGG8D1.e5340_e5984_s3126_r10724_r10726_p4133
 mc16_13TeV.364197.Sherpa_221_NNPDF30NNLO_Wtaunu_MAXHTPTV1000_E_CMS.deriv.DAOD_HIGG8D1.e5340_e5984_s3126_s3136_r10724_r10726_p4133
 mc16_13TeV.364197.Sherpa_221_NNPDF30NNLO_Wtaunu_MAXHTPTV1000_E_CMS.deriv.DAOD_HIGG8D1.e5340_e5984_s3126_r10724_r10726_p4133
 mc16_13TeV.364500.Sherpa_222_NNPDF30NNLO_eegamma_pty_7_15.deriv.DAOD_HIGG8D1.e5928_e5984_s3126_r10724_r10726_p4133
 mc16_13TeV.364501.Sherpa_222_NNPDF30NNLO_eegamma_pty_15_35.deriv.DAOD_HIGG8D1.e5928_e5984_s3126_r10724_r10726_p4133
 mc16_13TeV.364502.Sherpa_222_NNPDF30NNLO_eegamma_pty_35_70.deriv.DAOD_HIGG8D1.e5928_e5984_s3126_r10724_r10726_p4133
 mc16_13TeV.364503.Sherpa_222_NNPDF30NNLO_eegamma_pty_70_140.deriv.DAOD_HIGG8D1.e5928_e5984_s3126_r10724_r10726_p4133
 mc16_13TeV.364504.Sherpa_222_NNPDF30NNLO_eegamma_pty_140_E_CMS.deriv.DAOD_HIGG8D1.e5928_e5984_s3126_r10724_r10726_p4133
 mc16_13TeV.364505.Sherpa_222_NNPDF30NNLO_mumugamma_pty_7_15.deriv.DAOD_HIGG8D1.e5928_e5984_s3126_r10724_r10726_p4133
 mc16_13TeV.364506.Sherpa_222_NNPDF30NNLO_mumugamma_pty_15_35.deriv.DAOD_HIGG8D1.e5928_e5984_s3126_r10724_r10726_p4133
 mc16_13TeV.364507.Sherpa_222_NNPDF30NNLO_mumugamma_pty_35_70.deriv.DAOD_HIGG8D1.e5928_e5984_s3126_r10724_r10726_p4133
 mc16_13TeV.364508.Sherpa_222_NNPDF30NNLO_mumugamma_pty_70_140.deriv.DAOD_HIGG8D1.e5928_e5984_s3126_r10724_r10726_p4133
 mc16_13TeV.364509.Sherpa_222_NNPDF30NNLO_mumugamma_pty_140_E_CMS.deriv.DAOD_HIGG8D1.e5928_e5984_s3126_r10724_r10726_p4133
 mc16_13TeV.364511.Sherpa_222_NNPDF30NNLO_tautaugamma_pty_15_35.deriv.DAOD_HIGG8D1.e5928_e5984_s3126_r10724_r10726_p4133
 mc16_13TeV.364512.Sherpa_222_NNPDF30NNLO_tautaugamma_pty_35_70.deriv.DAOD_HIGG8D1.e5928_e5984_s3126_r10724_r10726_p4133
 mc16_13TeV.364513.Sherpa_222_NNPDF30NNLO_tautaugamma_pty_70_140.deriv.DAOD_HIGG8D1.e5982_e5984_s3126_r10724_r10726_p4133
 mc16_13TeV.364514.Sherpa_222_NNPDF30NNLO_tautaugamma_pty_140_E_CMS.deriv.DAOD_HIGG8D1.e5928_e5984_s3126_r10724_r10726_p4133
 mc16_13TeV.364522.Sherpa_222_NNPDF30NNLO_enugamma_pty_15_35.deriv.DAOD_HIGG8D1.e5928_e5984_s3126_r10724_r10726_p4133
 mc16_13TeV.364523.Sherpa_222_NNPDF30NNLO_enugamma_pty_35_70.deriv.DAOD_HIGG8D1.e5928_e5984_s3126_r10724_r10726_p4133
 mc16_13TeV.364524.Sherpa_222_NNPDF30NNLO_enugamma_pty_70_140.deriv.DAOD_HIGG8D1.e5928_e5984_s3126_r10724_r10726_p4133
 mc16_13TeV.364525.Sherpa_222_NNPDF30NNLO_enugamma_pty_140_E_CMS.deriv.DAOD_HIGG8D1.e5928_e5984_s3126_r10724_r10726_p4133
 mc16_13TeV.364527.Sherpa_222_NNPDF30NNLO_munugamma_pty_15_35.deriv.DAOD_HIGG8D1.e5928_e5984_s3126_r10724_r10726_p4133
 mc16_13TeV.364528.Sherpa_222_NNPDF30NNLO_munugamma_pty_35_70.deriv.DAOD_HIGG8D1.e5928_e5984_s3126_r10724_r10726_p4133
 mc16_13TeV.364529.Sherpa_222_NNPDF30NNLO_munugamma_pty_70_140.deriv.DAOD_HIGG8D1.e5928_e5984_s3126_r10724_r10726_p4133
 mc16_13TeV.364530.Sherpa_222_NNPDF30NNLO_munugamma_pty_140_E_CMS.deriv.DAOD_HIGG8D1.e5928_e5984_s3126_r10724_r10726_p4133
 mc16_13TeV.364532.Sherpa_222_NNPDF30NNLO_taunugamma_pty_15_35.deriv.DAOD_HIGG8D1.e5928_e5984_s3126_r10724_r10726_p4133
 mc16_13TeV.364533.Sherpa_222_NNPDF30NNLO_taunugamma_pty_35_70.deriv.DAOD_HIGG8D1.e5928_e5984_s3126_r10724_r10726_p4133

mc16_13TeV.364534.Sherpa_222_NNPDF30NNLO_taunugamma_pty_70_140.deriv.DAOD_HIGG8D1.e5928_e5984_s3126_r10724_r10726_p4133
 mc16_13TeV.364535.Sherpa_222_NNPDF30NNLO_taunugamma_pty_140_E_CMS.deriv.DAOD_HIGG8D1.e5928_e5984_s3126_r10724_r10726_p4133
 mc16_13TeV.410560.MadGraphPythia8EvtGen_A14_tZ_4fl_tchan_noAllHad.deriv.DAOD_HIGG8D1.e5803_e5984_s3126_r10724_r10726_p4133
 mc16_13TeV.410408.aMcAtNloPythia8EvtGen_tWZ_Ztoll_minDR1.deriv.DAOD_HIGG8D1.e6423_e5984_s3126_r10724_r10726_p4133
 mc16_13TeV.364242.Sherpa_222_NNPDF30NNLO_WWW_3l3v_EW6.deriv.DAOD_HIGG8D1.e5887_e5984_s3126_r10724_r10726_p4133
 mc16_13TeV.364243.Sherpa_222_NNPDF30NNLO_WWZ_4l2v_EW6.deriv.DAOD_HIGG8D1.e5887_e5984_s3126_r10724_r10726_p4133
 mc16_13TeV.364244.Sherpa_222_NNPDF30NNLO_WWZ_2l4v_EW6.deriv.DAOD_HIGG8D1.e5887_e5984_s3126_r10724_r10726_p4133
 mc16_13TeV.364245.Sherpa_222_NNPDF30NNLO_WZZ_5l1v_EW6.deriv.DAOD_HIGG8D1.e5887_e5984_s3126_r10724_r10726_p4133
 mc16_13TeV.364246.Sherpa_222_NNPDF30NNLO_WZZ_3l3v_EW6.deriv.DAOD_HIGG8D1.e5887_e5984_s3126_r10724_r10726_p4133
 mc16_13TeV.364247.Sherpa_222_NNPDF30NNLO_ZZZ_6l0v_EW6.deriv.DAOD_HIGG8D1.e5887_e5984_s3126_r10724_r10726_p4133
 mc16_13TeV.364248.Sherpa_222_NNPDF30NNLO_ZZZ_4l2v_EW6.deriv.DAOD_HIGG8D1.e5887_e5984_s3126_r10724_r10726_p4133
 mc16_13TeV.364249.Sherpa_222_NNPDF30NNLO_ZZZ_2l4v_EW6.deriv.DAOD_HIGG8D1.e5887_e5984_s3126_r10724_r10726_p4133
 mc16_13TeV.342284.Pythia8EvtGen_A14NNPDF23LO_WH125_inc.deriv.DAOD_HIGG8D1.e4246_e5984_s3126_r10724_r10726_p4133
 mc16_13TeV.342285.Pythia8EvtGen_A14NNPDF23LO_ZH125_inc.deriv.DAOD_HIGG8D1.e4246_e5984_s3126_r10724_r10726_p4133
 mc16_13TeV.341998.aMcAtNloHppEG_UEEE5_CTEQ6L1_CT10ME_tWH125_gamgam_yt_plus1.deriv.DAOD_HIGG8D1.e4394_e5984_s3126_r10724_r10726_p4133
 mc16_13TeV.410389.MadGraphPythia8EvtGen_A14NNPDF23_ttgamma_nonallhadronic.deriv.DAOD_HIGG8D1.e6155_e5984_s3126_r10724_r10726_p4133
 mc16_13TeV.410470.PhPy8EG_A14_ttbar_hdamp258p75_nonallhad.deriv.DAOD_HIGG8D1.e6337_e5984_s3126_r10724_r10726_p4133
 mc16_13TeV.410472.PhPy8EG_A14_ttbar_hdamp258p75_dil.deriv.DAOD_HIGG8D1.e6348_e5984_s3126_r10724_r10726_p4133
 mc16_13TeV.346343.PhPy8EG_A14NNPDF23_NNPDF30ME_ttH125_allhad.deriv.DAOD_HIGG8D1.e7148_e5984_s3126_r10724_r10726_p4133
 mc16_13TeV.346343.PhPy8EG_A14NNPDF23_NNPDF30ME_ttH125_allhad.deriv.DAOD_HIGG8D1.e7148_e5984_a875_r10724_r10726_p4133
 mc16_13TeV.346344.PhPy8EG_A14NNPDF23_NNPDF30ME_ttH125_semilep.deriv.DAOD_HIGG8D1.e7148_e5984_a875_r10724_r10726_p4133
 mc16_13TeV.346344.PhPy8EG_A14NNPDF23_NNPDF30ME_ttH125_semilep.deriv.DAOD_HIGG8D1.e7148_e5984_s3126_r10724_r10726_p4133
 mc16_13TeV.346345.PhPy8EG_A14NNPDF23_NNPDF30ME_ttH125_dilep.deriv.DAOD_HIGG8D1.e7148_e5984_a875_r10724_r10726_p4133
 mc16_13TeV.346345.PhPy8EG_A14NNPDF23_NNPDF30ME_ttH125_dilep.deriv.DAOD_HIGG8D1.e7148_e5984_s3126_r10724_r10726_p4133

¹⁸⁷⁷ **A Machine Learning Models**

¹⁸⁷⁸ The following section provides details of the various MVAs as well as a few studies performed
¹⁸⁷⁹ in support of this analysis, exploring alternate decisions and strategies.

¹⁸⁸⁰ **A.1 Higgs Reconstruction Models**

¹⁸⁸¹ **A.1.1 b-jet Identification Features - 2lSS**

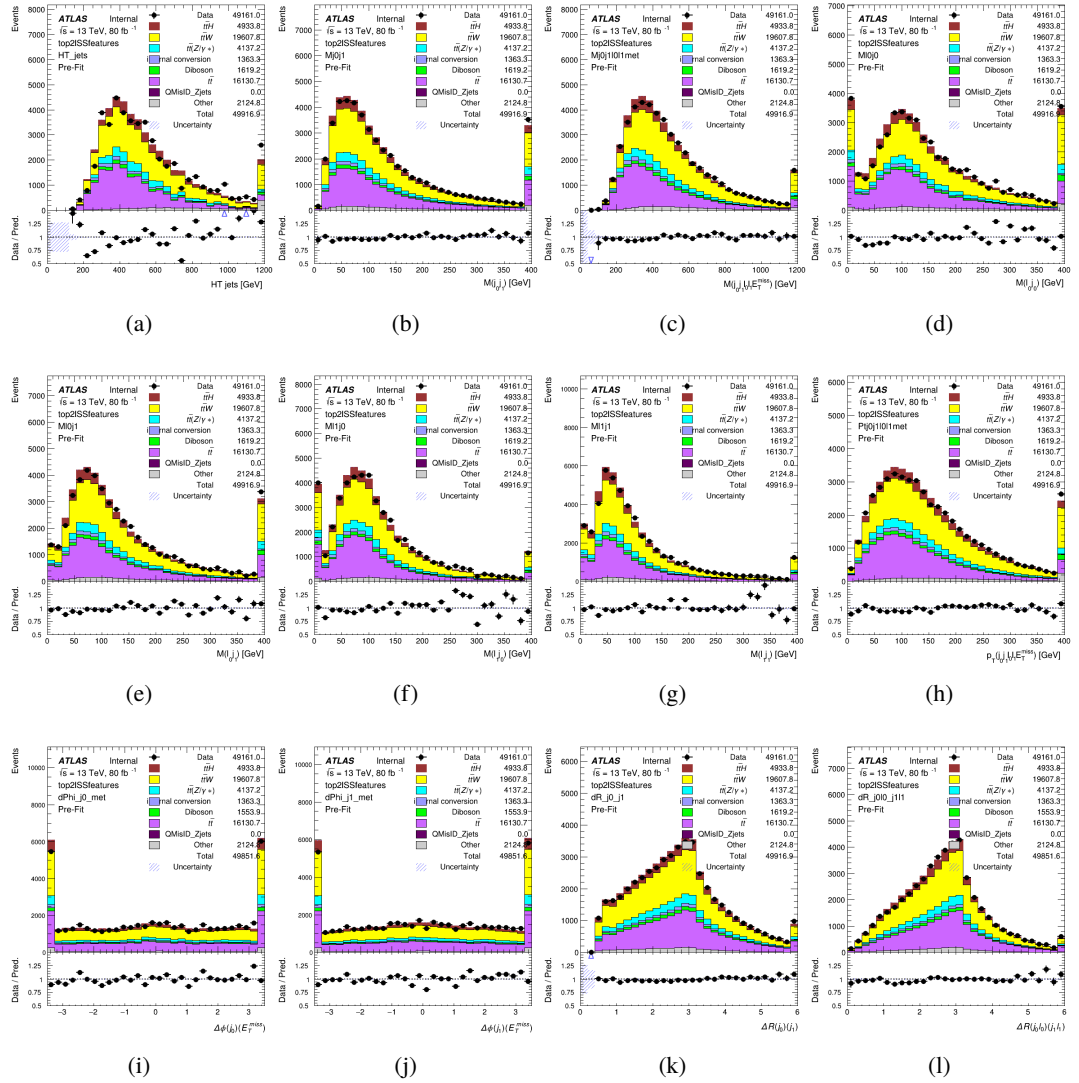


Figure A.1: Input features for top2lSS

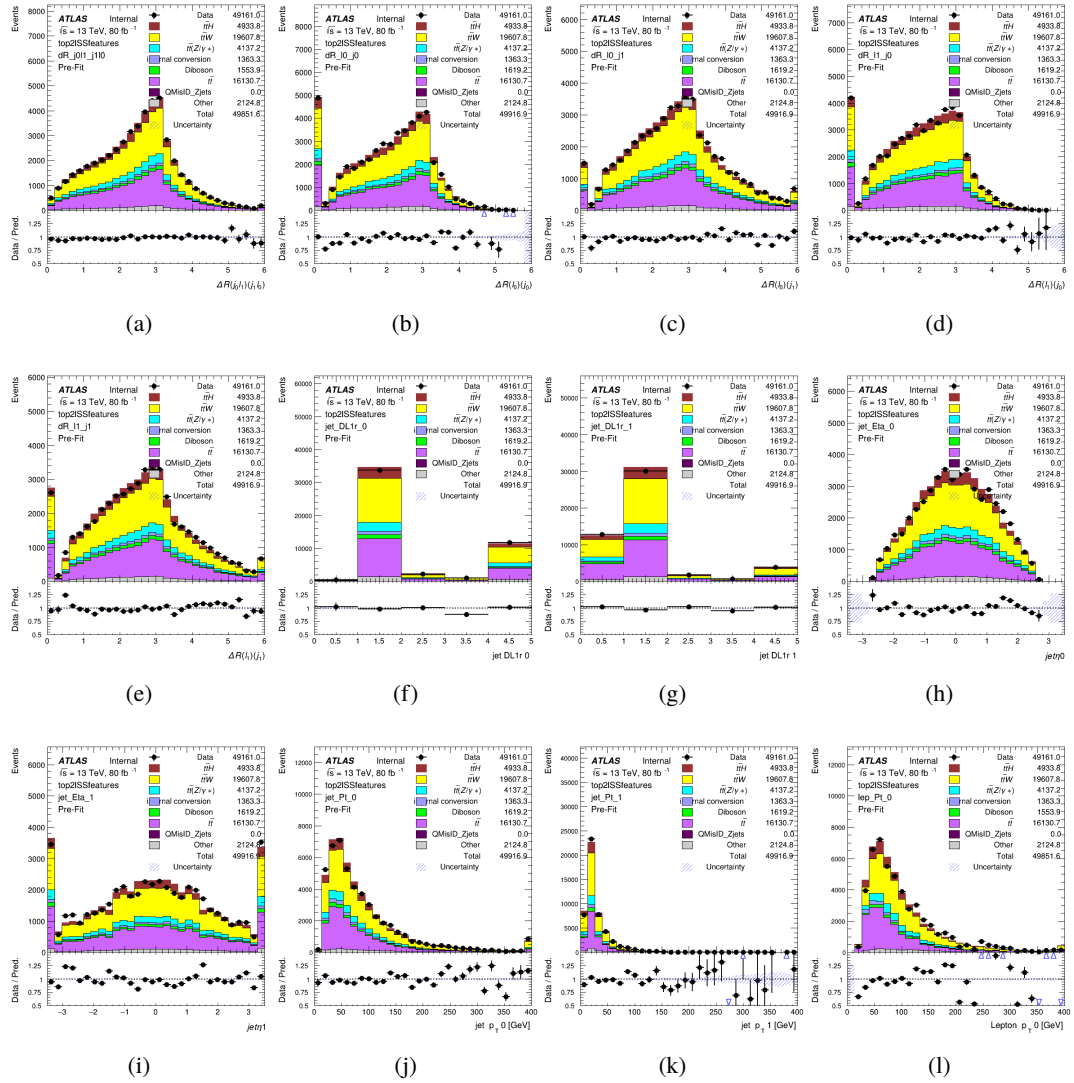


Figure A.2: Input features for top2lSS

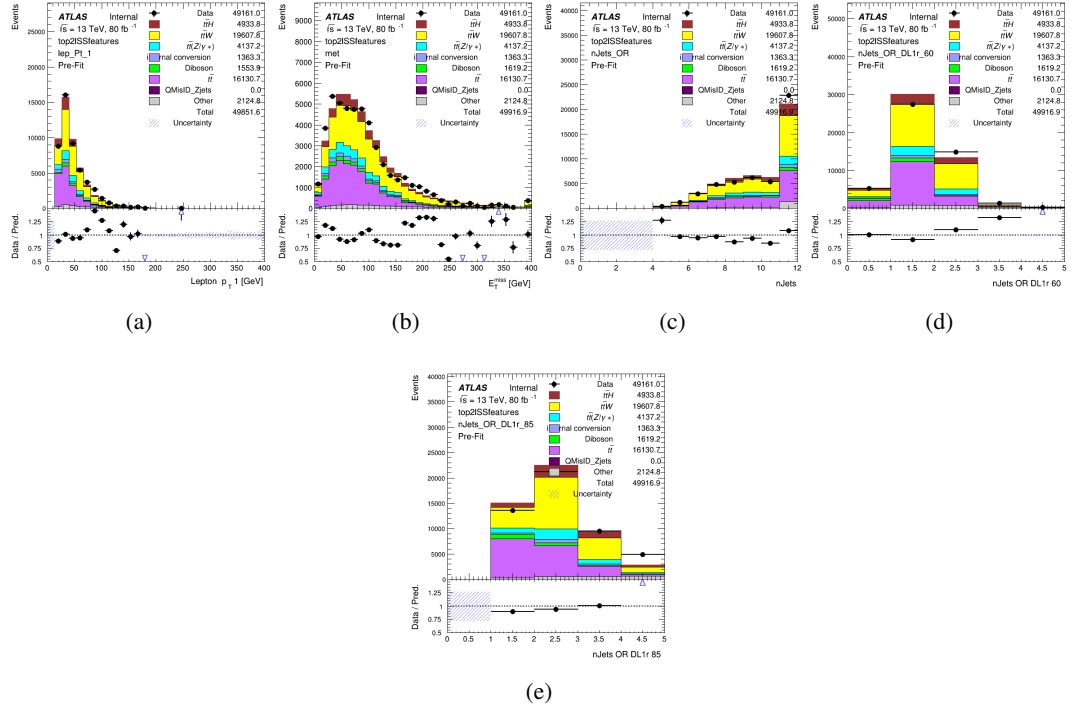


Figure A.3: Input features for top2ISS

1882 **A.1.2 b-jet Identification Features - 3l**

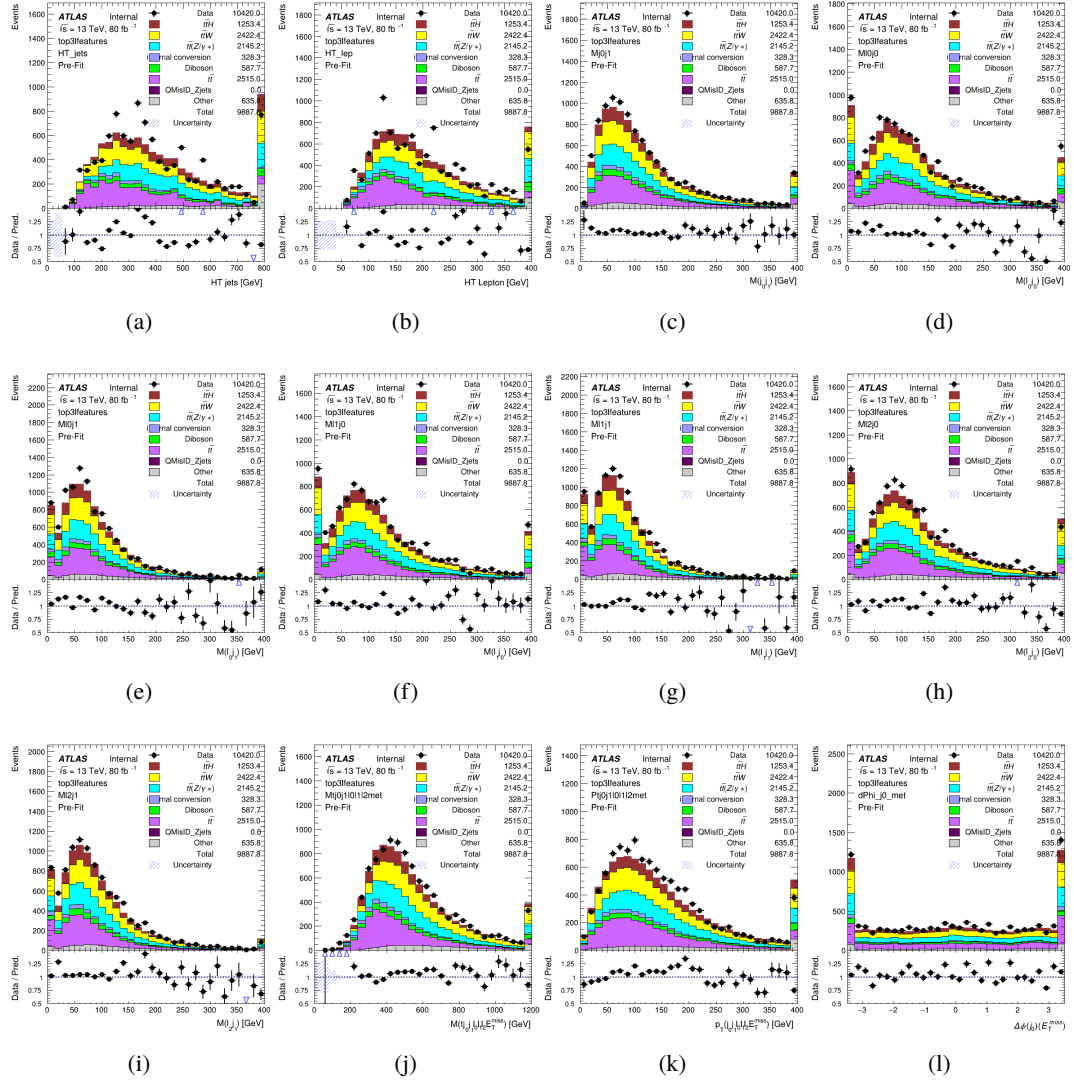


Figure A.4: Input features for top31

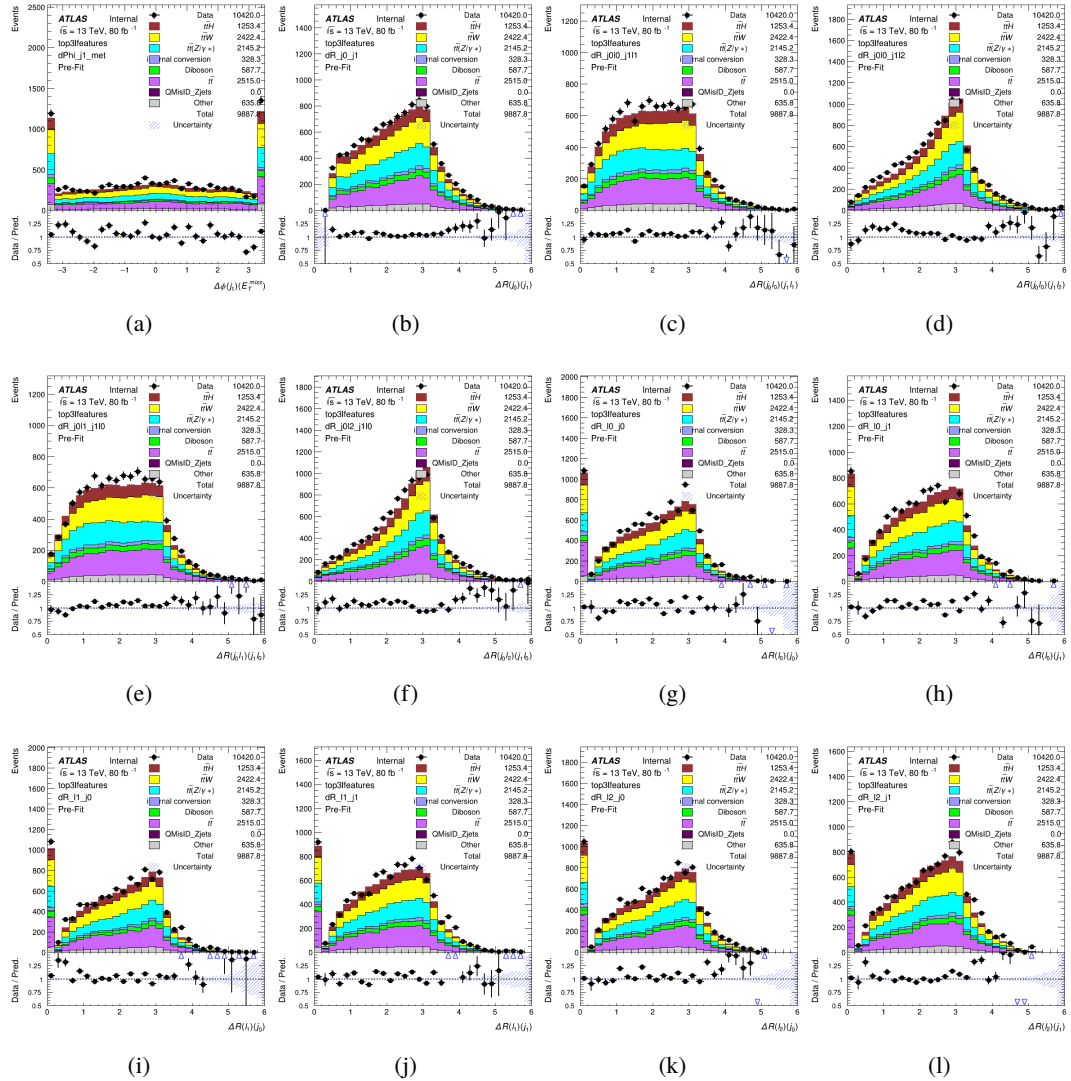


Figure A.5: Input features for top31

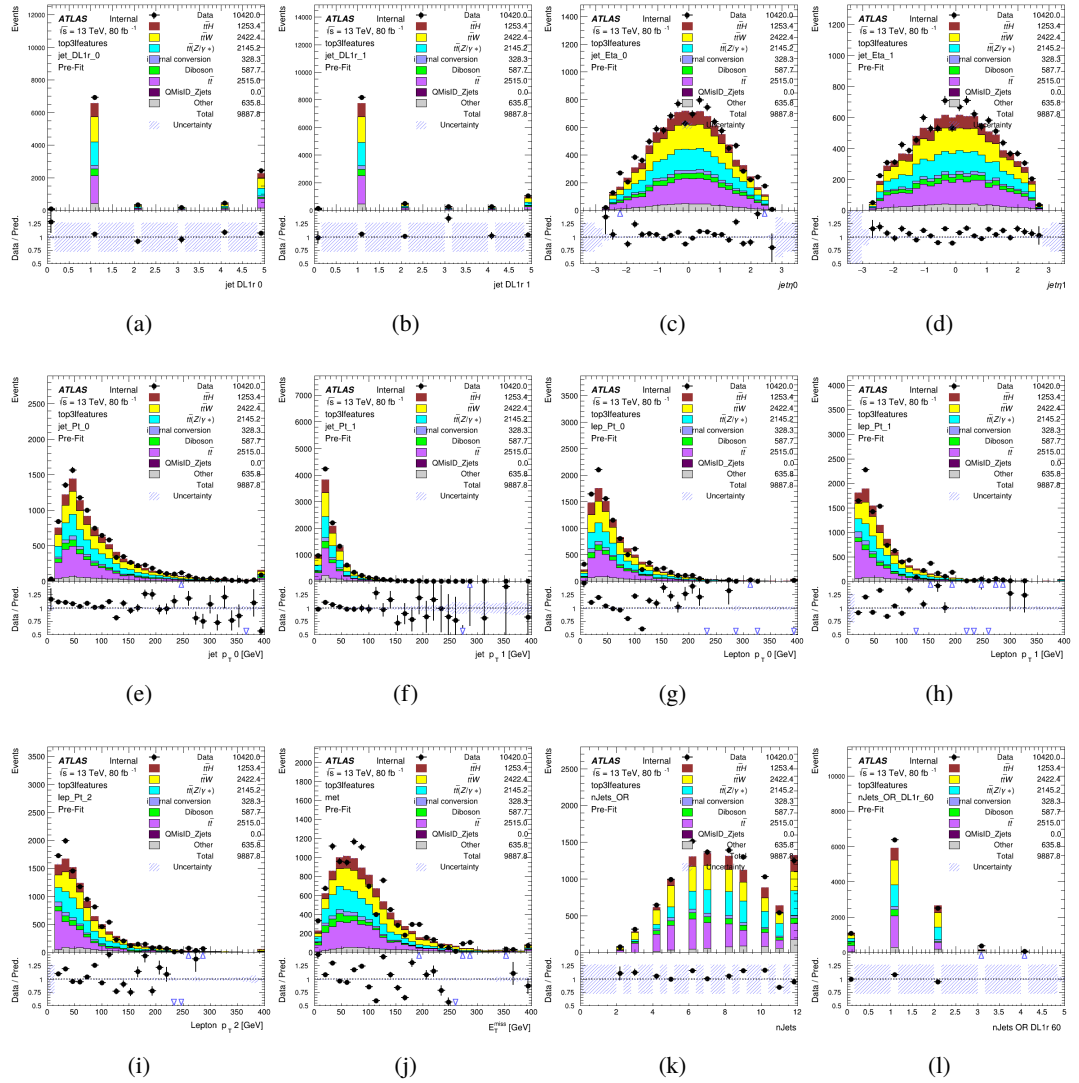
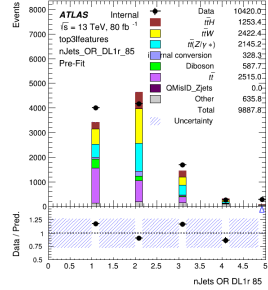


Figure A.6: Input features for top31



(a)

Figure A.7: Input features for top31

1883 **A.1.3 Higgs Reconstruction Features - 2lSS**

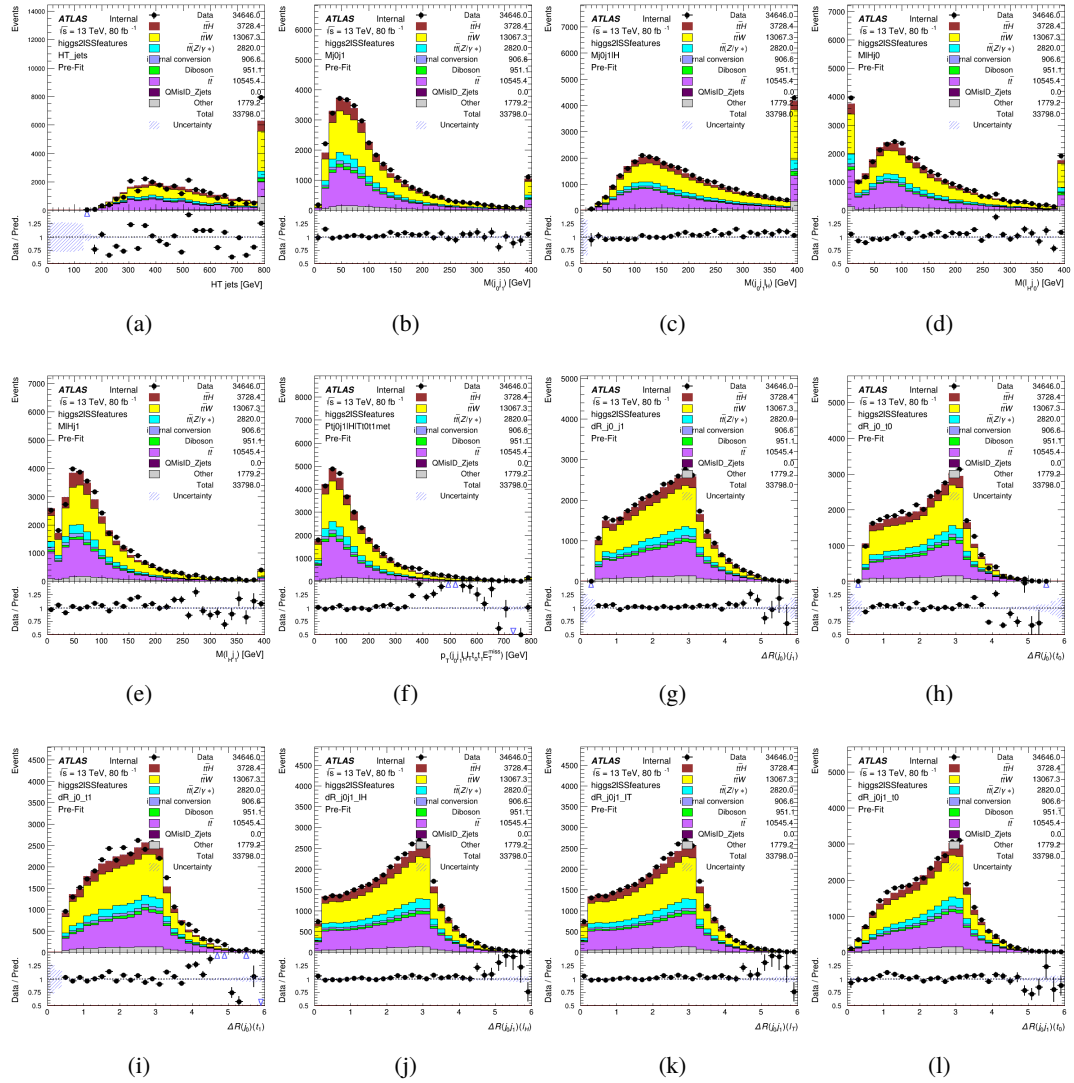


Figure A.8: Input features for higgs2lSS

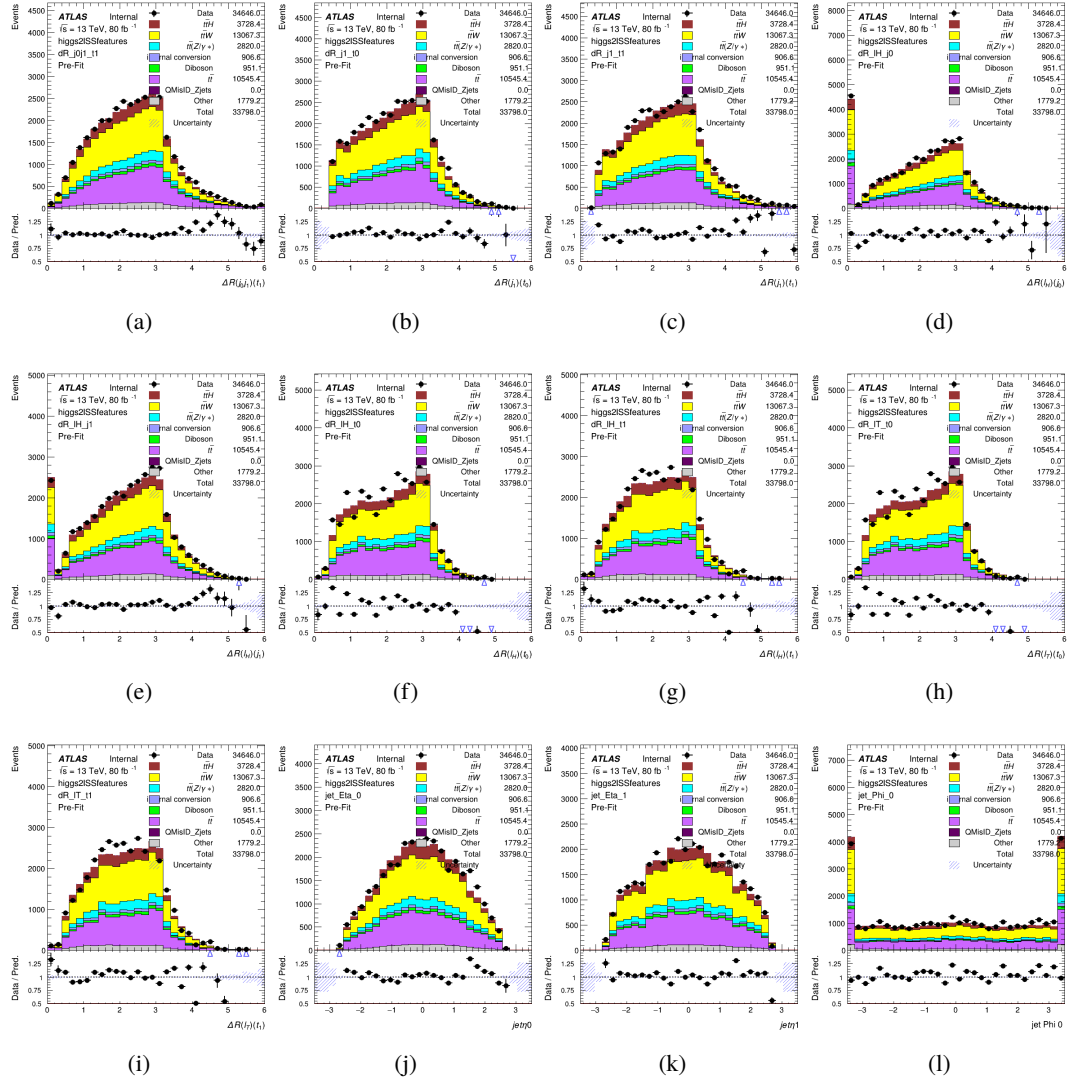


Figure A.9: Input features for higgs2lSS

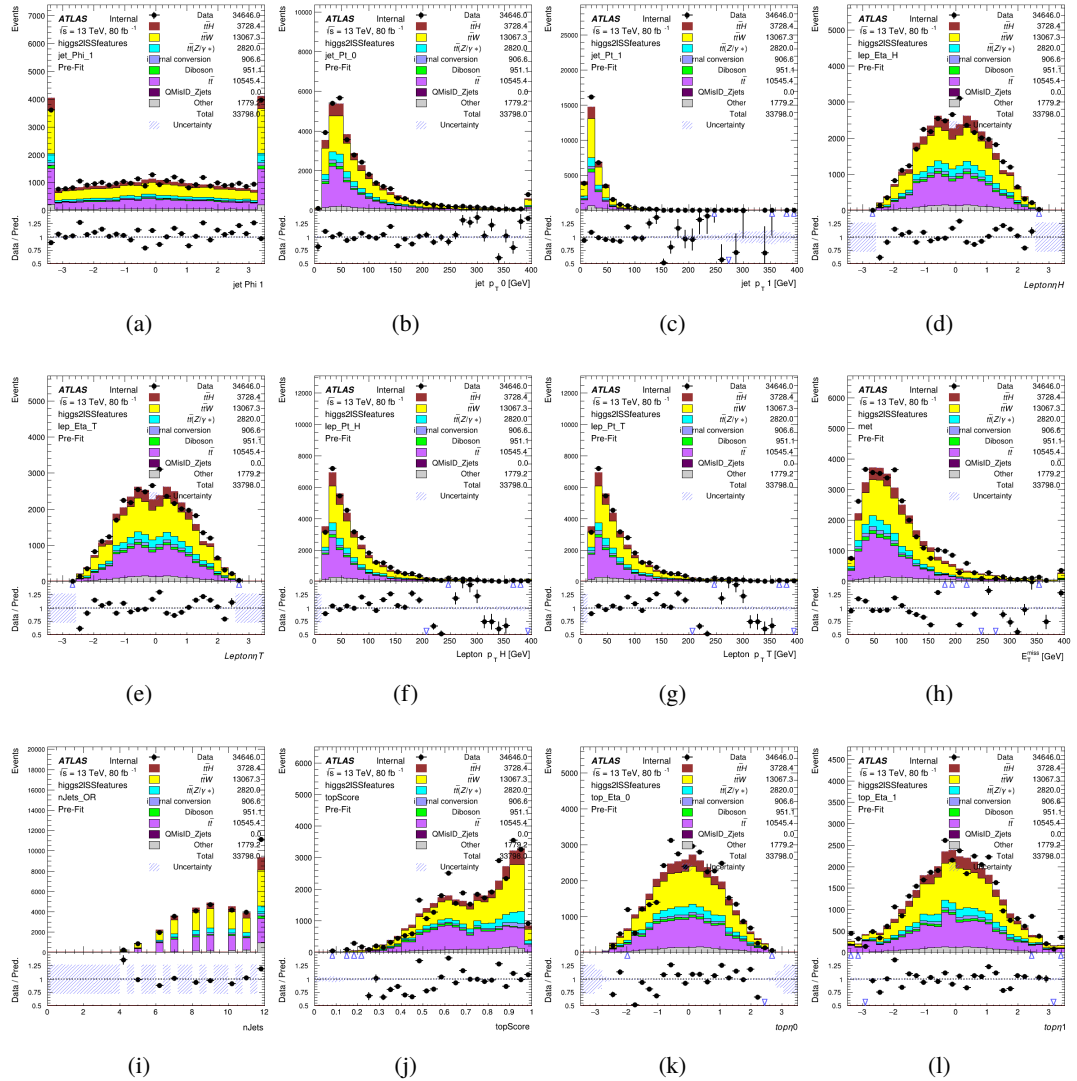


Figure A.10: Input features for higgs2IS

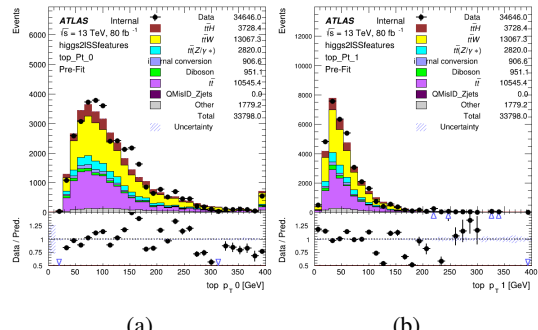


Figure A.11: Input features for higgs2lSS

1884 **A.1.4 Higgs Reconstruction Features - 3lS**

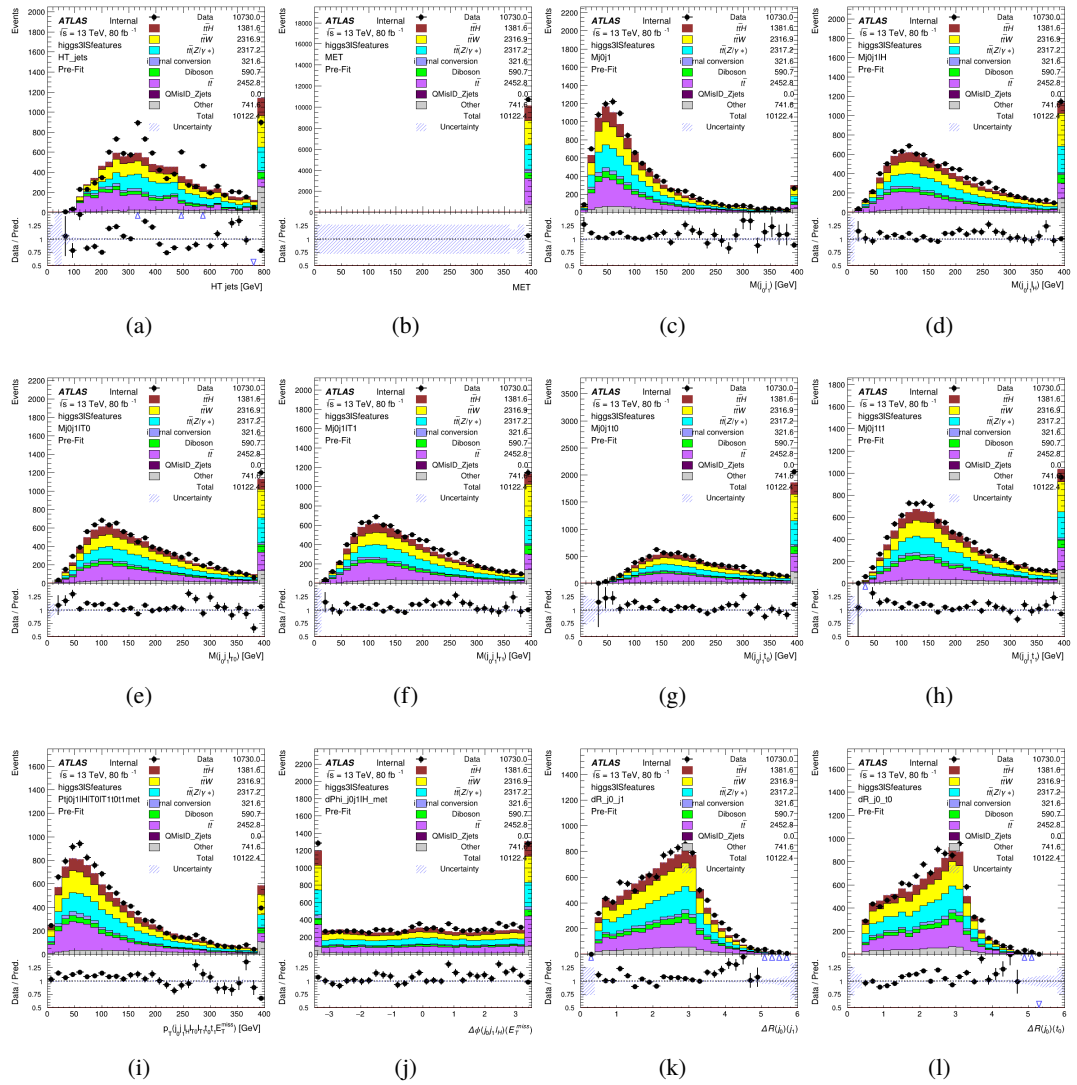


Figure A.12: Input features for higgs31S

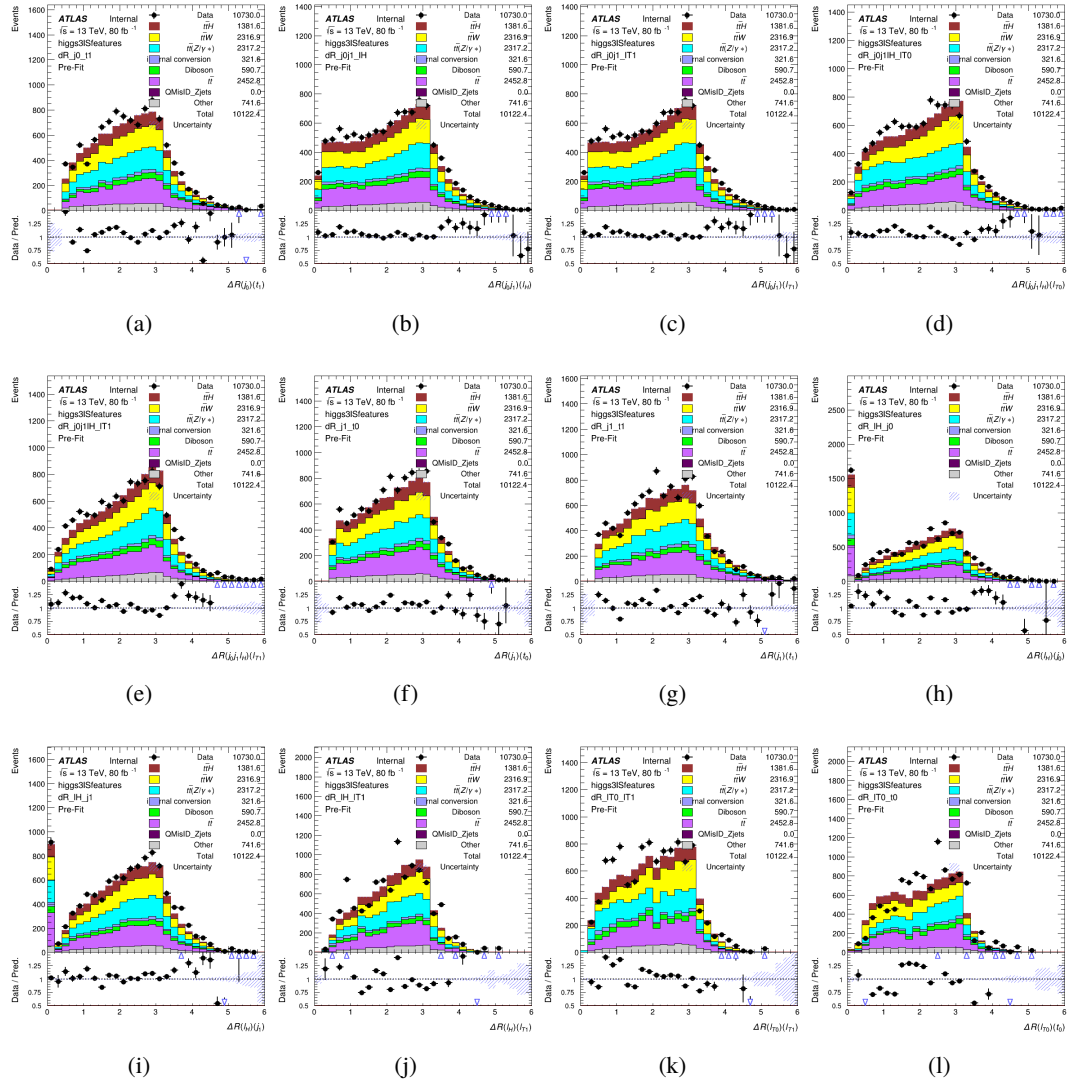


Figure A.13: Input features for higgs3S1S

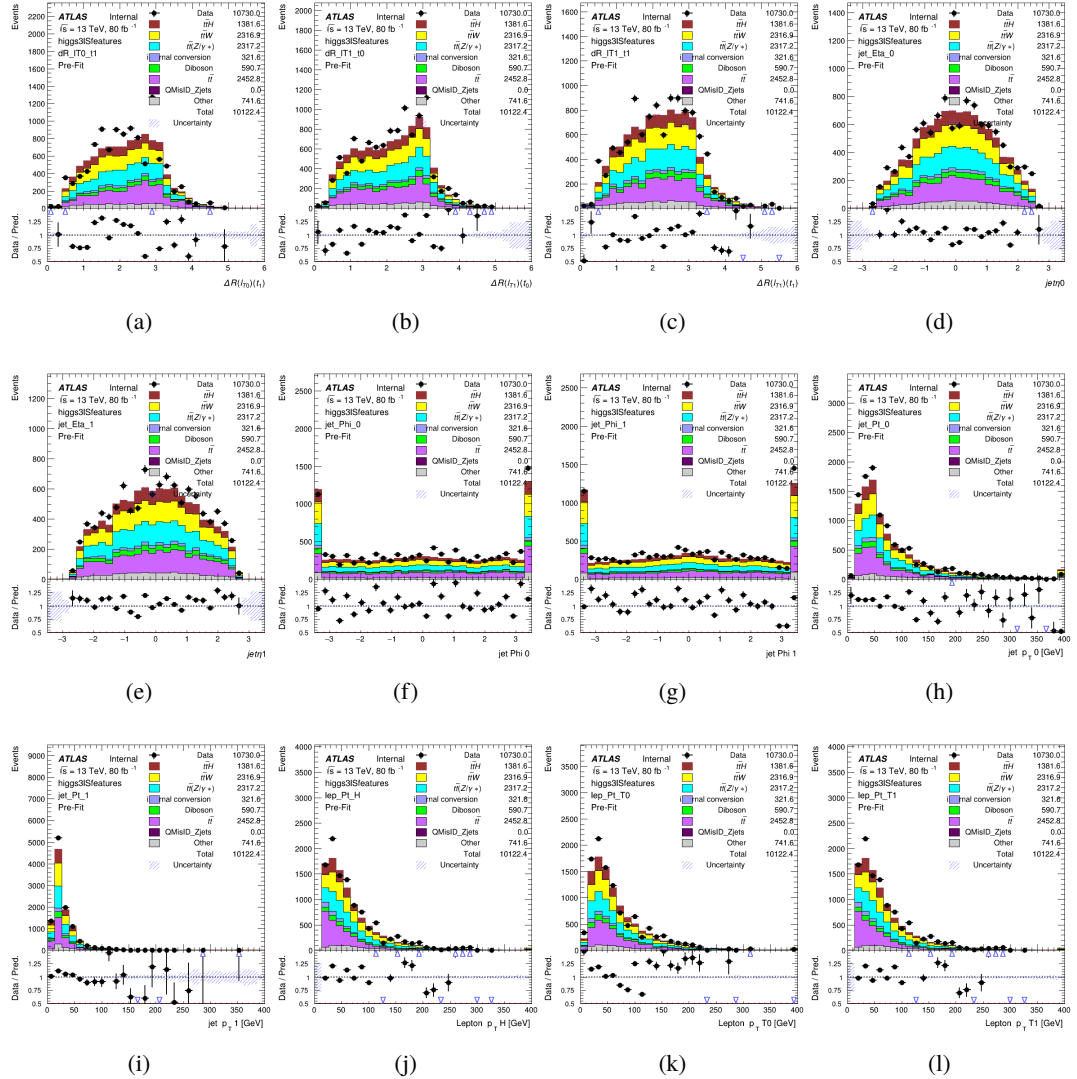


Figure A.14: Input features for higgs3IS

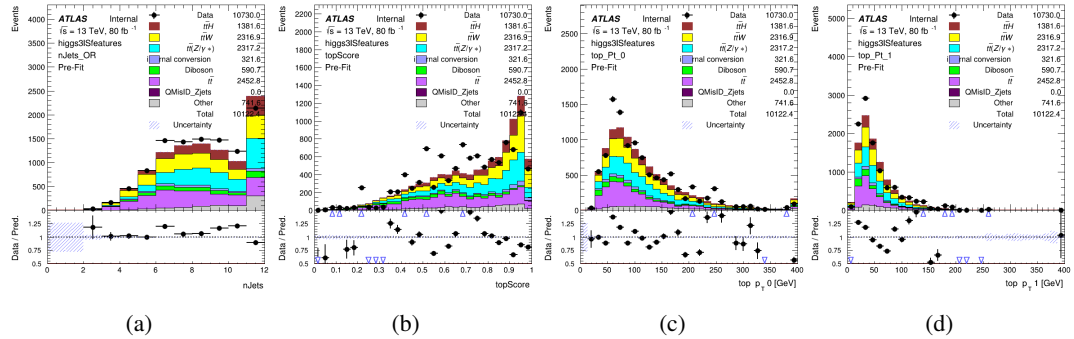


Figure A.15: Input features for higgs3IS

1885 **A.1.5 Higgs Reconstruction Features - 3lF**

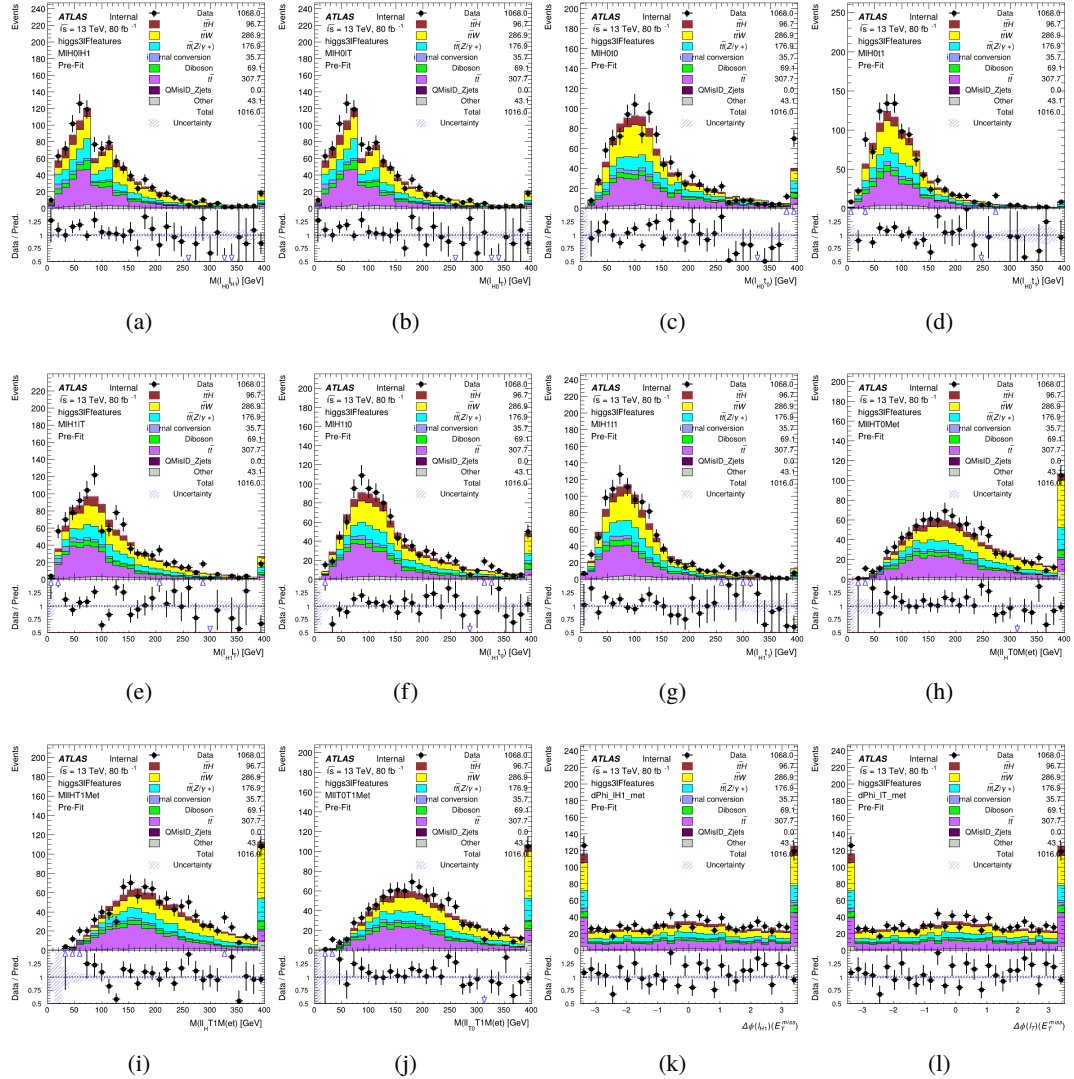


Figure A.16: Input features for higgs3IF

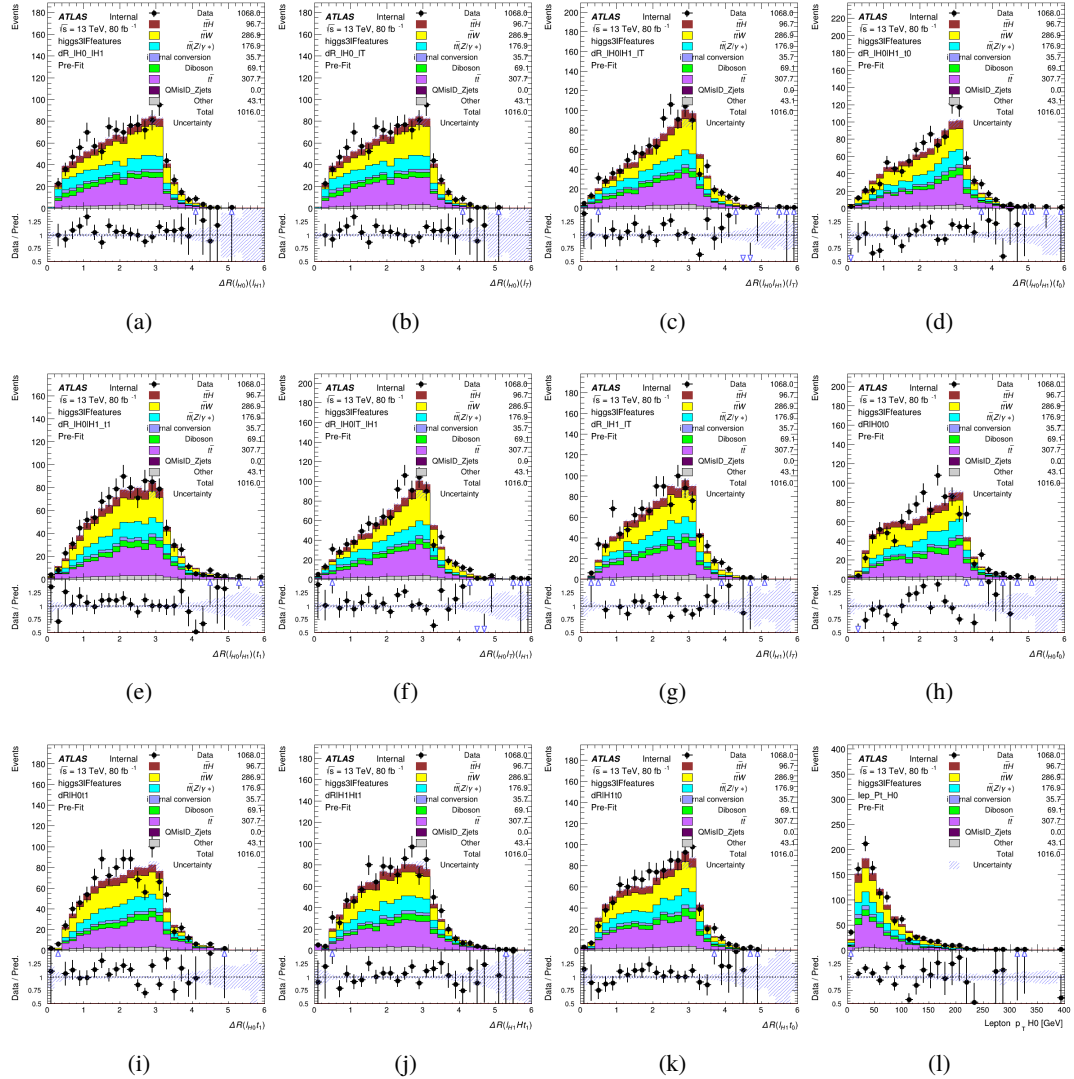


Figure A.17: Input features for higgs3IF

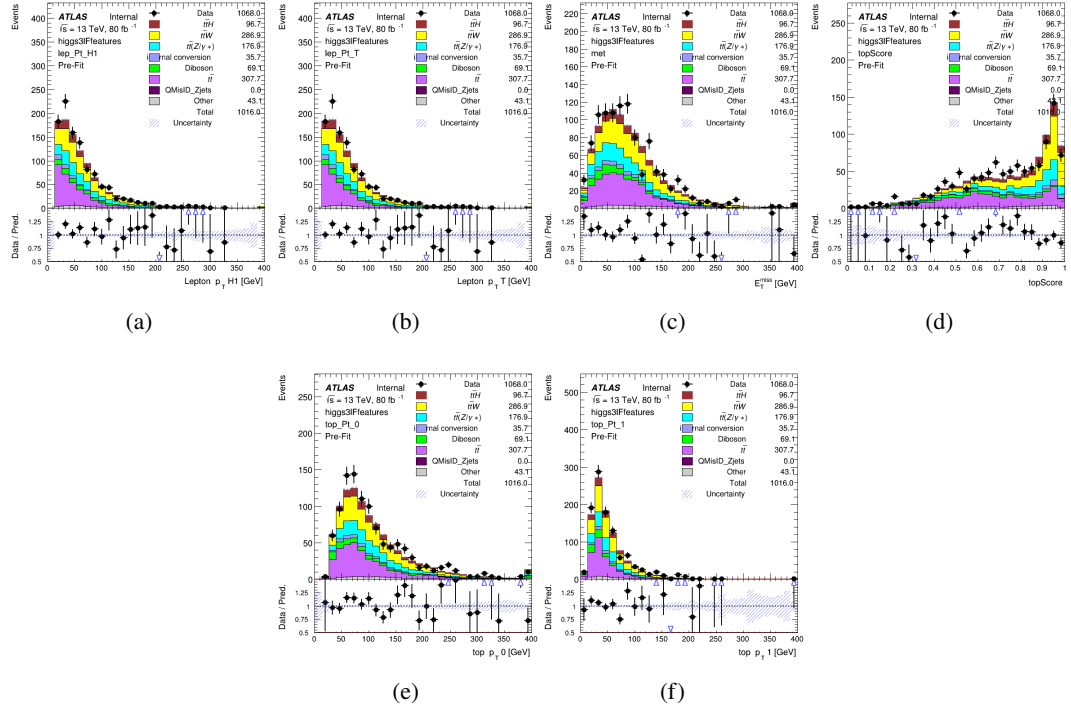


Figure A.18: Input features for higgs3lF

¹⁸⁸⁶ **A.2 Background Rejection MVAs**

¹⁸⁸⁷ **A.2.1 Background Rejection MVA Features - 2lSS**

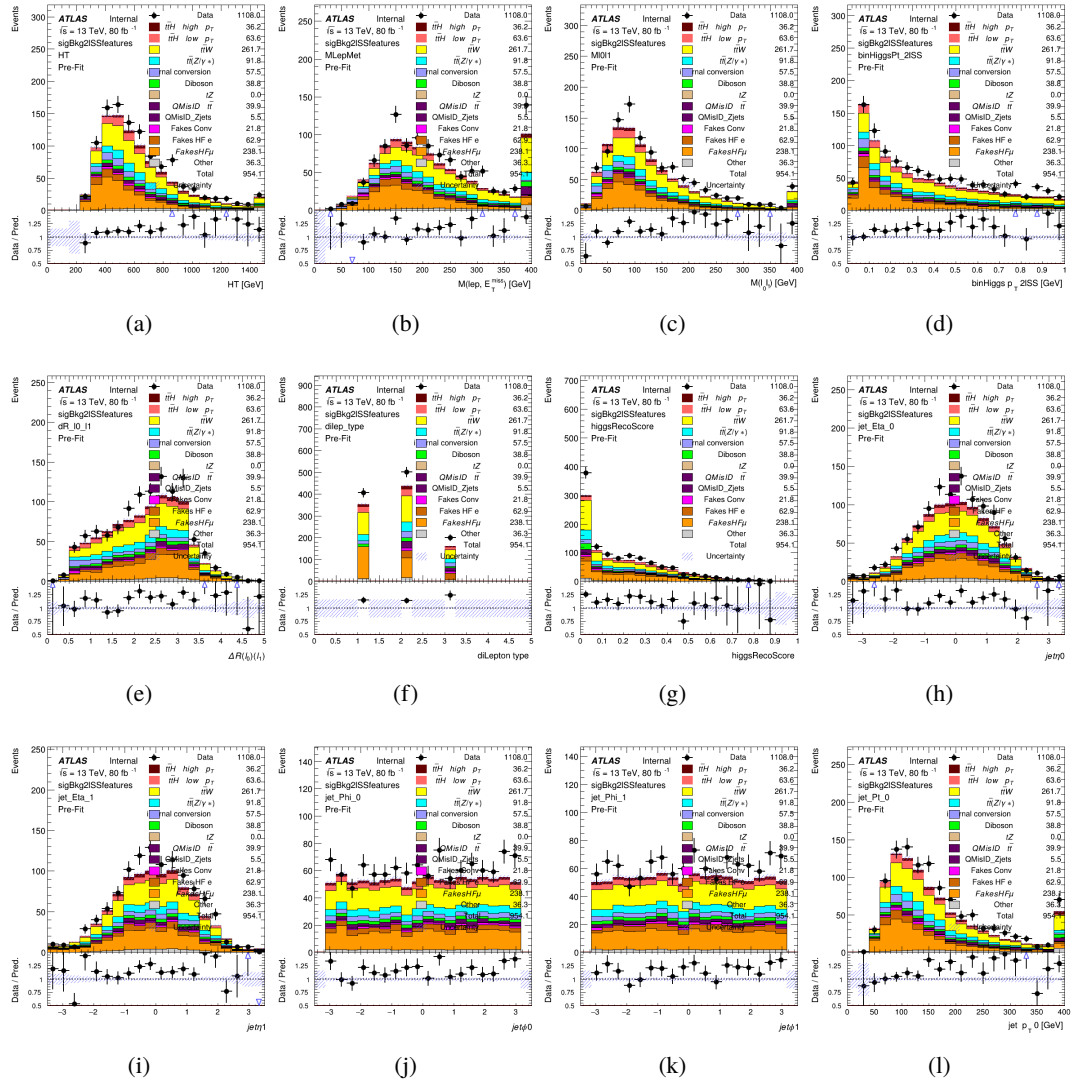
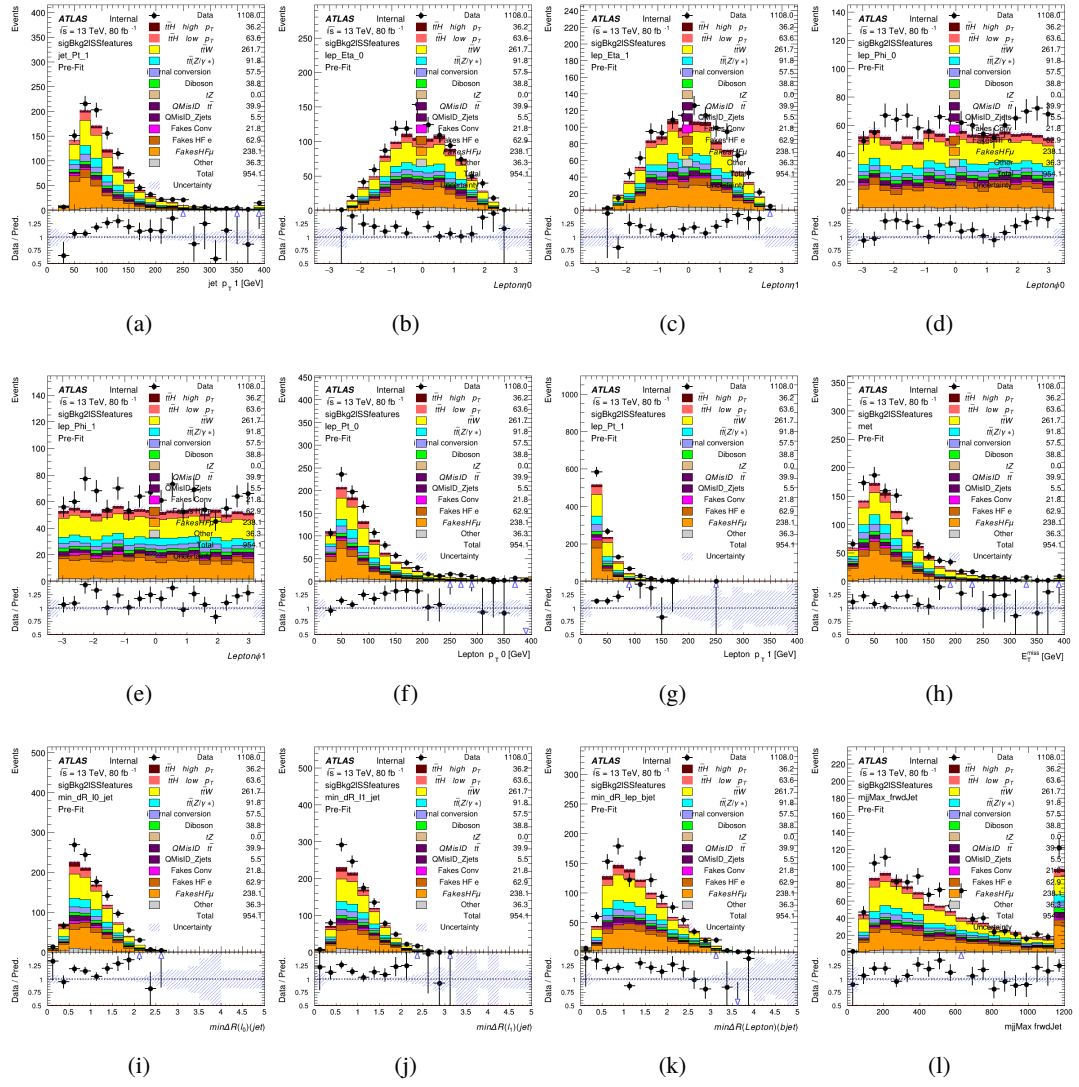


Figure A.19: Input features for sigBkg2lSS

Figure A.20: Input features for `sigBkg2lSS`

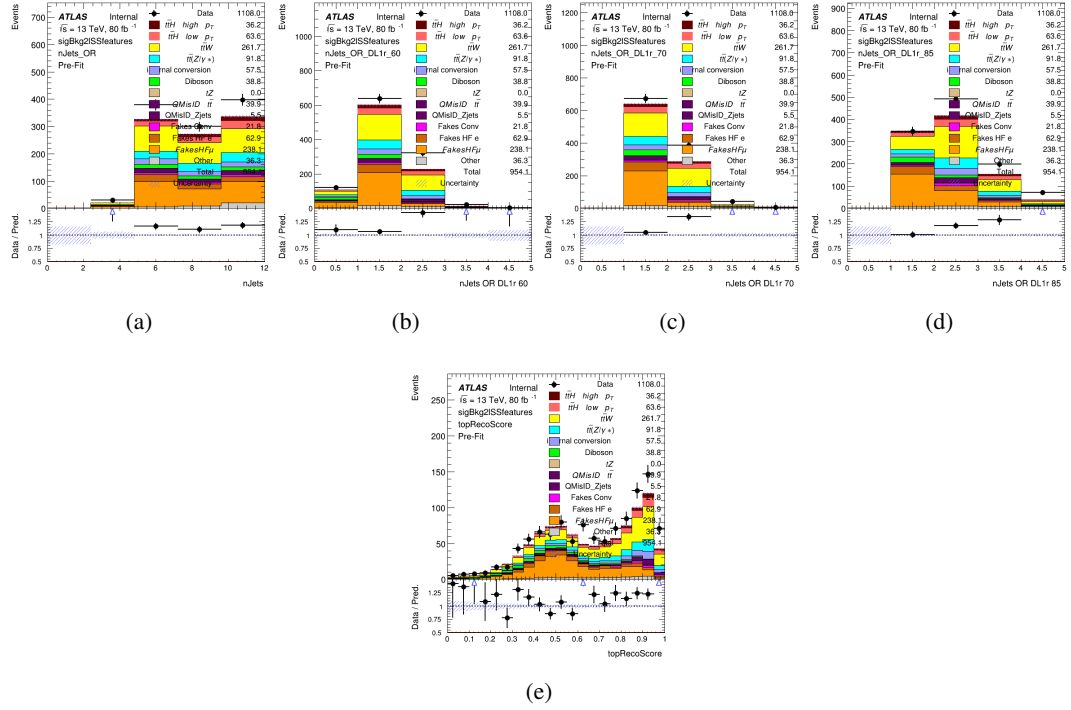


Figure A.21: Input features for sigBkg2lSS

1888 **A.2.2 Background Rejection MVA Features - 31**

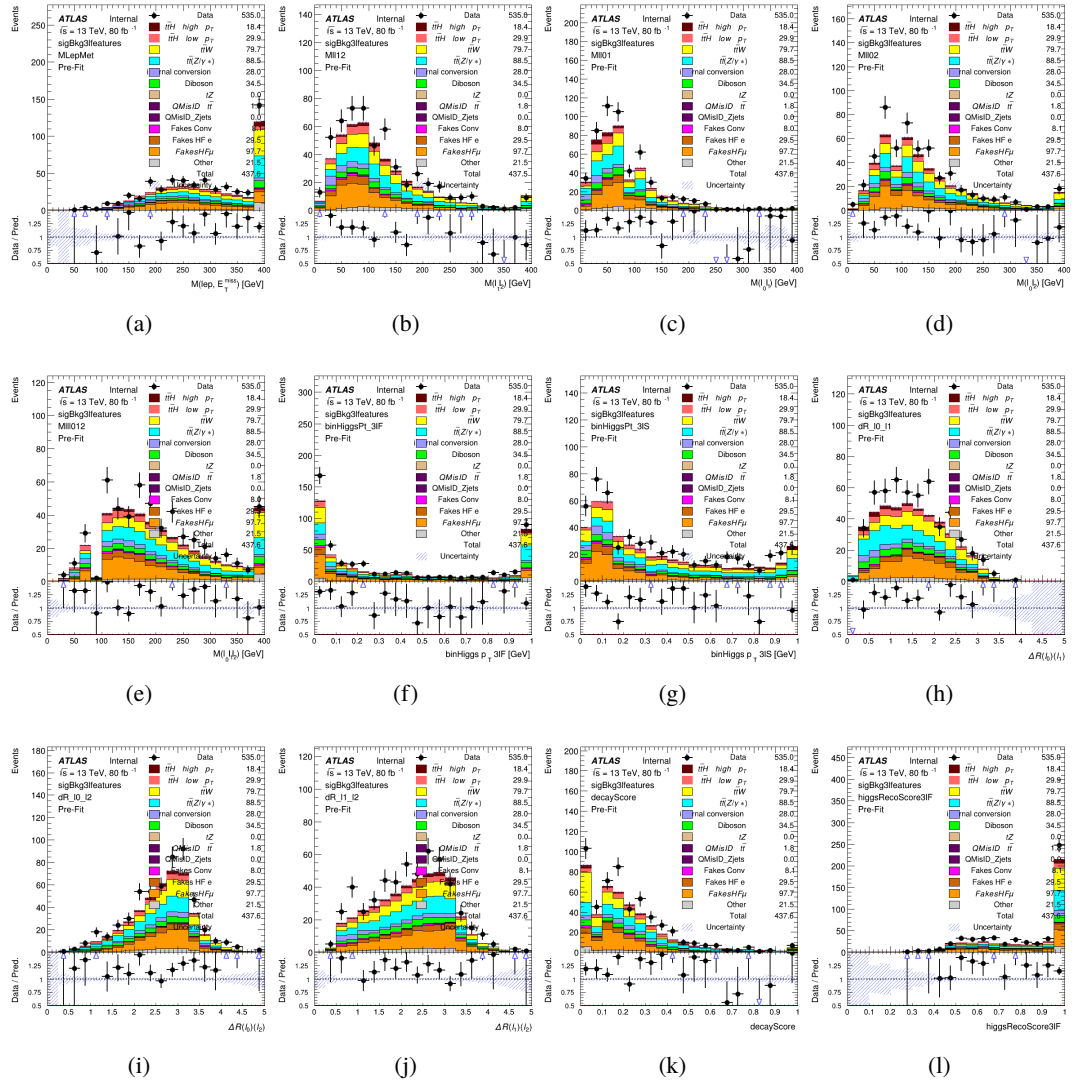


Figure A.22: Input features for sigBkg3l

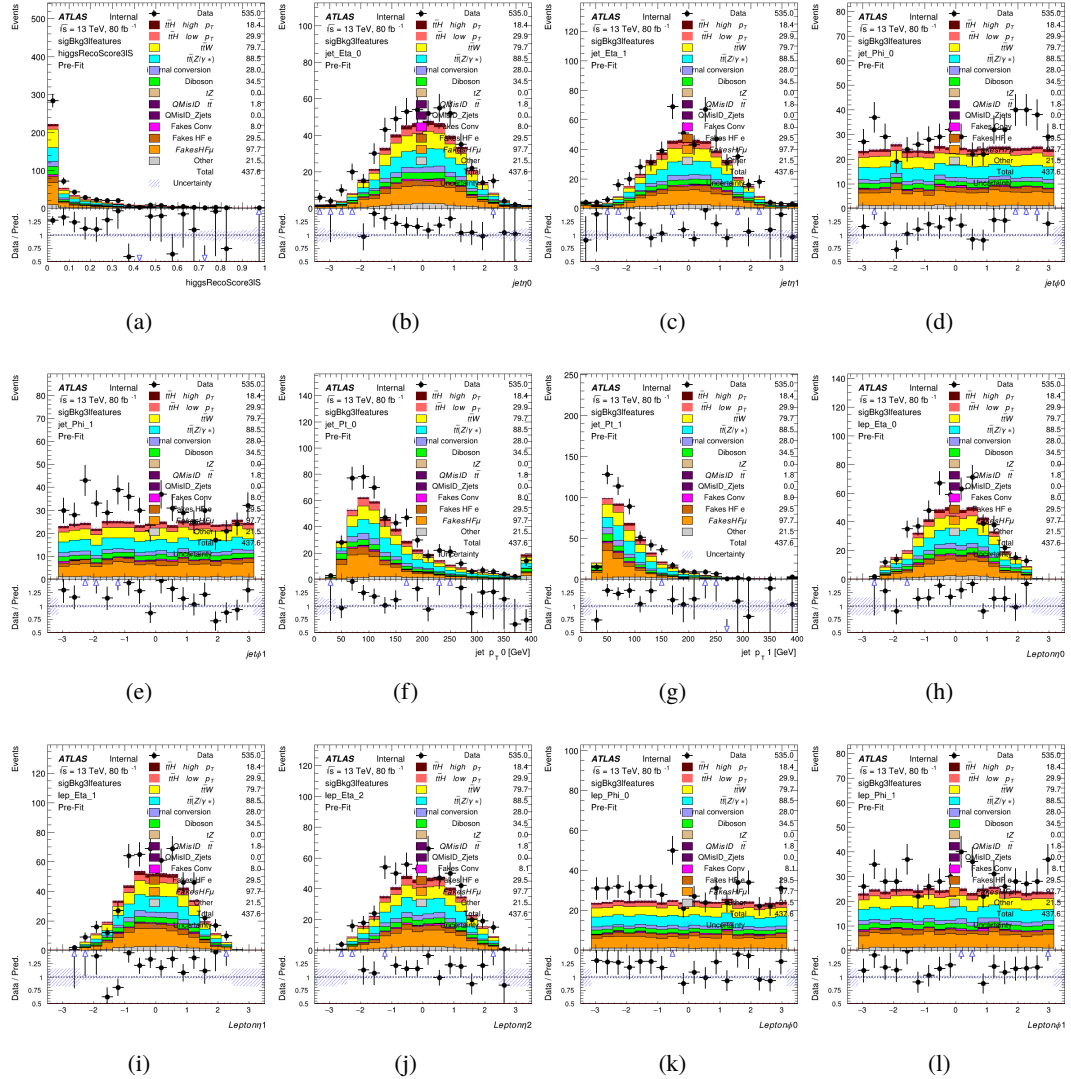
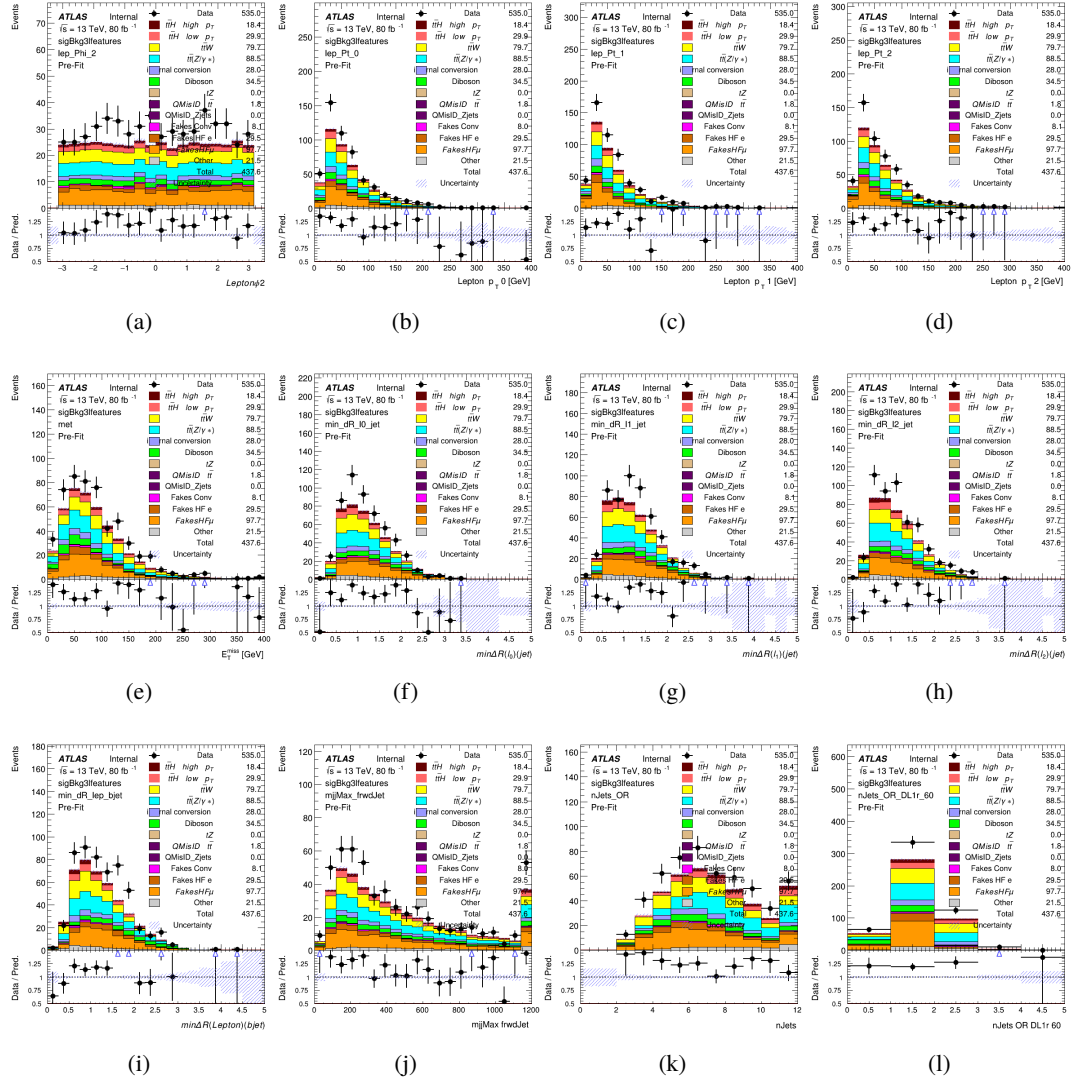


Figure A.23: Input features for sigBkg3l

Figure A.24: Input features for `sigBkg3l`

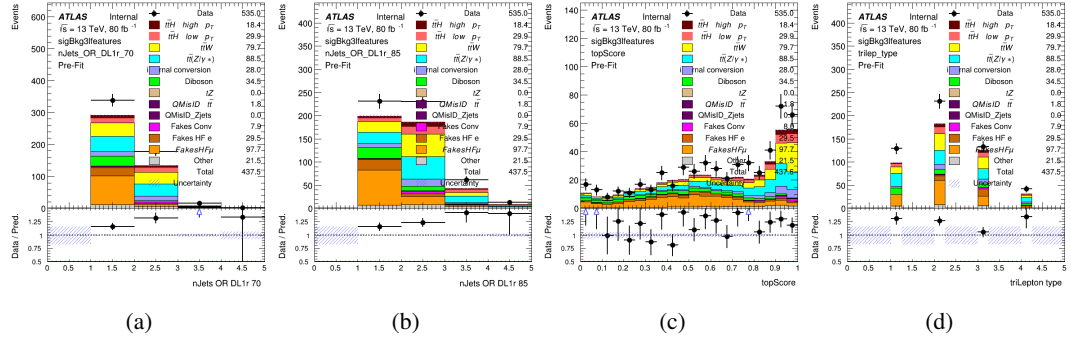


Figure A.25: Input features for sigBkg3l

A.3 Alternate b-jet Identification Algorithm

1889 The nominal analysis reconstructs the b-jets by considering different combinations of jets, and
 1890 asking a neural network to determine whether each combination consists of b-jets from top quark
 1891 decays. An alternate approach would be to give the neural network about all of the jets in an event
 1892 at once, and train it to select which two are most likely to be the b-jets from top decay. It was
 1893 hypothesized that this could perform better than considering each combination independently, as
 1894 the neural network could consider the event as a whole. While this is not found to be the case,
 1895 these studies are documented here as a point of interest and comparison.
 1896

1897 For these studies, the kinematics of the 10 highest p_T jets in each event are used for
 1898 training. This includes the vast majority of truth b-jets. Specifically the p_T , η , ϕ , E , and DL1r
 1899 score of each jet are used. For events with fewer than 10 jets, these values are substituted with 0.
 1900 The p_T , η , ϕ , and E of the leptons and E_T^{miss} are included as well. Categorical cross entropy is
 1901 used as the loss function.

Table 61: Accuracy of the NN in identifying b-jets from tops in 2lSS events for the alternate categorical method compared to the nominal method.

| Channel | Categorical | Nominal |
|---------|-------------|---------|
| 2lSS | 70.6% | 73.9% |
| 3l | 76.1% | 79.8% |

1902 **A.4 Binary Classification of the Higgs p_T**

1903 A two bin fit of the Higgs momentum is used because statistics are insufficient for any finer
 1904 resolution. This means separating high and low p_T events is sufficient for this analysis. As
 1905 such, rather than attempting the reconstruct the full Higgs p_T spectrum, a binary classification
 1906 approach is explored.

1907 A model is built to determine whether $t\bar{t}H$ events include a high p_T (>150 GeV) or low
 1908 p_T (<150 GeV) Higgs Boson. While this is now a classification model, it uses the same input
 1909 features described in section 18.4. Binary crossentropy is used as the loss function.

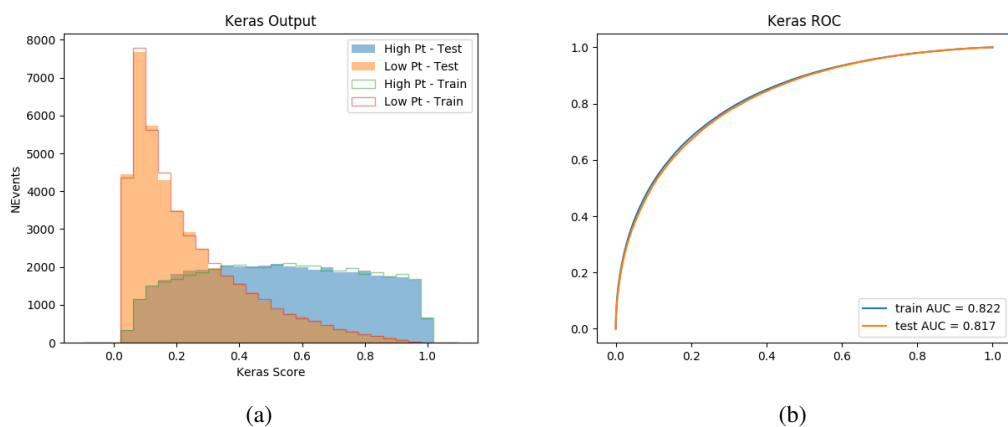


Figure A.26:

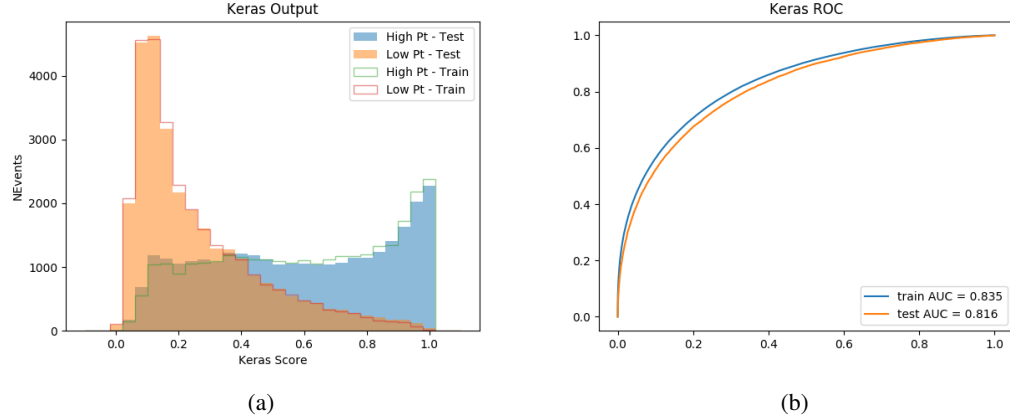


Figure A.27:

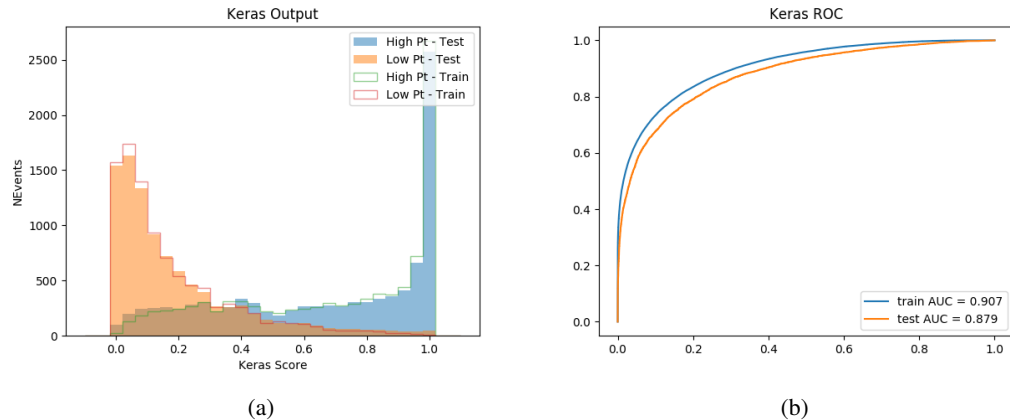


Figure A.28:

1910 A.5 Impact of Alternative Jet Selection

1911 A relatively low p_T threshold of 15 GeV is used to determine jet candidates, as the jets originating
 1912 from the Higgs decay are found to fall between 15 and 25 GeV a large fraction of the time. The
 1913 impact of different jet p_T cuts on our ability to reconstruct the Higgs p_T is explored here. The

1914 performance of the Higgs p_T prediction models is evaluated for jet p_T cuts of 10, 15, 20, and 25

1915 GeV.

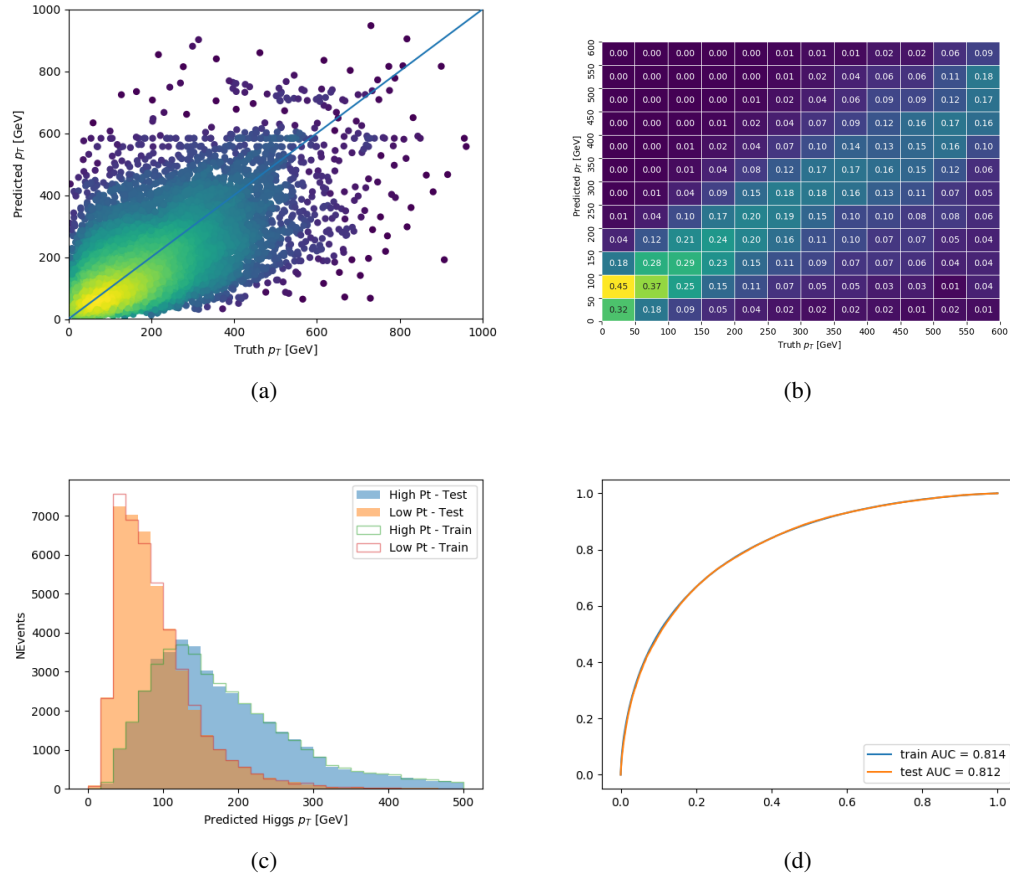


Figure A.29:

1916 **B**